INTERNATIONAL METALS REVIEWS

1979 Vol. 24 Nos. 5 and 6

Dendrite growth in eutectic alloys: the coupled zone
W. Kurz and D. J. Fisher

Near-threshold fatigue-crack propagation in steels
R. O. Ritchie

Practical aspects of electroslag remelting technology
A. Mitchell and R. M. Smailer

INTERNATIONAL METALS REVIEWS

1979 Volume 24 Numbers 5 and 6

International Metals Reviews

1979 Volume 24 Numbers 5 and 6

CONTENTS

INHALTSVERZEICHNIS

Eutektisch zusammengesezte Gußlegierungen sind von großer praktischer Bedeutung. Um die geforderten Eigenschaften im gegossenen Zustand zu erlangen ist eine gute Steuerung der Mikrostruktur dieser Legierungen erforderlich. Die im eutektischen Grundmaterial vorhandenen primären Phasen können diese Eigenschaften im guten und im schlechten Sinne beeinflussen. Ihr Aussehen muß daher genau kontrolliert werden. Dieser Aufsatz behandelt die Grundsätze und die jüngsten Fortschritte in unserer Erkenntnis des Bereichs des eutektischen Wachstums — der Kupplungszone. Wegen der naturgegebenen Schwierigkeiten und der Unmöglichkeit, mittels der Stabilitätsanalyse die eutektischen bis eutektisch plus dendritischen Übergänge vorauszusagen, wird hier die einfachere Methode des 'competitive growth' (konkurrierendes Wachstum) dargestellt. Da diese eine unabhängige Betrachtung eutektischen und des dendritischen Wachstums voraussetzt, wird zunächst die Theorie dieser Wachstumsformen beschrieben (für $G \geqslant 0$). Sodann wird das Prinzip des konkurrierenden Wachstums angewandt, d.h. das Prinzip, daß die im Mikrogefüge aufscheinenden Morphologien jene sein werden, welche die höchste Schnittflächentemperaturen oder die höchste Wachstumsrate haben (abhängig davon ob die Wachstumsrate oder das Unterkühlen die gesteuerte veränderliche Größe ist). Auf Grund dieser Theorie wird eine Abänderung der eutektischen Einstufung vorgeschlagen. Nach einer Behandlung der, zur Bestimmung der Form und des Ausmaßes der Kupplungszone, vorhandenen experimentellen Methoden, werden die experimentellen Ergebnisse mit der Theorie verglichen. Bezüglich der Gründe für das Vorhandenseins verschiedener Formen von Kupplungszone werden Schlußfolgerungen gemacht.

Die Kennzeichen der Daueranrißausbreitung in Stählen und Legierungen sind in den letzten Jahren Gegenstand mehrerer eingehender Studien gewesen, doch wurden in nur wenigen Fällen die Einzelheiten der sehr langsam wachsenden, schwellennahen Dauerrißausbreitung behandelt. Der Aufsatz untersucht die Einflüsse verschiedener mechanischer, mikrostruktureller und Umweltfaktore welche die Ausbreitung der Daueranrisse beeinflussen, welche in Stählen eine Wachstumsrate von weniger als 10^{-6}mm/Zyklus haben, wo die abwechselnde Belastungsintensität ΔK sich der sogenannten Belastungsschwellenintensität nähert ΔK_0, unter welcher das Wachstum von Rissen experimentell nicht mehr festzustellen ist. Der betonte Einfluß von Belastungsverhältnis. Materialstärke und Mikrogefüge auf ein solches schwellennahes Wachstum wird eingehend analysiert und als Funktionen möglicher Umwelteinflüsse und Rißverschließungskonzepte gedeutet. Diese Einflüsse werden mit dem Rißausdehnungsverhalten anderer technischer Stoffe mit schnellerem Wachstum verglichen.

Mehrere Gesichtspunkte des Elektroschlacken-Umschmelzverfahrens (ESU) werden von einem praktischen Standpunkt aus untersucht. Dazu gehören eine Besprechung der praktischen Maximalgröße der ESU Einrichtung; die Elektroschlacken-Gußtechnik; ESU Gußform Konstruktion und Schlackenschmelzverfahren.

TABLE DES MATIERES

Les alliages moulés de composition eutectique ont une grande importance pratique. Un bon réglage de la microstructure de ces alliages est essentiel pour obtenir les propriétés requises à l'état moulé. Les phases primaires présentes dans une matrice eutectique peuvent avoir un effet bénéfique ou désavantageux sur ces propriétés. C'est pourquoi il convient de régler soigneusement leur apparition. Cet article décrit les principes et les progrès récents dans notre connaissance de l'étendue de la croissance eutectique — la zone couplée. En raison des difficultés inhérentes et de l'impossibilité actuelle d'utiliser les analyses de stabilité pour prédire les transitions eutectique — eutectique et dendrite, il est présenté ici la solution plus simple de la 'croissance compétitive'. Comme celle-ci implique la considération séparée des croissances eutectique et dendritique, on traite d'abord de la théorie de ces formes de croissance (pour $G \geqslant 0$). On applique ensuite le principe de la croissance compétitive, c'est-à-dire le principe que les morphologies apparaissant dans la microstructure dans des conditions données seront celles ayant la température interfaciale la plus haute ou la vitesse de croissance la plus élevée (selon que la variable réglée est la vitesse de croissance ou la surfusion). En se basant sur cette théorie, il est proposé une classification modifiée des eutectiques. Après avoir discuté des techniques expérimentales utilisables pour déterminer la forme et l'extension de la zone couplée, on compare les résultats d'essai avec la théorie. Des conclusions sont tirées sur les raisons des différentes formes de la zone couplée.

Dendrite growth in eutectic alloys : the coupled zone

by W. Kurz and D. J. Fisher

Casting alloys of eutectic composition are of great practical importance. Good microstructural control of these alloys is essential in obtaining the required properties in the cast state. Primary phases present in a eutectic matrix may have either a beneficial or a detrimental effect on these properties. Therefore, their appearance must be carefully controlled. In this review the authors describe the fundamentals and recent advances in the understanding of the extent of eutectic growth — the coupled zone. Because of the inherent difficulties and the present inapplicability of stability analyses to predicting eutectic to eutectic plus dendrite transitions, the simpler 'competitive growth' approach is presented in this review. As this involves separate consideration of eutectic and dendrite growth, the theory of these growth forms for temperature gradients is first reviewed. The competitive-growth principle is then applied, i.e. the principle that the morphologies appearing in the microstructure, under given conditions, will be those having the highest interface temperature or the highest growth rate (depending on whether growth rate or undercooling is the controlled variable). On the basis of this theory, a modified classification of eutectics is proposed. After discussion of the experimental techniques available for determining the form and extent of the coupled zone, the experimental results are compared with theory. Conclusions are drawn concerning the reasons for the various forms of coupled zone.

LIST OF SYMBOLS

A	= constant in equation (2)
C	= concentration, wt-%, at.-%
C_B	= concentration of component B
C_e	= eutectic concentration, wt-%, at.-%
C_0	= initial alloy composition, wt-%, at.-%
C^*	= interface (tip) composition, wt-%, at.-%
ΔC	= range of concentration (equation (3)), wt-%, at.-%

The authors are in the Department of Materials Engineering, Swiss Federal Institute of Technology, Lausanne, Switzerland.

D	= diffusion coefficient of solute in liquid, mm^2s^{-1}
E_1	= exponential integral
erfc	= complementary error function
G	= temperature gradient, Kmm^{-1}
I	= nucleation rate, $mm^{-3}s^{-1}$
k	= distribution coefficient
K_i	= constants
L	= latent heat of fusion, Jmm^{-3}
m	= liquidus slope, $K (\%)^{-1}$
P	= Péclet number ($= RV/2D$)
r	= exponent in equation (9)
R	= tip radius of needle or plate, mm
s	= exponent in equation (10)
t	= time, s
T	= temperature, K, °C
T_e	= eutectic temperature, K, °C
T_i	= interface temperature, K, °C
T_l	= liquidus temperature, K, °C
T_q	= measurable temperature due to heat flow in system, K, °C
T_s	= solidus temperature, K, °C
ΔT	= temperature difference, undercooling, temperature, K
v_f	= volume fraction of minor eutectic phase
V	= growth rate of solid, mms^{-1}
w	= exponent in equation (21)
z	= distance perpendicular to solid/liquid interface, mm
θ	= Gibbs—Thompson coefficient ($= \sigma T_l/L$), Kmm
κ	= thermal conductivity, $Wmm^{-1}K^{-1}$
λ	= interphase spacing, μm
λ_{branch}	= spacing at which branching of faceted phase occurs, μm
λ_{ext}	= spacing which minimizes undercooling or maximizes growth rate, μm
σ	= specific interfacial energy, Jmm^{-2}
Ω	= supersaturation (equation (16))

For constants used for calculating the coupled zones shown in this paper, see Appendix 1.

Subscripts

n	= needle
p	= plate

The *aim* in this paper is to review the coupled-zone theory (alternatively described as the eutectic range) because its principles are of great importance in the field of microstructural control. Since the last review of the subject[1] many new facts have emerged and considerably increased

our understanding of it. Indeed, the whole theory must now be viewed in a completely different light. It will be shown, moreover, that although the coupled-zone principle is simple, a number of misconceptions concerning it still exist.

Eutectic alloys are extremely important in the casting industry (and in this one can include welding and soldering), owing to their peculiar characteristics, e.g.

(i)   their low melting points, compared with those of the pure components, which simplify melting and casting and result in lower energy consumption and less crucible erosion

(ii) their excellent flow properties, and better feeding behaviour owing to the smoother solid/liquid interfaces which are comparable to those of pure metals, when no primary dendrite formation occurs to obstruct partially solidified channels

(iii) the possibility of *in situ* formation of fine, homogeneous, two-phase alloys having composite properties: e.g. the combination of Fe and C in cast iron leads to many interesting properties, and this eutectic complements steel advantageously in cases where friction/dry lubrication, thermal, and damping properties, etc. are important

(iv) the growth of a lower density second phase such as C from a metallic solution of eutectic composition, which may help to decrease solidification contraction and its associated feeding problems.

Among the most common eutectic or near-eutectic alloys used in industry are:

cast iron (grey and white)

Al—Si (Silumin) casting alloys

wear-resistant welding alloys

solders.

Furthermore, directionally solidified eutectic alloys[2] will possibly increase in importance as the present generation of high-temperature materials reaches its operating limit. Another evolving area is the use of finely dispersed, two-phase alloys in superplastic forming. Finally, there is the closely related eutectoid transformation which is of importance in pearlitic steels and also exhibits a zone of coupled growth.[3] In all these areas, microstructural control is an essential aspect of production because it permits the fabrication of parts having specific properties. In the context of this review, structure control will be taken to mean only those steps which control the appearance or absence of primary phases (dendrites) in the microstructures of alloys of approximately eutectic composition (Fig. 1).

In order to obtain the desired mechanical properties, high cooling rates must often be used. High rates imply growth far from equilibrium. Therefore, it is not surprising that one observes,

under such conditions, microstructures which do not reflect the characteristics of the phase diagram. For example, the two microstructures of Fig. 1 were obtained by solidifying at two different cooling rates. At the high rate, 'off-eutectic' structures (Al dendrites and eutectic*) are observed, although the alloy is of eutectic composition. To obtain the fully eutectic microstructure at this cooling rate, it would be necessary to increase the initial Si content.

The appearance of dendrites leads to marked micro-inhomogeneities because dendrite spacings are generally some 10 times the eutectic interphase spacing. Such microstructures can have a detrimental effect on the properties. For example, high creep rates would result in directionally solidified eutectics. In brittle alloys, on the other hand, ductile dendrites can greatly increase the fracture energy.[5] It is important, therefore, to know what conditions lead to wholly eutectic, or to eutectic plus primary phase microstructures.

At present, it is still impossible to calculate such transitions for a casting with equiaxed solidification because of the time dependence of all the variables involved. In this review, therefore, the authors will treat mainly theory and experiments concerning steady-state *directional solidification*, a method which has furnished a large number of unambiguous results. By neglecting nucleation phenomena, and treating stationary states, a clearer insight can be obtained into the growth behaviour of alloys. This, in turn, will lead to a better qualitative understanding of real cast structures.

Before going into more detail, one must recall some important differences between equiaxed and directional solidification (Fig. 2, Table 1). The main points distinguishing equiaxed from directional solidification are that, in the former case:

(i)   the temperature gradient at the solid/liquid interface is negative

(ii) nucleation in the remaining melt accompanies growth

(iii) growth is radial

(iv) the growth rate varies

(v)   variation of the solidification conditions and the generally small grain size do not allow a steady state to be obtained.

Therefore, the results and conclusions drawn from directionally solidified specimens cannot be applied directly to the situation prevailing in an equiaxed structure, but should apply quite well to the columnar zone of a conventional casting.

The *coupled zone* is defined as the range of conditions (generally composition and undercool-

---

*In the review, the adjective 'eutectic' will be applied to microstructures arising from coupled, two-phase growth.
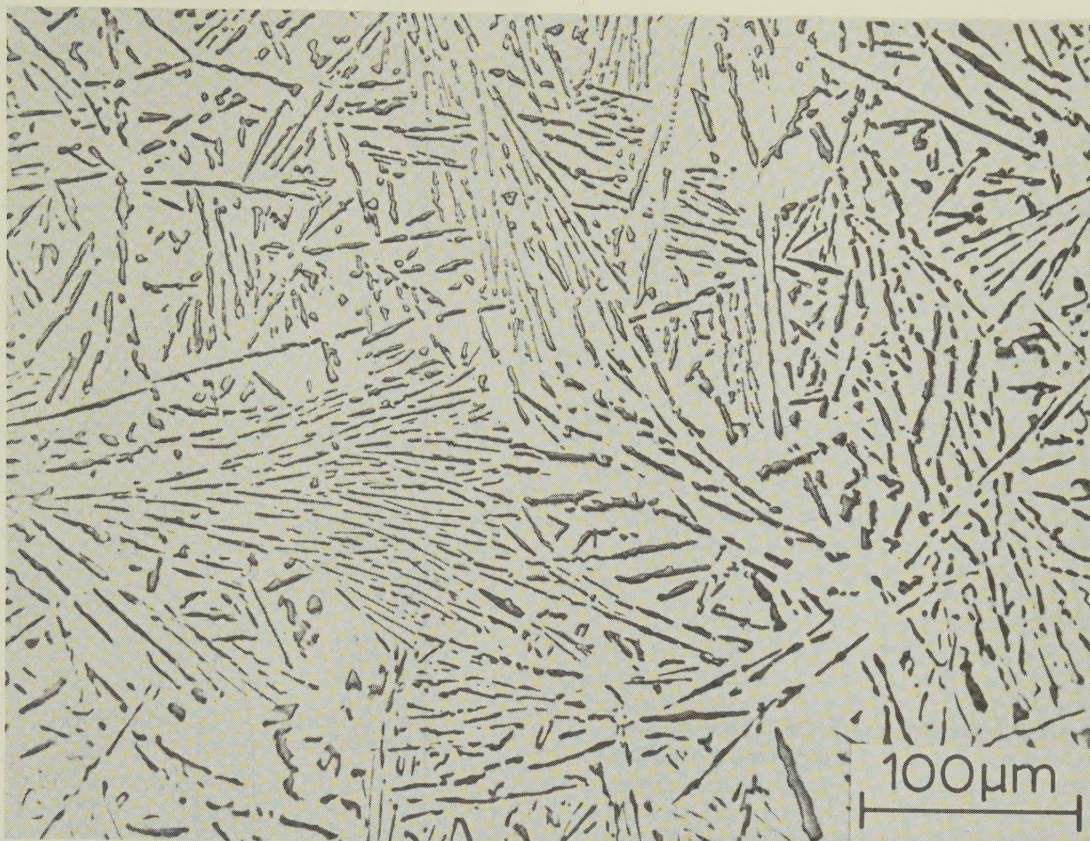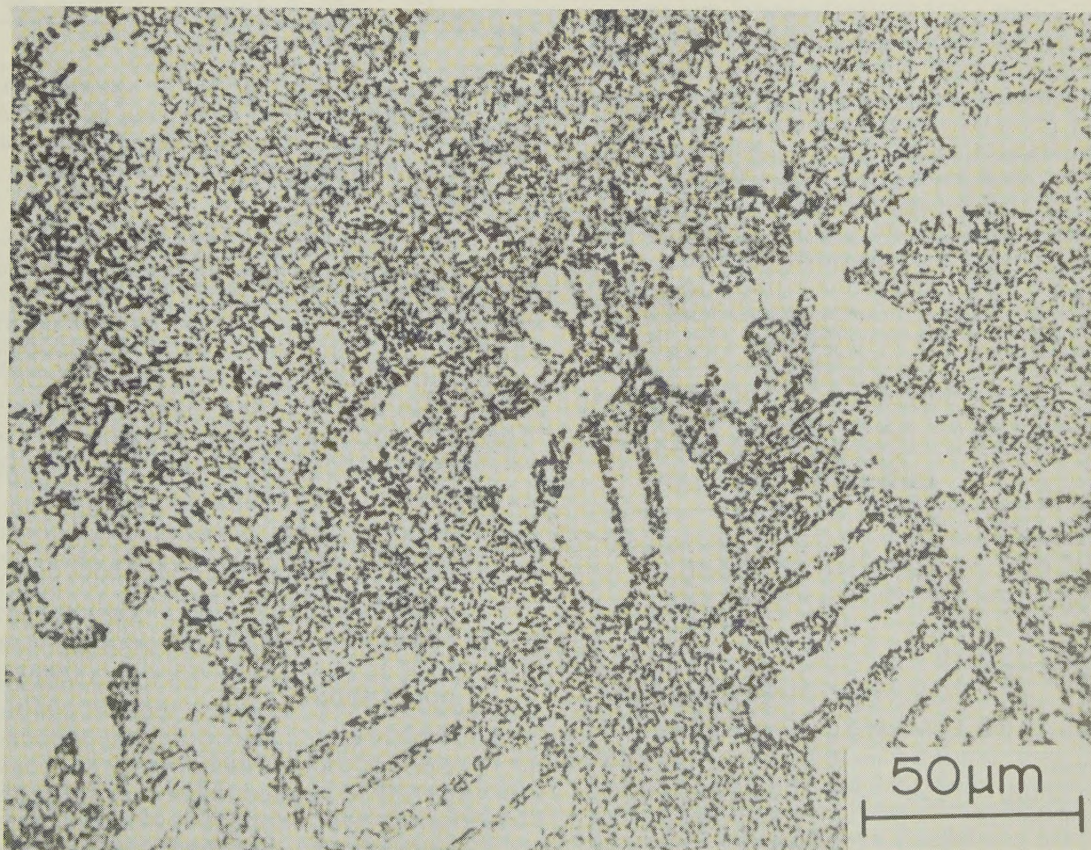
1 Al—12. 5 wt-%Si alloy *a* after slow cooling, showing only coarse and irregular eutectic, and *b* after chill casting, showing fine eutectic and primary Al dendrites due to skewed coupled zone[4]
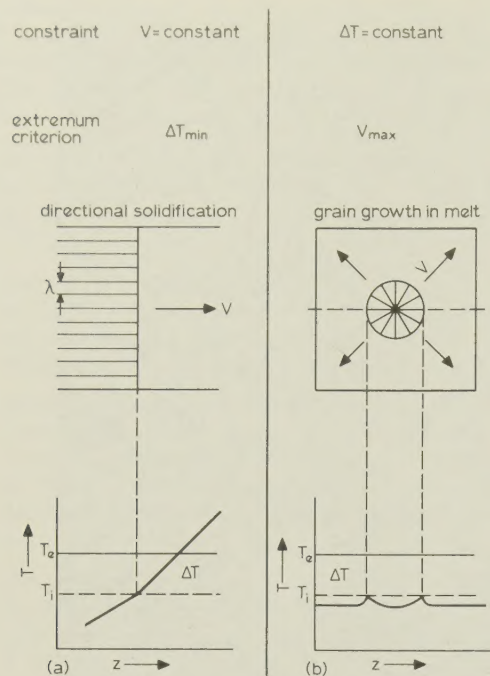
2   Schematic comparison of growth conditions during *a* directional and *b* equiaxed solidification: *see also* Table 1

ing values) which produces a wholly eutectic structure, i.e. without primary crystals. It will be seen below that the relative interface temperatures at a given growth rate, or relative growth rates, at a fixed undercooling, determine what morphology prevails under these non-equilibrium conditions. Metallurgists[6] had already ascribed to 'surfusion', such phenomena as the apparent 'wandering' of the eutectic point in the Al—Fe system.[7] However, the history of the coupled-zone concept really began with the work of Tammann and Botschwar,[8] who studied the growth rate, as a function of undercooling, in organic systems. From the results, it was seen that in a certain

Table 1   Principal differences between directional and equiaxed solidification

	Directional	Equiaxed
Process variable (imposed)	$V_{crucible}$	ΔT_{melt}
Internal variable (free)	ΔT	I, V
Evacuation of latent heat	Through solid	Through liquid and solid
Temperature gradient at solid/ liquid interface	> 0	< 0
V	~ const.	Varies with I and ΔT
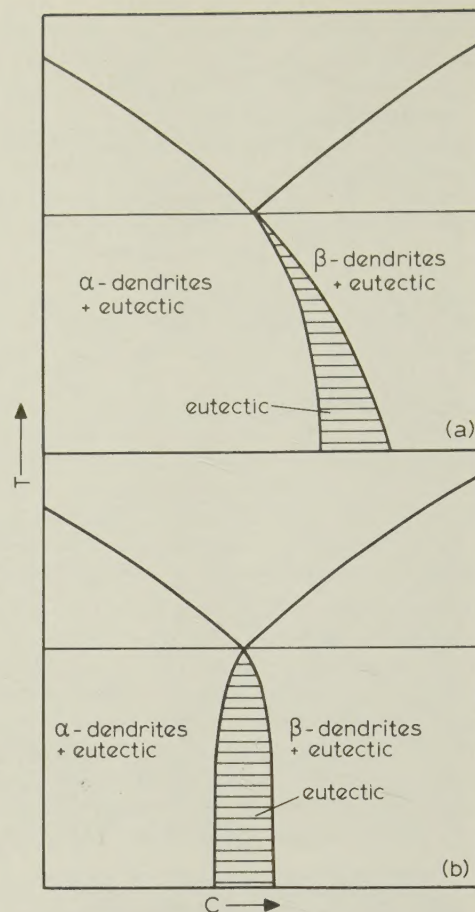
3   Two types of coupled zone: *a* skewed zone typical of certain nf—f systems such as Al—Si, Fe—C (Kofler's A zone); *b* symmetric zone typical of nf—nf systems such as Pb—Sn (Kofler's B zone)[13]

range (eutectic range), the eutectic could grow faster than primary crystals, thus stifling them. Thus, fully eutectic structures could be observed at compositions removed from the equilibrium eutectic point. This discovery of 'quasi-eutectic syncrystallisation' was followed up by Kofler and developed in an interesting series of publications[9–15] on organic eutectic growth. She showed that, in binary organic systems, three main types of coupled zone were possible:

A: skewed (Fig. 3*a*)

B: approximately symmetric about the eutectic composition (Fig. 3*b*)

C: mixed (this type has not yet been shown to exist in metallic alloys, and is ignored in what follows).

Before returning to metallic growth, it is interesting to note that coupled-zone theory has recently found a practical application in organic systems. Knowledge of these zones is essential in certain methods of radiation copolymerization.[16]

In 1967, Hunt and Jackson[17] extended Kofler's approach to metals (Pb—Sn). At the same time, a
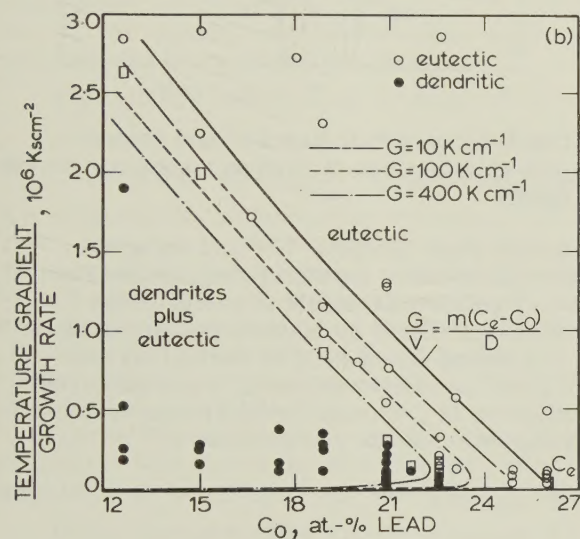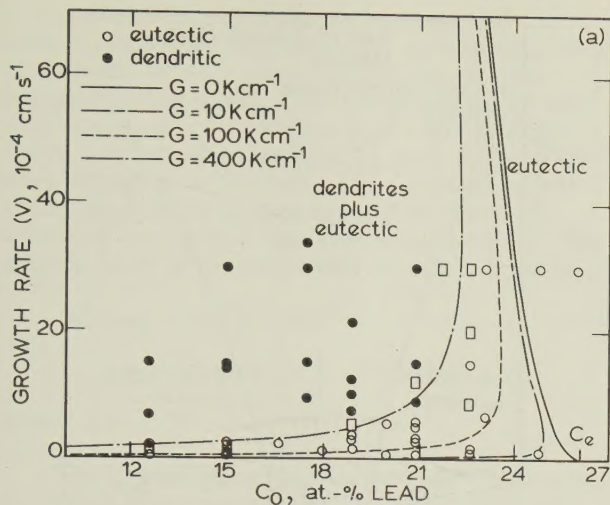
a V—C diagram for high V; b G/V—C diagram for low V, high G/V ratio

4 Coupled zone of Pb–Sn system as determined experimentally by Mollard and Flemings[18]: lines are first theoretical calculation of whole zone (low *and* high velocity) by Jackson[19]

series of exciting experiments was performed by Mollard and Flemings,[18] who showed that the widening of the coupled zone was not restricted to high growth rates but, with a positive temperature gradient, could also be obtained at low growth rates (high G/V ratio). These authors explained their results using simple constitutional super-cooling arguments.

Jackson[19] was the first to realize that both the Hunt and Jackson[17] theory (for directional solidification at high V) and the Mollard and Flemings[18] results (for high G/V) could be explained by calculating the local growth conditions separately for both eutectic and dendrites, and comparing the corresponding growth rates. Jackson's results, compared with the measurements of Mollard and Flemings, are shown in Fig. 4.
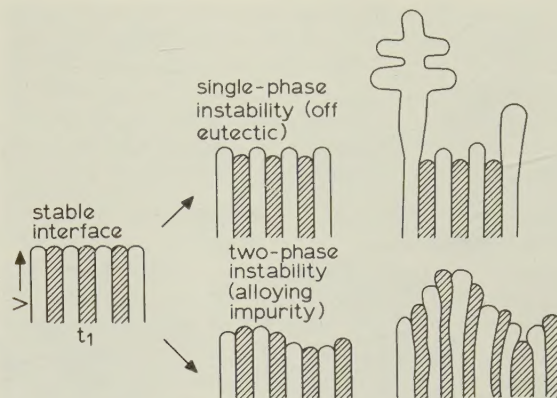
5 Two types of instability which may develop from plane, eutectic interface shown at left: single-phase instability to be expected on crossing vertical curves of Fig. 6; two-phase instability to be expected on crossing horizontal line in Fig. 6

Since that time, the theory has been further developed and will be treated in the sections below. The main difference between Jackson's approach and the newer one[20-22] is that Jackson calculated the dendrite growth rate using the constitutional supercooling ahead of the eutectic interface, whereas the newer theories calculate dendrite and eutectic growth rates independently (but include the temperature gradient in the growth law for the dendrite tip).

PRINCIPLES OF COUPLED-ZONE THEORY

The coupled zone represents the range of growth conditions within which morphologically stable, two-phase growth can be obtained. Such a stable interface is shown in Fig. 5, together with two possible types of morphological instability:

(i) single-phase instability: one of the two eutectic phases grows out from the eutectic interface, leading to a microstructure consisting of primary dendrites and eutectic. At medium growth rates, this form of instability is due to an off-eutectic composition of the melt

(ii) two-phase instability: when a third element is rejected by both phases, then generally at some critical G/V ratio, the plane front will break down to give eutectic cells or eutectic dendrites.

In coupled-zone theory, only the first type of instability (single phase) is treated.

To describe, quantitatively, the transition, from pure eutectic to eutectic and dendrites in the manner of Mullins and Sekerka,[23] would be a formidable task of mathematical physics. Cline[24] attempted this under the simplifying assumption that only long wavelength terms were important. This assumption was suggested to be incorrect by

Jordan and Hunt.[25] Their results on quenched interfaces seemed to show that the very first instabilities had a wavelength very close to that of the eutectic spacing. Only later were most of these instabilities overgrown by other, preferred, ones. This led to a dendrite spacing which was coarse when compared to the eutectic one.

Hurle and Jakeman[26] described a model in which the first instabilities had a wavelength of the same order as the lamellar width. However, they were not convinced that the results were realistic and did not pursue this line of thought. Strässler and Schneider[27] found, theoretically, that both short- and long-wavelength perturbations are important.

Because of this complication, the problem of calculating the coupled zone can, at present, be solved only by a much simpler approach (and one which is often resorted to in the field of phase transformations). It consists of four steps:

(i)   consider all the growth forms possible in the fully developed stationary state (in the present case, primary α- and β-crystals and eutectic)

(ii)   analyse the growth kinetics of these forms

(iii)   determine the interface temperatures of the growth forms as a function of V and (if necessary) G

(iv)   apply the competitive-growth principle,[8] i.e. suppose that the growth form having the highest interface temperature (lowest undercooling) will be the one preferred by the system.*

By using this approach, one can predict the growth morphology (wholly eutectic, or eutectic and primary phase) as a function of growth rate, melt composition, and temperature gradient (Fig. 6). As mentioned above, the result of increasing G is a widening of the zone at low growth rates corresponding to a decrease of single-phase instability (Fig. 5). At the same time, this will also shift the limit of planar composite growth (horizontal line in Fig. 6) to higher growth rates, corresponding to a decrease in two-phase instability (Fig. 5).

Burden and Hunt[20] proposed a new and elegant approach to calculating diagrams of the type shown in Fig. 6 (not taking into account the planar—cellular eutectic transition). On the basis of their earlier work on dendritic solidification in a posi-

---

*Tammann and Botschwar observed differences in growth rate of different growth forms as a function of T, and found that those structures developed which had the highest V for a given ΔT. This criterion of competitive growth is analogous to stating that the observed structures have a minimum of undercooling for a given growth rate. It is a very similar principle to that of bifurcation theory[28] in mathematical physics, but has not been rigorously justified.
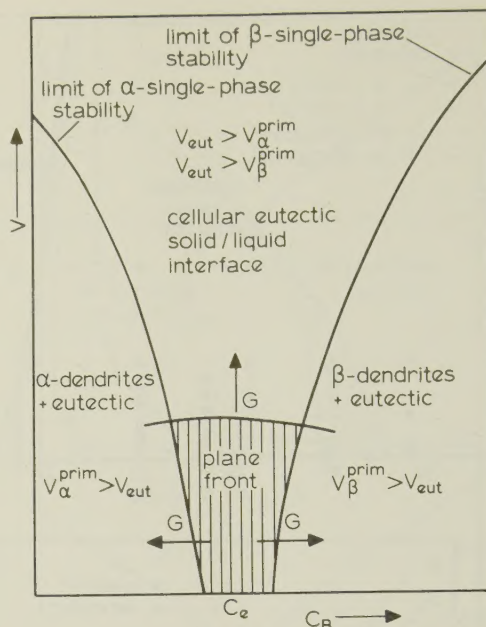
6   Coupled zone (V—C diagram) and growth-rate relationships of various competing growth forms

tive temperature gradient[29,30] and using the solution for eutectic growth of Jackson and Hunt,[31] the latter authors were able to calculate the growth temperatures of dendrite tips and eutectic as a function of G and V. (For normal eutectic growth with an isothermal solid/liquid interface, the influence of G is neglected.) The undercooling of the eutectic interface is given by[31]

$$\Delta T_{\text{eut}} = K_1 V^{0.5} \quad . \quad . \quad . \quad . \quad . \quad . \quad . \quad . \quad (1)$$

a symmetric zone; *b* skewed zone
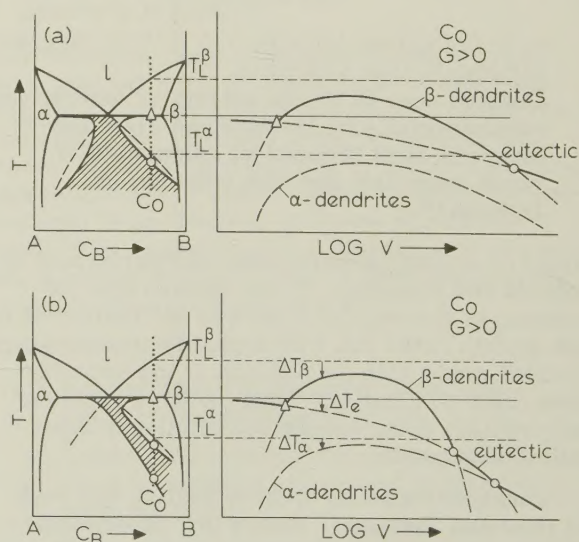
7   Coupled zone (T—C diagram) and temperature—V diagrams for different zone types: note that factors causing the difference between *a* and *b* are the different eutectic and β-dendrite behaviours in the two cases

The undercooling of dendrite tips obeys a similar growth law as far as isothermal growth ($G = 0$) is concerned. When growth occurs in a positive temperature gradient, their temperature—growth rate curve shows a maximum, and the eutectic curve may be cut twice (Fig. 7), once at low and once at high growth rates. The maximum of the curve for a dendrite lies somewhat below its stable or metastable liquidus temperature.[29] The overall form of the curve for dendrites is given by

$$\Delta T_{dend} = GD/V + K_2 V^{0.5} \quad \ldots \quad (2)$$

$$K_2 = A[-mC_0(1-k)\theta/D]^{0.5}$$

where $A = 2.83$.

The growth equations, (1) and (2), for an alloy C_0 with a phase diagram of the type shown are represented graphically at the right-hand side of Fig. 7. The 'equilibrium' solidification temperatures for the three growth forms are:

β-dendrites: stable liquidus temperature

α- and β-eutectic: eutectic temperature

α-dendrites: metastable liquidus temperature.

For a symmetric coupled zone, the form of the T—V curves for α- and β-primary crystal growth are very similar, simply being shifted with respect to each other along the temperature axis, to a degree which depends mainly on the composition (Fig. 7a). For a skewed zone, the curves are rather different; it is easy to see from Fig. 7b that in order to give a skewed zone, the rate of change of undercooling with velocity for the β-phase must be greater than that of the eutectic, and that of the eutectic must be greater than that of the α-phase.

Using the competitive-growth principle, together with equations (1) and (2), Burden and Hunt[20] obtained the 'half-width' (eutectic composition to zone boundary) of the symmetric zone

$$\Delta C = (1/m)[GD/V + (K_2 - K_1)V^{0.5}] \quad . \quad . \quad (3)$$

The coupled zone of Fig. 7a is of Kofler B type (Fig. 3b). The symmetry is characteristic of the normal[32] eutectic growth which one generally finds in simple metal—metal eutectics (e.g. Pb—Sn, Ag—Cu, etc.).

In the casting industry, the so-called *anomalous eutectics* — faceted and non-faceted (f—nf) eutectics growing by weak diffusive coupling — are of much greater importance (e.g. Fe—C, Al—Si). These eutectics often exhibit skewed coupled zones (Figs. 3a, 7b), a type of zone which cannot generally be predicted using the Burden and Hunt dendrite model. The reason for this will become apparent later in the review.

Fisher and Kurz[22,33] have suggested that the reason for the peculiar behaviour of f—nf eutectics is twofold:

(i) the solid/liquid eutectic interface of Al—Si or Fe—C is not isothermal (Fig. 8b). This

a

b
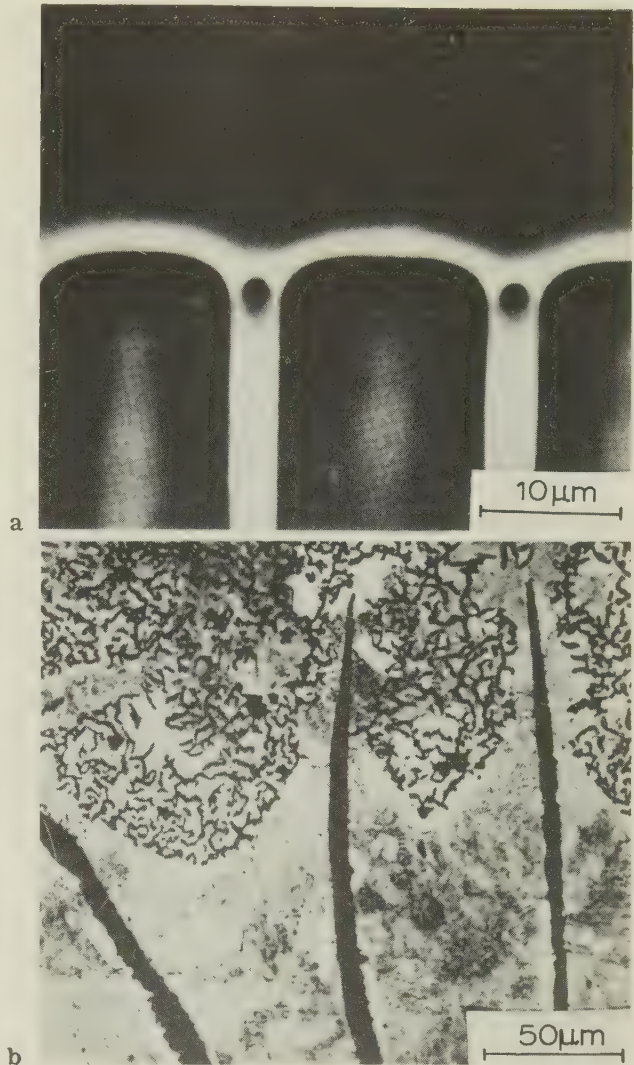
8 Eutectic interfaces of *a* class I eutectic (hexachloroethane/carbon tetrabromide[31]) and *b* class II eutectic (Fe/graphite[34])

markedly changes the ΔT—V relationship and also leads to an influence of the temperature gradient on ΔT and λ

(ii) the primary crystals of the faceted phase are no longer dendrites (needle form, Fig. 9a), but rather plates (Fig. 9b).

The authors propose a refined classification which takes into account the differences in the growth forms observed experimentally between different alloys (Table 2):

(i) *class I eutectics* comprise systems involving non-faceted components, having a low entropy of fusion (metals, plastic crystals). The isotropy of growth of these phases permits the eutectic structure always to grow close to the optimum (strongly coupled growth and easy branching)

(ii) *class II eutectics* comprise systems of the faceted and non-faceted type (one phase having

500μm

500μm
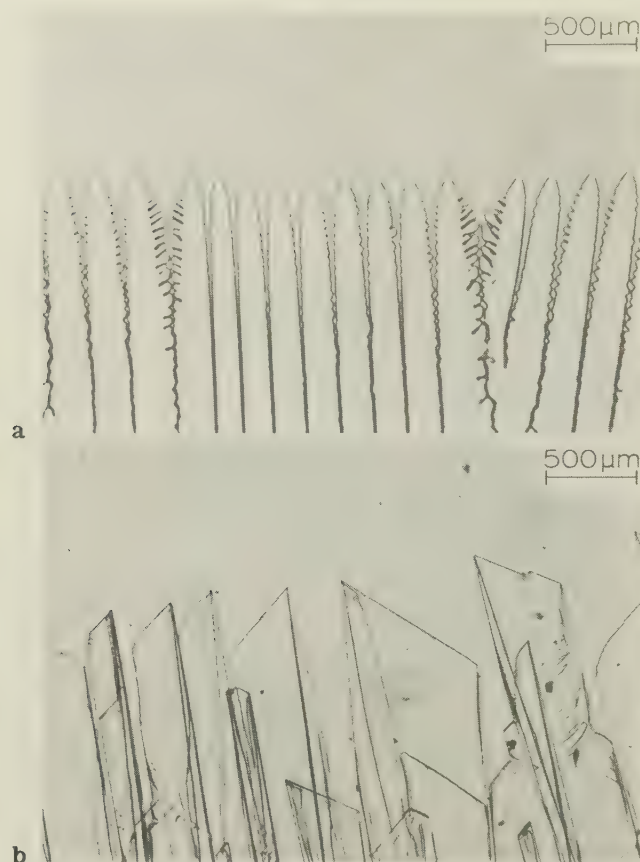
9   **Primary crystals: *a* needles (dendrites) of non-faceted pivalic acid, *b* plates of faceted naphthalene; $V \sim 3 \times 10^{-2}$ mms^{-1} (Ref. 22)**

a high entropy of fusion like C or Si). However, only faceted phases having a marked anisotropy of growth (owing either to the crystal structure or to certain defect growth mechanisms) will fall into this class because they lead to branching difficulties. Difficulties in branching of one phase will not allow the system to grow at the optimum but only at the

limit of stability for branching of the faceted phase.[33,35]

Eutectics of the f—nf type with isotropically growing faceted phases will fall into class I. As shown (Table 2), different systems will behave differently during solidification depending on whether the eutectic is of class I or II and whether the primary phases grow as needles or plates. Class II eutectics will always have irregular and coarse structures while the appearance of one primary phase as plates will lead to a skewed coupled zone.

EUTECTIC GROWTH

In the section above it has been shown that to calculate the coupled zone, one has to know the morphology of the eutectic interface. The morphology can generally be deduced from the as-solidified microstructure: class I eutectics (with isothermal interfaces) usually have regular structures which show, after directional growth, substantial structural perfection. Class II eutectics have non-isothermal interfaces which lead to very irregular structures as seen in the well known cast iron and Al—Si eutectics (Fig. 1*a*). The growth laws of each of these classes of eutectic are different and will be treated separately.

Class I eutectics

These regular eutectics (solid/liquid interface of the type shown in Fig. 8*a*) exhibit 'strong diffusion coupling'; this makes the mathematical model for their growth much easier to solve than that of class II eutectics. The expression 'strongly diffusion coupled growth' is often used, but does not really describe their principal characteristic. A definition in terms of branching tendency is more pertinent because, as will be shown below, the branching behaviour of eutectic phases determines the criteria to use in solving the problem theoretically. It is proposed that class I should be defined as easy branching eutectics. In this case, variation of interphase spacing is easy and allows

Table 2   Classification of eutectic systems according to growth forms of eutectic and primary phases

| Primary phases | Eutectic | |
	Class I	Class II
	Growth strongly coupled Structure regular, fine	Growth branching-limited Structure irregular, coarse
Growth form (α-needle, β-needle) resulting in symmetric coupled zone	Pb—Sn	. . .
	Ag—Cu	. . .
Growth form (α-needle, β-plate) resulting, together with class II eutectic, in skewed coupled zone	Fe—Fe$_3$C	Fe—C
	. . .	Al—Si

the alloy to adapt its morphology so as to be always close to the optimum growth morphology. Milestones in the understanding of class I eutectic growth are the papers by Zener,[36] Hillert,[37] Tiller,[38] and Jackson and Hunt.[31] According to these theories, eutectic-type growth can be considered to involve competition between two opposing effects:

(i)   diffusion in the untransformed matrix or liquid, where the growing phases are sources or sinks with respect to the diffusing elements. The diffusion boundary layer and, hence, the solute undercooling ΔT_{sol} would be zero at zero phase separation

(ii) interface energy, which would 'prefer' complete separation (no curvature) of the two phases in order to decrease the (reversible) excess energy content of the material.

These two opposing effects are usually quantified by assigning to each of them a contribution to the total undercooling of the eutectic (under steady-state growth at a fixed velocity), thus:

$$\Delta T_{tot} = \Delta T_{sol} + \Delta T_{curv} \quad \cdots \quad (4)$$

where ΔT_{tot} is the undercooling which is actually measured in an experiment, ΔT_{curv} is the undercooling due to the Gibbs—Thompson effect acting at curved interfaces, and ΔT_{sol} is the undercooling due to the local concentration in the liquid at the solid/liquid interface. (Here, the possible kinetic undercooling has been neglected because of its low value in low melting-entropy phases.)

The various analyses of the problem show that the magnitude of the average solute concentration, defining the solute undercooling, is directly proportional to the distance over which diffusion must take place, i.e. the spacing λ, and to the growth rate V, which determines how fast solute is rejected or absorbed at the interface. The curvature undercooling is inversely proportional to the spacing λ. Hence, the functional relationship between ΔT_{tot}, λ, and V becomes

$$\Delta T_{tot} = K_3 V \lambda + K_4 / \lambda \quad \cdots \quad (5)$$

where K_3 and K_4 are constants.

The only difference between the various analyses is the exactitude with which the solute diffusion and curvature effects have been represented mathematically, and merely results in different values for K_3 and K_4.

The form of equation (5) is shown in Fig. 10, where one may see clearly the opposing effects of solute and curvature undercooling. According to Tiller's[38] minimum undercooling criterion, the value of λ corresponding to the minimum of the curve should be the one preferred. Finding this minimum analytically, from equation (5), and
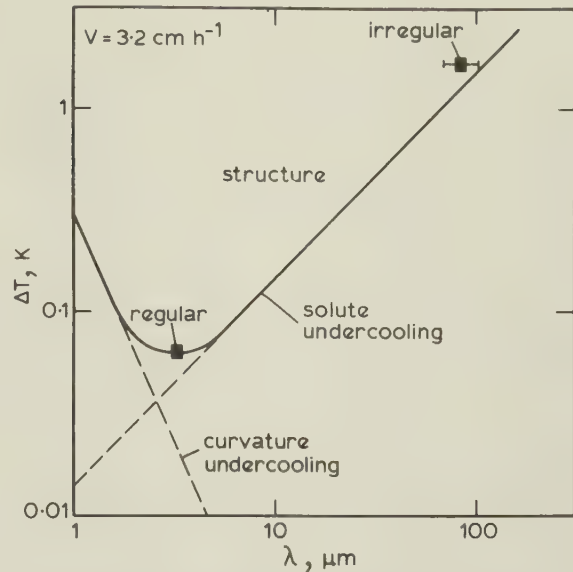
10   Undercooling ΔT as function of lamellar spacing λ for fixed growth rate: curve was calculated (Jackson—Hunt equation[31]) by fitting minimum to measured values of undercooling and spacing for regular camphor—naphthalene eutectic; irregularly growing eutectic which occurs at same composition shows much higher ΔT and λ values, but these lie almost on the theoretical curve: Jackson—Hunt theory, therefore, also seems to be applicable to irregular structures but the growth criterion is not the extremum criterion[35]

dropping the subscript to the total undercooling, one obtains

$$\lambda^2 V = K_4 / K_3 \quad \cdots \quad (6)$$

$$\Delta T / \sqrt{V} = 2\sqrt{K_3 K_4} = K_1 \quad \cdots \quad (7)$$

$$\Delta T \lambda = 2 K_4 \quad \cdots \quad (8)$$

Experimental values for the constants in equations (6) and (7) are given in Table 3.

As has been shown, especially by Tassa and Hunt,[21] this often-criticized theoretical criterion (analogous to the maximum growth rate criterion) can be experimentally verified with quite good precision, as far as easy-branching eutectic systems are concerned.

Class II eutectics

When one examines this class of irregular eutectic (solid/liquid interface of the type shown in Fig. 8b), one finds a striking difference in morphology compared with that of regular eutectics. Not only is the degree of regularity much lower, but the spacings are also much larger. In order to see this spacing difference clearly, one has to take account of the predicted[31] volume fraction dependence of eutectic spacings (Fig. 11). Using

Table 3 Experimentally determined spacing and undercooling results for eutectics

Eutectic	Spacing: $\lambda \sqrt{K_4/K_3} \ V^{-1/2}$ K_4/K_3, mm^{3}s^{-1}	Ref(s).	Undercooling: $\Delta T = K_1 V^{1/2}$ K_1, Ks$^{1/2}$mm$^{-1/2}$	Ref(s).
Ag—Pb	1.2×10^{-7}	39	4.4	39
Ag$_3$Sn—Sn	2.8×10^{-7}	39	4.2	39
Al—Al$_2$Cu	1.1×10^{-7}	39	0.73	39
	1.2×10^{-7}—1.4×10^{-7} (fn. of C_0)	21	3—3.4 (fn. of C_0)	21
Al—Al$_6$Mn	...		31.6	40
Al—Si	5.8×10^{-7}—3.1×10^{-6} (fn. of G)	41, 42	25.3—63.3 (fn. of G)	41, 42
Al—Zn	6.4×10^{-8}	39	1.5	39
			>18	43
Bi—Zn	6.9×10^{-8}	39	1.3	39
Cd—Pb	2.1×10^{-8}	39	2.6	39
Cd—Sn	7.2×10^{-8}	39	1.5	39
Cd—Zn	2.8×10^{-8}	39	1.5	39
Fe—C	5.6×10^{-6}	44	>100	45
Pb—Sn	2.5×10^{-8}	39	1.2	39, 46
	3.3×10^{-8}	47	4.1	47, 48
Sn—Zn	6.9×10^{-8}	39	8.2	39
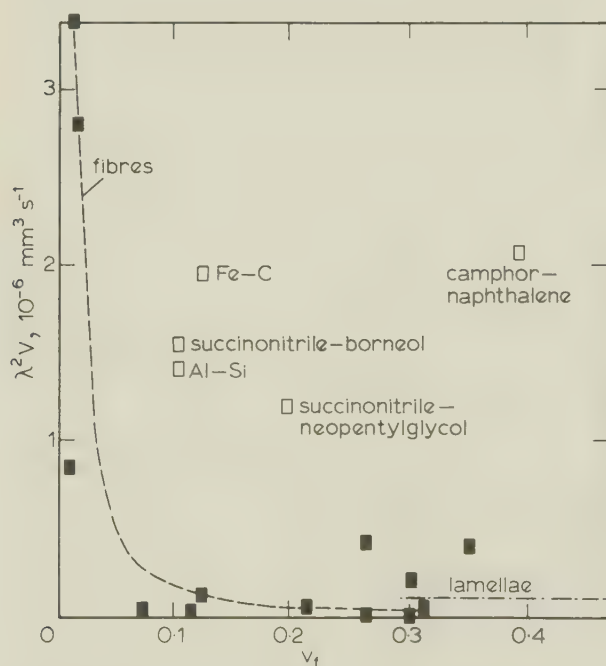
11 K_4/K_3 (equation (6)) as function of volume fraction of minor phase; dotted line is best fit to black points using Jackson—Hunt equations (below $v_f = 0.3$, rod eutectic, above $v_f = 0.3$, lamellar eutectic); large spacing of irregular eutectics is striking, e.g. Fe—C, Al—Si, succinonitrile—borneol, succinonitrile—neopentylglycol, camphor—naphthalene

these equations, it is seen that the Fe—C, Al—Si, and irregular organic eutectics will all have anomalously large spacings. This difference is less obvious in conventional log λ plots since some regular eutectics can have large spacings.[49,50]

By detailed study of organic eutectics, interesting facts were found which led to the development of a new theory.[35] The system, camphor—naphthalene, exhibits two distinct eutectic growth forms, one regular and one irregular. The experimental results on the λ—V relationship of the regular eutectic fit equation (6), which describes the growth of class I eutectics (Fig. 12a), very well. On the other hand, experimental spacing measurements on the irregular eutectic give much larger values. The coarseness of the structure has a direct effect on the undercooling of the growing eutectic. Assuming, as do Toloui and Hellawell,[41] that the non-optimized equation (5) holds for both regular and irregular structures, a coarse spacing will lead to a higher undercooling. Figure 10 shows that the theoretical relationship corresponds satisfactorily with experimental ΔT—λ values.[51] In Fig. 12b, the undercooling—growth rate relationship is given. A large magnitude for the constant K_1 (equation (7)) for the irregular eutectic is observed while the regular eutectic obeys the analysis. This difference in growth behaviour has a large influence on the extent of the coupled zone.

In order to explain the high undercooling for class II eutectics, a kinetic term has often been
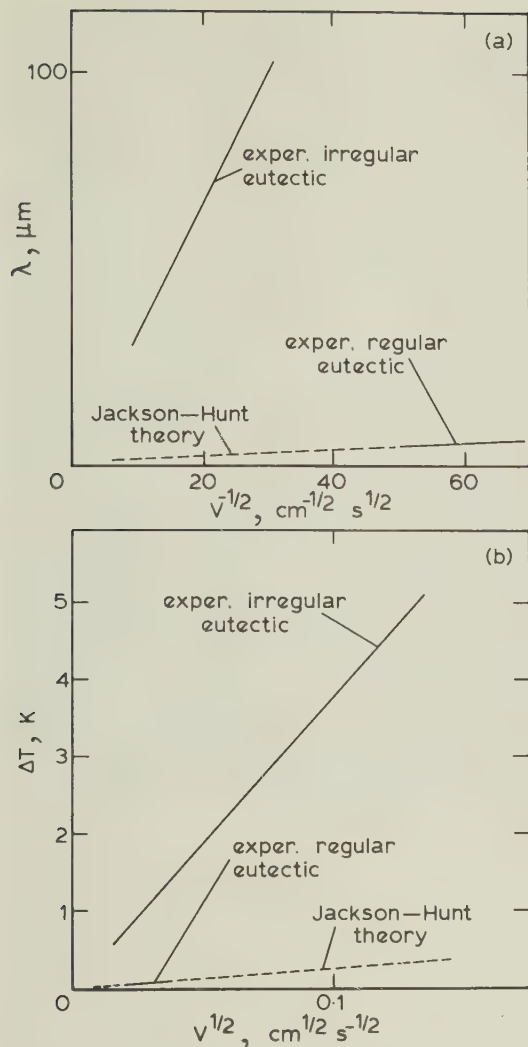
a interphase spacing as function of growth rate; *b* undercooling as function of growth rate

12 Comparison of theory (broken line) and experiment (solid line) for regular and irregular camphor—naphthalene eutectic

13 Growth criteria for eutectic structures: LCL (lower catastrophic limit) corresponds to extremum criterion; UCL (upper catastrophic limit) corresponds to breakdown of structure (Sundquist[58]); note development of depression in the low volume fraction phase at lower right; this is an instability which permits branching, and is proposed criterion determining spacing of class II eutectics[35]

introduced into equation (5).[52-55] However, it was shown,[56] for the growth of Si in eutectic Al—Si melts, that the kinetic undercooling of Si is much too low to explain the measured undercoolings. Fisher and Kurz[57] made careful measurements on organic substances, and also found relatively small faceted-phase undercoolings, compared to the high overall eutectic ones. The most reasonable explanation* for the latter is the high solute undercooling of a eutectic growing at spacings larger than the extremum value (an idea suggested for this class of alloy by Toloui and Hellawell[41]).
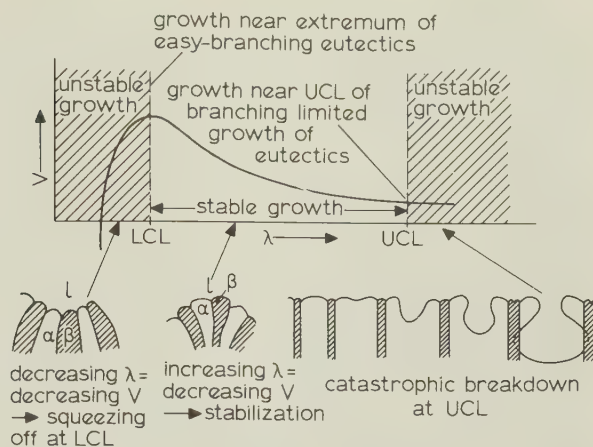
The reason proposed in the present review for non-optimum spacings is difficulty of branching of the faceted phase, arising from anisotropic

growth kinetics. Schematic solid/liquid interface morphologies are shown in Fig. 13, and indicate a large lag distance of the non-faceted phase when λ is large. Sundquist[58] defined an upper catastrophic limit (UCL), describing the situation in which the non-faceted phase's solid/liquid interface either touched the faceted phase (Fig. 13, lower right), or trapped a volume of melt. These cases corresponded to two possible interpretations of the 'breakdown' of the interface morphology equations at large spacings. Real phenomena, closely corresponding to each of these interpretations, have been observed in organic alloys.[51]

Observations of the branching behaviour of various faceted phases in f—nf eutectics led to the conclusion that, owing to increasing spacing, the solute build-up in front of the faceted (minor) phases caused morphological instability of this phase, thus creating new lamellae.[33,35,51] This effect can be seen in deeply etched specimens (Fig. 14) of the Co—W_6Co_7 eutectic[59] quenched during steady-state growth. Wave formation occurs in the width of the lamellae (Fig. 14*a*) and a subsequent, slight bending of the branches formed (Fig. 14*b*). By these mechanisms, a smaller local spacing is achieved. Branching limitations, owing to the kinetically imposed anisotropic growth of a faceted phase, lead to large λ values and, hence, to the large observed undercoolings of f—nf eutectics of class II, e.g. Fe—C and Al—Si.

There is another effect which has an important influence on the coupled zone. This is the decrease in interface undercooling and spacing, of class II eutectics, with increasing temperature gradient. This phenomenon was clearly demonstrated by

---

*Some other tentative explanations were discussed in Ref. 33 but these now seem less likely.

14   Typical branching mechanism in class II eutectics: formation of an instability in low-volume phase of Co–W$_6$Co$_7$ eutectic at *a* quenched interface, and *b* subsequent bending of branches[59]; growth direction upwards, Co matrix deep etched

Toloui and Hellawell,[41] who found experimentally for Al–Si that

$$\lambda^2 V = K_5 G^{-r} \qquad . \qquad . \qquad . \qquad . \qquad . \qquad . \qquad . \qquad (9)$$

$$\Delta T / \sqrt{V} = K_6 G^{-s} \qquad . \qquad . \qquad . \qquad . \qquad . \qquad . \qquad (10)$$

where

$$K_5 = 2.5 \times 10^{-6} \text{ K}^{2/3}\text{mm}^{7/3}\text{s}^{-1}$$

$$K_6 = 100 \text{ K}^{1/2}\text{s}^{1/2}\text{mm}^{-2}$$

$$r = 0.67$$

$$s = 0.5.$$

It seems that the effect on spacing has been detected in Fe–C* (Refs. 60, 61). By careful study of the two texts, the constants were found to be: $K_5 = 9.14 \times 10^{-6}$ K$^{2/3}$mm$^{7/3}$s^{-1}, $r = 0.7$.

    Looking again at the branching behaviour of organic eutectics, Fisher and Kurz[33] found that

---

*An opposite effect (i.e. increased spacing with increased gradient) has been reported for Al–Al$_3$Fe eutectic.[62] However, only a small range of temperature gradients was explored.

15   Local spacing at branching of borneol fibres in succinonitrile–borneol eutectic as function of temperature gradient for growth rate of 6.7×10^{-3} mms^{-1} (Ref. 33); cf Fig. 16 and Table 4

16 Solid/liquid interface morphologies of growing succinonitrile—borneol eutectic: *a* $G = 2.5$ Kmm^{-1}, $V = 6.7 \times 10^{-3}$ mms^{-1}, *b* $G = 40.5$ Kmm^{-1}, $V = 6.7 \times 10^{-3}$ mms^{-1} **(Refs. 35, 51); cf Fig. 15**

increasing the temperature gradient increased the branching tendency. This can be seen in Fig. 15. The exponent r (equation (9)), for the succinonitrile—borneol eutectic is 0.84. Figure 15 also shows that, owing to the large scatter, a wide range of G is needed to detect the effect. Figure 16 shows the corresponding longitudinal microstructures of the growing solid/liquid interface, at two extremes of temperature gradient, but for the same growth rate. The solid/liquid interfaces under these two conditions are quite different, and show, at high gradients, a tendency to isothermal growth. By solving the diffusion equation, for eutectic growth, the authors found that the instability of the minor phase is increased upon increasing G. This is due to the higher solute build-up ahead of the faceted phase, when the depression of the non-faceted phase is decreased and results in growth closer to the optimum. The mathematical model used by the authors[35] extended the approach of Sato and Sayama[63] in two ways:

(i)   the influence of the temperature gradient was incorporated by allowing only selfconsistent solutions of the interface equations. The respective local melting temperatures of any two points of the interface had to agree with the temperature difference calculated from the imposed temperature gradient and the physical displacement of the points in the growth direction

(ii) the interface stability of the minor phase was used to determine the maximum spacing λ_{branch} before branching occurred, rather than the minimum undercooling criterion.

By taking the mean value of λ_{ext} and λ_{branch}, the model gives results which are semiquantitatively correct, in that large spacings and undercoolings are predicted, and have a suitable dependence on growth rate and temperature gradient. The final solution, assuming a $\lambda^2 V$-type relationship, and using Al—Si data, obeyed equations (9) and (10). The exponents found are shown in Table 4, and exhibit reasonable agreement with experiment. Even the constants are of the correct order of magnitude. However, the model results are very sensitive to the data (especially Gibbs—Thompson coefficients) employed. Equations (7) and (10) can be used to compute the growth temperature of class I and class II eutectics, respectively.

GROWTH OF PRIMARY PHASES

In order to calculate the coupled zone, a comparison of the growth rates of eutectic and primary phases must be made. As the growth rate of isolated primary crystals is determined by their tips, only this part of the problem will be discussed. The primary phases may have a needle form, the familiar dendrite, or a platelike form when the kinetics of its growth lead to anisotropic shapes (Fig. 9*b*). Generally, metals will take up the optimum geometry for diffusion-controlled growth (i.e. the needle) while the faceted phase of class II eutectics will be normally constrained to grow in platelike form. The reason for branching difficulties of the eutectic, and plate formation of the primary crystals consisting of certain faceted phases, is the same, i.e. anisotropic growth of the faceted phase.

The problem, of steady-state tip growth of a needle or a plate, was first solved theoretically by Ivantsov.[64,65] His and subsequent analyses[66] all

treat the isothermal case of growth and are therefore not directly applicable to the situation prevailing during directional solidification ($G > 0$). Burden and Hunt[29] and Jin and Purdy[67] proposed simultaneously, and for the first time, solutions for needle-tip growth in a positive temperature gradient. As such solutions constitute a cornerstone in the understanding of the coupled zone, one of them will be discussed here in some detail before giving another solution to the problem which is rather approximate but more generally useful since it applies to both types of primary growth morphology, i.e. needles and plates, and to the case $G \geq 0$.

Needle growth in a positive temperature gradient

Using a simple Zener-type analysis, Burden and Hunt[29] found a relationship between the dendrite (needle) tip undercooling, temperature gradient, growth rate, and tip radius of curvature:

$$\Delta T_n = GD/V - (mVR/D)(1-k)C_0$$
$$- kRGD/V + 2\theta/R \quad . \quad . \quad . \quad (11)$$

This equation is analogous to the equation for eutectic growth (equation (5)). To obtain a unique solution, the tip geometry is usually optimized by applying the same argument as was used in the case of eutectic growth, i.e. minimum undercooling or maximum growth rate*. Performing this step, analytically, using a simplified version of equation (11) for the case $R \ll 1$ and $k < 1$

$$\Delta T_n = GD/V - (mVR/D)(1-k)C_0$$
$$+ 2\theta/R \quad . \quad . \quad . \quad . \quad . \quad (12)$$

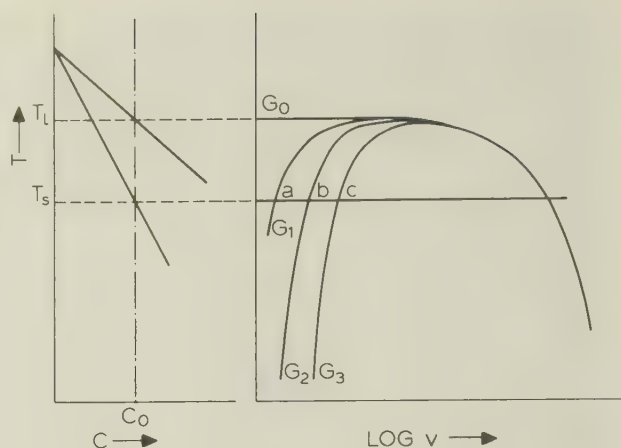Thus, one obtains (equation (2))

$$\Delta T_n = GD/V + K_2 V^{0.5}$$

It can easily be seen that the undercooling of a needle in a positive temperature gradient depends on two terms:

(i) at low rates, the first term results in a high undercooling, while

(ii) at high rates, the second term predominates, and again leads to a high undercooling.

Figure 17 demonstrates this behaviour schematically. Taking account of the stationary state only, there are two reference temperatures for very low growth rates:

(i) the solidus, for plane-front solidification

(ii) the liquidus for isothermal dendritic solidification with $G = 0$.

17 **Interface temperature (steady state) as function of growth rate for plane front ($T \approx \text{const} = T_s$) and needle growth (equation (2)): $G_3 > G_2 > G_1 > G_0 = 0$ Kmm^{-1}; crossover points a, b, c represent limits of stability of planar interface because, at higher velocities, needles have higher interface temperatures**

Applying the minimum undercooling (or maximum growth rate) argument to each of these growth morphologies, one sees that for $G = 0$ the dendritic structure will predominate during alloy solidification, except at very high V.

By applying competitive-growth arguments (*see* footnote on p. 182)*, in fact, two transitions in morphology with increasing growth rates can be predicted:

(i) planar to cellular (dendritic) at low $V(G > 0)$

(ii) cellular (dendritic) to planar at high V.

Such transitions are also predicted by the Mullins—Sekerka[23] interface stability analysis.

Increasing the temperature gradient increases the tip undercooling at decreasing growth rates. This result, which explains the Mollard and Flemings[18] experiments, can be understood on the basis of simple constitutional undercooling arguments: as shown in Fig. 18, a constitutionally undercooled region ahead of a planar solid/liquid interface will amplify perturbations of the interface and lead to cells. The cells will develop until the dendrite (cell) tip finds itself growing at its limit of stability. This is tantamount to assuming that the temperature gradient $d(T_q)/dz$, determined by heat flow, and the liquidus temperature gradient $d(T_l)/dz$, determined by the concentration gradient, will be equal in the intercellular liquid. Therefore,

---

*This has been shown recently to give tip radii which are consistently too small.[68] A new criterion based on the stability of the growing tip offers the prospect of reconciling theory and experiment.[69]

*Hillert[70] has tried to fit a single undercooling equation to the two growth morphologies in order to provide a continuous transition. However, interface stability is typical of a symmetry-breaking transition and is thus essentially discontinuous.

Table 4 Comparison of equations found for class II eutectic spacings* and undercoolings† as function of growth rate and temperature gradient

Experiment			Theory
Al–Si (Ref. 41)	Fe–C (Ref. 60)	Succinonitril– borneol (Refs. 35, 51)	Al–Si data (Refs. 35, 51)
r 0.67	0.70	0.84	0.81
s 0.50	...	...	0.41
K_5 2.5×10^{-6}	9.14×10^{-6}	2.77×10^{-5}	1.24×10^{-5}
$K^{0.67}s^{-1}mm^{2.33}$	$K^{0.7}s^{-1}mm^{2.3}$	$K^{0.84}s^{-1}mm^{2.16}$	$K^{0.81}s^{-1}mm^{2.2}$
K_6 100	...	...	156
$K^{1.5}s^{0.5}mm^{-1}$	...	...	$K^{1.41}s^{0.5}mm^{-0.91}$

*Spacing $\lambda^2 V = K_5 G^{-r}$.

†Undercooling $\Delta T / \sqrt{V} = K_6 G^{-s}$.

at the cell tips, a maximum constitutional temperature difference ΔT_c can exist, which can be evaluated by constitutional supercooling arguments. The criterion of no constitutional supercooling can be written in the form

$$G/V \geq \Delta T/D \quad . \quad . \quad . \quad . \quad . \quad . \quad . \quad (13)$$

with $\Delta T = m C_0(k-1)/k$ for growth with a planar interface. Therefore, the condition for no constitutional supercooling at the cell (or dendrite) tip at low growth rates (neglecting the second term in equation (2) which is small at low V), must be

$$\Delta T_c = GD/V \quad . \quad . \quad . \quad . \quad . \quad . \quad (14)$$

18 Growth conditions at *a* planar and *b* cellular (needlelike) solid/liquid interface: cellular or dendrite growth tends to eliminate zone of constitutional supercooling (hatched zone at lower left) and tips grow at limit of stability (equation (2))

19 Supersaturation at growing needle tip or plate edge (equation 16))

Needle and plate growth in positive temperature gradient

In order to take into account the platelike form of certain primary crystals, e.g. C in Fe—C, Si in Al—Si, or Ni_3Nb in Ni—Ni_3Nb, it is necessary to have analogous mathematical models for the growth of a needle and a plate in a positive temperature gradient. To this end, Kurz[71] has given approximate solutions. He simply replaced the solute diffusion undercooling ΔT_D in the unoptimized Burden and Hunt equation (the second term on the right-hand side of equation (12)) by

$$\Delta T_D = m C_0\{1 - 1/[1 + (k - 1)\Omega]\} . \quad (15)$$

This undercooling can be found using the definition of the supersaturation at the growing tip (Fig. 19)

$$\Omega = (C_1^* - C_0)/[C_1^*(1 - k)] \quad . \quad . \quad (16)$$

and the phase diagram. The supersaturation for a needle Ω_n or for an infinite plate Ω_p is after Ivantsov[64,65]:

$$\Omega_n = P\exp(P)E_1(P) \quad . \quad . \quad . \quad . \quad (17)$$

$$\Omega_p = \sqrt{\pi P}\exp(P)\operatorname{erfc}(\sqrt{P}) \quad . \quad . \quad . \quad (18)$$

where P is the Péclet number.

The undercooling of a needle or a plate can be found by numerically minimizing, with respect to the tip radius, the undercoolings given by the equations, for the needle

$$\Delta T_n = GDV + m C_0\{1 - 1/[1 + (k - 1)\Omega_n]\} + 2\theta/R \quad . \quad . \quad . \quad . \quad . \quad (19)$$
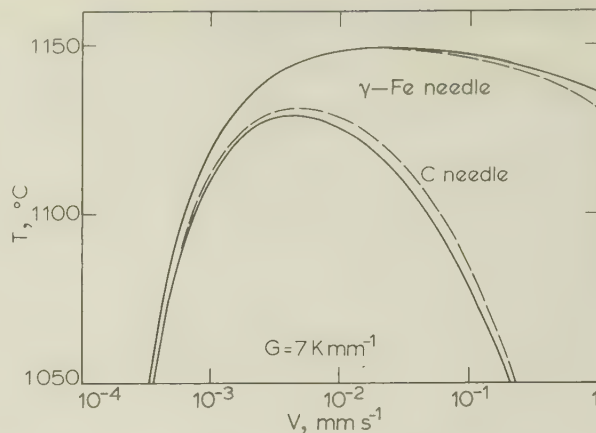
and for the plate

$$\Delta T_p = GD/V + mC_0\{1 - 1/[1 + (k - 1)\Omega_p]\} + \theta/R \quad . \quad . \quad . \quad . \quad . \quad (20)$$

By regression analysis of the results, one finds, for both equations, a very good fit to

$$\Delta T = GD/V + K_7 V^W \quad . \quad . \quad . \quad . \quad (21)$$

Comparison of this equation for needle growth with the Burden—Hunt equation (equation (2)) gives good agreement over the range of realistic growth conditions, when the constant A in equation (2) is

20 Comparison of Burden—Hunt equation (equation (2), $A = 5.5$) with extrema of equation (19) (Ref. 71): solid line equation (19), broken line equation (2)

increased from 2.83 to 5.5 (Fig. 20). This is reasonable because the more exact analysis of Burden and Hunt[29] also results in higher undercoolings when compared with the simple Zener analysis. Furthermore, Burden and Hunt had to increase their value of A from 2.83 to 4.5 to fit experimental results on the coupled zone of Pb—Sn.[20]

The constants (equation (21)) found for the Fe needle were $K_7 = 17.6$ Ks$^{0.46}$mm$^{-0.46}$ and $w = 0.46$, and those for the C plate were $K_7 = 932$ Ks$^{0.35}$mm$^{-0.35}$ and $w = 0.35$ (each for the case of growth in a eutectic Fe—C melt). The results for Fe needle, C needle, and C plate are given in Fig. 21 for two temperature gradients, and indicate a large difference in solute undercooling, of the C plate, compared with the C needle.

CALCULATION OF COUPLED ZONE

Equations (19) and (20) for the primary phases, after numerical minimization of ΔT with respect to R, lead, for both needles and plates, to equations of the type

$$\Delta T = GD/V + K_7 V^W \quad . \quad . \quad . \quad . \quad (21)$$

With the aid of equations (7) and (10) for eutectic growth, which have the general form as equation (1), i.e.

$$\Delta T = K'V^{0.5}$$

where K' equals K_1 for class I eutectics (equation (7)) or $K_6 G^{-S}$ for class II eutectics (equation (10)), the coupled zone for any given system growing in the stationary state with $G \geq 0$ can be derived by minimizing ΔT extrema among all of the possible morphologies: e.g. when dendrites have the lower ΔT, dendrites plus eutectic are observed, otherwise, only eutectic is found (Fig. 7). All these calculations are very simple and can be done with
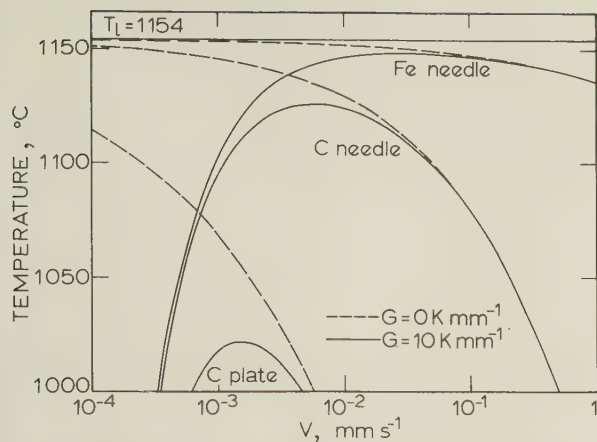
**21 Interface temperature as function of growth
rate for Fe (needle), C (needle), and C (plate) in
eutectic Fe—4.27 wt-%C alloy melt[71]**

the aid of a desk calculator (in the present case an
HP9825 was used) or even with a programmable.
pocket calculator. The limit of the coupled zone
can therefore simply be calculated by equating
equations (1) and (21):

$$GD/V + K_7 V^W = K' V^{0.5} \quad . \quad . \quad . \quad . \quad (22)$$

It should be noted that in such calculations several
optimization procedures are applied, i.e. with re-
spect to tip radius to determine the optimum
morphology for primary needle or plate, and with
respect to the different competing morphologies
to predict the structure — eutectic only or den-
drites and eutectic.

EXPERIMENTAL DETERMINATION OF COUPLED ZONE

There are some important differences in the
various experimental approaches to determining
the coupled zone. The following three principal
methods are found in the literature:

(i) isothermal (or nearly isothermal) solidifica-
     tion: nucleation and growth of small quantities
     of the melt, ranging from droplets[72-74] to
     small ingots[75]

(ii) directional solidification, at high rates, in a
     positive temperature gradient (low G/V)

(iii) directional solidification, at low rates, in a
      positive temperature gradient (high G/V).

Isothermal solidification

This method (involving probably non-isothermal
conditions) is the most interesting one when com-
paring laboratory experiments with 'real' castings,
because any interpretation of the results must take
into account the combined effects of nucleation and
growth. However, since there is no adequate
theory available for the interpretation of such

complicated growth situations, the results are not
of general use. Furthermore, one has to be very
careful in using these results because of the great
difficulty in measuring the temperature of the
growing interface.

The method can be carried out by quenching
small droplets into a liquid metal bath of known
temperature, and assuming that nucleation and
growth take place isothermally at that tempera-
ture.[72-74] As Chadwick[76] pointed out, however, it
can easily be shown, from the microstructures of
Sheil and Masuda's specimens, that the interphase
spacing of their Al—Al_2Cu eutectic, quenched into
a bath, 100 K below T_e, is still measurable using
the optical microscope ($\lambda \approx 0.5\ \mu m$). Using the
relationships of Tassa and Hunt,[21]

$$\Delta T/\sqrt{V} = 3.2\ \text{Ks}^{1/2}\text{mm}^{-1/2} \quad . \quad . \quad (23)$$

$$\lambda^2 V = 1.25 \times 10^{-7}\ \text{mm}^3\text{s}^{-1}$$

which they found for Al—Al_2Cu, one obtains

$$\Delta T\lambda = 1.12 \times 10^{-3}\ \text{Kmm} \quad . \quad . \quad . \quad . \quad (24)$$

Equation (24) indicates an undercooling of 2.24 K
for the structure with $\lambda \approx 0.5\ \mu m$ Conversely,
undercooling by 100 K would result in a spacing
of 11.2 nm. This shows clearly that one cannot
take the bath temperature to be the growth tem-
perature. It is probable, therefore, that all of the
coupled zones published by Scheil and co-workers
are much too narrow in composition range.

The interface temperature can also be ob-
tained by measuring the temperature of a small
volume of melt during transformation by means of
a thermocouple.[77,78] This gives satisfactory re-
sults when the undercooling is high and the growth
rate is low, as in the case of class II eutectics.

Table 5 lists published work carried out using
the techniques described above. It should be re-
membered that, with these methods, only the

**Table 5 Eutectic systems in which coupled
zone has been determined by iso-
thermal solidification experiments**

System	Eutectic	Ref.
Ag—Cu	Ag—Cu	75
Al—Cu	Al—Al_2Cu	74
Al—Fe	Al—Al_3Fe	71
Al—Ni	Al—Al_3Ni	74
Al—Si	Al—Si	73
Bi—Sn	Bi—Sn	79
C—Ni	Ni—C	73
Ti—Zn	Zn—Zn_{15}T	78

Table 6 Eutectic systems in which coupled zone has been determined using directional solidification at high growth rates

| System	Eutectic	Ref(s).
Al—Co	Al—Al_9Co_2	80
Al—Fe	Al—Al_3Fe	40, 81
	Al—Al_6Fe	62, 82
Al—Mn	Al—Al_6Mn	40
Al—Ni	Al—Al_3Ni	71
Al—Si	Al—Si	42, 76, 83
C—Fe	Fe—C; Fe—Fe_3C	84
C—Nb	Nb—Nb_2C	85
Cd—Pb	Cd—Pb	86
Cd—Zn	Cd—Zn	87
Nb—Ni	Ni—Ni_3Nb	88
Ni—Mo	Ni—NiMo	89
Pb—Sn	Pb—Sn	90
Ti—Zn	Zn—$Zn_{15}Ti$	91
	Monotectic	
Cu—Pb	Cu—Pb	(Ref. 92)
	Eutectoid	
C—Fe	Fe—Fe_3C	(Ref. 3)

widening of the zone at high growth rates can be determined (Fig. 7). This is due to the negative temperature gradient at the solid/liquid interface which exists when equiaxed grains are growing into an undercooled melt. The results are usually summarized in $T—C$ diagrams (phase diagrams).

Directional solidification at high growth rates

Several authors (Table 6) have determined the coupled zone by growing at high rates in a positive temperature gradient, G having no influence on the form of that part of the zone. These conditions lead to the widening of the zone with increasing undercooling below the waist of the zone (Fig. 7). The determination is normally carried out by growing specimens of various compositions at different rates, and detecting, by means of much tedious metallography, the transition between the fully eutectic and eutectic plus primary phase microstructures. In order to maintain unidirectional heat flow up to very high growth rates, a high temperature gradient is required in the solid. The maximum growth rate can be estimated using a simple heat balance.[90] The temperature gradient in the solid must be steep enough to allow the heat from the liquid, and that produced at the interface, to be conducted away. For a specimen of constant cross-section, under unidirectional heat flow conditions

$$G_S\kappa_S = G_l\kappa_l + VL \quad . \quad . \quad . \quad . \quad (25)$$
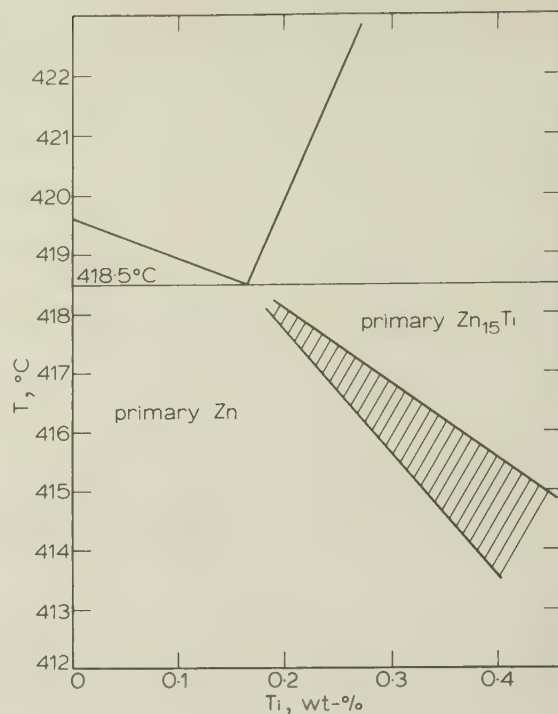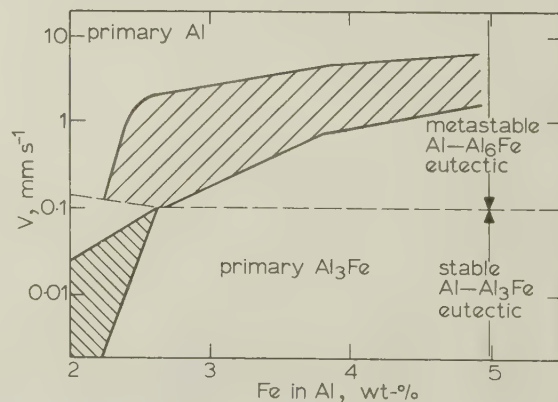
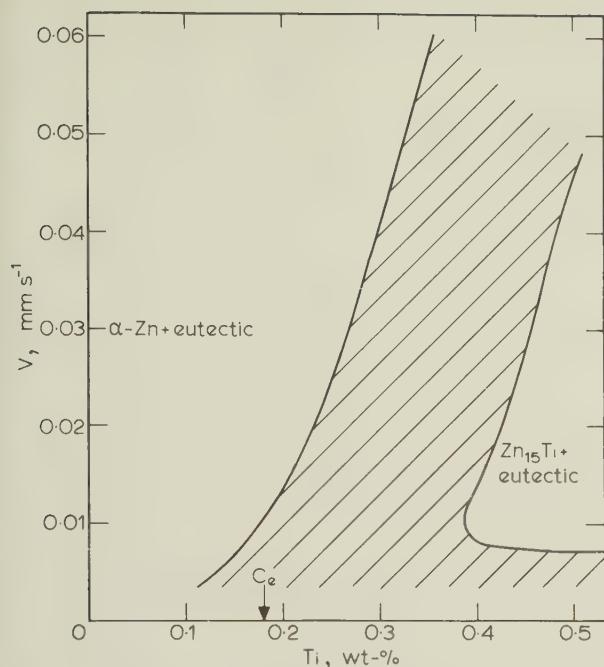**22 Coupled zone of Zn—Zn_{15}Ti eutectic grown under directional solidification condition[91]: cf Fig. 24**

The maximum rate will be reached when the temperature gradient in the liquid ahead of the solid/liquid interface is just positive, whence

$$V_{(max)} \leq G_S\kappa_S/L \quad . \quad . \quad . \quad . \quad . \quad . \quad (26)$$

The ratio κ_S/L (equation 26)) for Pb is 0.11 mm^2 K^{-1}s^{-1} and, for Al, is 0.23 mm^{2}K^{-1}s^{-1}. The maximum growth rates of these metals are therefore (supposing the very steep temperature gradient of 40 K^{-1}mm^{-1}), 4.4 and 9.2 mms^{-1}, respectively. This reasoning is in satisfactory agreement with experiment.[82,90] To obtain such high growth rates, it is necessary to use thin-

23 Coupled zone of Al—Al_3Fe/Al_6Fe eutectic grown under directional solidification conditions[82]

24 Coupled zone of Zn–Zn$_{15}$Ti eutectic grown under equiaxed growth conditions[78]: cf Fig. 22

Table 7 Eutectic systems in which coupled zone has been determined using directional solidification at high G/V ratios

System	Eutectic	Ref(s).
Binary		
Ag–Al	Al–Ag$_2$Al	94
Al–Au	Al–Al$_2$–Au	95
Al–Ca	Al–Al$_4$Ca	96
Al–Cu	Al–Al$_2$Cu	21, 25, 97
Al–Ni	Al–Al$_3$Ni	98
Au–Co	Au–Co	99
Cd–Cu	Cd–Cd$_3$Cu	100
Cr–Ni	Cr–Ni	101
Pb–Sn	Pb–Sn	18, 102, 103
Pb–Zn	Pb–Zn	100
Ternary		
Al–Cu–Mg	Al–Al$_2$Cu–Al$_2$CuMg	104
Al–Cu–Ni	Al–Al$_2$Cu–Al$_3$Ni	105, 106
Cd–Pb–Sn	Cd–Pb–Sn	107, 108
Cu–Mg–Ni	Cu–Cu$_2$Mg	109

walled crucibles, small specimen diameters, and intense liquid (water, metal) cooling.

The results are usually summarized in $V–C$ diagrams (Figs. 4*a* and 22). As Fig. 23 (Ref. 82) shows, a good deal of interesting information can be put into such a diagram. In the case of the Al–Fe system, a transition of the eutectic growth form from the stable Al–Al$_3$Fe to the metastable Al–Al$_6$Fe structure is observed, while only Al$_3$Fe crystals form as the primary phase.

Another interesting case is the Zn–Zn$_{15}$Ti eutectic because it has been examined by two different groups of workers: Goto *et al.*[91] measured the high-velocity coupled zone (Fig. 22) using directional solidification, while Leone and Kerr[78] determined the coupled zone via the first technique described: nucleation and growth (Fig. 24). Unfortunately, the growth constant K_1 (equation (1)) of that eutectic is not known, making direct comparison of the results in each publication impossible. One can only state that the overall form of the coupled zones is similar.

As Cline and Livingston[90] have shown, care has to be taken in interpreting metallographic results in the Pb–Sn system at high growth rates on the lead-rich side. Because of easy nucleation of lead dendrites in front of the solid/liquid interface (possibly owing to thermosolutal convection), determination of this boundary was impossible under conditions of directional solidification.

In Table 6, coupled zones, analogous to those in eutectic systems, have also been included for:

(i) the Cu–Pb monotectic where, on the Pb-rich side, the primary phase occurs not as dendrites, but as droplets[92]
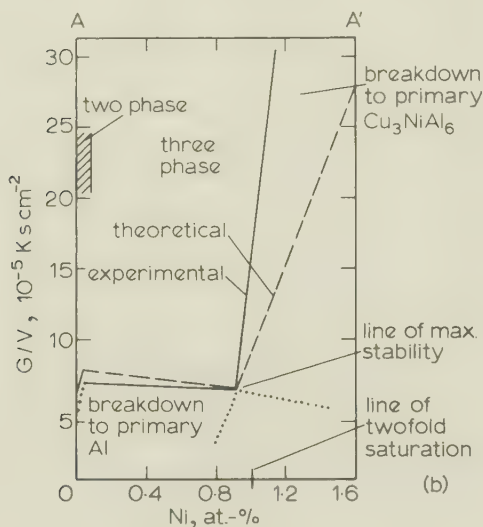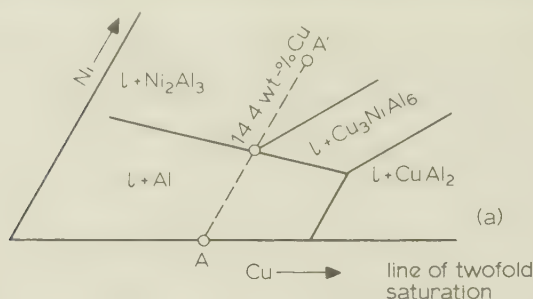
(ii) the Fe–Fe$_3$C eutectoid.[3]

Directional solidification at high G/V ratio

As mentioned in the opening section of the review, Mollard and Flemings[18] were the first to find that, at high G/V ratios, solidification of eutectic structures without primary phases was possible over a wide range of compositions (Fig. 4). The same phenomenon is seen in Fig. 7 as the widening of the coupled zone with decreasing undercooling (close to T_e). As seen from the $T–V$ diagrams at the right of Fig. 7, this range is determined by the increased dendrite undercooling with decreased growth rate when $G > 0$ (*see also* Fig. 17).

Sharp and Flemings[93] showed that the determination of this part of the coupled zone could be carried out in a much simpler way than systematically changing the variables G/V and concentration. In fact, the limit for wholly eutectic growth can be determined from the composition of the interdendritic eutectic. In this situation, the eutectic grows at conditions corresponding to those at the coupled-zone boundary. Therefore, using a small number of specimens, the whole range may be determined, provided that the analysis of the interdendritic eutectic can be performed with sufficient accuracy.

There is another technique which permits rapid determination of the coupled zone; Jones and Kurz[84] used an approach combining experiment and theory. By measuring the temperatures of the eutectic interface, and of dendrite tips, the neces-
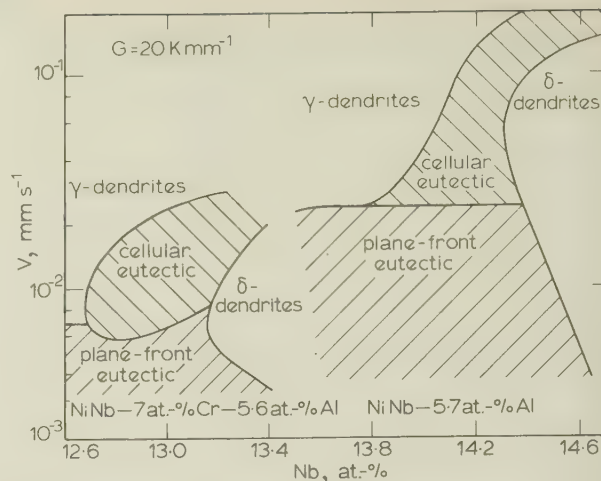
25 **Critical G/V ratios for ternary Al–Cu–Ni eutectic[105]; in higher order systems polyphase dendrites appear**

26 **Coupled zones for two directionally grown Ni/Ni$_3$Al–Ni$_3$Nb alloys[110]**

drastic effect on the eutectic composition, the eutectic range, and the critical speed for breakdown of the planar, eutectic, solid/liquid interface.
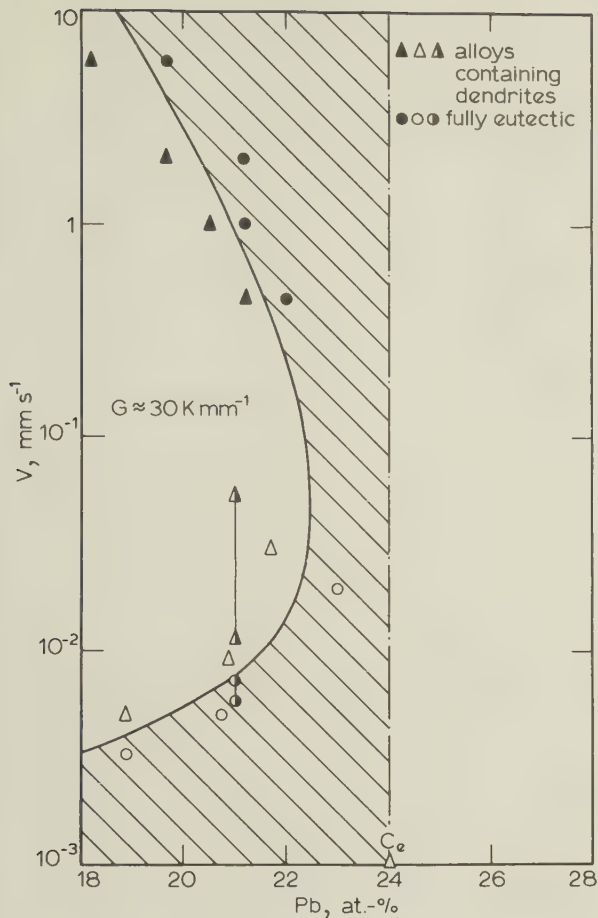
THEORY AND EXPERIMENT

In this section, the theories will be compared with experimental results on various eutectic alloys. Also, with the aid of these models, some conclusions will be drawn concerning the reasons for the differences in coupled zones.

Comparison of growth models

The two relevant approaches are those of (a) Burden and Hunt[20], (b) Fisher and Kurz[22] and Kurz.[71] The first model permits calculation of the coupled zone when the primary growth forms are both needlelike (dendritic), and for temperature gradients greater than zero. The second model is an extension of the first and permits the calculation of the coupled zone under more general conditions. However, the primary growth forms (needle or plate) have to be known. It has been shown that both methods of dendrite calculation are very similar when compared over a realistic range of growth conditions[71] (Fig. 20). For Burden and Hunt's simpler model, an increase in the constant A (equation (2)) is necessary to fit the experimental results. Such an adjustment also diminishes the discrepancy between the two models of Burden and Hunt. Using the method described in the section on 'Calculation of the coupled zone',[22,71] the coupled zone of the Sn-rich side of the Sn–Pb eutectic has been calculated. As may be seen from Fig. 27, the calculated zone fits the various experimental results quite closely. In order to get a good fit, the following properties of the alloy were changed compared to the values (in parentheses) used by Burden and Hunt[29] and Tassa and Hunt[21]:

$$m = -1.2 \ (-1.43)$$
$$D = 8 \times 10^{-6} \ (6.7 \times 10^{-6})$$
$$\theta = 1.8 \times 10^{-5} \ (6.2 \times 10^{-6}).$$

sary growth laws (equations (7), (19), and (20), respectively) could be fitted to the results and the whole zone calculated. On each side of the zone, only one to three measurements are then necessary.

Table 7 lists the coupled zones determined experimentally at high G/V ratios. It includes some ternary systems; Holder and Oliver[107] determined the iso-G/V contours of the coupled zone of the ternary Cd–Pb–Sn eutectic. Similar iso-ΔT contours had been given by Kofler[11] for high-V coupled zones in ternary organic systems. Rinaldi *et al.*[105] proposed a quantitative description of the different regions of stability which might occur in a ternary system, e.g. the two possible types of dendrite: single phase and two phase (Fig. 25).

There is one study[110] which combines measurements on directionally solidified specimens at low and high growth rates. In that report, the authors determined the eutectic range of various complex alloys of the Ni/Ni$_3$Al–Ni$_3$Nb (γ/γ'–δ) type which are being considered as possible gas turbine rotor-blade materials. For this application, it is essential to know what structures will be obtained using various growth conditions and compositions. Figure 26 shows a diagram, for two different γ/γ'–δ alloys, equivalent to that of Fig. 6. One can see that the addition of 7 at.-%Cr has a
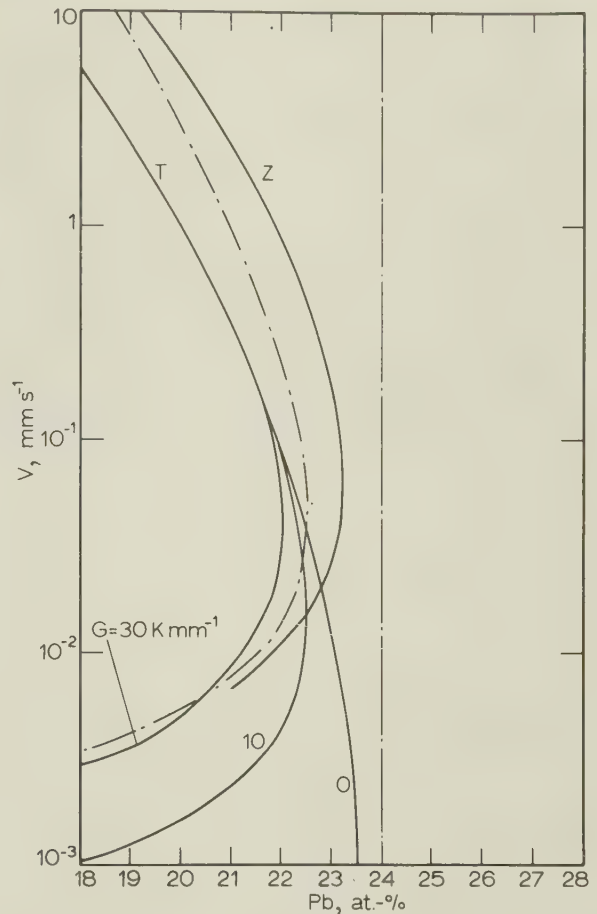
27 Coupled zone (hypoeutectic compositions) of directionally grown Sn—Pb system: solid line calculated with aid of equations (1) and (19); full symbols Ref. 90, open symbols Ref. 18, half-filled symbols Ref. 111
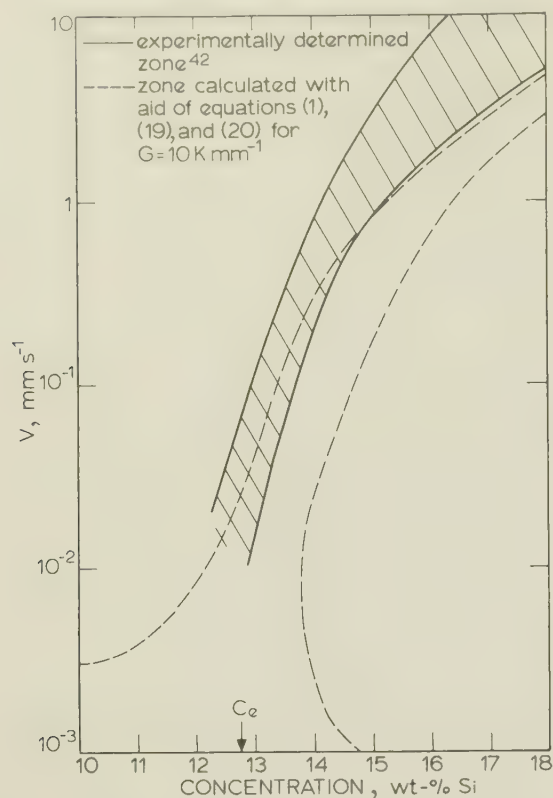

28 Application of two Burden—Hunt models to coupled-zone calculation of Sn—Pb system: T = Trivedi-type analysis, Z = Zener-type analysis (equation (2))[30]: chain-dotted curve is solid line in Fig. 27

The only significant change is in θ, which is also the most doubtful experimental quantity since it is the ratio of two quantities which are difficult to measure experimentally: the solid/liquid interfacial energy* and the entropy of fusion. In any case, it must be borne in mind that the model describing dendrite growth (equations (19), (20)) is very approximate. Therefore, the quantities used should not be taken as being exact, but only as being of the correct order of magnitude.

Comparing Fig. 28 with Fig. 27, one finds that both approaches agree reasonably well with experiment. As the approach of Fisher and Kurz also accounts for the skewed zones of class II eutectics, it will be used below to interpret experimental results. This model is also very crude as far as the description of faceted platelike primary crystals is concerned, because it assumes an infinitely wide plate having the smooth curvature of

a parabolic cylinder. Primary crystals of faceted phases of class II eutectics will have, in most cases, an aspect ratio of 1:10 and a faceted solid/liquid interface. A theory able to describe these facts mathematically would be very involved. The same applies to the theory of the growth of eutectics having non-isothermal interfaces. Substantial theoretical work will be needed before the observed morphologies can be described in a more quantitative manner.

Selected examples: comparison of theory and experiment

Class I eutectics

Experimentally, the Pb—Sn eutectic is the best documented system. Figure 27 summarizes the data for Sn-rich alloys (for a temperature gradient of about 30 Kmm⁻¹): the measurements of Mollard and Flemings[18] and of Verhoeven and Gibson[111,114] at low growth rates, and at high growth rates, the measurements of Cline and Livingston.[90]

---

*Recent measurements seem to indicate that the generally accepted σ-values of Turnbull[112] are much too low.[113]
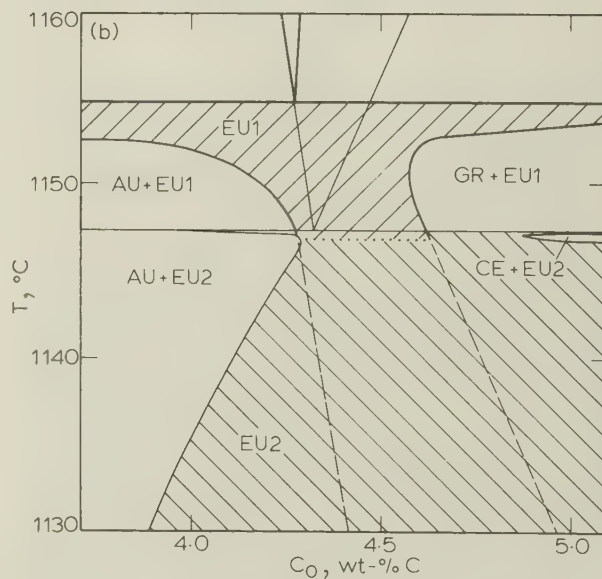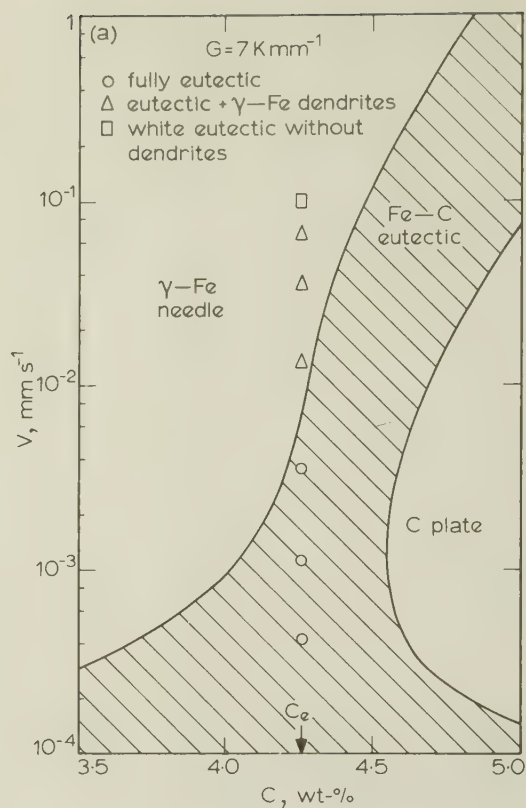
29 **Coupled zone of directionally grown Al–Si eutectic**

All the experimental results agree quite well. Especially interesting are the results of Verhoeven and Gibson,[111,114] which show a marked hysteresis, in the appearance and disappearance of Sn dendrites, found in experiments involving acceleration or deceleration, respectively. There was an even wider scatter (of a factor of five) in the critical growth rate for the appearance of dendrites. This was attributed to difficulty in dendrite nucleation. As Cline and Livingston have shown, the extent of the eutectic range on the Pb-rich side of the system is difficult to measure because of repeated nucleation of Pb dendrites ahead of the solid/liquid interface. Therefore, this side of the diagram has been omitted in Fig. 27.
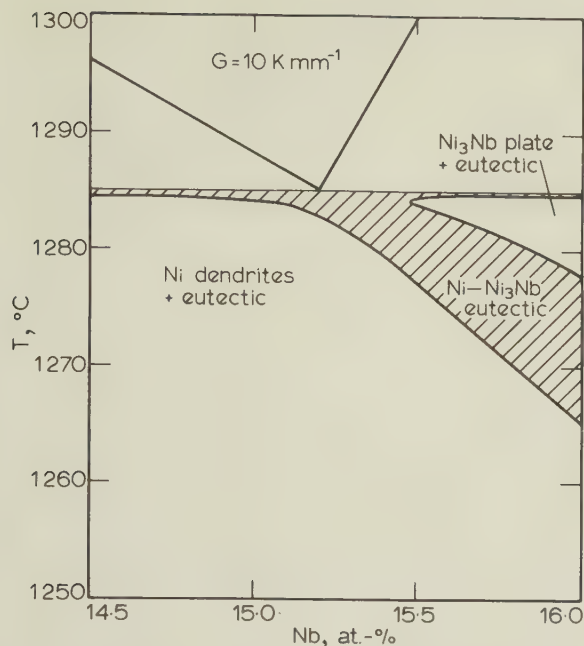
Tassa and Hunt[21] compared, in detail, their Trivedi-type analysis with experimental results for the Al–Al$_2$Cu system. For their measurements on Al dendrites, they found a good fit using the more exact Trivedi-type theory, but they had to use the simpler, Zener-type theory to fit the coupled zone. They explained this discrepancy using arguments regarding the relative importance of the diffusive and convective processes occurring around the dendrite tips when the latter are growing close to the eutectic interface.

Class II eutectics

Fisher and Kurz[22,55] tried to calculate the coupled zone of the Al–Si system, which belongs to class II. Their first approach,[55] which simply
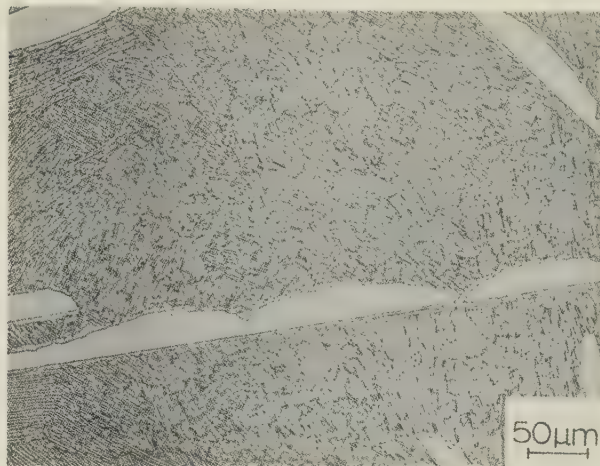

30 **Coupled zone of directionally grown Fe–C eutectic[84]: *a* *V–C* diagram showing calculated curves and experimental points; *b* *T–C* diagram with superimposed phase diagrams, stable (EU1) and metastable (EU2), AU = austenite dendrite, GR = graphite plate, CE = cementite plate; due to small growth constant *K*$_1$ of Fe–Fe$_3$C eutectic, its coupled zone is symmetric although primary Fe$_3$C is of plate form**

31   Theoretical coupled zone of directionally solidified Ni—Ni$_3$Nb eutectic

32   Ni—Ni$_3$Nb eutectic microstructure showing primary Ni$_3$Nb plates: Ni—14.7 at.-%Nb—5.7 at.-%Al; $V = 5.6 \times 10^{-3}$ mms^{-1}, $G \approx$ 20 Kmm^{-1} (Ref. 88)

included a kinetic undercooling term for eutectic and Si dendrite growth, was not satisfactory. Moreover, at the same time, Steen and Hellawell[56] pointed out that the kinetic undercooling of Si must be negligible. Taking account of this, and pursuing an idea proposed by Frederiksson[45] for Fe—C, they were able to compute the coupled zone for Al—Si, assuming a needlelike morphology for primary Al, and a platelike morphology for primary Si (Ref. 22). In Fig. 29, this zone is compared with that found by Steen and Hellawell.[42] The skewed form of the zone is well predicted, but as regards the degree of skewness of the zone, there is some discrepancy. This may be owing to the naivety of the model used, but may equally be owing to the fact that the experimentally determined coupled zone has been placed in doubt by later research, i.e. the undercooling, knowledge of which is necessary in order to plot the coupled zone, was deduced from the value of K_1 (equation (7)) for the Al—Si eutectic. This value was taken to be a constant, but has since been shown to depend on the temperature gradient as shown by equation (10) (Ref. 41). As the temperature gradient was not measured in every experiment, the true eutectic undercooling may well have varied in an unsuspected fashion throughout the experiments of Steen and Hellawell.[42]

Apart from some experiments on Ni—C,[73] the results of which are doubtful (*see* section on 'Isothermal solidification' above), there has been no determination of the extent of the eutectic range in alloys of the 'cast iron type' (Fe—, Ni—, Co—, Pt—, C). For this reason, Jones and Kurz[84] recently determined, experimentally, the transition from a fully eutectic to a eutectic plus dendrite structure,

in pure Fe—C alloys of eutectic composition (Fig. 30). Precise temperature measurements during solidification of only one alloy composition (*see* section on 'Directional solidification at high G/V ratio' above) allowed extrapolation, from the results, to give the entire boundary on the γ-Fe dendrite side of the coupled zone. Using values for the properties of graphite, they were also able to predict the graphite/eutectic boundary of the coupled zone (Fig. 30), a zone which is difficult to determine experimentally because of flotation of graphite, and the very steep liquidus which leads to nucleation of graphite ahead of the solid/liquid interface.

Finally, in Fig. 31, the calculated coupled zone of the directionally solidified eutectic, Ni—Ni$_3$Nb, is shown. Although the alloys are different, the general form of the calculated zone agrees with experiment (Fig. 26).[88,110] Figure 32 proves that the growth morphology of primary Ni$_3$Nb is platelike and should thus lead to the high undercooling of this primary phase which is necessary to give a skewed zone.

Having seen that one can have sufficient confidence in the available models for semiquantitatively predicting the extent of the coupled zone, it is interesting to check, in more detail, the agreement of theory and experiment in predicting the type of coupled zone (symmetric or skewed). As has been shown above (in the section on 'Principles of coupled-zone theory'), this will depend on the undercooling of the eutectic, which may be large because of branching limitations, and on the undercooling of one of the primary phases which may be large because of an anisotropy of growth which leads to a platelike morphology of that phase. Table 8 gives a list of (predominantly class II) systems which lead to skewed zones. Agreement with theory is satisfactory and seems to render the model plausible.

Table 8 Comparison of known coupled zones with predictions of present theory*

| Eutectic system	Eutectic micro-structure	Faceted phase	Kofler zone†	Ref(s).	Morphology of non-faceted faceted phase‡	Agreement with theory
Ag–Cu	Regular	...	B	75	n, n	Yes
Al–Al$_9$Co$_2$	Regular	Al$_9$Co$_2$	A	80	n, p	Yes
Al–Al$_2$Cu	Regular	Al$_2$Cu	B	72	n, p	No
Al–Al$_3$Fe	Irregular	Al$_3$Fe	A	72, 82	n, p	Yes
Al–Al$_6$Fe	Regular	Al$_6$Fe	A	82	n, p	Yes
Al–Al$_6$Mn	Irregular	Al$_6$Mn	A	40	n, p	Yes
Al–Al$_3$Ni	Regular	Al$_3$Ni	A	80/B, 74	n, p	Yes/No
Ai–Si	Irregular	Si	A	42, 77, 83	n, p	Yes
Cd–Zn	Regular	...	B	87	n, n	Yes
Fe–C	Irregular	C	A	84	n, p	Yes
Ni–Ni$_3$Nb	Regular	Ni$_3$Nb	A	88	n, p	Yes
Sn–Bi	Irregular	Bi	A	79	n, p	Yes
Zn–Zn$_{15}$Ti	Regular	Zn$_{15}$Ti	A	78, 91	n, p	Yes

*I.e. that a platelike form for the faceted phase leads to a high undercooling of that phase and hence, when associated with a high temperature gradient, to a skewed coupled zone.[22]

†A = asymmetric (skewed), only includes eutectic composition at low growth rates; B = symmetric, includes eutectic composition at all undercoolings.

‡n = needle; p = plate.

Predictions of theoretical models

In order to have a better overview of the factors which influence the location of the boundaries of the coupled zone it is easiest to go back to the model of Burden and Hunt[20] (equation (3), Fig. 33). One may see that the asymmetric (skewed) zone of many class II eutectics is caused essentially by a high eutectic undercooling (especially when $K_1 > \sim 15$ Ks$^{1/2}$ mm$^{-1/2}$) which shifts the α-eutectic limit to hypereutectic concentrations.
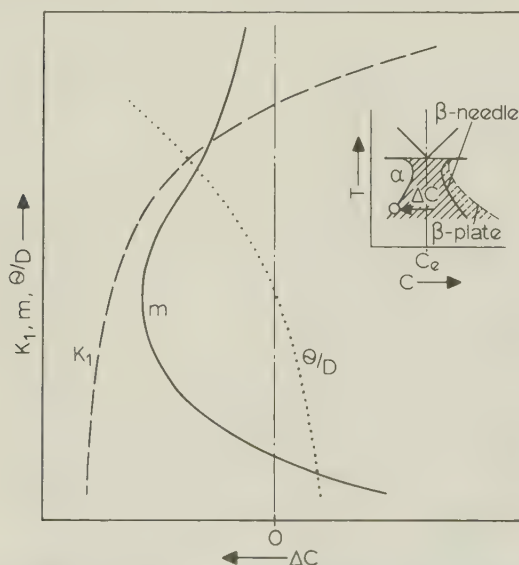

33 Effect of variation of parameters in equation (3) on form of coupled zone (*see* text)

The liquidus slope m has a complex effect: a decrease in m when m is high will increase the extent of the coupled zone while only very low values of m lead to a skewed zone. Therefore, one can conclude that the major factor favouring a skewed zone (i.e. a zone having an α-eutectic boundary lying in the hypereutectic concentration range) is a high eutectic undercooling constant K_1, which, in turn, generally goes together with a high average interphase spacing and an irregular microstructure.

When the α-eutectic boundary lies far within the hypereutectic range, a cutting off of the coupled zone can be avoided only by a corresponding shift of the β-eutectic limit. This can be understood with the aid of Fig. 33 by remembering that, roughly speaking, the platelike form of the β-primary will increase K_2 (equation (3)). This has a similar effect to that of decreasing K_1, and results in an increase of ΔC†. Very often, the asymmetry of the phase diagram (liquidus slopes, etc.) has been stated to be the cause of the skewed coupled zone. Calculations show, however, that these factors have only a very slight effect on the coupled zone, and are negligible in comparison to the other cited above.

Certain misinterpretations of experimental results might be avoided by remembering the

†One must remember, when using Fig. 33 to determine the β-eutectic limit, that the concentration axis must be reversed.
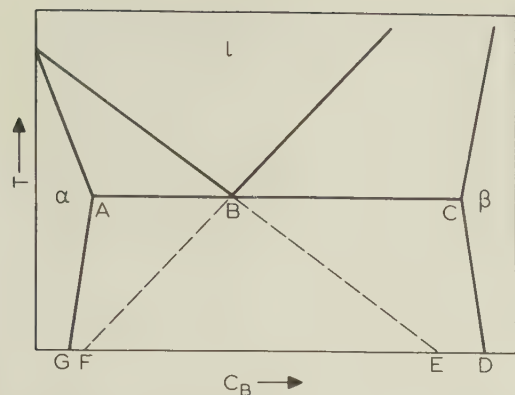
34 Limits for coupled zone: B, C, D, E, primary α impossible; A, B, F, G, primary β impossible

regions where the primary phases can or cannot appear (Fig. 34). For example, increasing K_1 will shift the α-eutectic boundary to the right in Fig. 34. The α-eutectic boundary will approach the metastable liquidus line (B—E) asymptotically. This line determines the maximum skewness, and zones like those in Fig. 5c and d of Chadwick[76] are therefore impossible. Figure 35 shows that this knowledge can be useful in interpreting results: as Gigliotti and Colligan[77] have shown, adding Na to Al—Si alloys shifts the coupled zone to higher Si concentrations (Fig. 35b). To avoid creation of an impossible zone, a parallel liquidus line, close to the α-eutectic limit, but lying in the coupled zone, must be drawn. This represents the new, Na-modified, liquidus (chain-dotted line). The results of Kobayashi et al.,[115] in fact, show a shift of the liquidus line to higher Si concentrations thus confirming the necessary change in the form of the phase diagram.

From the above examples, it can be seen that the prediction of coupled zones is quite feasible. This is particularly so when experiment and theory are combined,[84] since present models of dendrite growth predict the exponent (in the undercooling—growth rate relationship) quite well, but not the proportionality constant.[66] Experiment allows one to determine this constant. Nevertheless, theoretical research on dendrite growth is continuing, and recent work by Langer and Müller-Krumbhaar[69,116-118] seems to explain the discrepancy mentioned above. Their method predicts higher undercoolings than those given by the authors' equations. These arise since the system has to go to higher tip radii than predicted by the maximum growth rate criterion, before a tip-size changing transition can occur. It should be noted that this is analogous to the departure from minimum undercooling conditions, necessary to permit branching, in class II eutectics.[35]

CONCLUSIONS

The problems associated with the use of eutectic alloys in the casting and welding industry are a challenge to solidification theory. Here, structure
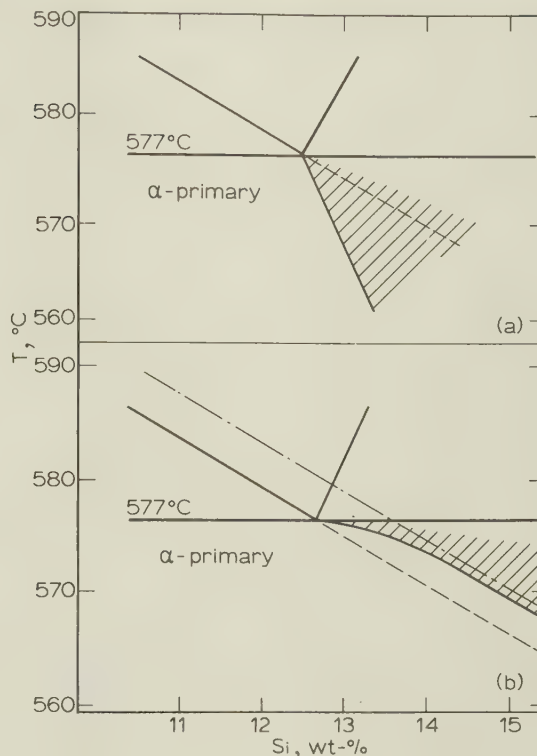
35 Coupled zone in a Al—Si system under equi-axed growth conditions[77]; b addition of Na apparently shifts zone into forbidden range (see Fig. 34); therefore, Na additions must also move the α-liquidus to higher Si concentrations (chain-dotted line)

control is of the utmost importance. In the present paper the authors have reviewed a simple but unified approach to understanding the reasons for the presence or absence of primary phases in the microstructure of nominally eutectic alloys. The principle of competitive growth between possible, steady-state growth forms is applied because no presently available stability analysis enables one to treat eutectic to eutectic plus dendrite transitions properly. The different competing growth forms considered are: (a) regular (class I) eutectic, (b) irregular (class II) eutectic, (c) primary phase of needle form (dendrite), and (d) primary phase of plate form (faceted crystal).

The growth morphologies of the two forms of eutectic are very different because of different branching behaviours. Class I eutectics do not have branching difficulties and can therefore always adapt their structure to the optimum growth morphology. Class II eutectics, on the other hand, grow in a very different manner, because they have to grow at the *limit of stability* of the *faceted* phase so as to permit this phase to branch. This leads to typically coarse and irregular structures associated with much higher undercoolings than those of class I eutectics.

The anisotropy of the growth kinetics of most faceted phases, which is responsible for the

branching difficulties of class II eutectics, may also lead to a non-optimum (plate) morphology for the primary crystals of the phase. The form of the coupled zone of different systems can be understood if one knows the growth laws of the competing growth forms. By simply comparing the interface temperatures or growth rates the expected structure (eutectic only or eutectic and a primary phase) can be predicted. By this means the coupled zone of an unknown system can be easily obtained, as in the case of Fe—C, using a combined theoretical and experimental approach. With the aid of the model developed here, some insight can be gained into the reasons for the appearance of primary phases in nominally eutectic alloys. The proportionality constants for growth of eutectic and primary phases are the main factors determining whether the zone is symmetric or skewed. It is also shown that no zone can be skewed beyond the metastable liquidus line, i.e. α-dendrites cannot appear outside the metastable two-phase region $\alpha + 1$.

Finally, it can be concluded, on the basis of comparisons between theory and experiment, that although a complete, quantitative interpretation is still lacking, the present state of coupled-zone theory already allows a reasonable understanding of the factors determining the form of different coupled zones.

An important problem which remains to be solved is the description of morphological transitions in eutectic systems, during non-stationary and equiaxed growth.

ACKNOWLEDGMENTS

REFERENCES

1.   L. M. Hogan: *J. Aust. Inst. Met.*, 1964, **9**, 228.
2.   W. Kurz and P. R. Sahm: 'Gerichtet erstarrte eutektische Werkstoffe'; 1975, Heidelberg, Springer.
3.   G. A. Chadwick and D. V. Edmonds: 'Chemical metallurgy of iron and steel', 264; 1973, London, The Iron and Steel Institute.
4.   A. Hellawell: *Prog. Mater. Sci.*, 1970, **15**, (1), 1.
5.   R. Glardon and W. Kurz: 'New developments and applications in composites', (eds. D. Kuhlmann-Wilsdorf and W. C. Harrigan); 1979, New York, AIME.
6.   A. M. Portevin: *J. Inst. Met.*, 1923, **29**, 239.
7.   E. H. Dix: *Proc. ASTM*, 1925, **25**, 120.
8.   G. Tammann and A. A. Botschwar: *Z. anorg. Chem.*, 1926, **157**, 27.
9.   A. Kofler: *Ber. Deutsch. Chem. Ges.*, 1943, **76**, 391.
10.   A. Kofler: *ibid.*, 1944, **77**, 110.
11.   A. Kofler: *Z. Elektrochem.*, 1945, **51**, 38.
12.   A. Kofler: *Monatsh. Chem.*, 1948, **78**, 58.
13.   A. Kofler: *Z. Metallkd.*, 1950, **41**, 221.
14.   A. Kofler: *Microchem.*, 1953, **40**, 311.
15.   A. Kofler: *ibid.*, 405.
16.   G. Hardy, G. Nagy, J. Varga, and G. Nemeshegyi: *Eur. Polymer J.*, 1973, **9**, 399.
17.   J. D. Hunt and K. A. Jackson: *Trans. AIME*, 1967, **239**, 864.
18.   F. Mollard and M. C. Flemings: *ibid.*, 1534.
19.   K. A. Jackson: *ibid.*, 1968, **242**, 1275.
20.   M. H. Burden and J. D. Hunt: *J. Cryst. Growth*, 1974, **22**, 328.
21.   M. Tassa and J. D. Hunt: *ibid.*, 1976, **34**, 38.
22.   D. J. Fisher and W. Kurz: 'Solidification and casting of metals', 57; 1979, London, The Metals Society.
23.   W. W. Mullins and R. F. Sekerka: *J. Appl. Phys.*, 1964, **35**, 444.
24.   H. E. Cline: *Trans. AIME*, 1968, **242**, 1613.
25.   R. M. Jordan and J. D. Hunt: *J. Cryst. Growth*, 1971, **11**, 141.
26.   D. T. J. Hurle and E. Jakeman: *ibid.*, 1968, **3/4**, 574.
27.   S. Strässler and W. R. Schneider: *Phys. Cond. Matter*, 1974, **17**, 153.
28.   I. Stakgold: *SIAM Rev.*, 1971, **13**, 289.
29.   M. H. Burden and J. D. Hunt: *J. Cryst. Growth*, 1974, **22**, 109.
30.   M. H. Burden and J. D. Hunt: *ibid.*, 99.
31.   K. A. Jackson and J. D. Hunt: *Trans. AIME*, 1966, **236**, 1129.
32.   E. Sheil: *Z. Metallkd.*, 1954, **45**, 298.
33.   D. J. Fisher and W. Kurz: 'Quality control of engineering alloys and the role of metals science', (eds. H. Nieswaag and J. W. Schut), 59; 1978, Delft, The Netherlands, Delft University of Technology.
34.   B. Lux and W. Kurz: 'The solidification of metals', 193; 1968, London, The Iron and Steel Institute.
35.   D. J. Fisher and W. Kurz: to be published in *Acta Metall.*
36.   C. Zener: *Trans. AIME*, 1946, **167**, 550
37.   M. Hillert: *Jernkontorets Ann.*, 1957, **141**, 757.
38.   W. A. Tiller: 'Liquid metals and solidification', 276; 1958, Cleveland, Ohio, American Society for Metals.
39.   A. Moore and R. Elliott: 'The solidification of metals', 167; 1968, London, The Iron and Steel Institute.
40.   J. A. Eady, L. M. Hogan, and P. G. Davies: *J. Aust. Inst. Met.*, 1975, **20**, 23.
41.   B. Toloui and A. Hellawell: *Acta Metall.*, 1976, **24**, 565.
42.   H. A. H. Steen and A. Hellawell: *ibid.*, 1972, **20**, 363.
43.   W. M. Rumball: *Can. J. Phys.*, 1968, **46**, 83.

44. M. Hillert and P.O. Soderholm: 'The metallurgy of cast iron', (eds. B. Lux, F. Mollard, and I. Minkoff), 197; 1975, St Saphorin, Switzerland, Georgi Publishing Co.
45. H. Fredriksson: *Metall. Trans.*, 1975, **6A**, 1658.
46. A. Moore and R. Elliott: *J. Inst. Met.*, 1967, **95**, 369.
47. J. D. Hunt and J. P. Chilton: *ibid.*, 1963—64, **92**, 21.
48. R. M. Jordan and J. D. Hunt: *Metall. Trans.*, 1971, **2**, 3401.
49. J. C. Hubert, W. Kurz, and B. Lux: *J. Cryst. Growth*, 1973, **18**, 241.
50. Y. Umehara and S. Koda: *J. Jpn Inst. Met.*, 1974, **38**, 42.
51. D. J. Fisher: ScD thesis, Department of Materials Engineering, Swiss Federal Institute of Technology, 1978.
52. W. A. Tiller: 'Recent research in cast iron', (ed. H. D. Merchant), 129; 1968, London, Gordon and Breach.
53. G. Lesoult and M. Turpin: 'The metallurgy of cast iron', (eds. B. Lux, F. Mollard, and I. Minkoff), 255; 1975, St Saphorin, Switzerland, Georgi Publishing Co.
54. H. Fredriksson and S. E. Wetterfall: 'The metallurgy of cast iron', (eds. B. Lux, F. Mollard, and I. Minkoff), 227; 1975, St Saphorin, Switzerland, Georgi Publishing Co.
55. D. J. Fisher and W. Kurz: *Aluminium*, 1976, **52**, 363.
56. H. A. H. Steen and A. Hellawell: *Acta Metall.*, 1975, **23**, 529.
57. D. J. Fisher and W. Kurz: unpublished work.
58. B. E. Sundquist: *Acta Metall.*, 1968, **16**, 1413.
59. M. A. Taha and K. Schwerdtfeger: personal communication, 1977.
60. R. Gagnaux: personal communication, concerning Ref. 61, 1978.
61. E. Schürmann and H. Löblich: *Giessereiforschung*, 1977, **29**, 67; (*see also* '43rd int. foundry congress', Paper 17, 1976, Bucharest).
62. C. M. Adam and L. M. Hogan: *J. Aust. Inst. Met.*, 1972, **17**, 81.
63. T. Sato and Y. Sayama: *J. Cryst. Growth*, 1974, **22**, 259.
64. G. P. Ivantsov: *Dokl. Akad. Nauk SSR*, 1947, **58**, 567.
65. G. P. Ivantsov: *Growth of Crystals (USSR)*, 1961, **3**, 53.
66. M. E. Glicksman, R. J. Schaefer, and J. D. Ayers: *Metall. Trans.*, 1976, **7A**, 1747.
67. I. Jin and G. R. Purdy: *J. Cryst. Growth*, 1974, **23**, 29.
68. R. D. Doherty, B. Cantor, and S. J. M. Fairs: *Metall. Trans.*, 1978, **9A**, 621.
69. J. S. Langer and H. Müller-Krumbhaar: *J. Cryst. Growth*, 1977, **42**, 11.
70. M. Hillert: 'Proc. conf. in-situ composites III', (eds. J. L. Walter *et al.*; 1979, Lexington, Mass., Ginn Custom.
71. W. Kurz: *Z. Metallkd.*, 1978, **69**, 433.
72. E. Scheil and Y. Masuda: *Aluminium*, 1955, **31**, 51.
73. E. Scheil: *Giesserei*, 1959, **24**, 1313.
74. E. Scheil and R. Zimmermann: *Z. Metallkd.*, 1957, **48**, 509.
75. B. L. Jones, G. M. Weston, and R. T. Southin: *J. Cryst. Growth*, 1971, **10**, 313.
76. G. A. Chadwick: 'The solidification of metals', 138; 1968, London, The Iron and Steel Institute.
77. M. F. X. Gigliotti and G. A. Colligan: *Metall. Trans.*, 1972, **3**, 933.
78. G. L. Leone and H. W. Kerr: *J. Cryst. Growth*, 1976, **32**, 111.
79. M. F. X. Gigliotti, G. L. F. Powell and G. A. Colligan: *Metall. Trans.*, 1970, **1**, 1038.
80. R. S. Barclay, H. W. Kerr, and P. Niessen: *J. Mater. Sci.*, 1971, **6**, 1168.
81. C. M. Adam and L. M. Hogan: *Acta Metall.*, 1975, **23**, 345.
82. I. R. Hughes and H. Jones: *J. Mater. Sci.*, 1976, **11**, 1781.
83. D. C. Jenkinson and L. M. Hogan: *J. Cryst. Growth*, 1975, **28**, 171.
84. H. Jones and W. Kurz: to be published in *Metall. Trans.*
85. S. A. David and H. D. Brody: *Metall. Trans.*, 1974, **5**, 2309.
86. M. Sahoo and R. W. Smith: *J. Mater. Sci.*, 1978, **13**, 283.
87. M. Sahoo, R. A. Porter, and R. W. Smith: *ibid.*, 1976, **11**, 1680.
88. F. D. Lemkey: 'Eutectic superalloys strengthened by δ Ni_3Nb lamellae and γ' Ni_3Al precipitates', Report NASA Cr—2278, 1973, Hartford, Conn., USA, United Technologies Research Center.
89. A. S. Tortika, A. I. Somov, and Y. P. Kurilo: *Phys. Met. Metallogr. (USSR)*, 1975, **40**, 171.
90. H. E. Cline and J. D. Livingston: *Trans. AIME*, 1969, **245**, 1987.
91. S. Goto, K. Esashi, S. Koda, and S. Morozumi: *J. Jpn Inst. Met.*, 1973, **37**, 466.
92. J. D. Livingston and H. E. Cline: *Trans. AIME*, 1969, **245**, 351.
93. R. M. Sharp and M. C. Flemings: *Metall. Trans.*, 1973, **4**, 997.
94. G. R. Armstrong and A. Hellawell: *Acta Metall.*, 1974, **22**, 1383.
95. G. Piatti and G. Pellegrini: *J. Mater. Sci.*, 1976, **11**, 913.
96. G. Pellegrini, G. Gabetta, and G. Piatti: *Mater. Sci. Eng.*, 1978, **34**, 171.
97. G. Pflieger and F. Durand: *Comptes Rendus*, 1970, **271**, 1544.
98. A. S. Tortika, A. I. Somov, and Y. P. Kurilo: *Phys. Met. Metallogr.*, 1974, **38**, 136.
99. P. R. Sahm and H. R. Killias: *J. Mater. Sci.*, 1970, **5**, 1027.
100. T. Momono and K. Ikawa: *J. Jpn Inst. Met.*, 1977, **41**, 498.
101. E. H. Myers and R. H. Hopkins: *J. Cryst. Growth*, 1970, **7**, 231.
102. K. G. Davis and L. M. Hogan: *J. Aust. Inst. Met.*, 1970, **15**, 29.
103. K. G. Davis and P. Fryzuk: *Can. Met. Q.*, 1971, **10**, 273.
104. G. Garmong: *Metall. Trans.*, 1971, **2**, 2025.

105. M. D. Rinaldi, R. M. Sharp, and M. C. Flemings: *ibid.*, 1972, **3**, 3139.

106. E. M. Dunn, K. P. Young, and M. C. Flemings: *ibid.*, 1978, **9B**, 267.

107. J. D. Holder and B. Oliver: *ibid.*, 1974, **5**, 2423.

108. H. Q. Bao and F. Durand: *J. Cryst. Growth*, 1972, **15**, 291.

109. P. J. Fehrenbach, H. W. Kerr, and P. Niessen: *ibid.*, 1972, **16**, 209.

110. E. R. Thompson and E. H. Kraft: Final Report on Project no. P—9310—MS, 1975, Hartford, Conn., USA, United Technologies Research Center.

111. J. D. Verhoeven and E. D. Gibson: *Metall. Trans.*, 1973, **4**, 2581.

112. D. Turnbull: *J. Appl. Phys.*, 1950, **21**, 1022.

113. D. H. Rasmussen, J. H. Perepezko, and C. R. Loper: 'Rapidly quenched metals', (eds. N. J. Grant and B. C. Giessen), 51; 1976, Cambridge, Mass., MIT Press.

114. J. D. Verhoeven and E. D. Gibson: *Metall. Trans.*, 1972, **3**, 1893.

115. K. Kobayashi, P. H. Shingu, and R. Ozaki: *Scr. Metall.*, 1976, **10**, 525.

116. J. S. Langer and H. Müller-Krumbhaar: *Acta Metall.*, 1978, **26**, 1681.

117. J. S. Langer and H. Müller-Krumbhaar: *ibid.*, 1689.

118. H. Müller-Krumbhaar and J. S. Langer: *ibid.*, 1697.

Appendix I

CONSTANTS USED FOR CALCULATING COUPLED ZONES SHOWN IN PRESENT REVIEW

Constant	Al–Si	Fe–C	Fe–Fe$_3$C	Sn–Pb	Ni–Ni$_3$Nb
C_e	12.7 wt-%	4.26 wt-%	4.3 wt-%	24 at.-%	15.2 at.-%
D_α, mm^{2}s^{-1}	5×10^{-3}	5×10^{-3}	5×10^{-3}	8×10^{-4}	10^{-3}
D_β, mm^{2}s^{-1}	5×10^{-3}	5×10^{-3}	5×10^{-3}	...	10^{-3}
k_α	0.13	0.49	0.49	0.06	0.9
k_β	0.05	0.001	0.64	...	0.9
K_1, Ks$^{1/2}$mm$^{-1/2}$	25	108	3	4.1	16
m_α, K (%)$^{-1}$	6.7	140	140	1.2	15
m_β, K (%)$^{-1}$	32	400	50	...	50
T_e, °C	577.2	1158.6	1154	183	1285
β, needle (n), or plate (p)	p	p	p	n	p
θ_α, Kmm	2.12×10^{-4}	3×10^{-4}	3×10^{-4}	1.8×10^{-4}	1.8×10^{-4}
θ_β, Kmm	2.5×10^{-4}	2×10^{-4}	3×10^{-4}	...	3×10^{-4}

Near-threshold fatigue-crack propagation in steels
by R. O. Ritchie

The characteristics of fatigue-crack propagation in metals and alloys have been the subject of several extensive reviews in recent years, but in very few instances have the details of ultralow growth rate, near-threshold fatigue-crack propagation been similarly discussed. In this review the effects are examined of various mechanical, microstructural, and environmental factors which influence fatigue-crack propagation in steels at growth rates less than 10^{-6} mm/cycle, where the alternating stress intensity ΔK approaches the so-called threshold stress intensity ΔK_0, below which crack growth cannot be experimentally detected. The marked influences of load ratio, material strength, and microstructure on such near-threshold growth are analysed in detail and rationalized in terms of possible environmental contributions and crack-closure concepts. These effects are contrasted with crack-propagation behaviour in other engineering materials and at higher growth rates.

LIST OF SYMBOLS

a	= crack length
a_0	= constant characteristic of material/material condition in expression for ΔK, equation (3)
da/dN	= fatigue-crack propagation rate per cycle
A	= constant in Paris power law for fatigue-crack growth, equation (1)
B, B'	= constants dependent upon material and temperature in expression for ΔK_0, equation (13)
C	= constant in expression for ΔK_0 in absence of environment, equation (10)
C_H	= local concentration of hydrogen at point of maximum dilatation
C_0	= equilibrium concentration of hydrogen in unstressed lattice
ΔCOD	= cyclic crack-tip opening displacement

E	= elastic modulus
K_c, K_{Ic}	= stress intensities at final failure (fracture toughness)
K_{max}, K_{min}	= maximum and minimum stress intensities during cycle
ΔK	= alternating stress intensity $(K_{max} - K_{min})$
ΔK_{eff}	= effective alternating stress intensity taking into account crack closure
ΔK_0	= threshold stress intensity for no crack growth
m	= exponent in Paris power law, equation (1)
N	= number of cycles
R	= load or stress ratio (K_{min}/K_{max})
R_0	= gas constant
T	= absolute temperature
$\bar{v}$	= partial molar volume of hydrogen in iron (2 cm^3 mol^{-1})
α	= constant relating reduction in cohesive strength to local hydrogen concentration C_H
ρ'	= Neuber's effective crack-tip radius
ρ^*	= limiting microstructural dimension at threshold
$\bar{\sigma}$	= hydrostatic stress
σ_F	= critical local fracture stress at threshold
σ_u	= ultimate tensile strength (UTS)
σ_y	= monotonic yield strength
σ_y'	= cyclic yield strength
$\Delta\sigma$	= alternating stress
$\Delta\sigma_e$	= fatigue limit or endurance strength
$\Delta\sigma_H$	= reduction in cohesive strength due to hydrogen
$\Delta\sigma_{TH}$	= alternating threshold stress for no crack growth

R. O. Ritchie, MA, PhD, MIM, CEng, is in the Department of Mechanical Engineering, Massachusetts Institute of Technology, Cambridge, Mass., USA.

In many safety-critical engineering applications, where design against fatigue is based on the so-called defect-tolerant approach, the prime consideration in dictating the lifetime of a component is taken as the time or number of cycles to propagate a subcritical crack from an assumed

initial defect size (often taken as the largest un-detected flaw) to critical size where final failure occurs either catastrophically or at the limit load. The widespread adoption of this approach over the last decade for design against cyclic loading has spurred a multitude of investigators to charac-terize the rate of growth of fatigue cracks in the majority of engineering materials as a function of such variables as microstructure, mean stress, environment, frequency, and so forth. The majority of these data, however, have been generated for growth rates typically in excess of 10^{-6} mm/cycle. Although this information is vital for many struc-tural engineering applications (i.e. determining safe non-destructive inspection intervals in air-craft), in recent years there has been a rapidly increasing need for fatigue-crack propagation data pertaining to extremely low growth rates (less than 10^{-6} mm/cycle) where the alternating stress intensity ΔK approaches a so-called thres-hold value ΔK_0, below which cracks remain dormant or grow at undectable rates. The reasons for this are several. First, there are fundamental aspects in that this topic represents a compara-tively unexplored area of fatigue research com-pared to the vast amount of information on fatigue-crack propagation at higher growth rates. Essentially, little is known from a mechanics or metallurgical point of view about micro-mechanisms of crack propagation at near-threshold growth rates, and furthermore, there is still a substantial lack of reliable engineering data. Secondly, there is the practical concern of structural and materials engineers to design components which can withstand extremely high frequency, low-amplitude loadings for lifetimes in the range 10^{10}–10^{12} cycles. A high-speed rotor operating at 3000 rev min^{-1} in a steam turbine, for example, may be expected to see 10^{10} cycles of stress over a typical lifetime of 20 years. Should fatigue-crack propagation be occurring at the seemingly insignificant near-threshold growth rate of 3×10^{-9} mm/cycle, this would still repre-sent a total growth of 30 mm during the life of the rotor, which could clearly result in catastrophic failure. In fact, a knowledge of low growth rate, fatigue-crack propagation data and, in particular, information regarding the existence of a threshold stress intensity, has been shown to be essential in the analysis of such problems as cracking in tur-bine blades,[1] turbine shafts,[2,3] and alternator rotors,[3] and acoustic fatigue of welds in gas circuitry in nuclear-reactor systems.[2-4]

There now exist results in the literature on near-threshold fatigue-crack growth for a wide range of materials, including ferritic,[5-20] mar-tensitic,[5,19-29] and austenitic,[19,30-32] steels, titanium[5,33,34] and titanium alloys,[34-41] and several aluminium,[5,19,22,41-43] copper,[5,44] and nickel,[1,5] alloys. It is apparent from such data that near-threshold crack-growth rates and the value of the threshold ΔK_0 are particularly sensitive to several mechanical and microstruc-tural variables, namely, mean stress or load

ratio,[5,28,31-44] prior stress history,[9,19] crack size,[45] cyclic frequency,[22,32,42] mono-tonic[11,16,18,24] and cyclic[26,27,43,44] strength, grain size,[16,18,26,27,29,33,36] and grain-boundary composition.[25] However, the influence of environ-mental factors on near-threshold crack growth has remained somewhat of a controversy. Al-though it is well documented that fatigue-crack propagation at rates exceeding 10^{-5} mm/cycle is generally accelerated in the presence of an environment compared to inert conditions, initial studies by Paris and co-workers, in low-strength steels[6,7] and titanium alloys[35] in air, water, hydrogen, and dry argon, did not reveal any such environmentally-sensitive propagation at ultralow growth rates. Furthermore, by extrapolation of higher (midrange) growth-rate data to near-threshold rates (a procedure, incidentally, which should be regarded with extreme caution), results of certain authors[46,47] suggest that near-threshold crack propagation may indeed be *decelerated* in the presence of an 'aggressive' environment (e.g. salt water) compared to seemingly more inert environments such as air. Other data,[21,22,31,39-41] however, for various materials tested *in vacuo* suggest the contrary behaviour of an environmental contribution to cracking at near-threshold rates. Conclusive information to resolve these issues is still lacking.

In design, the concept of a fatigue-crack pro-pagation threshold is still infrequently utilized, except where there is an obvious source of very high frequency loading,[1-4] since it is often con-sidered to be overly conservative. However, there has been a recent growing awareness in the nuclear industry that, for design and continued safe operation of reactor plants, such near-thres-hold data are required for both pressure-vessel and reactor-coolant piping steels (e.g. A533B, A508 low-alloy steels, and 304 and 316 stainless steels, respectively) tested in simulated reactor environments. Such data, measured in air, pres-surized-water, and boiling-water reactor environments, are now appearing in the litera-ture.[48,49] Similar data on candidate pressure-vessel steels for coal-gasifier and coal-lique-faction use, e.g. 2.25Cr–1Mo steels, in simulated environments, however, are not available, although near-threshold fatigue-crack growth is a possi-bility in the pressure-vessel wall as a result of high-cycle low-amplitude stresses generated from small pressure and temperature fluctuations of the system. Such 'operational transients' could arise from real variations in coal feedrates, 'clusters' of pulverized coal, combustion instabil-ities, and pressure fluctuations in feed and dis-charge lines for gases. Furthermore, typical atmospheres in coal-conversion pressure vessels, namely, mixtures of water vapour, hydrogen, hydrogen sulphide, carbon monoxide, carbon di-oxide, ammonia, methane, and other hydrocarbons at pressures exceeding 10 MPa with metal-wall temperatures around 350°C (Ref. 50), may well accelerate this slow subcritical growth.

It is the purpose in the present paper to provide a critical review of existing information on near-threshold fatigue-crack propagation in steels, and, in particular, to discuss these data in the light of possible environmental interactions and crack-closure concepts. Where possible, effects are contrasted with crack-propagation behaviour at higher growth rates (exceeding 10^{-6} mm/cycle) and in other engineering materials.

EXPERIMENTAL MEASUREMENT OF NEAR-THRESHOLD GROWTH

It is pertinent at this stage to examine how such low growth rates are measured experimentally and, in particular, how the value of the threshold stress intensity ΔK_0 can be defined. Whereas fatigue-crack propagation at conventional growth rates (i.e. greater than around 10^{-5} mm/cycle) is typically measured under constant load (increasing stress intensity K) conditions, it is generally more realistic to measure near-threshold growth rates, and the value of the threshold ΔK_0 under decreasing K conditions, in order to minimize transient residual-stress effects.

In strict terms, the threshold stress intensity ΔK_0 should represent the alternating stress intensity where the growth rate is infinitesimal. However, for the purposes of practical measurement it is more useful to adopt an operational definition for ΔK_0. This is best achieved in terms of a maximum growth rate, calculated from the accuracy of the crack monitoring technique and the number of cycles elapsed.[21] In the system

used by the present author,[24-27] crack length is continuously monitored using the dc electrical-potential technique,[51-53] and the threshold ΔK_0 is computed from the highest stress intensity at which no growth can be detected within 10^7 cycles. In this particular case, the crack monitoring technique is at least accurate to 0.1 mm on absolute crack length such that the threshold can be defined in terms of a maximum growth rate of 10^{-8} mm/cycle. Threshold levels are approached using a load-shedding technique involving a procedure of successive load reduction followed by crack growth. Measurements of crack growth rate are taken at each load level, over increments of 1—1.5 mm increase in crack length, after which the load is reduced by not more than 10%, and the same procedure followed. Larger reductions in load are liable to give premature crack arrest from retardation effects owing to residual plastic deformation. The increments, over which measurements of growth rate are taken, should represent distances at least four times larger than the maximum plastic zone size generated at the previous (higher) load level to minimize these retardation effects caused by change in load. Furthermore, frequency must be maintained constant during this procedure since significant environmentally-induced transient crack-growth rate effects can result from variations in cyclic frequency.[54] Following ΔK_0 measurement, the load may be increased in increments and a similar procedure adopted to measure growth rates. In this way, near-threshold data can be monitored under both decreasing K and increasing K conditions in the same specimen. Provided care is taken to minimize transient effects caused
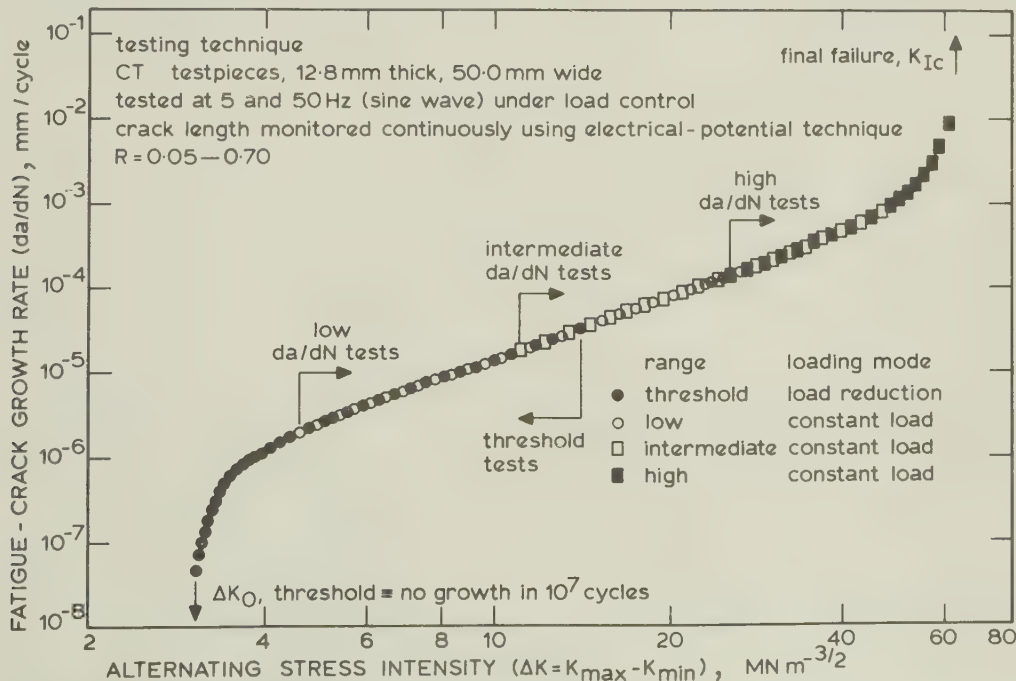
1   Typical test procedures for obtaining fatigue-crack propagation data spanning entire range of growth rates from threshold levels to final failure

by changing the load, growth-rate data should be identical when measured by these two procedures.

A typical test procedure for obtaining fatigue-crack propagation-rate data spanning the entire range of growth rates from threshold levels to final failure is shown schematically in Fig. 1.

Other techniques have been used to measure the threshold. These include determining an S/N curve for cracked specimens with lifetime plotted against the initial value of ΔK, rather than stress,[5,17,20] and a decreasing K technique achieved by cycling under constant deflection control.[42,55] Although relatively simple to instrument, for conventional compact and centre-cracked tension specimens, the latter technique suffers from the fact that the decrease in K is not rapid enough for efficient near-threshold crack-growth measurement.[55]

The load-shedding (decreasing K) technique can be easily automated using a suitable crack monitoring technique and computer-controlled closed-loop testing machines. Such systems, utilizing a programmed constant decrease of the normalized K-gradient, i.e. $|\Delta K^{-1}.\mathrm{d}\Delta K/\mathrm{d}a|$ or $|K_{\max}^{-1}.\mathrm{d}K_{\max}/\mathrm{d}a|$, have been developed using several crack measurement techniques, namely, crack-opening displacement monitoring,[56] electrical-potential methods,[30] eddy-current crack following,[28] and elastic-compliance techniques.[57]

To provide some consistency in the measurement of near-threshold crack-growth rates and ΔK_0 values, the American Society for Testing and Materials E.24.04 subcommittee is presently developing a standard for proposed test methods similar to the procedures described above. Such guidelines for the establishment of fatigue-crack growth rates below 10^{-5} mm/cycle are likely to be incorporated as modifications to the recently proposed ASTM Standard E647—78T for measurement of constant-load-amplitude growth rates above 10^{-5} mm/cycle.

## GENERAL NATURE OF FATIGUE-CRACK PROPAGATION IN STEELS

The application of linear-elastic fracture mechanics and related small-scale crack-tip plasticity has provided an empirical basis for describing the phenomenon of fatigue-crack propagation.[58] Most studies have confirmed that the crack-growth increment per cycle ($\mathrm{d}a/\mathrm{d}N$) is principally a function of the alternating stress intensity ΔK through a power-law expression of the form[59]:

$$\mathrm{d}a/\mathrm{d}N = A(\Delta K)^m \ . \qquad . \qquad . \qquad . \qquad . \qquad . \qquad (1)$$

where A and m are experimentally-determined scaling constants, and ΔK is given by the difference between the maximum and minimum stress intensities for each cycle, i.e. $\Delta K = K_{\max} - K_{\min}$. This expression provides an adequate engineering description of behaviour at the midrange of growth rates, typically 10^{-5}–10^{-3} mm/cycle. At higher growth rates, however, when $K_{\max}$ approaches the fracture toughness (K_{Ic}, K_c) or limit-load failure, equation (1) often underestimates the propagation
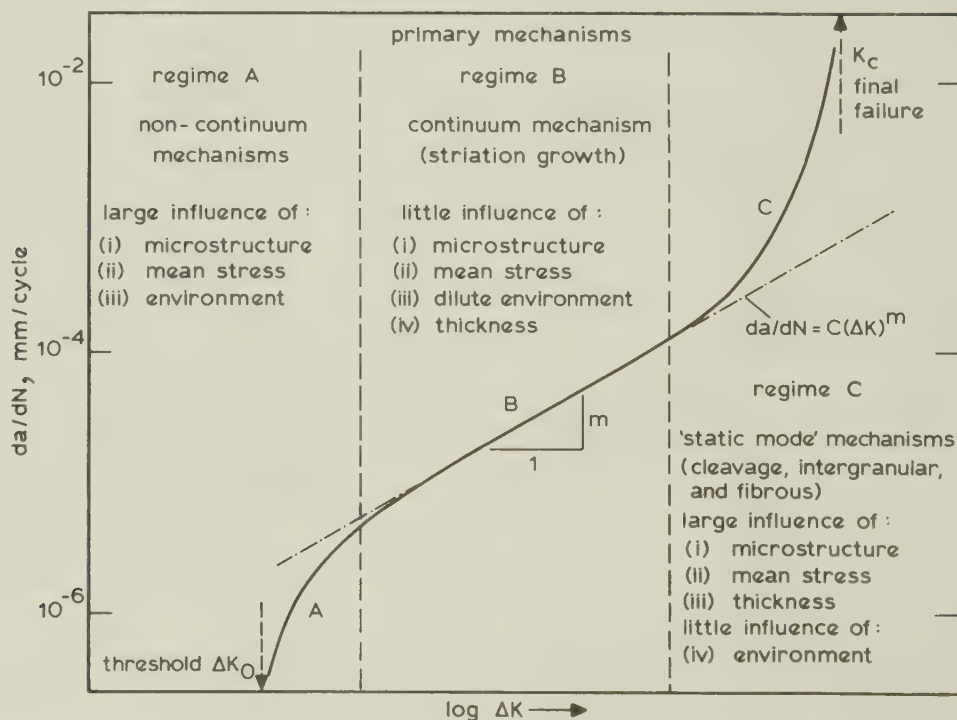
2   Schematic variation of fatigue-crack growth rate $\mathrm{d}a/\mathrm{d}N$ with alternating stress intensity ΔK in steels, showing regimes of primary crack-growth mechanisms
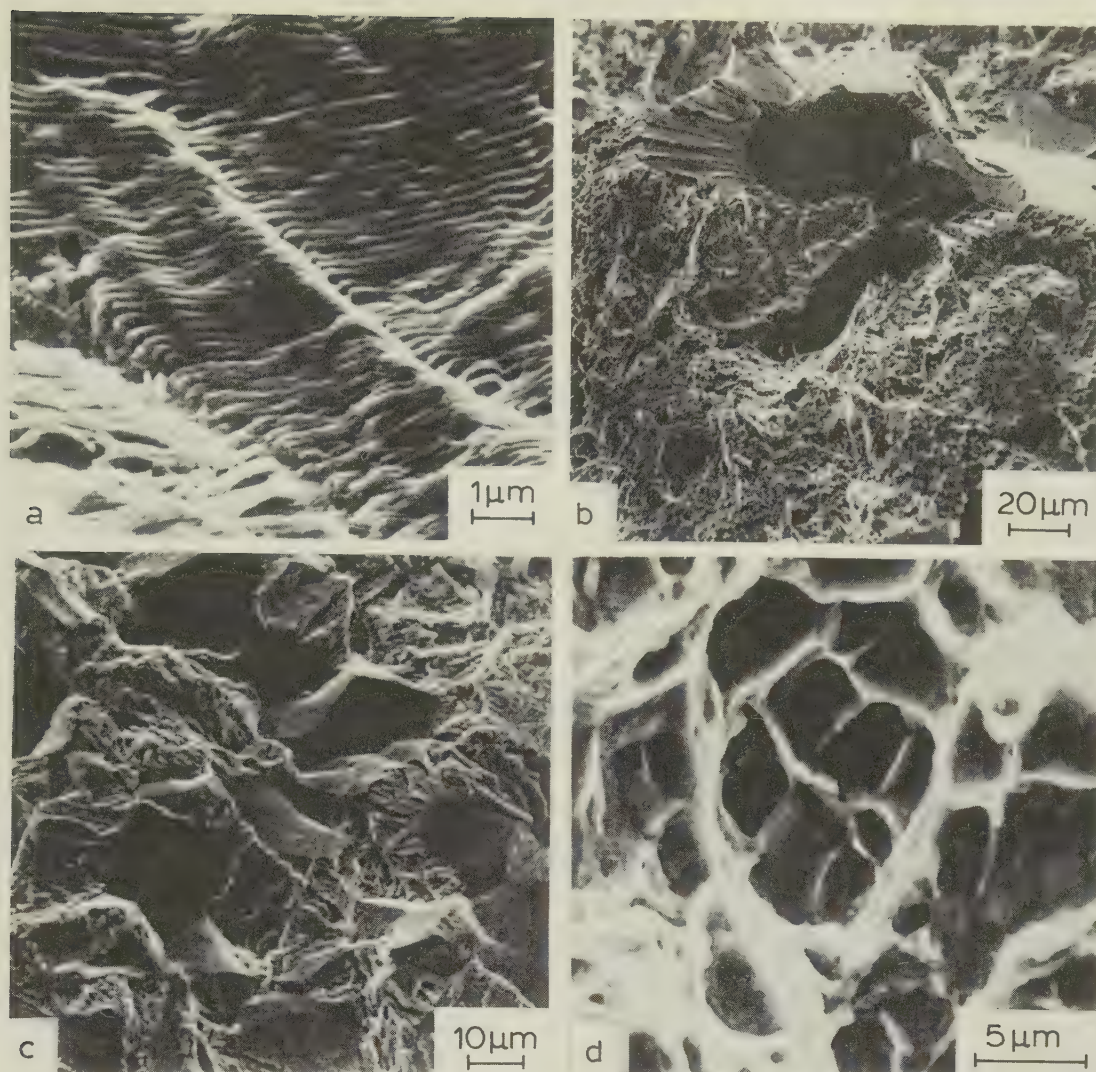
a ductile striations in 9Ni–4Co steel at $\Delta K = 30$ MN m$^{-3/2}$; *b* additional cleavage fracture in mild steel at $\Delta K = 40$ MN m$^{-3/2}$; *c* additional intergranular fracture in 4Ni–1.5Cr steel at $\Delta K = 40$ MN m$^{-3/2}$; *d* microvoid coalescence in 9Ni–4Co steel at $\Delta K = 70$ MN m$^{-3/2}$

3   Fractography of fatigue-crack propagation at intermediate (regime B) and high (regime C) growth rates in steels tested in moist air at $R = 0.1$

rate, whereas at lower (near-threshold) growth rates it is generally conservative as ΔK approaches the threshold stress intensity ΔK_0 (Fig. 2).

In steels, this sigmoidal variation of growth rates with ΔK has been characterized in terms of different primary mechanisms of fracture (Fig. 2). At the midrange of growth rates (regime B, where equation (1) applies), fatigue failure generally is observed to occur by a transgranular ductile striation mechanism[60,61] as shown in Fig. 3*a*, and there is often little experimentally observed variation of growth rates with microstructure and mean stress.[62–64] At higher growth rates (regime C), when K_{max} approaches K_{Ic}, static fracture modes, such as cleavage, intergranular and fibrous fracture (Fig. 3*b–d*), occur in addition to striation growth, resulting in a marked sensitivity of propagation rates to both microstructure and mean

stress.[62–65] At low (near-threshold) growth rates (regime A), there is similarly a strong influence of microstructure and mean stress, although it is uncertain whether this can be *directly* related to a change in fracture mode. However, at such near-threshold stress intensities, the scale of plasticity approaches the order of the microstructural size scales, and measured propagation rates become less than an interatomic spacing per cycle, indicating that crack growth is not occurring uniformly over the entire crack front.

An indication of this deviation from continuum crack-growth mechanisms at near-threshold levels can be seen by comparing measured crack-propagation data with predictions based on crack-tip opening displacements as shown in Fig. 4. The latter model, originally proposed by McClintock,[66] considers striation growth to occur by alternating
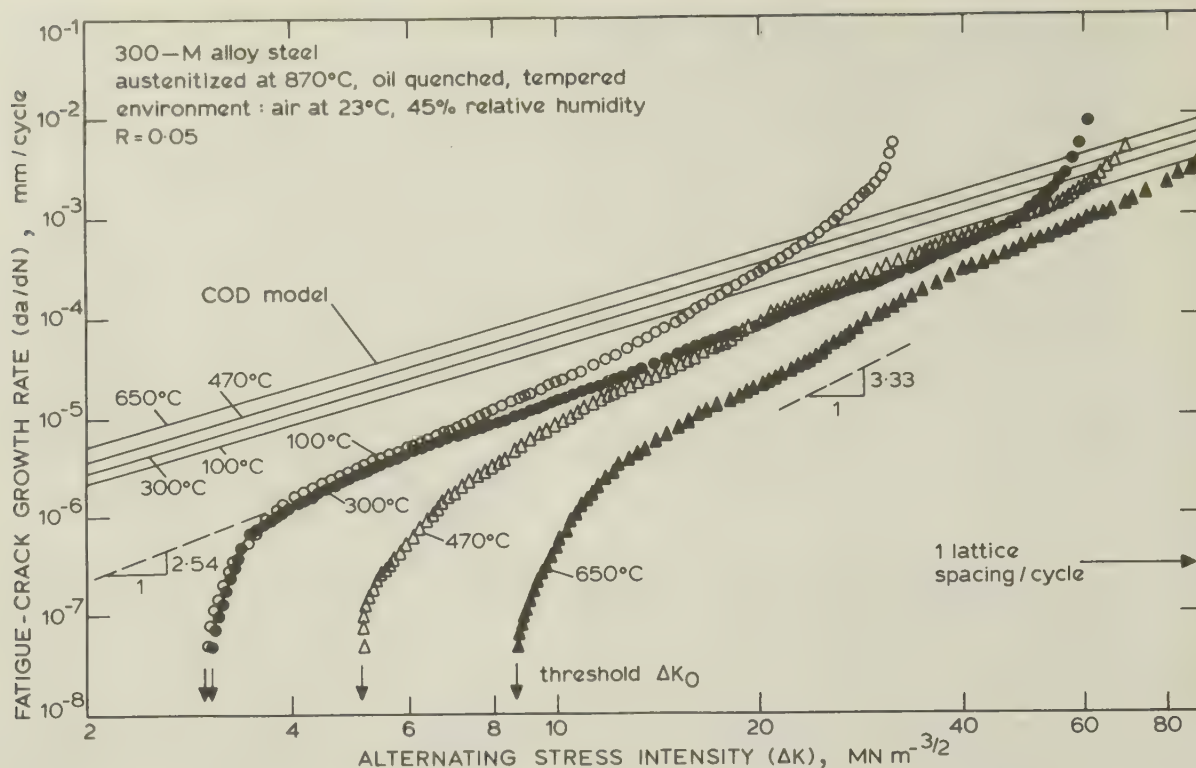
4 Variation of fatigue-crack propagation in moist air at $R = 0.05$ with ΔK for ultrahigh-strength 300—M martensitic steel, quenched and tempered between 100° and 650°C to vary tensile strength from 2300 to 1190 MN m^{-2}, respectively; solid lines indicate predictions based on COD model for crack growth (equation (2))

shear[61] such that the crack-growth increment per cycle should equal the cyclic crack-tip opening displacement ΔCOD, i.e.

$$\frac{\mathrm{d}a}{\mathrm{d}N} = \Delta COD \approx 0.49 \, \frac{\Delta K^2}{2\sigma_y' E} \qquad . \qquad . \qquad . \quad (2)$$

where σ_y' is the cyclic flow stress and E the elastic modulus. It is clear from Fig. 4 that whereas such continuum models provide a reasonable description of crack-propagation behaviour at the midrange of growth rates, marked deviations are apparent at near-threshold levels.

There is no unifying picture of how the environment may influence such fatigue-crack propagation. At medium to high growth rates, several mechanisms have been proposed which rely on an increased chemical-reaction rate at the crack surface. In one class of mechanisms, the accelerating effect of the environment has been ascribed to increased mechanical failure caused by hydrogen (produced by an enhanced cathodic-reaction rate or by adsorption from a hydrogen-containing gas such as H_2 or H_2S) entering the lattice. This is the basis of 'hydrogen embrittlement' theories, which suggest that the hydrogen atoms are transported by diffusion or dislocation motion,[67] ahead of the crack tip, where they may induce hardening or softening,[38] or accumulate at interfaces (grain boundaries, internal voids, and cracks) and lead to decohesion,[68,69] or, in some circumstances,

internal gas pressures.[38] In certain materials, such as titanium and zirconium alloys, the presence of hydrogen may lead further to the precipitation of brittle hydrides.[38,70,71] Other mechanisms interpret environmentally-enhanced fatigue-crack growth in terms of an increased anodic dissolution rate at the crack tip (active-path corrosion theories). Whereas it is now generally accepted that environmental effects in *high-strength* steels are principally hydrogen embrittlement,[72] in many materials, e.g. aluminium alloys, it is possible that both anodic and cathodic processes act in concert for moist or aqueous environments. Both processes result in increased growth rates from the rupture of protective oxide, and, in film-forming solutions, the environmental contribution to cracking can be considered as a function of the interaction between the rate of oxide rupture from emerging dislocations at the crack tip, the rate of passivation, and the rate of metal dissolution or hydrogen production at the bared surface.[46]

Lower strength steels, i.e. with yield strengths below 750 MN m^{-2}, post a particularly interesting problem in this regard since they are largely insensitive to environmentally-assisted cracking under sustained loading in low-pressure hydrogen-containing and dilute aqueous environments. However, on cyclic loading such steels, which range from AISI 1020 mild steel to ASTM A533B and A542 nuclear and coal-gasifier pressure-

vessel steels, suffer significant environmental-assisted fatigue-crack propagation rates in hydrogen[73-75] and hydrogen sulphide gas,[49,73,74] distilled and salt water,[47,76] simulated nuclear-reactor environments,[48,49] and *low-pressure* gas mixtures typical of gasifier atmospheres.[73,74] Furthermore, measured crack-propagation rates appear to be frequency dependent at the midrange of growth rates (i.e. regime B in Fig. 2), and frequency independent at somewhat lower propagation rates.[76] However, little information has been obtained for the environmental contribution to cyclic cracking at near-threshold growth rates below 10^{-6} mm/cycle in these steels, and, moreover, no mechanistic basis for this effect has been developed, although it is widely considered to be hydrogen related in origin.

Mechanical and environmental behaviour associated with fatigue-crack propagation has been well documented, being the subject of many extensive reviews (*see*, for example, Refs. 65 and 77). However, in most cases, behaviour at very low, near-threshold rates has been overlooked. To rectify this, the effects of various mechanical, metallurgical, and environmental factors on near-threshold fatigue are examined in detail below.

NEAR-THRESHOLD FATIGUE-CRACK PROPAGATION

Mechanical factors

Mean stress (or load ratio)

In fatigue studies, the effect of mean stress is often expressed in terms of the stress or load ratio $R(= K_{min}/K_{max})$. Whereas little influence of R can be seen for the midrange of growth rates, near-threshold propagation is generally extremely sensitive to the load ratio. Studies in a wide range of steels and non-ferrous alloys, tested in ambient-temperature air,[5-28,31-44] indicate that the value of ΔK_0 is markedly decreased, and that propagation rates are increased, as the load ratio is raised within a range of R from 0 to 0.9. Typical data, for a normalized medium-carbon steel,[78] are shown in Fig. 5. The load-ratio dependence on near-threshold growth, however, is found to be reduced at negative R values,[79] with increasing temperature,[6] with increasing strength in tempered martensitic steels,[26] and in inert atmospheres.[21,37,39-41,80] For the last case, Beevers and co-workers[21,37] observed that, for tempered martensitic En 24 steel and Ti—6Al—4V tested *in vacuo*, near-threshold crack-propagation rates and the value of ΔK_0 were completely independent of load ratio (Fig. 6). This lack of an R-dependence for tests under inert conditions has been confirmed for low-alloy martensitic steels *in vacuo* by Irving and Kurzfeld[81] and for 316 stainless steel *in vacuo* and in helium by Priddle *et al.*[31] Other studies of martensitic stainless steels[80] and of Ti—6Al—4V (Refs. 39, 40), however, show that by testing *in vacuo*, the dependence of ΔK_0 on load ratio is
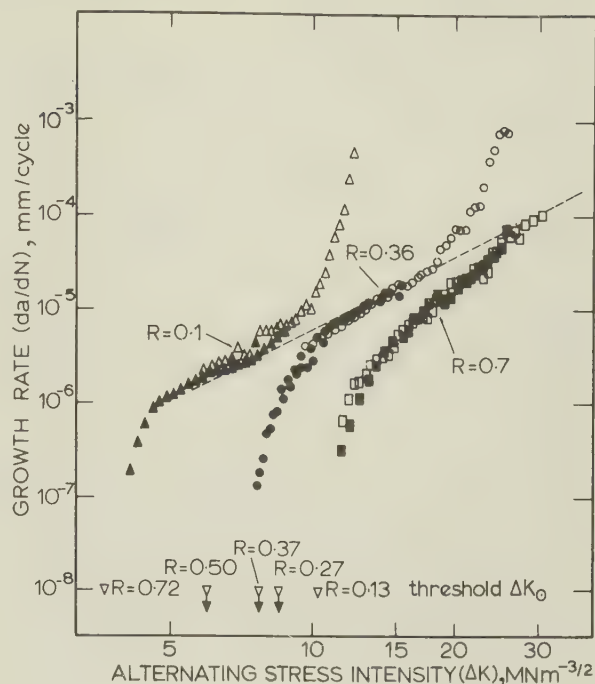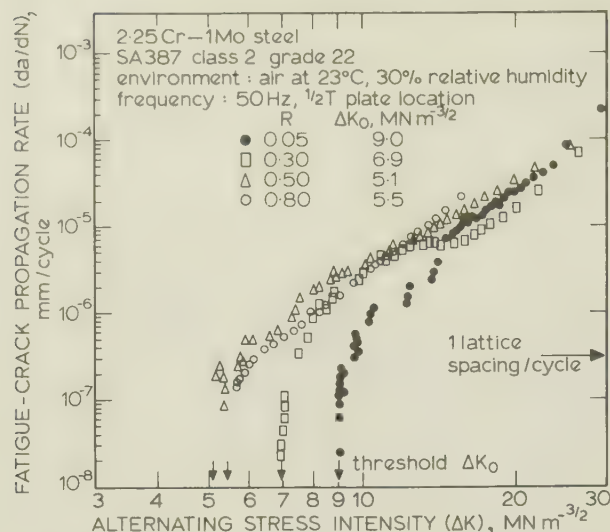

5   Influence of load ratio from $R = 0.10$ to 0.72 on fatigue-crack growth in a normalized 0.55C—2.23Mn pearlitic—martensitic steel of $\sigma_y = 743$ MN m^{-2} (after Ref. 78)

markedly reduced yet not completely eliminated, although in all cases the value of the threshold was significantly higher than in air. Such results are a strong indication that marked effects of load
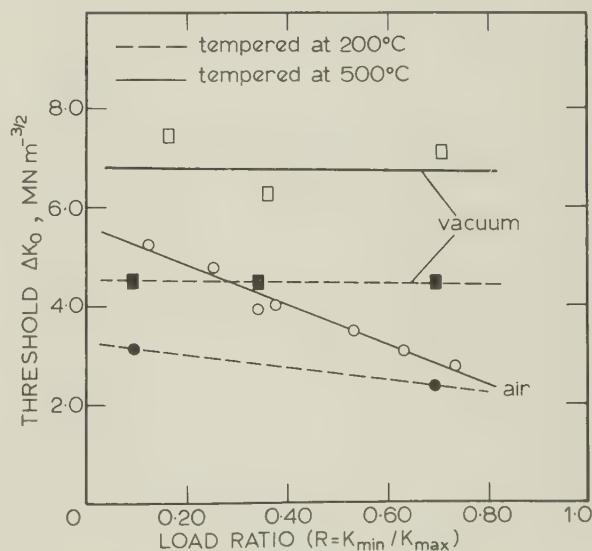

6.   Variation of threshold ΔK_0 with load ratio R for martensitic 1.4Ni—1Cr—0.3Mo high-strength steel (En 24), tempered at 200°C ($\sigma_y = 1570$ MN m^{-2}) and at 500°C ($\sigma_y = 1274$ MN m^{-2}); tests in laboratory air (40% relative humidity) and vacuum (10^{-3} Pa) (after Refs. 21 and 81)

7   Influence of load ratio from $R = 0.05$ to 0.80 on near-threshold fatigue-crack growth in air for normalized 2.25Cr–1Mo pressure-vessel steel (SA387) of $\sigma_y = 290$ MN m^{-2} (after Ref. 83)

ratio on near-threshold fatigue-crack propagation can be attributed, at least partially, to some environment interaction. The lack of a load-ratio effect on higher (midrange) growth rates is consistent with this argument, since at such faster propagation rates, the pertinent environmental reactions may not be able to keep pace with the crack velocity. Other explanations[6,7,19,35,42,79] of the load-ratio effect have centred around the phenomenon of crack closure, first identified by Elber[82] in aluminium alloys at much higher stress intensities. The relative merits of the environmental and closure explanations are discussed below.

In low-strength ferritic steels, both Cooke and Beevers,[12] and Masounave and Baïlon[15] found for a particular microstructure and strength
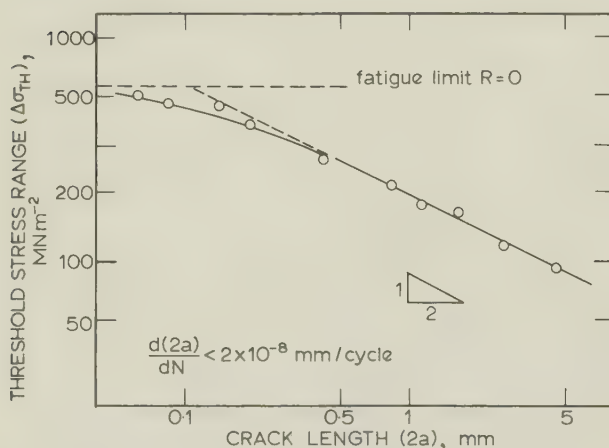
level that the effect of load ratio was consistent with the threshold occurring at a constant value of K_{max} or $\Delta K_0/1-R$. Such behaviour is without explanation, and has not been observed in higher strength steels or other materials.

The influence of load ratio on the fatigue-crack propagation threshold ΔK_0 in normalized 2.25Cr–1Mo steel (SA387 Class 2, Grade 22), a potential steel for coal-gasifier pressure-vessel construction, is shown in Fig. 7 for tests in ambient-temperature moist air at a strength level of 290 MN m^{-2} (Ref. 83). It is apparent that the values of ΔK_0 decreases with increasing load ratio up to $R = 0.5$, consistent with a constant value of K_{max} at the threshold. Above $R = 0.5$, ΔK_0 remains constant, similar to behaviour reported for aluminium alloys.[42] As noted above, explanations for this effect are uncertain.

Testpiece geometry and crack size

Provided conditions of linear elasticity are reasonably valid, fatigue-crack growth can be generally considered to be geometry independent, apart from variations in growth rate owing to changes in specimen thickness, e.g. departure from plane-strain conditions. In such instances, small differences in the growth rate between specimens of different thickness can arise because of nominal yielding, changes in fatigue-fracture mechanism near final failure, and perhaps closure effects.[84] However, for near-threshold fatigue-crack growth, effects of thickness and specimen geometry should be minimal because the low stress intensities involved invariably impose a condition of predominately plane strain. This has been borne out by experiments in low-strength steels[55] and aluminium alloys[32] tested over a range of specimen geometries and thicknesses.

The influence of crack size, on the other hand, has been shown to be particularly important. Classic experiments by Kitagawa and Takahashi[45] in low-strength steel have shown that, whereas the condition for the non-propagation of a surface flaw could be related to a constant threshold stress intensity ΔK_0 for crack lengths in excess of around 1 mm, below this crack size, a transition occurred in which the fatigue-limit stress became the threshold condition for growth (Fig. 8). Topper and co-workers[85,86] have attempted to rationalize these data by defining the alternating stress intensity ΔK at elastic stresses $\Delta \sigma$ in terms of

$$\Delta K = \Delta \sigma \sqrt{\pi(a + a_0)} \quad . \quad . \quad . \quad . \quad . \quad (3)$$

where a is the crack length and a_0 a constant characteristic of a given material and material condition. Thus, by defining the threshold ΔK_0 in the usual way as the minimum value of ΔK for crack growth, the threshold stress range $\Delta \sigma_{TH}$ is given by

$$\Delta \sigma_{TH} = \frac{\Delta K_0}{\sqrt{\pi(a + a_0)}} \quad . \quad . \quad . \quad . \quad . \quad (4)$$

8   Effect of crack size on fatigue-threshold conditions in Japanese HT80 steel (after Ref. 45)

such that as crack sizes become small, of the order of a_0

$$\Delta\sigma_{TH} = \frac{\Delta K_0}{\sqrt{\pi a_0}} = \Delta\sigma_e \quad . \quad . \quad . \quad . \quad . \quad (5)$$

where $\Delta\sigma_e$ is the fatigue limit corrected for the appropriate R value. Equations (4) and (5) reproduce exactly the data trend shown in Fig. 8, but at present there is no physical interpretation of the constant a_0.

There is also limited evidence that near-threshold crack-growth rates are accelerated, and the value of the threshold ΔK_0 decreased, at shorter crack lengths, i.e. for microcracks,[85-87] which, if substantiated, would provide a very feasible explanation to the existence of non-propagating cracks. A more complete review of the differences and similarities between the near-threshold fatigue-crack propagation behaviour of micro- and macrocracks can be found in Ref. 88.

Frequency and wave shape

For fatigue-crack propagation in the midrange of growth rates, the general effect of decreasing the cyclic frequency is to increase the crack-growth increment per cycle, due to enhanced environmental effects.[77] At near-threshold growth rates, however, very limited data exist, simply because of the limitations imposed by the high-frequency response of conventional testing machines, and the time factor involved in measuring low growth rates at very low frequencies. Results[55] on 2219–T851 aluminium alloy indicated no effect on near-threshold growth over a frequency range of 25–150 Hz. Tests in 2024–T3 aluminium alloy at frequencies between 342 and 832 Hz (Ref. 42), conversely, showed an increase in crack propagation rate and a twofold decrease in ΔK_0 with increasing frequency, which was tentatively attributed to creep effects due to crack-tip heating. In D6ac steel, however, increasing the frequency from 100 to 375 Hz resulted in lower near-threshold growth rates for tests in dry argon, and no effect in room air.[22]

For low-strength ferritic steels, such as HSLA pipeline steels X–65 (Ref. 47) and A533–B and A508 nuclear pressure-vessel steels,[49] tested in water environments at frequencies between 0.01 and 10 Hz, there is evidence showing marked frequency-dependent crack propagation behaviour for growth rates in excess of 10^{-5} mm/cycle, which becomes frequency independent at lower growth rates as the threshold is approached. Similar results have been seen in higher strength HY 130 marine steels tested in salt solution.[76] Companion tests in hydrogen sulphide gas[49] resulted in similar growth rates without any effect of frequency, even above 10^{-5} mm/cycle. The environmentally-enhanced growth rates in water and hydrogen sulphide, compared to those measured in air, were accounted for in terms of hydrogen embrittlement, although the mechanism for the

embrittlement was not defined and no attempt was made to explain the transition from frequency-independent to frequency-dependent propagation rates in water above 10^{-5} mm/cycle.

The effect of wave form (i.e. sinusoidal, square, and triangular) on near-threshold growth has been examined in aluminium alloys and stainless steels in room air.[32] For both materials no change in ΔK_0 was observed for the various wave forms. In the same experiments, decreasing the frequency from 130 to 0.5 Hz for all wave shapes led to a decrease in ΔK_0, perhaps reflecting the influence of the environment at low growth rates.

Microstructural factors

Material strength

Fatigue-crack propagation in metals has been generally found to be largely unaffected by yield strength.[89] In fact, for steels, raising the strength by nearly an order of magnitude does not change crack-propagation rates over the midrange of growth rates by much more than a factor of two or three.[65] However, at near-threshold levels below 10^{-6} mm/cycle, a surprisingly large dependence of material strength has been observed on the value of the threshold ΔK_0 and on subsequent growth rates. In low-strength ferritic–pearlitic steels with yield strengths less than 500 MN m^{-2}, for example, values of the threshold have been observed to decrease significantly with increasing strength.[11,16,18] An even larger effect has been reported for high- and ultrahigh-strength martensitic steels (yield strengths between 1000 and 2000 MN m^{-2}) with the exception that the controlling measure of strength was the cyclic, rather than the monotonic, yield stress.[26,27] Specifically, increasing the cyclic strength led to marked increases in near-threshold propagation rates (Fig. 4), and a significant reduction in ΔK_0 (Fig. 9). Cyclic softening can thus be regarded as extremely beneficial to improving near-threshold fatigue-crack growth resistance in steels.[26,27] In low-alloy pressure-vessel steel, variations in monotonic yield strength between 300 and 400 MN m^{-2} resulting from differences in cooling rate experienced through the thickness of a 184 mm thick plate, did not give rise to significant changes in near-threshold fatigue-crack growth resistance in a 2.25Cr–1Mo steel, SA387 (Ref. 83). However, in 0.5Cr–0.5Mo–0.25V steel,[90] coarse-grained precipitation-hardened ferritic microstructures showed significantly lower growth rates near ΔK_0 than higher strength bainitic or martensitic structures.

The effect of strength on near-threshold crack-propagation behaviour is significantly less at high R values,[26,27,80,91] and not so evident in ferritic–pearlitic steels.[91] The latter probably results from the fact that data on the lower strength steels cover a relatively narrow range of strengths and are subject to considerably more scatter. Furthermore, varying the strength in such steels generally involves variations in the
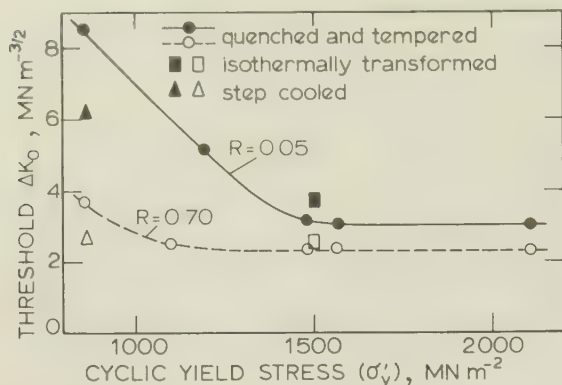
**9   Variation of threshold ΔK_0 with cyclic yield
strength at $R = 0.05$ and 0.70 for $0.4C$—$1.76Ni$—
$0.76Cr$—$1.6Si$ ultrahigh-strength steel (300—M)
tested in moist laboratory air**

ferrite grain size which is also known to have a
marked influence on near-threshold behav-
iour.[16,18,29]

Results in non-ferrous alloys, however,
reveal somewhat different behaviour. Small re-
ductions in the threshold ΔK_0 have been observed
in aluminium bronze[44] and Al—Zn—Mg alloys[43]
as the cyclic strength is decreased. This is pre-
cisely the opposite of behaviour observed in
steels, but the magnitude of the effect is very
much smaller, for example, increasing the cyclic
flow stress by a factor of nearly two in the alu-
minium alloy only results in an increase in ΔK_0
from 2.5 to 3.7 MN m$^{-3/2}$ (Ref. 43), whereas a
similar increase in strength in a tempered mar-
tensitic 300—M steel leads to a decrease in ΔK_0
from 8.5 to 3.0 MN m$^{-3/2}$ (Ref. 26).

Explanations for these effects are again un-
certain. The small increase in ΔK_0 with increase
in flow stress for the non-ferrous materials have
been attributed to a decrease in the alternating
plastic crack-tip opening displacement.[43,44]
However, reference to Fig. 4 clearly shows that
such explanations are not applicable to steels. In
this figure, growth-rate predictions based on the
COD model (equation (2)) are compared with
experimental data for an ultrahigh-strength mar-
tensitic steel 300—M, tempered over a range of
temperatures from 100° to 650°C to vary the
tensile strength from 2340 to 1190 MN m^{-2},
respectively. It is apparent that not only does the
COD model predict a far too small dependence of
growth rates on strength but also predictions are
in the wrong direction, i.e. higher strength re-
sults in a marked increase in near-threshold
growth rates whereas COD predictions show a
small decrease.

The dependence of near-threshold growth-
rate behaviour on material strength in steels has
been rationalized, however, in terms of environ-
mental arguments[24,27] and notch-sensitivity
effects,[92] as described below and in the 'Discus-
sion' section of this paper. A comparison of

growth rates in a single material, with varying
strength, *in vacuo* is required to help resolve this
issue.

An intriguing aspect of the strength effect in
steels is the fact that whereas the fatigue-crack
propagation threshold ΔK_0 is *decreased* with in-
creasing strength, the well known fatigue limit
$\Delta\sigma_e$, or endurance strength, is *increased*.[26,88,90]
Both parameters represent limits for fatigue
damage,[88] but the threshold ΔK_0 must be regarded
as the minimum stress intensity below which long
macrocracks do not grow, whereas the fatigue limit
is generally the minimum stress below which short
macrocracks do not *initiate* (i.e. by coalescence of
microcracks). Following the work of Topper and
co-workers[85,86] and McEvily,[92] one can rational-
ize this apparent inconsistency in the effect of
strength by equating the characteristic length con-
stant a_0 in equations (3)—(5) to Neuber's effective
crack-tip radius ρ', such that

$$\Delta K_0 = \Delta\sigma_{TH}\sqrt{\pi(a + \rho')}$$

$$= \lim_{a \to \rho'} \Delta\sigma_e\sqrt{\pi\rho'} \qquad . \quad . \quad . \quad . \quad . \quad (6)$$

where $\Delta\sigma_{TH}$ is the threshold stress and a the crack
length. Since the fatigue limit for steels (at $R = -1$)
is generally found to be half the ultimate strength
($\sigma_u/2$), correcting for $R = 0$ using the Goodman
relationship yields

$$\Delta\sigma_e = 2\sigma_u/3 \qquad . \quad . \quad . \quad . \quad . \quad . \quad (7)$$

consistent with the experimentally observed
increase in fatigue limit with increasing strength.
However, from the studies of Kuhn and Hardrath,[93]
the Neuber constant ρ' appears inversely propor-
tional to the ultimate tensile strength (raised to
the 4th power), and the following empirical rela-
tionship is found for steels

$$\sqrt{\rho'} = \frac{530}{\sigma_u^2} \qquad . \quad . \quad . \quad . \quad . \quad . \quad (8)$$

where ρ' is in inches and σ_u in ksi. Combining
equations (6)—(8) gives

$$\Delta K_0 = \Delta\sigma_e\sqrt{\pi\rho'}$$

$$\approx \left(\frac{2\sigma_u}{3}\right)\left(\frac{.530\sqrt{\pi}}{\sigma_u^2}\right) \propto \frac{1}{\sigma_u} \qquad . \quad . \quad . \quad (9)$$

consistent with the experimentally observed
decrease in threshold ΔK_0 with increasing strength.
By comparison with Fig. 8, this indicates that at
short crack lengths ($a \approx \rho'$), the threshold stress
$\Delta\sigma_{TH}$ will be *increased* as the strength level is
raised, whereas at long crack lengths ($a \gg \rho'$),
$\Delta\sigma_{TH}$ will be *decreased*. These predictions are
plotted in Fig. 10 using data from 300—M high-
strength steel tempered between 100° and 650°C
(Refs. 26, 27, 94) and equations (6)—(9). As dis-
cussed by Fine and Ritchie,[88] this result is
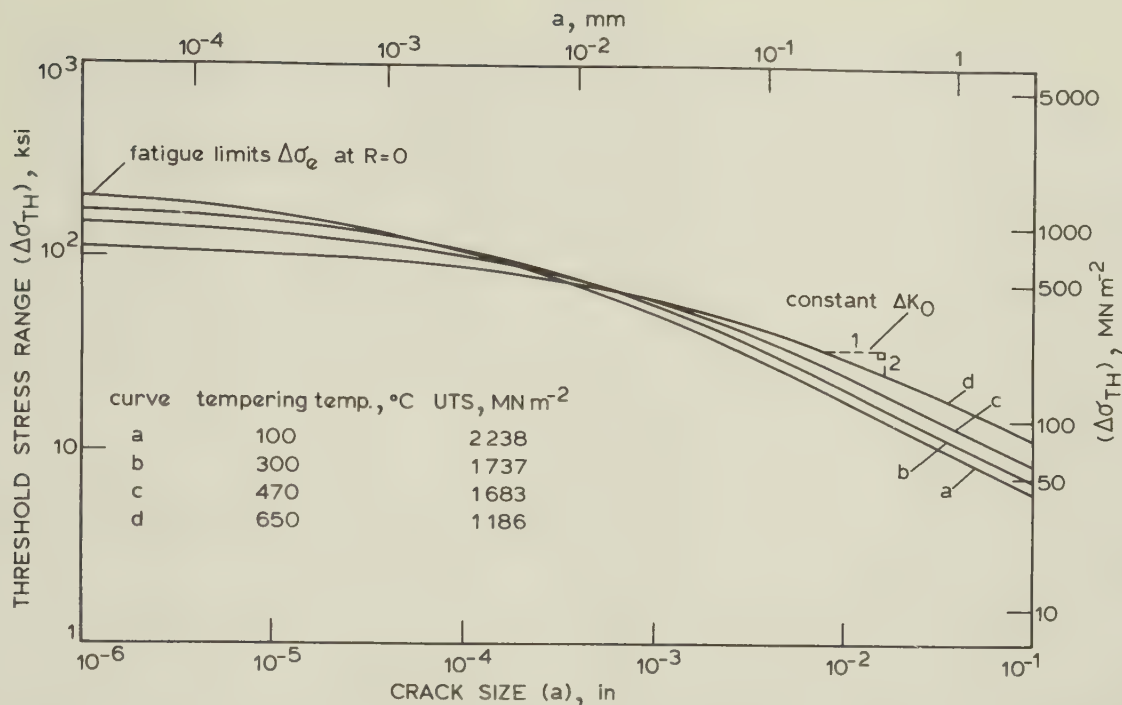
10 Predicted variation of threshold stress $\Delta\sigma_{TH}$ at $R = 0$ with crack size a from equations (6)—(9) based on data for 300—M ultrahigh-strength steel tempered between 100° and 650°C to vary tensile strength

particularly significant for the alloy design of steels with improved resistance to very high cycle fatigue damage, since the optimum microstructures desired will depend upon whether structural design is to be based on initiation or propagation of a 'fatal' flaw.

Grain size

Whereas refining grain size can be beneficial in raising the fatigue limit or endurance strength of (planar slip) materials,[95] the effect of grain size on fatigue-crack propagation has been observed to
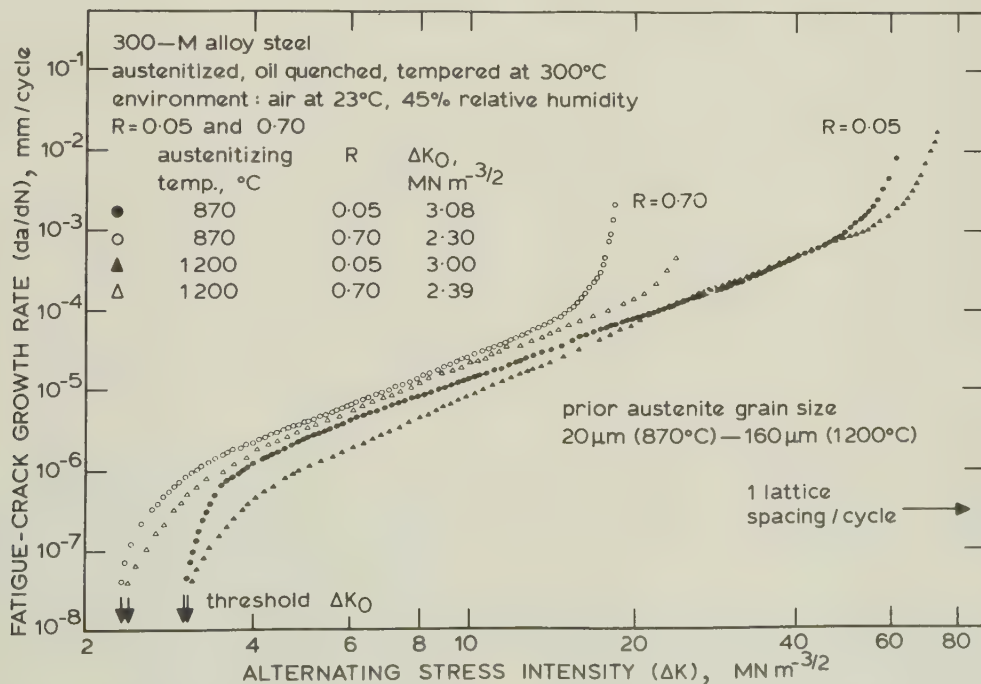
11 Effect of prior austenite grain size (20—160 μm) on fatigue-crack growth in cyclic softening 300—M ultrahigh-strength steel ($\sigma_y = 1700$ MN m^{-2}) at $R = 0.05$ and 0.70 in moist laboratory air
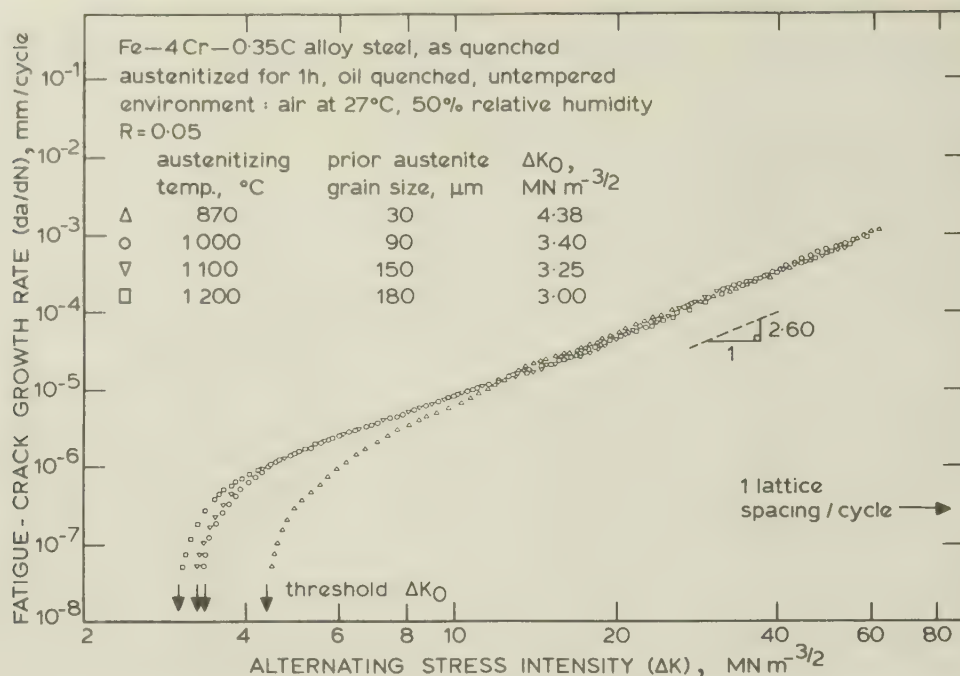
12 Effect of prior austenite grain size (30—180 μm) on fatigue-crack growth in cyclic-hardening as-quenched Fe—Cr—C high-strength steel ($\sigma_y = 1300$ MN m^{-2}) at $R = 0.05$ in moist laboratory air

be negligible in most studies at intermediate growth rates.[29,95-97] At low growth rates in room air, however, several workers[16,18,24,27,33,36,98] have observed improved resistance to near-threshold crack propagation with coarser grain sizes. Robinson and Beevers[33] report an order of magnitude decrease in near-threshold growth rates in α-titanium after coarsening the grain size from 20 to 200 μm. Similar effects have been seen in Ti—6Al—4V (Refs. 36, 98) and other basic α + β

13 Variation of threshold ΔK_0 with grain size for steels at $R = 0.05$: for ferritic—pearlitic low-strength steels grain size refers to ferritic grain size, whereas for martensitic high-strength steels, grain size refers to prior austenite grain size

titanium-alloy systems.[98] Furthermore, a marked increase in threshold ΔK_0 values has been observed in a range of low-strength steels by increasing the ferrite grain size.[16,18] In all of these studies, however, no attempt was made to control strength, and the effect of coarsening the grain size may well have been masked by a concurrent decrease in strength, which is known to increase markedly the threshold in steels.[27] Comparisons at constant yield strength have been made in two high-strength steels, 300—M (Refs. 24—27) and Fe—Cr—C (Ref. 29), where it was found that, in the cyclic softening 300—M, coarsening the prior austenite grain size by almost an order of magnitude decreased near-threshold growth rates yet left ΔK_0 unchanged (Fig. 11), whereas, in cyclic hardening Fe—Cr—C, similar coarsening of the structure increased near-threshold rates and reduced the threshold (Fig. 12). The variation of threshold with grain size for low- and high-strength steels is shown in Fig. 13, and clearly shows the contrasting behaviour between the two classes of steels.[29]

Several explanations have been proposed to explain the grain-size effect, none of which is entirely satisfactory. It has been suggested, for example, that since near-threshold growth is 'microstructurally-sensitive', it may be confined to specific crystallographic planes so that in coarser structures, greater deviations of the crack path may occur from the plane of maximum tensile stress.[16] Other authors[24,99] have reasoned for high-strength steels that, since plastic zones are often confined within a single grain during near-threshold growth, the probability that hydro-

gen atoms, generated by chemical reactions with the environment at the crack tip, can be swept into the grain boundaries by dislocation motion,[67] is much smaller if the grain size is very large. Effectively, this hypothesis states, that by coarsening the grain size, the environmental contribution to near-threshold growth is reduced, and this is consistent with an observed decrease in hydrogen-embrittlement susceptibility of high-strength steels as the grain size is increased.[100] However, the conflicting results observed in Fe—Cr—C steel[29] are not consistent with this explanation. A study of the influence of grain size (at constant strength) in inert environments is required before this effect can be resolved.

Structure

Very little information is available at present on the relative resistance to near-threshold fatigue-crack propagation of particular microstructures in metals (i.e. pearlite *v.* tempered martensite *v.* bainite, etc.), aside from data where particular structures have been compared at different strength levels. For example, in aluminium alloys,[43] underaged structures appear to have fractionally better resistance than peak and over-aged structures whereas in tempered martensitic steels, spheroidized structures offer far the best resistance.[27] Comparisons at constant strength have been made in 300—M ultrahigh-strength steel[26,27] between isothermally-transformed structures containing an interlath network of retained austenite (volume fraction ~12%) within a lower bainite—tempered-martensite matrix, and quenched and tempered fully martensitic structures containing no austenite. Here, if the structures are compared at equivalent monotonic yield strength, quenched and tempered microstructures offer greater resistance owing to their lower cyclic yield strength* (Fig. 14). However, when compared at equivalent cyclic strength, isothermally-transformed structures offer marginally superior resistance, in the form of higher thresholds (Fig. 9), which is indicative[101] of their superior resistance to environmentally-induced cracking under monotonic loads. A similar small beneficial effect of interlath retained austenite on near-threshold crack-propagation resistance in tempered martensite steels has been observed for a 9Ni—4Co—0.2C high-strength aerospace steel HP 9—4—20 tested in moist air.[102] It was reasoned in this case that the role of the austenite effectively was to reduce the environmental contribution to cracking (i.e. from hydrogen embrittlement) by slowing down the rate of diffusion of adsorbed hydrogen atoms ahead of the crack tip. Alloy additions of silicon, similarly, may lead to a reduction in diffusivity of hydrogen in iron.[103-105] Accordingly, silicon-modified 4340

(300—M), with its lower susceptibility to sustained-load environmentally-assisted cracking,[101,106,107] displays superior near-threshold crack-propagation resistance in moist air compared with unmodified 4340 at the same strength level, as shown in Fig. 15 (Ref. 108). In general, it appears that microstructures with superior resistance to hydrogen-assisted or stress corrosion cracking under monotonic loads will have a similar superior resistance to near-threshold fatigue-crack growth.[108]

A particularly striking effect of microstructure has been observed in AISI 1018 mild steel, where the production of duplex ferrite—martensite structures can lead to increased near-threshold crack-propagation resistance and increased strength compared to conventionally heat-treated steel.[109] By suitable heat-treatment procedures, duplex microstructures where the martensitic phase α' is continuous and totally encapsulates the ferritic phase α were found to have increased strength ($\sigma_y = 452$ MN m^{-2}) and a significantly higher threshold ($\Delta K_0 \approx 20$ MN m$^{-3/2}$), than similar structures where the ferritic phase surrounds the martensite ($\sigma_y = 293$ MN m^{-2}, $\Delta K_0 \approx 10$ MN m$^{-3/2}$), as shown in Fig. 16. The result is contrary to what one might expect for the relationship between strength and near-threshold behaviour and is without explanation, yet it does introduce a very promising way of improving the fatigue-crack propagation resistance of low-carbon steels without compromising other mechanical properties.

For non-ferrous metals, studies in Ti—6Al—4V at roughly constant strength (monotonic yield strengths between 835 and 1000 MN m^{-2}) have revealed a strong effect of structure near the threshold.[36] Ranked in order of greatest resistance to near-threshold growth, β-annealed structures were superior to transformed β, followed by as-received and martensitic structures. These microstructural differences were more pronounced at low R values, as has been similarly observed in ultrahigh-strength steels,[26] and far less pronounced for tests *in vacuo*.[37] This latter fact once again reinforces the argument that microstructural influences on near-threshold fatigue-crack propagation are often primarily a consequence of environmental effects, rather than inherent mechanical effects.

The effect of non-metallic inclusion content on near-threshold fatigue behaviour has been examined in a medium-strength pearlitic rail steel.[110] Here it was found that, whereas decreasing the volume fraction of inclusions (sulphide stringers and oxide-type) led to marked increases in the fatigue or endurance limit, no systematic effect was observed on the value of the threshold ΔK_0. However, other studies[111] on the influence of steelmaking practice on somewhat higher fatigue-crack propagation rates in nuclear pressure-vessel steel A533B have shown that the absence of elongated Type 2 MnS inclusions and galaxies of alumina inclusions by calcium treating or

---

*Isothermally-transformed structures do not cyclically soften due to deformation-induced transformation of retained austenite to martensite.[26]
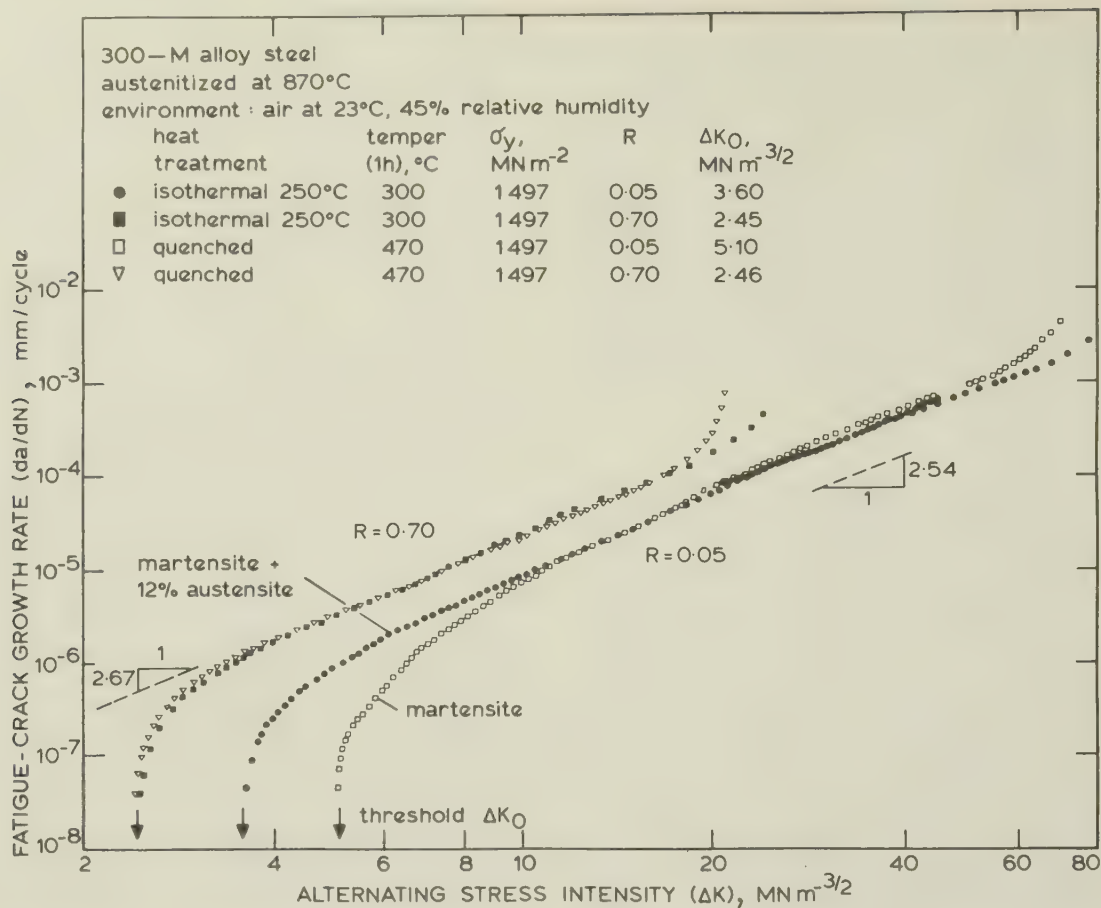
14   Comparison in martensitic 300—M high-strength steel at constant monotonic strength of isothermally-transformed structure, containing 12% retained austenite, with quenched and tempered structure containing no austenite, at $R = 0.05$ and 0.70 in moist laboratory air; quenched and tempered structure undergoes cyclic softening ($\sigma_y' = 1200$ MN m^{-2}) whereas isothermally-transformed structure remains cyclically stable ($\sigma_y' = 1500$ MN m^{-2})

electroslag remelting results in a significant improvement in the isotropy of fatigue-crack growth behaviour and lower overall growth rates.

Impurity-induced grain-boundary segregation

It is well known that the toughness of low-alloy steels can be severely impaired by heat-treatment procedures which result in the segregation of residual-impurity elements, such as P, S, Sb, and so forth, to grain boundaries (temper embrittlement). Recently, it has become clear that impurity segregation can also degrade creep, stress corrosion, and hydrogen-induced cracking resistance.[25] There has been one study[25] on the effect of prior impurity segregation on near-threshold fatigue-crack propagation, conducted in an ultra-high-strength martensitic steel (300—M), tested in moist room air in the unembrittled and temper embrittled* conditions (at the same yield strength and prior austenite grain size). Here it was

found that, although no difference in crack propagation rates was observed between unembrittled and embrittled structures at the midrange of growth rates, at near-threshold levels, impurity-induced embrittlement gave rise to vastly accelerated growth rates and a reduction in ΔK_0 by almost 30% at both low and high load ratios (Fig. 17). This was accompanied by a significant increase in the proportion of intergranular fracture in the embrittled steel close to the threshold. This large effect at very low growth rates, compared to little or no effect at higher intermediate rates, is again indicative of an enhanced environmental contribution to cracking in the impurity-embrittled structure, perhaps caused by an interaction between residual-impurity elements and hydrogen atoms (generated by chemical reactions with the moist air atmosphere at the crack tip) in prior austenite grain boundaries (*see* 'Discussion' section below).
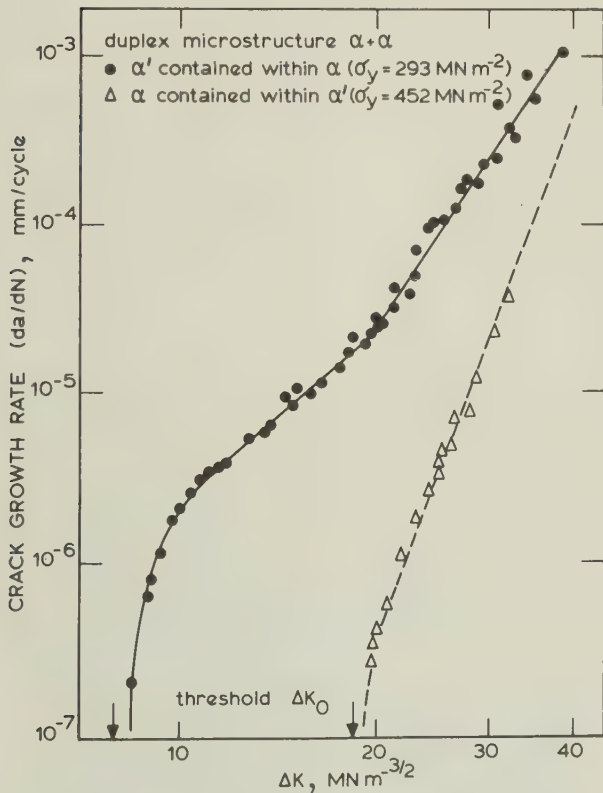
Weld microstructure

Little information exists on the influence of welds and weld microstructure on near-threshold fatigue-

---

*Auger studies indicated that the embrittlement resulted from a build-up of P, Si, Mn, and Ni in prior austenite grain boundaries.[25]

AISI 4340 and 300—M alloy steels
austenitized at 870°C, oil quenched, tempered
environment : air at 23°C, 45% relative humidity
R = 0.05 and 0.70

steel	temper (1h), °C	σ_y, MN m^{-2}	R	ΔK_0, MN m$^{-3/2}$
● 4340	300	1497	0.05	3.80
○ 4340	300	1497	0.70	2.44
▲ 300—M	470	1497	0.05	5.10
△ 300—M	470	1497	0.70	2.46
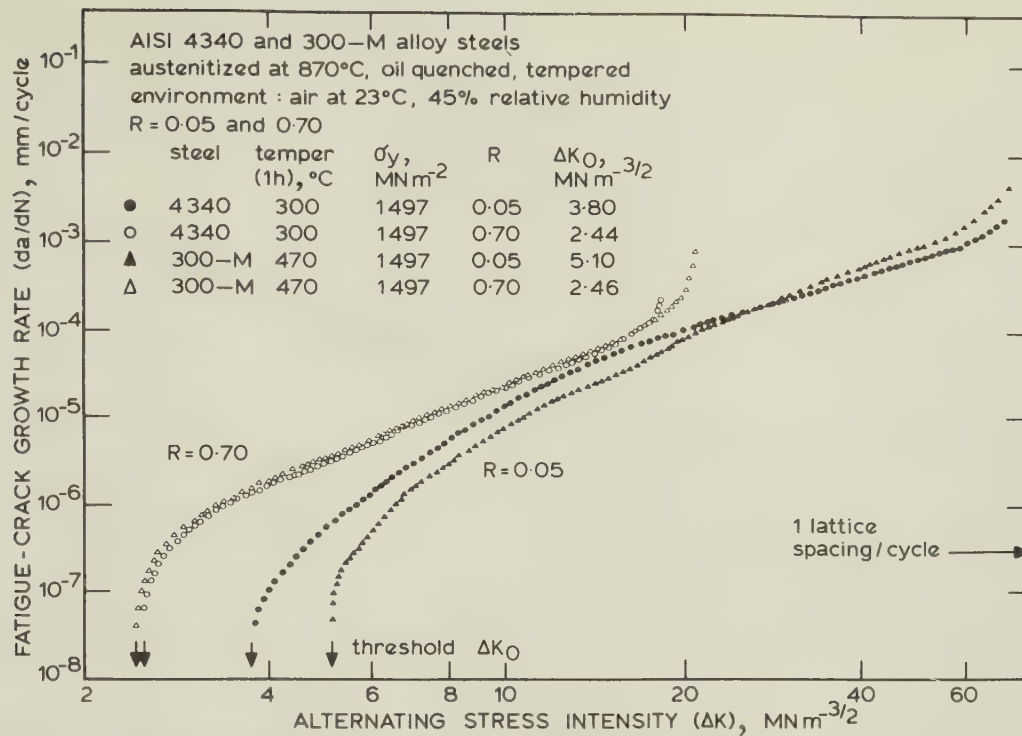
15 Comparison, at constant yield strength ($\sigma_y = 1497$ MN m^{-2}), of fatigue-crack growth behaviour of quenched and tempered 4340 and 300—M (4340 modified with 1.3%Si) ultrahigh-strength steels in moist laboratory air at $R = 0.05$ and 0.70 (after Ref. 108)

16 Variation of fatigue-crack growth rate with ΔK for duplex microstructures in AISI 1018 mild steel; duplex structures consist of ferrite α and martensite α' (after Ref. 109)

crack propagation, except for a few studies on austenitic stainless steels.[30,112] In general, stainless steel weldments show little or no deterioration in fatigue-crack propagation resistance when compared to parent metal at intermediate growth rates.[113] At low growth rates, however, Type 304 and 316 weldments show faster crack propagation rates than in parent metal, both at ambient[30] and higher[112] temperatures in air. No explanations exist for this behaviour, apart from suggestions regarding the possible deleterious effect of the variable and coarser grained structure within the weld.[30] Limited results for weldments of mild steel indicate no change in threshold ΔK_0 values between parent metal, heat-affected zone areas, and weld metal.[17]

Environmental factors

Temperature

Effects of temperature on near-threshold fatigue-crack growth behaviour have been studied primarily in steels.[6,17,31] Pook and Greenham[17] observed no change in ΔK_0 between ambient temperature and 300°C for tests on mild steel in air at low R values, whereas thresholds were higher at 300°C for tests at high R values. Conversely, Paris *et al.*,[6] in A533B and A508 nuclear pressure-vessel steels, found the largest sensitivity of the threshold to temperatures at low R values (i.e. $R = 0.1$), and observed no change in ΔK_0 over the temperature range, ambient to 350°C, at high R values (i.e. $R = 0.7$). Furthermore, although fatigue-crack growth (at $R = 0.1$) was
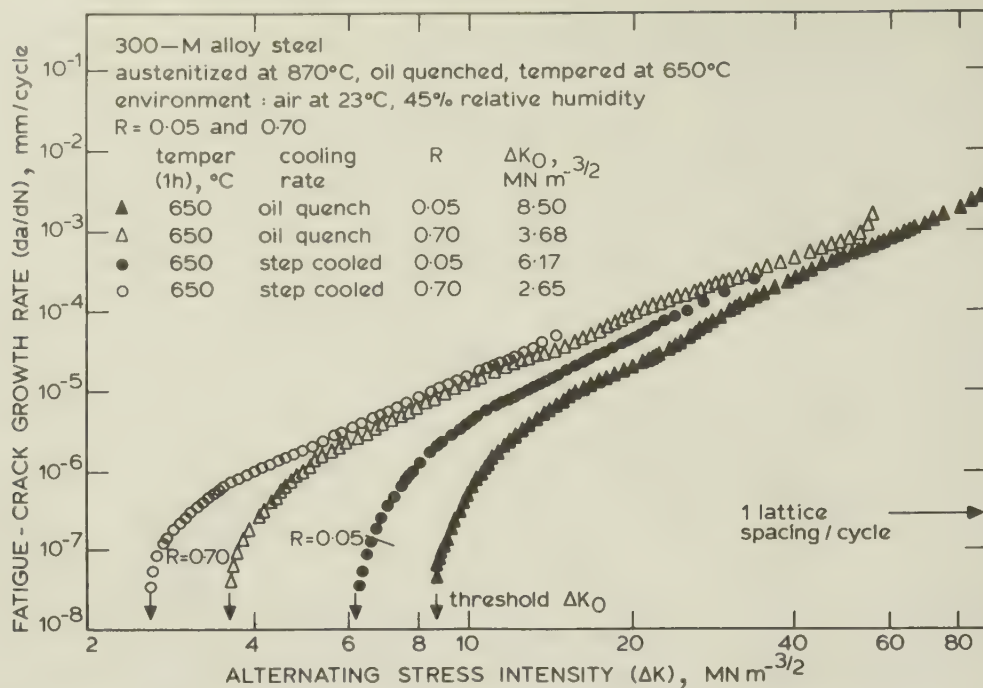
17   **Effect of prior impurity-induced embrittlement on fatigue in 300—M high-strength steel at** $R = 0.05$
and 0.70 in moist laboratory air; step-cooled structure is temper embrittled, oil-quenched structure
is unembrittled at same strength level ($\sigma_y = 1070$ MN m^{-2})

most sensitive to temperature close to the thres-
hold, there was no systematic increase in ΔK_0
with increasing temperature. Threshold values
were found to be highest at ambient temperature
and at 350°C, and lowest at 180°C. No explanations
have been proposed for this behaviour. Threshold
values for 316 stainless steel, however, were
observed to increase with temperature over the
range 20°—700°C for tests in air, and to remain
constant over the same range of temperature for
tests *in vacuo* and in helium.[31] In the latter case,
the evidence implies that the influence of temper-
ature on near-threshold fatigue behaviour in
stainless steel at least is primarily a function of
environmental factors.

Pressure

For high-strength martensitic steels tested in
low-pressure (10—100 kPa) hydrogen gas, rates of
crack growth under sustained loading have been
found to be sensitive to the pressure of the sur-
rounding gas to a degree dependent upon tempera-
ture (*see* e.g. Refs. 58, 114—117). At temperatures
below about 0°C, steady-state growth rates appear
to vary with the square root of the hydrogen
pressure, between 0° and 40°C growth rates appear
proportional to the first power of pressure, where-
as between 40° and 80°C the dependence is to the
1.5-power of pressure.[115] Limited studies under
cyclic loading, where the environmental contri-
bution to cracking can be considered to be hydro-
gen embrittlement, tend to support these pressure
dependences. However, there are no reported
studies on the effect of pressure, in any environ-

ment, on near-threshold crack-propagation rates,
either for low pressure (10—100 kPa) atmospheres
where hydrogen embrittlement predominates, or
for high-temperature (350°C), high-pressure
(10 MPa) atmospheres where hydrogen attack[118]
predominates. Since the latter environments are
particularly important with regard to pressure-
vessel steels for coal gasification or liquification
processes and pipeline steels for potential hydro-
gen transport, this is an area where there is a
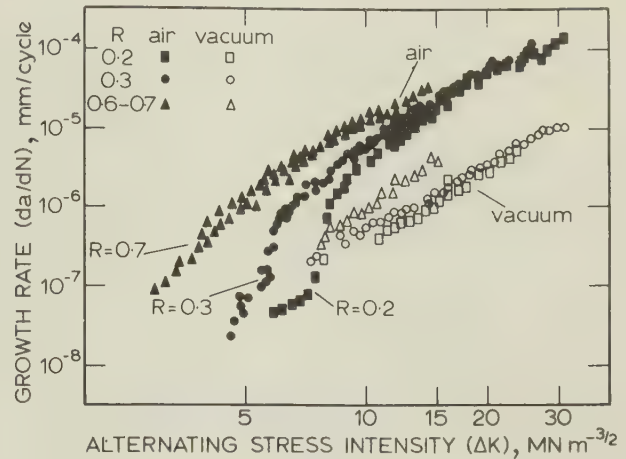great need for future study.

Environmental species

Whereas it is generally accepted that the nature of
the environment plays a prominent role in influ-
encing intermediate growth-rate fatigue-crack
propagation behaviour, opinion is still somewhat
divided with respect to the influence of the
environment at near-threshold rates. On the one
hand, there are the initial results of Paris and
co-workers[6,7,35] on low-strength steels and
titanium alloys which showed no variation in
threshold behaviour with change in environment,
for tests at high frequency (160 Hz). Specifically,
no change in near-threshold growth rates and the
value of ΔK_0 at ambient temperature were ob-
served for: (a) A533—B nuclear pressure-vessel
steel (Fig. 18) tested in air and distilled water[6];
(b) low-strength T—1 steel tested in air, distilled
water, and hydrogen gas[7]; and (c) Ti—6Al—4V
tested in air and dry argon of unspecified purity.[35]
Somewhat similar results have been seen in high-
strength D6ac steel and a 7050—T73651 aluminium
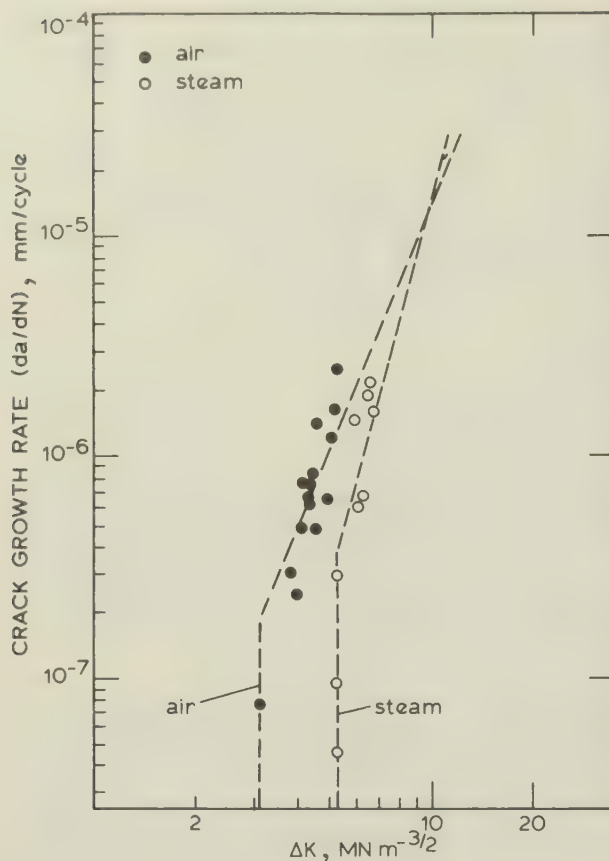alloy,[22] where threshold ΔK_0 values were un-

18 Near-threshold fatigue-crack propagation in ASTM A533B nuclear pressure-vessel steel $(0.2C{-}1.5Mn{-}0.7Ni{-}0.5Mo)$, tested between 60 and 160 Hz at $R = 0.1$, showing a comparison of data for distilled water with 'best-fit' data line for room-temperature air (after Ref. 6)
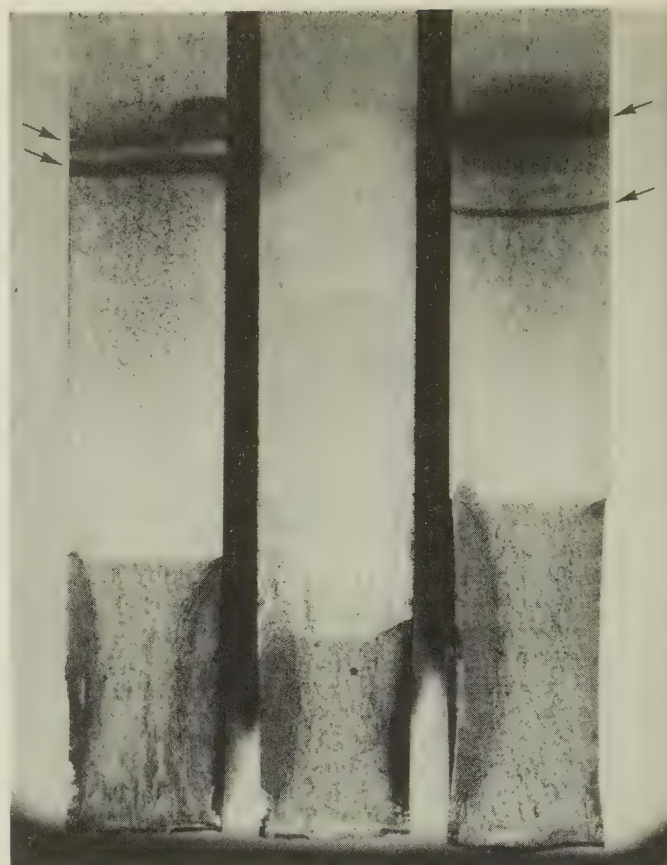

19 Near-threshold fatigue-crack propagation in high-strength martensitic En 24 steel (tempered at 500°C), showing influence of load ratio from $R = 0.17$ to 0.73 in moist laboratory air and in vacuum $(10^{-3}$ Pa) environments (after Ref. 21)

air.[21,31,37-40,80,81] Cooke et al.[21] found an increase in ΔK_0 from 5 to 7 MN m$^{-3/2}$ at $R = 0.1$ and from 3 to 7 MN m$^{-3/2}$ at $R = 0.7$ for En 24 steel, tempered at 500°C, tested *in vacuo* $(10^{-3}$ Pa) compared to air (Figs. 6 and 19). Similar studies on both high-purity and commercial-purity heats of the same steel (UK equivalent of 4340) tempered at 200°C, confirmed the marked reductions in near-threshold growth rates and the increase in ΔK_0 for tests *in vacuo* compared to air[81] (Fig. 6). In both cases, growth rates *in vacuo* were independent of load ratio over the range $R = 0.1{-}0.7$ (Refs. 21, 81). More recent data by Lindley and Richards[80] for 13%Cr martensitic stainless steels (En 56 and FV520B) also reveal appreciable increases in ΔK_0 *in vacuo* $(10^{-3}$ Pa) compared with air at 70 Hz, although for these steels a slight R-ratio dependence on ΔK_0 was still apparent in the inert environment. Similar behaviour has been observed in non-ferrous alloys. In Ti–6Al–4V, for example, several independent studies[37,39,40] have shown increases in ΔK_0, for tests *in vacuo* compared with air, of the order of 3–8 MN m$^{-3/2}$ at $R = 0.35$. Furthermore, Bathias et al.[32] measured an increase in ΔK_0 from 3.5 to 6.1 MN m$^{-3/2}$ at $R = 0.01$ in T651 aluminium alloy by testing in a vacuum of 10^{-3} Pa compared with air. One is led to believe here that the difference between these two opposing sets of results lies principally in the nature of the 'inert' environment, i.e. high vacuum (better than 10^{-3} Pa) $v.$ dry argon. First, how pure must the argon atmosphere be to produce no environmental action at the particular test frequency, and secondly, are rewelding effects occurring for cracking *in vacuo*? Typically impurity contents of argon atmospheres are generally quoted as being in the region of 20–50 ppm water vapour, plus smaller quantities of oxygen, nitrogen, and hydrogen, which correspond to an

changed in air and dry and wet argon atmospheres at 100–374 Hz, although near-threshold growth rates were marginally lower in dry argon compared to air in the steel and significantly lower in the aluminium alloy. On the other hand, there are results where significant decreases in near-threshold growth rates were observed by comparing crack propagation *in vacuo* to laboratory

20   Near-threshold fatigue-crack propagation in Ni—Cr—Mo—V A471 rotor steel ($\sigma_y = 880$ MN m^{-2}) tested at $R = 0.35$, 100 Hz in air and steam at 100°C, showing reduction in growth rates owing to environmental effects (after Ref. 120)
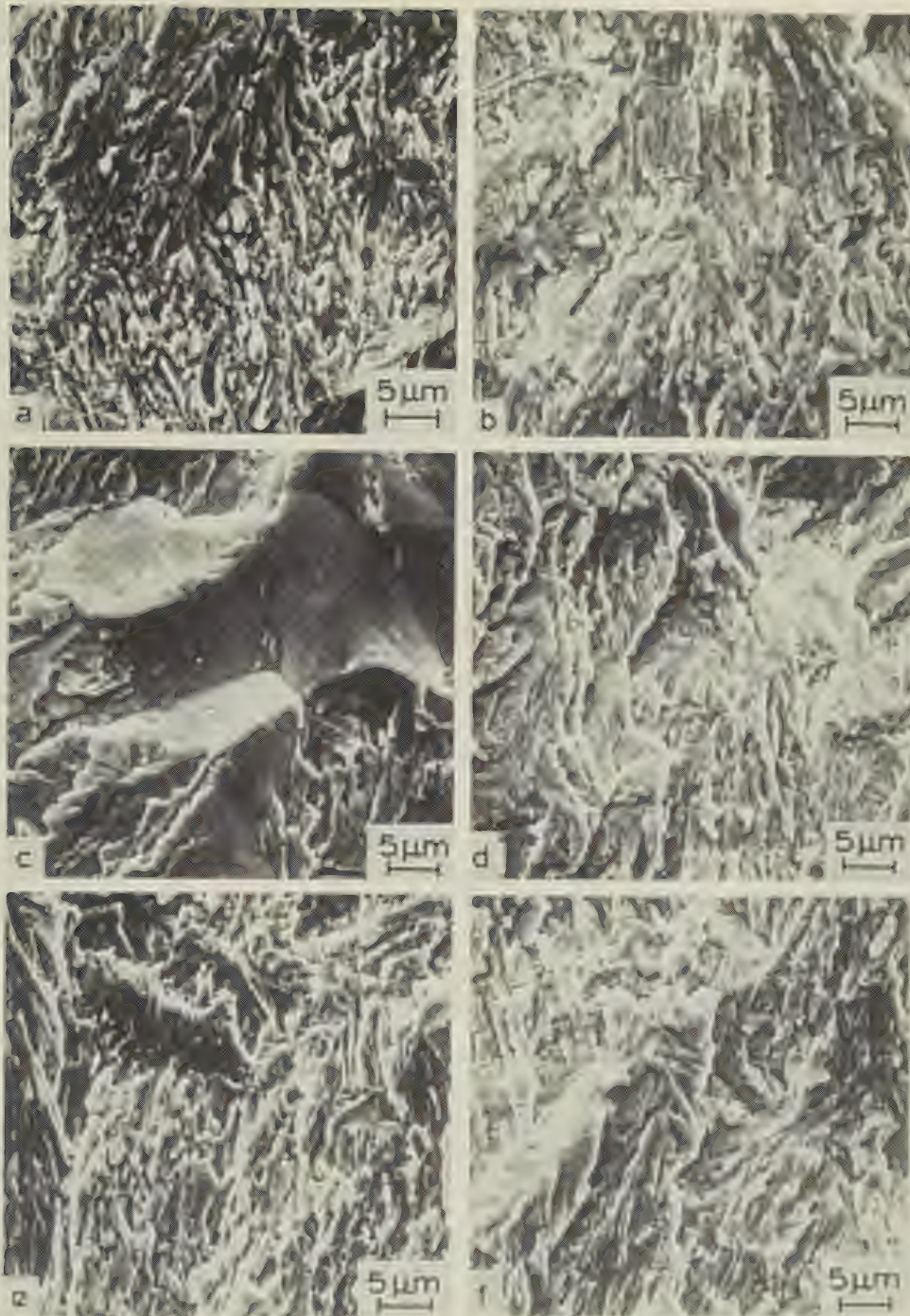

a   b   c

a and *c* near-threshold growth rates; *b* growth rates $>10^{-6}$ mm/cycle

21   Bands of corrosion products on fatigue test-pieces of 9Ni—4Co high-strength steel (HP 9—4—20)

effective partial pressure of water vapour in the region of 2 to 10^{-2} Pa, constituting a poor vacuum.[37] Comparison of fatigue behaviour in Ti—6Al—4V in rigorously purified argon and in a 10^{-5} Pa vacuum revealed that propagation rates were almost identical at high growth rates, but differed by a factor of two in the region 10^{-5}—10^{-4} mm/cycle (Ref. 119). Differences at near-threshold growth rates would be expected to be even more significant. Accordingly, it is felt that the absence of environmental effects in the former set of results[6,7,35] can be rationalized in terms of the fact that comparisons were not made with a truly inert reference environment.[37] Further, the extremely high frequencies utilized in these tests would reduce significantly any environmental influence. Precise resolution of this issue, however, must await near-threshold fatigue-crack propagation data, for a single material, *in vacuo*, purified argon, and more aggressive environments, such as air, H$_2$O, H$_2$, H$_2$S, etc., over a range of frequencies. Additional evidence for an environmental effect on near-threshold behaviour can be found in the work of Pook and co-workers.[17,20] They observed that, for zero-tension loading in

mild steel at ambient temperature, the value of ΔK_0 was reduced from 7.3 MN m$^{-3/2}$ in SAE 30 oil to 6.0 MN m$^{-3/2}$ in air, and significantly reduced to 2.0 MN m$^{-3/2}$ in brine.

There is also an added complication in aggressive or wet corrosive environments that near-threshold growth rates may be *reduced* compared with more inert atmospheres. This may arise from 'oxide-wedging' effects, where the presence of thick corrosion products in the crack may prevent further access for environmental species (akin to passivation), or from certain environments which promote crack branching or meandering. An example of these effects can be seen from the work of Tu and Seth[120] on A470 and A471 Ni—Cr—Mo—V rotor steels where near-threshold growth rates were reduced and the threshold increased when tests were conducted in steam as opposed to air at 100°C (Fig. 20).

Thus, although the extent of data is still somewhat limited, there is good direct evidence in the literature to support the hypothesis that near-threshold fatigue-crack propagation is environmentally sensitive. However, as with any corrosion-

a and *b* transgranular mode close to threshold at $\Delta K = 5.5$ MN m$^{-3/2}$; *c* and *d* transgranular and intergranular modes at $\Delta K = 6.5$ MN m$^{-3/2}$; *e* and *f* total absence of intergranular mode at higher growth rates at $\Delta K = 11$ MN m$^{-3/2}$

22 Fractography of near-threshold fatigue-crack growth in HP 9–4–20 high-strength aerospace steel ($\sigma_y = 1300$ MN m^{-2}), tested in moist laboratory air at $R = 0.1$

related process, there is unlikely to be a single unifying mechanism for the extent of the environmentally-assisted contribution to cracking in all materials, and clearly much research is still needed to characterize these interactions.

FRACTOGRAPHY OF NEAR-THRESHOLD GROWTH

Although the precise mechanisms of fatigue-crack propagation at low stress intensities are unknown, the morphology of near-threshold fracture surfaces

has been well characterized. Macroscopically, a band of corrosion product is generally seen on fracture surfaces at the exact location where growth rates have been less than 10^{-6}–10^{-7} mm/cycle (Refs. 13, 21, 23, 102). An example of this is shown in Fig. 21 for ambient-temperature air tests on a high-strength 9Ni–4Co aerospace steel (HP 9–4–20); no such corrosion product is apparent at higher growth rates.[102] This is clearly indicative of significant environmental action at near-threshold levels, even in air.

Microscopically, near-threshold growth has been termed 'microstructurally-sensitive'[13,21,33,34,36,37,41] owing to the presence of isolated planar transgranular or intergranular facets within a flat, ductile transgranular mode. Examples of such microstructurally-sensitive growth are shown in Fig. 22 for ambient-temperature air tests on HP 9–4–20 steel, and should be compared with growth mechanisms at much higher growth rates (i.e. regimes B and C in Fig. 2) shown in Fig. 3d for the same steel. Note the presence of intergranular facets within a planar transgranular mode at stress intensities just above the threshold (Fig. 22c). Very close to the threshold, the proportion of facets is generally small (~1%), increasing to a maximum of anywhere from 10 to 80% as ΔK is increased, and then gradually diminishing at higher K values in the midgrowth rate regime. The maximum proportion of facets appears to occur when the *cyclic* plastic-zone size approaches the grain size,[13,21,33,34,36,37,41,81,99] whereas the disappearance of facets seems to occur when the *maximum* plastic-zone size exceeds the grain size.[99] Such facets are intergranular in ferritic steels,[10,13,21,23–27,41,63,78,80,81,99,102] and transgranular in austenitic stainless steels[30–32,41,121] and alloys of titanium,[33–37,41,70] aluminium,[41] copper,[41,44] and nickel.[41] A survey of such fractures presented by Beevers[41] identifies the transgranular facets, termed 'cyclic cleavage', with {111} planes in stainless steels,[121] nickel superalloys, and Al 2219–T6, {001} planes in Al–Zn–Mg, and {10$\bar{1}$7} in Ti–6Al–4V (Ref. 70), and so forth. It has been demonstrated, by spiking the loading sequence, that such cyclic-cleavage facets in titanium alloys[70] and 316 stainless steel,[121] form as a result of continued load cycling, and thus are not cleavage cracking in the true sense.

In high-strength martensitic steels, the presence of intergranular facets at near-threshold growth rates appears to be additionally related to the possibility of impurity-induced grain-boundary segregation.[25,27,81,122,123] This can be appreciated by varying the tempering temperature in 4340-type martensitic steels, where microstructures subject to impurity segregation during austenitizing,[122,123] tempered martensite embrittlement,[122,123] or temper embrittlement[25] show significantly more evidence of intergranular separation at near-threshold growth rates. Similar results have been observed by comparing high-purity heats with commercial (impure) heats of

En 24 steel,[81] although, somewhat surprisingly, in many cases the presence or absence of intergranular fracture did not appear to have much direct effect on near-threshold crack velocities.

A more important and clearly interrelated aspect of such near-threshold facets is that they appear to be primarily environmentally-induced. First, facets are not observed at intermediate growth rates[25–27] and are largely suppressed for tests *in vacuo*, dry air, and helium atmospheres.[21,31,37,80,81] Furthermore, intergranular cracking in high-strength steels is commonly associated with hydrogen embrittlement,[68,69] and cleavage on {10$\bar{1}$7} in Ti–Al alloys coincides with the habit plane of the hydrides.[71]

Aside from the presence of the facets, few mechanistic conclusions have been made from fractographic studies of near-threshold fatigue surfaces, principally because the fine-scale details (i.e. striation spacings should they exist) are below the resolution obtained from scanning microscopy or replica work. Fractures appear microscopically very planar and transgranular, and, in general, resemble low-magnification images of fractures at intermediate growth rates. Certain authors[14] have claimed that near-threshold propagation occurs locally by a Mode II mechanism involving regions of intense shear, although such features have not been observed in most fractographic studies on steels. For a more complete survey of near-threshold fracture-surface morphology the reader is referred to Refs. 41 and 81.

DISCUSSION

Environmental effects

It is apparent from the above that, unlike fatigue-crack propagation at intermediate growth rates, near-threshold behaviour is particularly sensitive to microstructural factors such as cyclic strength, grain size, grain-boundary composition, structure, and so forth, in addition to being markedly dependent upon the mean load or R ratio. This microstructural dependence is particularly encouraging for the metallurgist since it implies that there is a potential for the alloy design of materials with improved resistance to very high cycle, low-amplitude fatigue-crack propagation, a procedure which is extremely limited for the microstructurally-insensitive intermediate growth rates short of increasing the elastic modulus. Furthermore, on the basis of somewhat restricted and often conflicting results, it appears that such near-threshold growth is dependent on the nature of the environment. The question which arises is whether such microstructural effects can be traced to this environmental interaction or to some other phenomena such as crack closure.[82] In view of the limited data available and the complexities of varying environmental mechanisms between different materials, a conclusive answer to this ques-

tion is not possible at present. However, by examining behaviour in high-strength steels, where the primary mechanism of environmental attack during fatigue-crack growth in moist air, water, and low-pressure hydrogen environments is hydrogen embrittlement,[72] some consistent, yet necessarily simplistic, explanation can be developed.[27]

In the absence of any environment, there are two physical models[124,125] for the existence of a fatigue-crack propagation threshold which give an expression for ΔK_0 in the form

$$\Delta K_0 = C \sqrt{\pi \rho^*}\ \sigma_F \quad . \quad . \quad . \quad . \quad . \quad (10)$$

In the model of Weiss and Lal,[124] ρ^* is taken as the limiting microstructural dimension over which a certain local critical fracture stress σ_F must be attained ahead of the crack tip for propagation to occur, the constant C being numerically equal to $\sqrt{3/2}$. The model of Sadananda and Shaninian,[125] on the other hand, equates the threshold with the minimum stress σ_F to nucleate a dislocation at the crack tip, where ρ^* is the minimum distance that the dislocation can exist away from the tip (taken as the Burgers vector). In this form, equation (10) does not predict any variation of ΔK_0 with mechanical and microstructural factors (e.g. load ratio, strength, and so forth) under totally inert conditions, consistent with the very limited experimental data available.[21,32,37,81]

However, in the presence of 'hydrogen-producing' environments, cyclic stressing will lead to chemical reactive surface at the crack tip where atomic hydrogen, evolved by cathodic reactions or adsorbed from the gas phase, can enter the lattice and diffuse under the driving force of the stress gradient into the region ahead of the crack tip. In the proposed hydrogen-embrittlement mechanisms for high-strength steels,[38,68,69] hydrogen is considered to diffuse to the point of maximum hydrostatic tension (i.e. maximum dilatation), and lead to a reduction in cohesive strength. The enrichment of hydrogen ahead of the crack tip is a function of the magnitude of the hydrostatic tension $\bar{\sigma}$, and is given thermodynamically by

$$\frac{C_H}{C_0} = \exp\left(\frac{\bar{\sigma}\bar{v}}{R_0 T}\right) \quad . \quad . \quad . \quad . \quad (11)$$

where C_H is the local hydrogen concentration at the point of maximum dilatation, C_0 the equilibrium hydrogen concentration in the unstressed lattice, $\bar{v}$ the partial molar volume of hydrogen in iron, R_0 the gas constant, and T the absolute temperature.[68] Thus, if the reduction in cohesive strength due to hydrogen $\Delta\sigma_H$ is assumed to be proportional to C_H, i.e. $\Delta\sigma_H = \alpha C_H$, then in the presence of a hydrogen-producing environment, the Weiss and Lal expression for the threshold becomes:

$$\Delta K_0 = \sqrt{3\pi\rho^*/2}\ (\sigma_F - \Delta\sigma_H) \quad . \quad . \quad . \quad (12)$$

By combining equations (11) and (12), and incorpor-

ating an expression for the maximum hydrostatic tension, it can be shown[27] that

$$\Delta K_0 = \sqrt{3\pi\rho^*/2}\left(\frac{\sigma_F - \alpha C_0 \exp(B\sigma_y)}{1 + \dfrac{\alpha C_0 \rho^{*1/2}}{(1-R)}\ B' \exp(B\sigma_y)}\right)$$

$$\quad . \quad . \quad . \quad (13)$$

where σ_y is the yield strength, R the load ratio, and B and B' are constants dependent upon temperature. At ambient temperatures in steels $B = 8 \times 10^{-4}\ (MN\ m^{-2})^{-1}$ and $B' = 5 \times 10^{-2}$ $(MN\ m^{-3/2})^{-1}$.

Because of uncertainty in the magnitude of various parameters in the model[68,69] for hydrogen embrittlement (i.e. C_0 and α), it is perhaps premature at this stage to utilize the above relationships in a predictive capacity. However, such equations do provide a useful basis for rationalizing the observed near-threshold fatigue-crack propagation behaviour in high-strength steels. First, the occurrence of intergranular fracture in high-strength steels during near-threshold crack growth in moist air (Fig. 22) or hydrogen-containing gas atmospheres, and the absence of such fracture for tests under inert conditions[21,31,80,81] lends strong support to a hydrogen-embrittlement contribution to crack growth. Secondly, on the basis of equation (12), values of ΔK_0 should be larger in inert environments, consistent with all reported experimental results (e.g. Figs. 6 and 19). Thirdly, the load-ratio and yield-strength effects on near-threshold growth (e.g. Figs. 5—7 and 19, and 4 and 9, respectively) are capable of interpretation since an increase in either parameter will result in a larger hydrostatic stress state $\bar{\sigma}$, which, in turn, raises the local concentration of hydrogen ahead of the crack tip (equation (11)) leading to a reduction in ΔK_0 (equations (12) and (13)). Moreover, since the influence of load ratio arises from such environmental interactions, it follows that in inert atmospheres, near-threshold growth rates and threshold values should be less affected by load ratio, consistent with results[21,80,81] for austenitic and martensitic low-alloy and stainless steels tested in air and vacuum (e.g. Figs. 6 and 19). Thus, the observed effects of load ratio and strength on fatigue-threshold behaviour in high-strength steels can be thought of in terms of an enhanced environmental contribution to crack growth arising from an increase in hydrostatic tension. Additionally, increasing the load ratio will raise K_{max}, which, in turn, leads to a larger plastic stress gradient ahead of the crack tip, thus providing a greater driving force for the transport of hydrogen into the region of maximum triaxiality.

Results,[26,102] showing improved resistance to near-threshold fatigue-crack propagation in tempered martensitic structures containing almost continuous networks of interlath retained austenite (e.g. Fig. 14) are also consistent with this environmental model, since hydrogen diffusivity in the fcc

austenite is three to four orders of magnitude lower than in the bcc phase.[101,126] Furthermore, the lower growth rates observed[27] in coarser grained structures (e.g. Fig. 11) can be rationalized in terms of a lower probability of hydrogen atoms reaching a grain boundary,[99] as discussed above, although more recent data showing a decrease in ΔK_0 with increasing prior austenite grain size (Fig. 12) cast some doubt on this explanation.[29] However, heat treatments used to vary prior austenite grain size in steels (e.g. by increasing austenitizing temperatures) are liable to result in other microstructural changes,[29] such as varying the distribution of grain-boundary embrittling impurity elements.[127] Finally, the effect of such impurity segregation in reducing the threshold (Fig. 17) is readily explained in terms of this analysis, since the presence of residual impurities in grain boundaries will also lead to reduced cohesion.[25] There is also a possibility of synergistic effects between hydrogen and impurity atoms[25] arising from the fact that such impurities may act as recombination poisons for atomic hydrogen.[128]

It is apparent, therefore, that by considering the environmental contribution of hydrogen to crack growth, near-threshold fatigue behaviour in high-strength steels can be usefully rationalized in terms of microstructure and load-ratio effects. As described in Ref. 27, the model can be utilized semiquantitatively by assigning reasonable values to equation (13), such that the experimentally observed trend of decreasing ΔK_0 with increasing strength in steels can be correctly reproduced (Fig. 23). Further verification, however, must await more extensive data showing the influence of mechanical and microstructural factors on near-threshold fatigue-crack propagation in high-strength steels under environmental and, particularly, inert conditions.

It is important to realize that the model described above is only strictly valid for higher strength steels where the environmental contribution to cracking in the presence of hydrogen-producing environments can be modelled in terms of a 'decohesion' mechanism of hydrogen embrittlement.[38,68,69] Lower strength steels, such as mild steel and certain pressure-vessel steels (e.g. A387) where yield strengths are below 500 MN m^{-2}, similarly show marked effects of microstructure and mean stress at near-threshold growth rates in moist air, and yet the possible enrichment of hydrogen ahead of the crack tip, predicted from equation (11), would be very small owing to the lower magnitude of the hydrostatic tension. Thus, any explanation of the characteristics of near-threshold fatigue-crack growth behaviour for such low-strength steels in terms of a decohesion hydrogen-embrittlement model must be regarded as unlikely. However, as discussed above, such steels do show marked environmentally-enhanced fatigue-crack propagation above 10^{-6} mm/cycle in H$_2$, H$_2$S, and water environments,[47-49,73-75] and there are indications that similar hydrogen-assisted crack
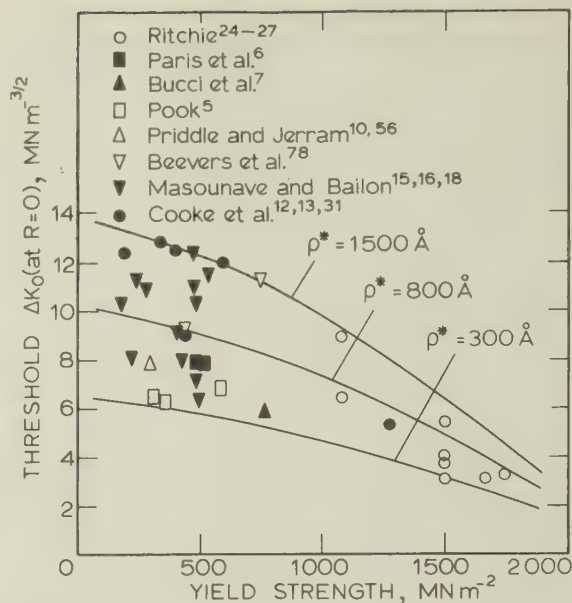
23   Variation of published data on threshold ΔK_0 at $R = 0$ with strength for steels, showing predictions of environmental model (equation (13))

propagation occurs at much slower near-threshold growth rates.[83] Mechanisms for this hydrogen-assisted growth, which certain authors[47,49] have termed hydrogen embrittlement, are presently unknown, yet are unlikely to be similar to classic hydrogen-embrittlement mechanisms (i.e. decohesion) operative in higher strength steels. Thus, until this hydrogen-induced contribution to cracking is understood, particularly close to ΔK_0, rationalization of near-threshold fatigue-crack propagation behaviour in low-strength steels is clearly not possible.

Crack-closure effects

To justify the existence of a fatigue-crack propagation threshold and to explain various characteristics of subsequent near-threshold crack growth, many authors have used arguments based on the phenomenon of crack closure.[6,7,14,19,28,35,42, 79,129,130] However, in the light of existing information, the role of closure on ultralow crack-propagation behaviour is somewhat open to question, as discussed below.

The concept of crack closure, first described by Elber[82] for crack growth at high stress intensities, relies on the fact that, as a result of plastic deformation left in the wake of a growing fatigue crack, it is possible that some closure of the crack surfaces may occur at positive loads during the loading cycle. Since the crack is unable to propagate while it remains closed, the net effect of closure is to reduce the applied ΔK value (computed from applied load and crack-length measurements) to some lower effective value ΔK_{eff} actu-

ally experienced at the crack tip. It follows from this argument that a threshold for crack growth will be reached when the crack remains closed throughout the entire loading cycle. Certain Japanese workers have claimed to verify this by reporting that at the threshold the range of effective stress intensity ΔK_{eff}, based on surface compliance measurements, has no finite value.[129,130] Subsequent more extensive studies on a wider range of steels, however, failed to substantiate this claim.[19] Other authors[6,7,28,35,42] have utilized the closure concept to explain the load-ratio effect on the assumption that as the mean load is raised, the crack will remain open for a larger portion of the cycle, thereby increasing ΔK_{eff} and hence the growth rate. Such arguments have been applied to near-threshold behaviour in steels,[6,7,28] titanium,[35] and aluminium[42] alloys, but with little or no experimental verification. There are, however, several basic problems with this explanation for near-threshold behaviour. First, it is difficult using closure arguments to account for the fact that the influence of load ratio becomes minimal at intermediate growth rates (regime B in Fig. 2) where closure is equally likely to occur. To counter this, it has been suggested[14,131] that the closure effect may be enhanced in the near-threshold region because of the presence of a shear mode of fracture although, as discussed above, the notion that near-threshold failure mechanisms are essentially Mode II in nature does not appear to be universal and, further, it is by no means certain why this in itself should increase closure loads. Secondly, certain workers have observed that the level of closure in inert environments is greater than[132-134] (or at least equal to [135]) the level in air. If the origin of the load-ratio effect were simply crack closure, this would imply that near-threshold growth rates would be more sensitive to load ratio in inert atmospheres, which is contrary to all experimental observations.[21,31,37,39,40,80,81] Thirdly, there is now a large body of evidence[131,136,137] to suggest that crack closure is essentially a surface (plane stress) effect, having a minimal consequence on crack growth under plane-strain conditions. Since near-threshold growth is invariably measured under plane-strain conditions, it seems unlikely that crack closure could be primarily responsible for the marked dependence on load ratio. The issue, however, must remain somewhat unresolved since there is still a certain degree of uncertainty in the experimental measurement of closure; the electrical-potential and compliance techniques used often yield inconsistent results.[138,139]

Undoubtedly, crack closure does occur during fatigue-crack growth, but in the light of recent evidence by Wei *et al.*,[140] which showed no sensible correlation between crack-propagation kinetics and ΔK_{eff}, models based on this concept to explain crack-growth behaviour patterns at near-threshold levels must be regarded as questionable.

CONCLUDING REMARKS

In this paper, an attempt has been made critically to review existing information on the characteristics of near-threshold fatigue-crack propagation in steels with particular emphasis on the possible role of environmental contributions to crack growth. However, despite a rapidly increasing interest in this field over the past five years, there is still virtually no mechanistic basis for near-threshold behaviour and still a comparative lack of reliable engineering data. Further, it is clearly apparent that many fundamental questions remain unanswered, such as the precise role of the environment especially in low-strength steels and the relevance of crack closure. Additionally, the usefulness of threshold data to the problem of short cracks, which are most often found in service, is largely unsolved, particularly in the light of the relationship between threshold data, representing the fracture-mechanics approach to growth (or lack of growth) from long cracks, and the *S—N* and fatigue-limit data, representing principally initiation from short cracks. At first glance, it would seem that both parameters are closely related since they both describe limits for fatigue damage, and yet, as described, by raising the strength of a steel the fatigue limit is generally increased whereas the threshold is decreased. Thus, for alloy-design purposes, procedures designed to optimize high-cycle crack-propagation resistance will not necessarily guarantee similar optimum resistance to crack initiation. Hence, before recommendations can be made for the selection of a suitable material to withstand high-frequency low-amplitude cyclic loading, the relative importance of crack initiation and crack propagation must be clearly established.

The relevance of near-threshold crack-growth data, however, cannot be underestimated. Defects introduced during fabrication or developed in service become potential sources for catastrophic failure from subcritical cracking at seemingly immeasurable growth rates where components are subject to high-frequency low-amplitude cyclic loading. This is especially important where such fluctuations are superimposed on a mean operating stress which results in extremely high load ratios. Examples of the use of threshold data for design and post-failure analysis are now becoming more numerous, particularly in the electrical-supply industry for high-speed rotating equipment and components subject to acoustic fatigue. However, in other applications, such as large-scale nuclear and coal-conversion pressure vessels where small operational transient stresses may result in significant near-threshold crack growth over long periods of time, relevant low growth-rate data for typical environments are still lacking. Although widely recognized in certain countries (*see* e.g. Refs. 2–4, 80, and 141), relatively few studies are in progress in the USA and, despite the achievements of the last five years, there still remains an important need for both

fundamental and applied research on near-
threshold fatigue behaviour.

ACKNOWLEDGMENT

REFERENCES

1.   S. W. Hopkins, C. A. Rau, G. R. Leverant, and
      A. Yuen: 'Fatigue crack growth under spec-
      trum loads', STP 595, 125; 1976, Philadelphia,
      Pa, American Society for Testing and
      Materials.
2.   I. Gray, M. D. Heaton, and G. Oates: Proc. of
      British Steel Corporation Conf. on 'Mechan-
      ics and mechanisms of crack growth',
      Cambridge University, April 1974, 264.
3.   M. D. Heaton: 'The mechanics and physics of
      fracture', 34; 1975, London, The Metals
      Society.
4.   J. R. Griffiths and G. Oates: *Met. Sci.*, 1977,
      11, 285.
5.   L. P. Pook: 'Stress analysis and growth of
      cracks', STP 513, 106; 1972, Philadelphia, Pa,
      American Society for Testing and Materials.
6.   P. C. Paris, R. J. Bucci, E. T. Wessel, W. G
      Clark, and T. R. Mager: *ibid.*, 141.
7.   R. J. Bucci, W. G. Clark, and P. C. Paris:
      ibid., 177.
8.   M. Klesnil and P. Lukáš: *Mater. Sci. Eng.*,
      1972, **9**, 231.
9.   M. Klesnil and P. Lukáš: *Eng. Fract. Mech.*,
      1972, **4**, 77.
10.   E. K. Priddle: 'Constant amplitude fatigue
      crack propagation in a mild steel at low
      stress intensity: the effect of mean stress on
      propagation rate', Technical Report RD/B/
      N2233, May 1972, Berkeley Nuclear Labora-
      tories, Central Electricity Generating Board.
11.   H. Kitagawa, H. Nishitani, and J. Matsumoto:
      'Proc. 3rd int. congr. on fracture', Vol. 5,
      Paper V—444/A; 1973, Düsseldorf, Verein
      Deutscher Eisenhüttenleute.
12.   R. J. Cooke and C. J. Beevers: *Eng. Fract.
      Mech.*, 1973, **5**, 1061.
13.   R. J. Cooke and C. J. Beevers: *Mater. Sci.
      Eng.*, 1974, **13**, 201.
14.   A. Otsuka, K. Mori, and T. Miyata: *Eng. Fract.
      Mech.*, 1975, **7**, 429.
15.   J. Masounave and J.-P. Baïlon: *Scr. Metall.*,
      1975, **9**, 723.
16.   J. Masounave and J.-P. Baïlon: *ibid.*, 1976,
      10, 165.
17.   L. P. Pook and A. F. Greenham: 'Proc.
      fatigue testing and design conf.', Vol. 2,
      30. 1; 1976, London, Society of Environmental
      Engineers.

18.   J. Masounave and J.-P. Baïlon: 'Proc. 2nd
      int. conf. on mechanical behavior of
      materials', 636; 1976, Metals Park, Ohio,
      American Society for Metals.
19.   M. Kikukawa, M. Jono, and K. Tanaka: *ibid.*,
      716.
20.   L. P. Pook: *Met. Sci.*, 1977, **11**, 382.
21.   R. J. Cooke, P. E. Irving, G. S. Booth, and
      C. J. Beevers: *Eng. Fract. Mech.*, 1975, **7**, 69.
22.   J. Mautz and V. Weiss: 'Cracks and frac-
      ture', STP 601, 154; 1976, Philadelphia, Pa,
      American Society for Testing and Materials.
23.   E. K. Priddle: 'Fracture 1977', (ed. D. M. R.
      Taplin), Vol. 2, 1249; 1977, Waterloo, Ont.,
      University of Waterloo Press.
24.   R. O. Ritchie: *ibid.*, 1325.
25.   R. O. Ritchie: *Metall. Trans.*, 1977, **8A**, 1131.
26.   R. O. Ritchie: *J. Eng. Mater. Technol. (Trans.
      ASME, H)*, 1977, **99**, 195.
27.   R. O. Ritchie: *Met. Sci.*, 1977, **11**, 368.
28.   A. Ohta and E. Sasaki: *Eng. Fract. Mech.*,
      1977, **9**, 307.
29.   M. F. Carlson and R. O. Ritchie: *Scr. Metall.*,
      1977, **11**, 1113.
30.   A. C. Pickard, R. O. Ritchie, and J. F. Knott:
      Met. Technol., 1975, **2**, 253.
31.   E. K. Priddle, F. Walker, and C. Wiltshire:
      'Proc. conf. on influence of environment on
      fatigue', 137; 1977, London, Institution of
      Mechanical Engineers.
32.   C. Bathias, A. Pineau, J. Pluvinage, and P.
      Rabbe: 'Fracture 1977', (ed. D. M. R. Taplin),
      Vol. 2, 1283; 1977, Waterloo, Ont., University
      of Waterloo Press.
33.   J. L. Robinson and C. J. Beevers: *Met. Sci. J.*,
      1973, **7**, 153.
34.   J. L. Robinson, P. E. Irving, and C. J. Beevers:
      'Proc. 3rd int. congr. on fracture', Vol. 5,
      Paper V—343; 1973, Düsseldorf, Verein
      Deutscher Eisenhüttenleute.
35.   R. J. Bucci, P. C. Paris, R. W. Hertzberg, R. A.
      Schmidt, and A. F. Anderson: 'Stress analysis
      and growth of cracks', STP 513, 125; 1972,
      Philadelphia, Pa, American Society for Test-
      ing and Materials.
36.   **P. E. Irving and C. J. Beevers: *Mater. Sci. Eng.*,
      1974, 14, 229.**
      P. E. Irving and C. J. Beevers: *Metall. Trans.*,
      1974, **5**, 391.
38.   A. W. Thompson and I. M. Bernstein: 'Advan-
      ces in corrosion science and technology',
      (eds. M. G. Fontana and R. W. Staehle), Vol. 7,
      53; 1979, New York, Plenum Press.
39.   R. Ebara, K. Inoue, S. Crosby, J. Groeger, and
      A. J. McEvily: 'Proc. 2nd int. conf. on
      mechanical behavior of materials', 685;
      1976, Metals Park, Ohio, American Society
      for Metals.
40.   A. J. McEvily and J. Groeger: 'Fracture 1977',
      (ed. D. M. R. Taplin), Vol. 2, 1293; 1977,
      Waterloo, Ont., University of Waterloo
      Press.
41.   C. J. Beevers: *Met. Sci.*, 1977, **11**, 362.
42.   R. A. Schmidt and P. C. Paris: 'Progress in
      flaw growth and fracture toughness testing',

STP 536, 79; 1973, Philadelphia, Pa, American
Society for Testing and Materials.

43. J. F. Knott and A. C. Pickard: *Met. Sci.*, 1977, **11**, 399.

44. A. C. Pickard, R. O. Ritchie, and J. F. Knott: 'Proc. 4th int. conf. on strength of metals and alloys', Aug. 1976, 473; Nancy, France, INPL.

45. H. Kitagawa and S. Takahashi: 'Proc 2nd int. conf. on mechanical behavior of materials', 627; 1976, Metals Park, Ohio, American Society for Metals.

46. F. P. Ford and T. P. Hoar: 'The microstructure and design of alloys', Vol. 1, 467; 1974, London, The Metals Society.

47. O. Vosikovsky: *J. Eng. Mater. Technol. (Trans. ASME, H)*, 1975, **97**, 298.

48. T. R. Mager, D. M. Moon, and J. D. Landes: *J. Pressure Vessel Technol. (Trans. ASME, J)*, 1977, **99**, 238.

49. W. H. Bamford and D. M. Moon: 'Corrosion 79', Proc. NACE Meeting, March 1979; Houston, Texas, NACE.

50. Proc. of Workshop on Materials Problems and Research Opportunities in Coal Conversion, April 1974, Vols. I and II; Washington, DC, ERDA.

51. R. O. Ritchie, G. G. Garrett, and J. F. Knott: *Int. J. Fract. Mech.*, 1971, **7**, 462.

52. R. O. Ritchie and K. J. Bathe: *Int. J. Fract.*, 1979, **15**, 47.

53. G. H. Aronson and R. O. Ritchie: *J. Test. Eval.*, 1979, **7**, 208.

54. P. S. Pao, W. Wei, and R. P. Wei: 'Environment sensitive fracture of engineering materials', (ed. Z. A. Foroulis), 565; 1979, New York, AIME.

55. S. J. Hudak, A. Saxena, R. J. Bucci, and R. C. Malcolm: Third Semi-Annual Report to AFML, Westinghouse Research and Development Laboratories, Pittsburgh, March 1977.

56. K. Jerram and E. K. Priddle: *J. Mech. Eng. Sci.*, 1973, **15**, 271.

57. A. Saxena, S. J. Hudak, J. K. Donald, and D. W. Schmidt: Scientific Paper 77—IE7—FANWL—P1, Westinghouse Research and Development Laboratories, Pittsburgh, May 1977.

58. H. H. Johnson and P. C. Paris: *Eng. Fract. Mech.*, 1968, **1**, (1), 3.

59. P. C. Paris and F. Erdogan: *J. Basic Eng. (Trans. ASME. D)*, 1963, **85**, 528.

60. C. Laird and G. C. Smith: *Philos. Mag.*, 1962, **7**, 847.

61. R. M. N. Pelloux: *Eng. Fract. Mech.*, 1970, **1**, (4), 697.

62. C. E. Richards and T. C. Lindley: *ibid.*, 1972, **4**, 951.

63. R. O. Ritchie and J. F. Knott: *Acta. Metall.*, 1973, **21**, 639.

64. R. O. Ritchie and J. F. Knott: *Mater. Sci. Eng.*, 1974, **14**, 7.

65. T. C. Lindley, C. E. Richards, and R. O. Ritchie: *Metall. Met. Form.*, 1976, **43**, 268.

66. F. A. McClintock: 'Fatigue crack propaga-

tion', STP 415, 170; 1967, Philadelphia, Pa, American Society for Testing and Materials.

67. J. K. Tien: 'Effect of hydrogen on behavior of materials', (eds. A. W. Thompson and I. M. Bernstein), 301; 1976, New York, AIME.

68. R. A. Oriani and P. H. Josephic: *Acta Metall.*, 1974, **22**, 1065.

69. W. W. Gerberich and Y. T. Chen: *Metall. Trans.*, 1975, **6A**, 271.

70. N. E. Paton, J. C. Williams, J. C. Chesnutt, and A. W. Thompson: Proc. AGARD Conf. on 'Alloy design for fatigue and fracture resistance', No. 185, April 1975, 4—1; Neuilly sur Seine, France, NATO.

71. N. E. Paton and R. A. Spurling: *Metall. Trans.*, 1976, **7A**, 1769.

72. R. P. Wei and J. D. Landes: *Mater. Res. Standards*, 1969, **9**, 25.

73. H. G. Nelson: 'Proc. 2nd int. conf. on mechanical behavior of materials', 690; 1976, Metals Park, Ohio, American Society for Metals.

74. H. G. Nelson: 'Effects of hydrogen on behavior of materials', (eds. A. W. Thompson and I. M. Bernstein), 602; 1976, New York, AIME.

75. R. P. Wei and G. W. Simmons: 'Fracture mechanics and surface chemistry studies of steels for coal gasification systems', Lehigh University Report No. IFSM—77—87, Dec. 1977.

76. O. Vosikovsky: *J. Test. Eval.*, 1978, **6**, 175.

77. W. J. Plumbridge: *J. Mater. Sci.*, 1972, **7**, 939.

78. C. J. Beevers, R. J. Cooke, J. F. Knott, and R. O. Ritchie: *Met. Sci.*, 1975, **9**, 119.

79. A. Ohta and E. Sasaki: *Eng. Fract. Mech.*, 1977, **9**, 655.

80. T. C. Lindley and C. E. Richards: 'Fatigue crack growth at low stresses in steels', Central Electricity Generating Board Laboratory Note No. RD/L/N 135/78, Aug. 1978, Central Electricity Research Laboratories, Leatherhead, Surrey.

81. P. E. Irving and A. Kurzfeld: *Met. Sci.*, 1978, **12**, 495.

82. W. Elber: 'Damage tolerance in aircraft structures', STP 486, 230; 1971, Philadelphia, Pa, American Society for Testing and Materials.

83. S. Suresh, C. M. Moss, and R. O. Ritchie: 'Proc. 2nd Japan Institute of Metals int. symp. on hydrogen in metals', Sendai, Japan, Nov. 1979, Paper 27B23.

84. R. O. Ritchie, R. F. Smith, and J. F. Knott: *Met. Sci.*, 1975, **9**, 485.

85. M. H. El Haddad, T. H. Topper, and K. N. Smith: *J. Eng. Mater. Technol. (Trans. ASME, H)*, 1979, **101**, 42.

86. M. H. El Haddad, T. H. Topper, and K. N. Smith: *Eng. Fract. Mech.*, 1979, **11**, 573.

87. N. E. Dowling: 'Cyclic stress—strain and plastic deformation aspects of fatigue crack growth', STP 637, 97; 1977, Philadelphia, Pa, American Society for Testing and Materials.

88. M. E. Fine and R. O. Ritchie: 'Fatigue and microstructure', (ed. M. Meshii), 245; 1979,

Metals Park, Ohio, American Society for Metals.

89. J. Barsom, E. J. Imhof, and S. T. Rolfe: *Eng. Fract. Mech.*, 1970, **2**, 301.

90. J. P. Benson and D. V. Edmonds: *Met. Sci.*, 1978, **12**, 223.

91. O. Vosikovsky: *Eng. Fract. Mech.*, 1979, **11**, 595.

92. A. J. McEvily: 'Recent research on mechanical behavior of solids'; 1979, Tokyo, University of Tokyo Press.

93. P. Kuhn and H. Hardrath: NACE Technical Report No. NACE TN 2805, 1952.

94. R. O. Ritchie: 'Proc. int. conf. on fundamentals of tribology'; 1979, Cambridge, Mass., MIT Press.

95. R. M. Pelloux: 'Ultrafine-grain metals', 231; 1970, Syracuse, NY, Syracuse University Press.

96. A. W. Thompson and R. J. Bucci: *Metall. Trans.*, 1973, **4**, 1173.

97. A. W. Thompson: *Eng. Fract. Mech.*, 1975, **7**, 61.

98. G. R. Yoder, L. A. Cooley, and T. W. Crooker: *J. Eng. Mater. Technol. (Trans. ASME, H)*, 1979, **101**, 86.

99. J. D. Frandsen and H. L. Marcus: *Scr. Metall.*, 1975, **9**, 1089.

100. J. F. Lesser and W. W. Gerberich: *Metall. Trans.*, 1976, **7A**, 953.

101. R. O. Ritchie, M. H. Castro Cedēno, V. F. Zackay, and E. R. Parker: *ibid.*, 1978, **9A**, 35.

102. R. O. Ritchie, V. A. Chang, and N. E. Paton: *J. Fatigue Eng. Mater. Structures*, 1979, 1.

103. A. S. Tetelman: 'Fundamental aspects of stress corrosion cracking', (ed. R. W. Staehle), 446; 1969, Houston, Texas, NACE.

104. E. E. Fletcher, W. E. Berry, and G. A. Elsen: *ibid.*, 457.

105. W. W. Gerberich: 'Hydrogen in metals', (eds. I. M. Bernstein and A. W. Thompson), 115; 1974, Metals Park, Ohio, American Society for Metals.

106. C. B. Gilpin and N. A. Tiner: *Corrosion*, 1966, **22**, 271.

107. C. S. Carter: *ibid.*, 1969, **25**, 423.

108. R. O. Ritchie: 'Environment sensitive fracture of engineering materials', (ed. Z. A. Foroulis), 538; 1979, New York, AIME.

109. H. Suzuki and A. J. McEvily: *Metall. Trans.*, 1979, **10A**, 475.

110. G. J. Fowler: *Mater. Sci. Eng.*, 1979, **39**, 121.

111. A. D. Wilson: *J. Pressure Vessel Technol. (Trans. ASME, J)*, 1977, **99**, 459.

112. P. Shaninian, H. H. Smith, and J. R. Hawthorne: *Weld. J. Res. Suppl.*, 1972, **51**, 527.

113. L. A. James: *At. Energy Rev.*, 1976, **14**, 37.

114. N. G. Nelson and D. P. Williams: *Metall. Trans.*, 1970, **1**, 63.

115. G. W. Simmons, P. S. Pao, and R. P. Wei: *ibid.*, 1978, **9A**, 1147.

116. S. J. Hudak and R. P. Wei: *ibid.*, 1976, **7A**, 235.

117. R. P. Gangloff and R. P. Wei: *ibid.*, 1977, **8A**, 1043.

118. P. G. Shewmon: *ibid.*, 1976, **7A**, 279.

119. R. P. Wei and D. L. Ritter: *J. Mater.*, 1972, **7**, 240.

120. L. K. L. Tu and B. B. Seth: *J. Test. Eval.*, 1978, **6**, 66.

121. E. K. Priddle and F. E. Walker: *J. Mater. Sci.*, 1976, **11**, 386.

122. R. O. Ritchie: *Eng. Fract. Mech.*, 1975, **7**, 187.

123. R. O. Ritchie: PhD thesis, University of Cambridge, 1973.

124. V. Weiss and D. N. Lal: *Metall. Trans.*, 1974, **5**, 1946.

125. K. Sadananda and P. Shaninian: *Int. J. Fract.*, 1977, **13**, 585.

126. J. H. Shively, R. F. Hehemann, and A. R. Troiano: *Corrosion*, 1966, **22**, 253.

127. G. Clark, R. O. Ritchie, and J. F. Knott: *Nature Phys. Sci.*, 1972, **239**, 104.

128. R. M. Latanision and H. Opperhauser: *Metall. Trans.*, 1974, **5**, 483.

129. H. Nisitani and K. Takeo: *Eng. Fract. Mech.*, 1974, **6**, 253.

130. A. Ohta and E. Sasaki: *Int. J. Fract.*, 1975, **11**, 1049.

131. A. J. McEvily: *Met. Sci.*, 1977, **11**, 274.

132. O. Buck, J. D. Frandsen, and H. L. Marcus: *Eng. Fract. Mech.*, 1975, **7**, 167.

133. P. E. Irving, J. L. Robinson, and C. J. Beevers: *ibid.*, 619.

134. P. E. Irving, J. L. Robinson, and C. J. Beevers: *Int. J. Fract.*, 1973, **9**, 105.

135. V. Bachmann and D. Munz: *ibid.*, 1975, **11**, 713.

136. T. C. Lindley and C. E. Richards: *Mater. Sci. Eng.*, 1974, **14**, 281.

137. F. J. Pitoniak, A. F. Grandt, L. T. Montulli, and P. F. Packman: *Eng. Fract. Mech.*, 1974, **6**, 663.

138. C. K. Clarke and G. C. Cassatt: *ibid.*, 1977, **9**, 675.

139. V. Bachmann and D. Munz: *ibid.*, 1979, **11**, 61.

140. K. D. Unangst, T. T. Shih, and R. P. Wei: *ibid.*, 1977, **9**, 725.

141. 'Crack arrest threshold ΔK_{th}'; French Round Robin Program on Threshold Testing, Groupe de la Commission de Fatigue, May 1978. (Translated by ASTM for E. 24.04 Subcommittee on Subcritical Crack Growth.)

Practical aspects of electroslag remelting technology

by A. Mitchell and R. M. Smailer

Several features of the electroslag remelting (ESR) process are reviewed from a practical viewpoint. These include: a consideration of the maximum practical size of ESR equipment; electroslag casting technology; ESR mould design; and slag-melting practices.

WHAT IS THE OPTIMUM SIZE FOR AN ESR FURNACE ?

'Bigger is better' is an axiom which has controlled metallurgical process development in innumerable cases. In liquid-ferrous processing, the convincing scale-up arguments based on throughput for specific furnace volume have given rise to the ever-increasing size of almost every process unit from blast furnaces to degassing vessels. The electroslag remelting (ESR) furnace, however, is a distinctly different case from the conventional liquid-metal processing unit since it involves not only the melting of steel and its treatment but also solidification. The former requires the efficient generation and use of heat energy, the latter its efficient, rapid dissipation. It is inevitable, therefore, that the conventional ESR furnace will reach some optimum dimension determined by the compromise between heat extraction through the ingot's ruling section and heat input into the electrode/slag interface. This compromise position will be reached at different ingot sections for different materials, varying as the constraints on permissible solidification structure are varied. It is the purpose in the following discussion to review the factors known to control this compromise, and also to place ESR in relation to competing processes in the light of this concept.

The solidification compromise

Good-quality ESR ingots with no significant structural defects have been made[1] in low-alloy steels in diameters up to 2300 mm. However, in most alloys it is now clear that some maximum practical size of ESR ingot must exist. There is nothing in the ESR process which would cause deviations

Professor Mitchell is in the Department of Metallurgical Engineering, University of British Columbia, Vancouver, BC, Canada, and Mr Smailer is with the Research Division, Lukens Steel Co., Coatesville, Pa, USA.

from the well established laws governing solidification and structure. Consequently, we may make estimates of both the maximum and optimum ESR ingot size using the relationships which connect local solidification rate and structure.

The computation methods used to establish the ingot thermal regime in ESR are reasonably well established.[2] The initial application of such computations was to predict the liquidus surface or 'pool profile' in commercial practices. Most of these practices had been developed following the concept that a particularly good (or bad) ingot structure was associated with a particular pool profile. It soon became apparent, however,[3] that the pool profile is a poor measure of structure except in the extreme cases of ingots developing gross macrosegregation defects.[4] The microstructure was shown to be controlled, as one might expect, by the local solidification time (LST),[5-7] which is not a simple function of the pool profile. Mellberg[8] and Ballantyne et al.[5] all point out that because the heat balance of the solidifying region contains a substantial imposed heat flow additional to the sensible and latent-heat releases, the solidification rate and temperature gradients are not linked as they are in a conventional casting. For this reason the LST is a complex function of melting rate and the pool profile is not a good guide to the resulting structure. For any given alloy, the LST may be calculated as the metal's residence time between liquidus and solidus, and derived as a function of melting rate as shown by Ballantyne et al.[5] The result of such a computation is shown in Fig. 1, and demonstrates the following features.

First, the function of LST against melting rate clearly has a minimum, indicating that the structure will be at its finest dendrite spacing at this minimum position. From the point of view of microsegregation, this minimum position represents the optimum structure obtainable in the alloy grade and ingot diameter chosen. Second, the absolute values of LST and their radial and axial variation are defined and can be related to the expected alloy structure in respect of both micro- and macrosegration. By combining this latter relation with the previously defined optimum position we thus have a mechanism for predicting what maximum size—melting rate relationship we may anticipate in the alloy. This computation is illustrated in Fig. 2, where the authors have arbitrarily chosen a critical LST of 800 s as being adequate for the alloy structure required and have thence computed the maximum permissible melt-
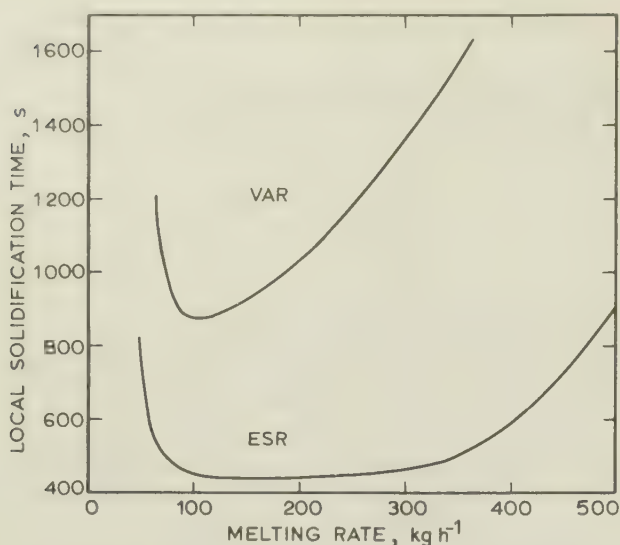
1   Local solidification time at centreline as function of melt rate for 300 mm dia. ingots of alloy U-700

ing rate for that LST as a function of ingot diameter. We see that the specific metal throughput per unit volume of furnace passes through a maximum, indicating an optimum ingot diameter from the point of view of power efficiency. Also, if one arbitrarily imposes a lower limit of possible operating melting rate on the process (for practical reasons of stability, etc.), one may observe a maximum permissible ingot diameter of ESR ingots in the alloy. By this means the intuitive assessments made by remelters for many years may be quantified, at least in respect of the normal ingot structure, if not with regard to solidification instabilities such as freckles.

The LST criterion has two clear limitations in its application to all remelting techniques. The first is that it presupposes a clear definition of
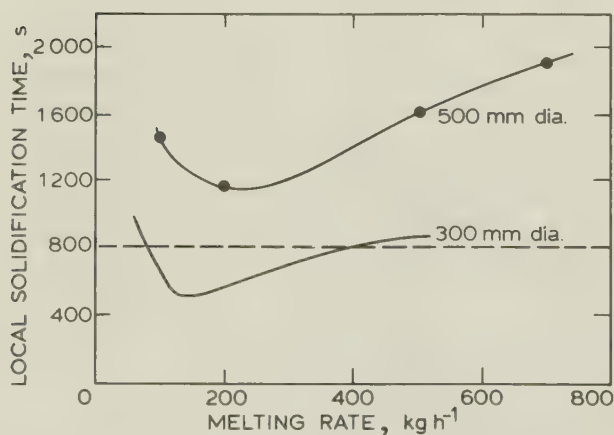
2   Centreline LST as function of melting rate for ESR ingots of alloy IN 718: dotted line represents good commercial structure

'acceptable structure'; the second is that it can be applied only to structural variations caused directly by the LST. The ingot quality which is acceptable by industrial standards varies considerably between both alloy qualities and applications. The same standards are not applied to 1500 mm dia. ingots of low-alloy steels as are applied to 300 mm dia. ingots of aircraft-quality superalloys, and for this reason generalizations on the LST values required are misleading. Once the LST value is established for a particular application, however, it may be used with good assurance to extrapolate structures between ingot sizes and melting rates. The structural transition from columnar to equiaxed grains is not related solely to LST in a remelting process.[5,9] It is clear that equiaxed grains cannot be nucleated in this case by supercooling, but are more probably related to the persistence of dendrite fragments swept into the liquid phase by stirring. For any given alloy, this 'fragment residence time' will be related both to LST and to the movement of the liquid phase. Since the latter parameter is probably a reproducible function of melting rate in any given practice, one might use LST as a guide to structure even in such a case, but there is no clearly predictable relationship with theoretical results. The same limitation can be applied to the relationship between LST and macrosegregation, as discussed by Kou *et al.*[4]

The portion of the computation which gives values for the LST based on geometry and heat flow is a reasonably accurate and straightforward procedure. Like most process models, it contains numerous adjustable parameters and approximations, but these have been refined using full-scale experiments to the point at which good agreement may be expected between theory and practice. The principal difficulty in using the concepts outlined above appears to be in the interpretation of the computed LST values. For example, Ballantyne *et al.*[5] calculate that in the case of Udimet 700 in 325 mm dia. ingots, the vacuum arc remelting (VAR) LST is double that of ESR at any given melt rate. Following the conventional solidification theories which relate structure parameters such as primary and secondary dendrite spacings, microsegregation, etc. to LST,[9] it can be seen that the improvement in structure owing to a halving of LST is not very significant in cases where the LST is already producing a columnar structure with secondary dendrite spacings in the region of 0.1 mm. Such structures are already adequate for the industrial requirements of the alloy. However, in a range of LST values where the corresponding structure borders between columnar and coarse equiaxed, small changes in LST result in large differences of ingot structure. In these instances, the LST differences between ESR and VAR are very significant indeed. Consequently, one may conclude that in the higher range of permissible melting rates (i.e. higher range of LST values) ESR will offer an advantage over VAR either in giving higher melting rates
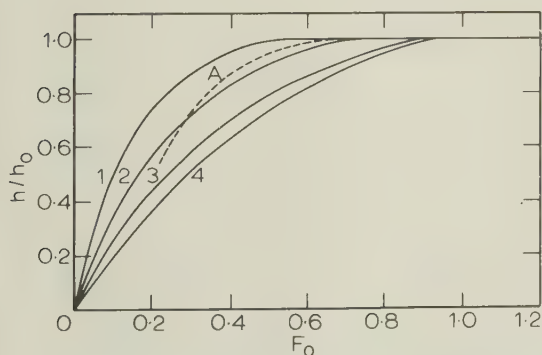
for the same structure or in permitting the manu-
facture of larger diameter ingots of acceptable
structure.

The extent to which the above discussion will
influence the choice of melting rate and ingot size
obviously depends on the range of LST values
appropriate to the alloy concerned. Numerous
workers have examined ESR (and VAR) ingots
with a view to relating observed structure and
melting rate. Their results and observations are
summarized by Ballantyne et al.,[5] who conclude
that accuracy of empirical structure prediction
is very low and, of course, is also very costly in
time and material. It is possible, however, to
derive a value of a maximum permissible LST on
the basis of observation. Using this technique, the
desired acceptable structure may be used as a
criterion for computation by relating it to the
equivalent LST value. This technique has been
used[10] to characterize carbide structures in
ingots of ESR M2 high-speed steel, leading to a
melt-rate criterion for the alloy wherein the LST
is not permitted to exceed 2000 s. The same
technique is also used for Inconel 718, where the
LST is held to a maximum of 1200 s for an accept-
able proportion and composition of Lave's phase
in the ingot structure.[11]

From the above discussion, one may deduce
that the optimum size for an ESR ingot may be
estimated by extrapolation from known ESR ingot
structures on the basis of computed LST values.
The estimation of ESR structures from first
principles, however, is as yet very uncertain.
Consequently, the compromise in ingot structural
quality between ingot diameter and melting rate
is still a matter for qualitative discussion.

Melting rate

The literature contains numerous reports[6,7,12-15]
of studies linking ingot structure with melt rate.

4a Melting cycle for 400 mm dia. ESR ingot of
M2 steel
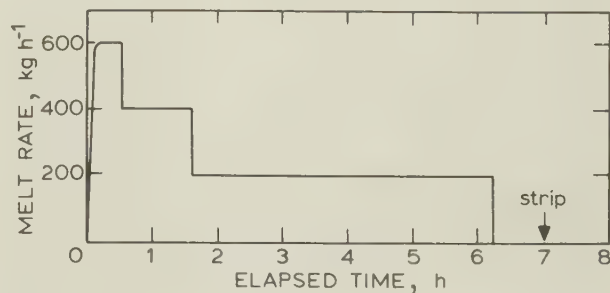
4b Data of Fig. 4a replotted on an elapsed-time
basis
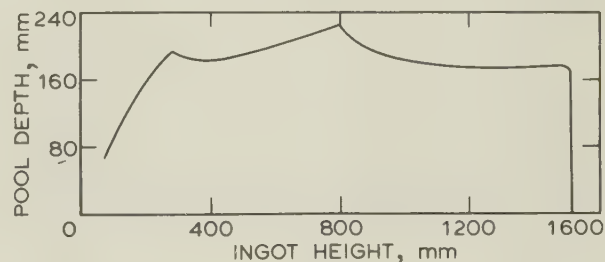
4c Pool depth cycle corresponding to Figs. 4a
and 4b

Only in three of these,[13-15] however, is there any
discussion of the definition of melt rate and its
true value. It is clear that, from a practical
standpoint, the industry has used any of four
definitions of melt rate to characterize its process
and product, namely:

(i) instantaneous melt rate

(ii) average melt rate, excluding hot-topping time

(iii) overall average melt rate from power-on to
power-off

(iv) production rate, i.e. installation output per
unit time.

Each of these definitions has advantages and draw-
backs in describing the process, but from the
viewpoint of optimizing furnace size only the last
of the above has any industrial significance. On
the other hand, in optimizing ingot quality, only the
first is of value. It must be decided, then, how to

3 Dimensionless pool depth h_0/h as function of
Fourier number Fo for series of calculated and
experimental Peclet numbers Pe: $h_0 =$ pool
depth at t, $h =$ ingot length at t, $Fo = \alpha t/r^2$,
$Pe = Vr/\alpha$, $V =$ melt rate, $r =$ ingot radius,
$\alpha =$ thermal conductivity

relate instantaneous melt rate to overall production rate in furnace optimization.

First, let us consider the procedure and decisions involved in obtaining the maximum instantaneous melt rate. It has been indicated above that the melt rate for any alloy in any ingot dimension may be characterized by a single parameter, the LST. The appropriate maximum instantaneous melt rate will therefore be that which gives the maximum permissible LST at the ingot centreline, at all ingot lengths. The thermal regime of a remelting process is such that there is a progressive decrease in specific heat flow out of the ingot as the process high-temperature region moves away from the water-cooled base. A number of workers have commented on this effect and its significance.[2,15-17] The progressive approach to a steady-state thermal regime is described by Paton *et al.*[17] and Ballantyne and Mitchell[15] in terms of dimensionless parameters as shown in Fig. 3. From the figure it may be seen that at a constant melt rate the dimensionless pool depth increases for an ingot length approximately equal to three times the diameter, then attains a steady state. The LST is found to follow a similar regime, and hence if one is to produce the maximum permissible LST at all ingot lengths one must programme the melt rate from very high initial values to some suitable value in the steady-state region.

Programmed melt-rate schemes have been proposed and used for ESR, based on both pool depth and LST. Ballantyne and Mitchell[15] outline such programmes for two ingots, of 400 mm dia. M2-speed steel (Figs. 4a-4c) and 1000 mm dia. AISI 4340 steel (Fig. 5). The programme shown in Fig. 6 represents a sequence in which the
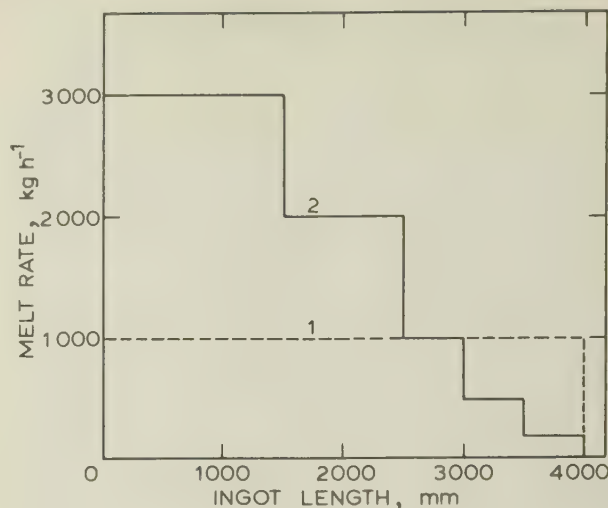
6a   Melt-rate programmes to be followed in Figs. 6b and 6c
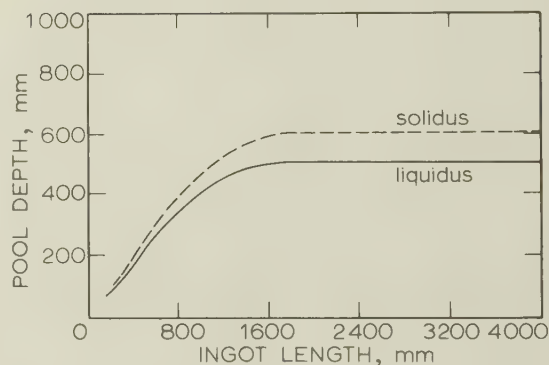
6b   Pool depth as function of ingot length for melt programme no. 1
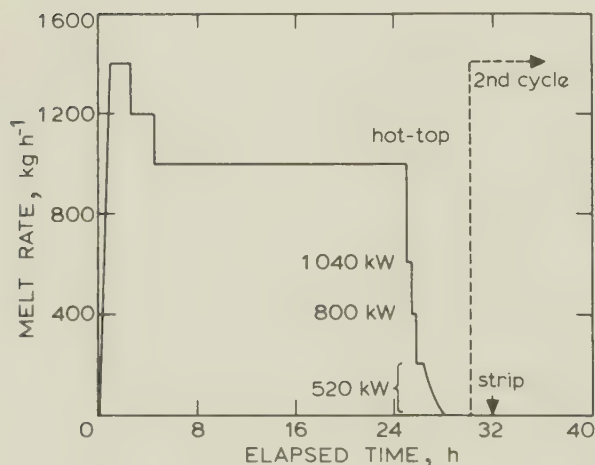
5   Melt cycle for 1000 mm dia. ESR ingot of SAE 4340, maintaining pool depth of less than 400 mm
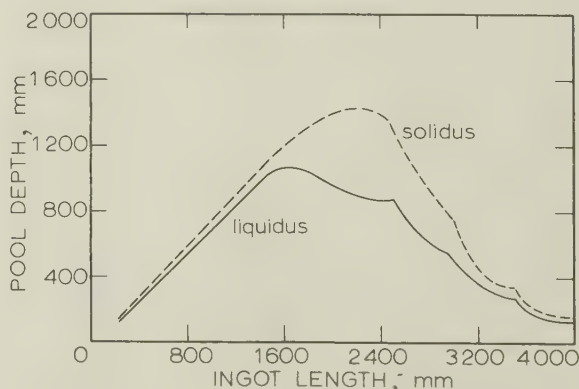
6c   Pool depth as function of ingot length for melt programme no. 2: note small final pool volume which facilitates hot-topping

centreline LST does not exceed 2500 s; that of Fig. 4 one in which the centreline LST does not exceed 1500 s, a value shown[10] to be the maximum for correct carbide structures in M2.

The value of specifying the LST carefully has been discussed.[18] Here, the penalty incurred in overall production rate is calculated for a 10% underestimate of the permissible LST in a 1000 mm dia. ingot of AISI 4340, as shown in Fig. 7. The penalty incurred in overall production rate in this case is approximately 14%. It is very evident, therefore, that a careful assessment of LST is necessary, recalling the discussion (section above on 'Solidification compromise') of the requirements in defining acceptable structure. However, once having arrived at a defined LST the melt rate may be adjusted progressively to follow the changing heat-flow conditions rather than using the constant rates adopted by earlier workers.[6,7,10,12]

There are several important advantages of melt programming at the maximum permissible rate, in addition to the direct improvement in productivity. The relationship between instantaneous melt rate and overall average melt rate includes the time taken to hot-top the ingot, which in turn is closely related to the volume of liquid metal present at the time the hot-topping process starts. Melting sequences for hot-topping have not specifically been discussed in the literature, but none the less some general conclusions may be drawn. The optimization of the hot-topping cycle evidently becomes more important as the ingot diameter increases, and as the ingot diameter/length ratio increases. Indeed, in an example ingot of, say, 1000 mm dia. and having a length of 3000 mm, the process never attains a steady state and consists entirely of starting and hot-topping. In determining ingot shape, then, at a given weight,

careful attention must be paid to the metal quality resulting from the hot-topping practice. The influence of the shape on ingot yield has been discussed in detail by Wahlster,[19] who concludes that in large ingots (>20 t), savings in yield of 5–10% may be made by a judicious choice of length/diameter ratio. It is also noteworthy that Wahlster's upper limits for yield are between 90 and 95% in this size range as compared with 70–85% for conventional ingots. Most of this yield increase is due to the quality of the hot-top, and as a direct corollary good hot-topping is a prequisite for economic operation of a large ESR furnace. In considering how to adapt the optimum instantaneous melt-rate programme to give the maximum overall production rate, therefore, the requirements of the hot-topping cycle must be included.

The physical process involved in hot-topping is one in which the heat supplied to the ingot top surface must be equal to that heat required to maintain a liquid slag/metal interface. The metal flow from the electrode compensating for solidification shrinkage is thus able to feed the solidifying volume. Any heat and/or metal flow in excess of the above requirement will only serve to slow down the hot-topping process and increase the total time required. We are therefore presented with two simple conditions which must be met for adequate hot-topping: (a) the metal liquid volume at the start of the cycle must be minimized, and (b) the ESR furnace must operate with stability at low melting rates.

The programming process can be arranged so as to minimize the pool volume at the head of the ingot. This is illustrated by means of Figs. 6a–6c, which show how the pool depth evolves in two cases, those of constant (Fig. 6b) and programmed (Fig. 6c) melt rates. Clearly, the use of a varying melt rate leads in this case to an increase in metal quality by reducing the LST in the ingot head as well as giving a much smaller volume of liquid metal for hot-topping. The difference in pool volume in the two cases leads to a decrease in hot-topping time by a factor of three in the programmed case over the constant-rate case. This advantage becomes of greater importance in large ingots.

Once having minimized the pool volume, the process must be terminated following the conditions outlined above. Very little work is reported on the precise methods of accomplishing the melt-rate reductions required, but it is clear[19] that the process may be run with stability at low rates only if there are significant changes made to either the electrode diameter or the slag composition.

With the inclusion of hot-topping time and programmed melt rate, the average melt rate from power-on to power-off is significantly different from a simple average melt rate. This factor has been discussed[15] as it relates to productivity, with the conclusion that some compromise on hot-top quality may be necessary to attain high production rates. For this reason, the
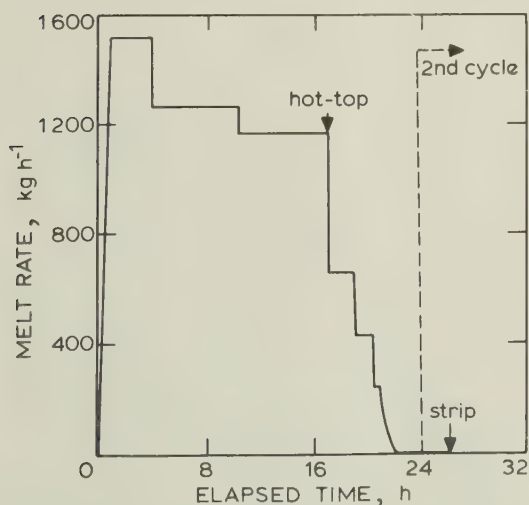
7 **Melt-rate programme of Fig. 5 recomputed for increase of maximum centreline LST from 2200 to 2500 s**

balance between yield and productivity is held[6] to reach an optimum position at about 1500 mm dia. ingots for low-alloy steels. This conclusion is supported by later work,[18] using programmed melt-rate procedures.

It may be concluded from the above discussion that there are two limiting cases of ESR production which need distinctly differing philosophies in melting practice. The first of these cases is one in which the structure requirement is very high and there is a clearly defined maximum permissible LST. Such cases are to be found in the melting of high-speed steels and superalloys. In this event, the length/diameter ratio of the ingots is normally large and the hot-topping time small because the ingot diameter is small. The requirement of the process is therefore to maintain the melt rate compatible with the low LST in order to maintain the highest quality. The size of furnace required for such processing is evidently small, with an ingot diameter defined as shown in Figs. 1 and 2. From the point of view of production rate, the furnace must provide for rapid turnaround between melts to compensate for the intrinsically low average melt rates, by minimizing downtime. For alloys in these categories, the LST values required for high quality are evidently in the range 1000—1800 s and consequently the maximum attainable ingot sections in practice are around 500—700 mm.

The second type of ESR practice is much less well defined than the first. This class of ingot is one in which the required quality is not accurately characterized by an LST value because it depends on both the end use and the processing after ESR. The problems associated with this class of alloy are discussed below.

Large ESR ingots

There are few descriptions in the literature of the results of physical examinations carried out on large ESR ingots (>20 t), although the furnaces which produce such ingots are well reviewed.[20-24] In the low-alloy steels which comprise the bulk of such large-ingot production, the quality of the material produced at low LST values is evidently very high in comparison to conventional air-melt steels.[25-27] There appears to be general agreement in the literature[28] that these large ESR ingots are certainly of adequate quality for the foreseen applications. The pertinent question is whether or not they are possibly of a needlessly high quality and therefore the process requirements may be relaxed with the object of increasing productivity and reducing cost. The effect of reducing the LST requirement in promoting production rate has been discussed above and it is clear that from a structure standpoint the permitted LST should be lengthened to the maximum.

In determining the required ingot quality there has been considerable discussion of the effect of forging on ESR ingots. The literature contains numerous reports[19,20,28] of the advantages offered by ESR technology in providing properties equivalent to conventional forgings at a much lower forging ratio. For example, the studies[27] on rolled material in heavy section indicate that the optimum property is attained at area reductions of 3—4; studies[29,30] on forged material show adequate properties at a forging ratio of 1.7. When combined with the ESR freedom from top-end defects, these reports imply that the ESR ingot may be very close in dimension and weight to the finished forging, leading to a yield of 85—90%, instead of the conventional 50—60%, in very large ingots. However, the case for high forging ratios in conventional ingots is far from clear, since Kawaguchi[31] reports that satisfactory forgings from 400 t ingots have been made without upset forging and at a forging ratio of 1.7, by a correct choice of length/diameter ratio in the starting conventional ingot. Should this report prove to be generally applicable to large ingots, a substantial fraction of the advantage suggested for ESR will be removed.

In discussing the relaxation of solidification requirements in large ingots, it is necessary to examine the practicality of melting at the very high absolute rates required by such relaxations. If one considers the case of a 1500 mm dia. ingot, the projected maximum melt rate permitted by a forging steel LST is about 2200 kgh^{-1}. The average melt rate quoted by Wahlster[20] for a 2300 mm dia. ingot of forging steel is about 3000 kgh^{-1}, leading to a desirable maximum of 4500 kgh^{-1} for high-productivity programmed melting. At a good average power efficiency of 1.3 kWhkg^{-1}, these two estimates lead to a maximum required power input of 2.8 and 5.9 MW, respectively. The power rating of a 1500 mm dia. ESR furnace should therefore be about 3.7 MVA (single phase 60 V, 62 kA); one of 2300 mm dia. approximately 7.9 MVA (single phase 60 V, 130 kA). These are obviously levels of power which pose considerable problems to both the user and designer.

In order to deliver the high power levels a number of designs have been proposed, and piloted for large ESR furnaces with varying degrees of success. A schematic diagram of these systems is shown in Fig. 8. The single-phase system, operating at line frequency (50—60 Hz) produces a very large unbalanced load on the primary supply and is permissible only in supply network conditions where such a load may be balanced by other, nearby installations. In addition, the use of 50—60 Hz power in the single-phase configuration requires very careful attention to furnace design, and has led to the 'coaxial' concept[32] (Fig. 8a) in which the inductive loop of the furnace is essentially eliminated. By this means, the power factor of the furnace is kept to an acceptable level and the problem of excessive phase angle between current and voltage consequently avoided. This design has been used successfully in furnaces manufacturing ingots of up to 1100 mm dia. and

60 Hz ac

(a)

5—60 Hz ac
or dc

(b)
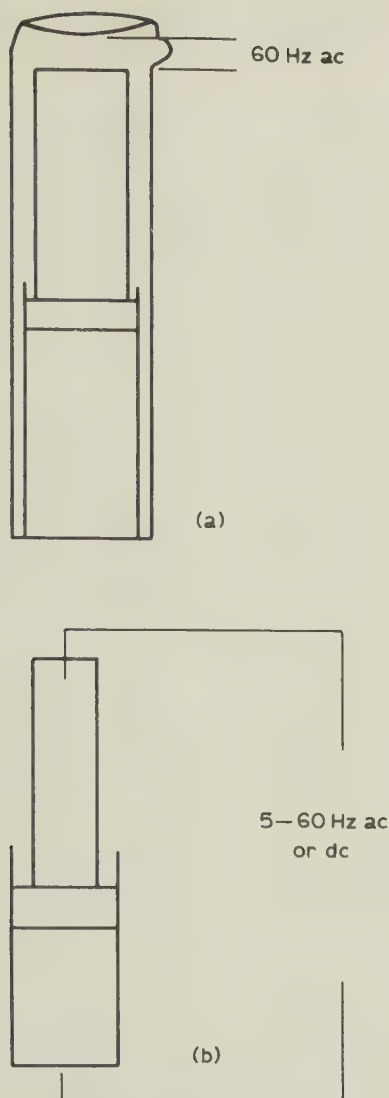
8   Schematic of two types of ESR furnace: *a*
'coaxial' furnace circuitry; *b* furnace with
large inductive loop

also for the manufacture of slabs of 750 × 2000 mm
in section.

It appears that the other basic design of
50—60 Hz ESR furnace (Fig. 8*b*), which has a very
substantial inductive loop, may be used without
difficulty in ingot sections of up to 1000 mm dia.
However, once this size has been reached, the
power factor becomes unacceptably low and some
other design must be sought. The alternatives
are the use of either lower frequency power or the
use of multiple electrode/multiple phase or both.
The configuration which employs three-electrode,
three-phase line frequency has been employed
sucessfully for large slab ingots as well as small
round-section ingots. The principal disadvantage
appears to be that common to all multielectrode
configuration, namely, that the low fill ratio
necessitated by several electrodes requires either

electrode changing during melting or unrealistic-
ally long electrodes. The problems associated
with electrode changing have been discussed in
previous work.[33] By using lower frequency power
in an effort to reduce inductive losses in a con-
ventional furnace design, the power supply intro-
duces both advantages and disadvantages. The
principal advantage, apart from increasing the
power factor, is that the supply is based on a
balanced three-phase input and hence is very
acceptable to the steelworks supply network. This
supply also has a smoothing effect on line transi-
ents arising from other high-power installations
such as arc furnaces and rolling mills. The prim-
ary disadvantage is that the low-frequency power
(in the range 1—10 Hz) is in the frequency range
where both mechanical vibration influences on the
installation and also medical influences on the
personnel become distinct hazards of the operation.

It appears that although the fundamental pro-
blems of supplying power to a large ESR furnace
are not serious enough to prevent the development
of very large furnaces, they are sufficiently
troublesome to place a severe restriction on the
designer. In this context, one must again raise the
question of whether or not ESR quality is really
necessary in large ingots.

Alternatives to ESR in large ingots

The ESR process offers several unique features
in both chemical reactions and thermal regime:
(a) it is possible to use highly basic slags not
feasible in a process using refractory containers;
(b) 'fine-tuning' additions may be made in alloy
composition; (c) losses of volatile alloy elements
may be prevented; (d) inclusion composition and
distribution may be closely controlled; and (e) it
is also possible to exert a considerable degree
of control over the ingot structure. However, the
utility of many of the above advantages becomes
questionable in large ingots.

Let us consider first the chemical aspects.
The use of basic ESR slags in removing sulphur
to very low levels has frequently been quoted[25]
as a major advantage of ESR. At present, ingot
chemistries in ESR steels are commonly in the
range 0.003—0.005 wt-%S and on occasions as low
as 0.001 wt-%S. However, with the advent of
modern ladle-refining practices, such as calcium—
argon blowing and rare-earth treatment, the above
sulphur levels are no longer unique to ESR. In
terms of cost, ladle refining is less than 20% of
the cost of ESR and so is a much cheaper route to
low-sulphur steels in large ingots.[34] The use of
highly basic slags also introduces the problem of
hydrogen into ESR. At present this has been
established[35] as a serious drawback in large ESR
ingots, but no clear solution has appeared. The
current situation has evolved into one of ameliora-
tion rather than cure, by stringent hydrogen
specification on the electrode, careful drying of
the slag before use, and exclusion of atmospheric
moisture by the use of dry-air protection over the

melt. The conventional ESR process will not remove hydrogen from the steel.

Although alloy additions may be made during ESR, thereby significantly altering the ingot composition, this method appears to be too difficult to control for use as a production tool. In practice the only additions made to the process are deoxidants or make-up additions of slag.

The merits of eliminating inclusions by ESR are well established but considerably less has been written on the subject of inclusion composition control. In speciality steels, particularly such grades as H13 and 52100, the inclusion composition is known to have an influence on fatigue life[36] and ESR offers an extremely versatile tool for accomplishing such control. However, the same effect has not been established in forging steels of the compositions commonly required in large ingots. It must be concluded, therefore, that inclusion composition control is only of possible potential benefit in the large-ingot field.

It may be seen from the above argument that while ESR does indeed offer some distinct advantages in chemical control, the cost of the process makes such control an extremely expensive undertaking when almost all the objectives can be attained by alternative routes at much lower cost. For large ingots, then, the rationale for using ESR must lie in solidification control, and it is in this light that we should examine alternative processes.

The closest alternative process is that of electroslag hot-topping (ESHT). This process has been described by several workers[37-41] and is in industrial use. The process sequence consists of casting an ingot by the conventional route, followed by a hot-topping sequence in which an electrode is melted by electroslag into the hot-top region. It appears that the minimum quantity of metal to be added by electroslag is about 4% of the ingot weight, to compensate for shrinkage. The maximum amount is essentially limited only by the ingot size requirement.

Sections from ingots made by this process show substantial improvements over conventionally cast ingots of the same size.[40,41] Both secondary and primary pipe are eliminated and the basal cone of high inclusion concentration is greatly reduced. These results, however, have been demonstrated only for small ingots (<7 t), and it is not yet certain that similar improvements will exist for larger ingots made by ESHT.

The LST in ESHT will certainly be larger than for ESR in small ingots where the heat-transfer conditions are such that the ingot surface heat transfer is the ruling section. However, in large-diameter ingots the situation is considerably less clear and the centre-region LST in ESHT may not be greatly different from the ESR case. In that event, the argument to be made for ESR is substantially weakened, since it is clear

from the published estimates[18] of ESHT productivity that it will be a much cheaper process than ESR.

Two other alternative processes for large-ingot production have been described, based on heavy-section electroslag welding. The MHKW process (Midvale–Heppenstall–Klöckner Werke) uses a conventionally cast ingot, from which the centre has been removed, as a consumable mould for an ESR 'ingot'. The resulting composite structure is then used as a substitute for a large ingot in the forging sequence. The process is described by Cooper[42] in detail, and has been used to fabricate 80 t composites.

Workers in the USSR have developed[43] a method for welding very heavy sections by ESR. In this technique two ingots are welded together to form the composite, which is then used as a substitute ingot in forging. The results reported by Paton *et al.*[43] indicate that the metallurgical quality of the weld is at least as good as that of the parent ingots in the weldment and hence that the composite has uniformly high mechanical properties. It appears that ingot sections up to 1500 mm dia. have been welded by this method, giving composites of over 100 t in weight.

The economic advantages of each of the above alternatives over ESR are not completely clearcut, since each of them relies to a certain extent on the availability of other facilities. For example, ESHT requires the casting of a conventional ingot and therefore the melting of the appropriate quantity of steel. Electroslag remelting can be carried out using composite, or sequential, electrodes originating from much smaller steelmaking facilities. The MHKW process also requires an appropriately sized conventional ingot. However, for most steelmaking installations at present concerned with the manufacture of high-quality large ingots, the viability of large-diameter ESR furnaces is very questionable in the face of the alternative methods.

It may be concluded, therefore, that for the practical requirements of large-ingot technology, the maximum practical size of ESR furnace is not greater than about 1500 mm dia. For ingots larger than this size, the more economical route is through the use of extensive liquid-steel refining,

(a)   (b)   (c)
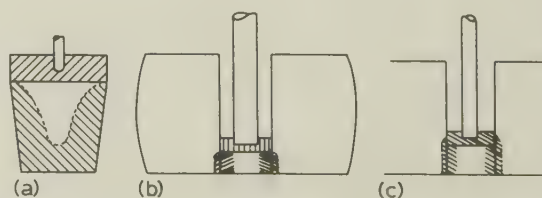
9   **Alternatives to ESR for large-ingot fabrication:** *a* electroslag hot-topping; *b* central-zone remelting; *c* electroslag welding

followed by either ESHT, MHKW, or welding processes, and illustrated in Fig. 9.

AS-CAST ESR MATERIAL

Although the majority of electroslag ingots are produced as round-section cylinders, clearly the process can be used to produce other shapes. Numerous production installations make square-section or slab-section ingots with ensuing advantages in subsequent mechanical-working steps. It is logical, therefore, to extend this philosophy to the limit of ESR capabilities in casting metal to the required shape and size. In laboratory experiments, it is clear that this limit is very far from a simple cylinder; indeed, one report[44] demonstrates the casting of dentures by ESR. However, with ESR, as in so many other processes, the limits of feasible technology and practical economics are very different. Much of the work reported to date is in the nature of demonstration technology and little appears to be of production status at present. In the authors' examination of this aspect of ESR they will show why this particular development has been rather slow, and also why its future prospects are difficult to predict. Two questions in particular will be addressed, namely:

(i) are the as-cast/heat-treated material properties adequate?

(ii) does shape casting lend itself to commercially viable production?

Material properties

A number of property determinations has been carried out of ESR material in the as-cast/heat-treated condition. Electroslag material used in the cast, heat-treated condition has generally been termed electroslag cast.[45] The work reported on electroslag casting (ESC) in the literature is confined almost exclusively to alloy steels, ranging from forging grades to stainless steels. The three main report themes on ESC are directed to the production of valves and tube fittings; shafts, gears, and rolls; and tools, dies, and die blocks.

The production of valves and steam fittings for the petrochemical and nuclear industries has been reported on several occasions.[46-54] The melting method used in the USSR for valves and pressure fittings is a progressive filling of a water-cooled copper mould as shown[50] in Figs. 10—12. The results of this procedure are reported for steel 15 Kh1M1F (0.13C—0.21Si—0.62Mn—1.25Cr—1.10Mo—0.24V—0.013P—0.003S) by Dubrovskaya *et al.*,[55] who state that the 100000 h stress rupture life of the component was superior to conventional parts. Rabinovitch *et al.*[56] also report results for valve bodies, made from steels 15 Kh1M1F and also 0X18H10T (0.06C—0.47Si—1.34Mn—17.5Cr—0.35Ti—10.17Ni—0.017P—0.004S), in which the properties are
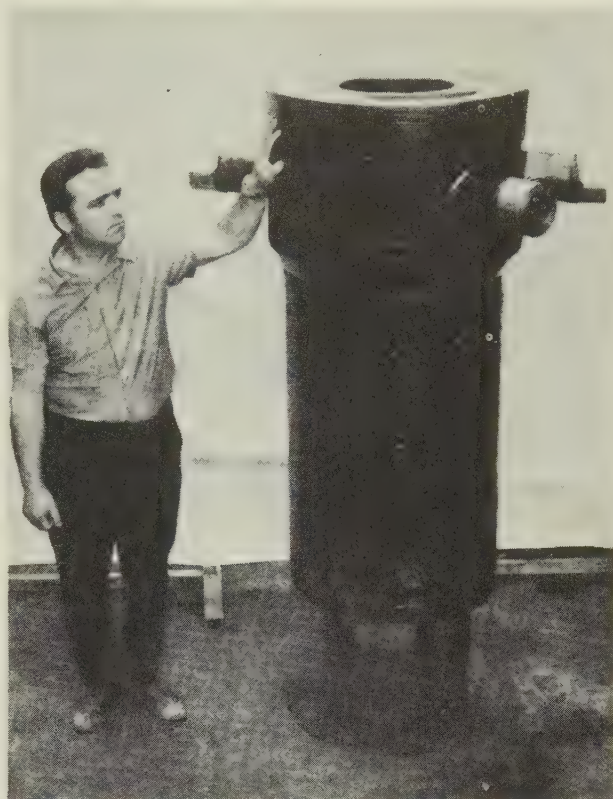
10 Electroslag-cast pressure vessel

11 Electroslag-cast gear ring

12   Electroslag-cast pressure-vessel entry nozzles
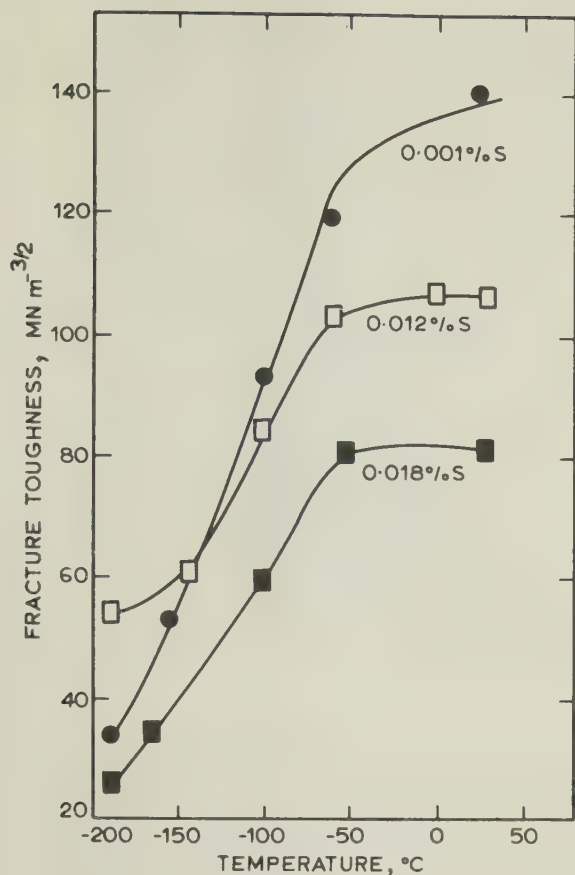

1 straight tube, 2 source material, 3 ring-type mould, 4 molten-slag bath, 5 molten-metal pool, 6 slag film, 7 start piece, 8 feed roller for source material, 9 drawing apparatus, 10 electric power source, 11 cooling water

13   'YOZO' process of Mitsubishi Heavy Industries Ltd: products pipe, tube; flux CaF_2—CaO—SiO_2—Al_2O_3

considerably better than conventional steels, in respect of yield strength, ultimate tensile strength, elongation, and fatigue life up to 100000 h. Other versions of the same basic results are extensively quoted in the Soviet literature.[47,48,50] It would appear from the context of the above reports that the valve bodies and fittings are being widely used in both conventional and nuclear power plant. However, there are no published reports of studies carried out on such components by agencies outside the USSR working to, for example, ASTM or ASME code standards.

Tubes and fittings for the petrochemical industry have been manufactured by ESC for some time.[46-49] The Mitsubishi corporation makes extensive use of this method ('YOZO') to produce reformer tube in HK alloys, as shown[57] in Fig. 13. The production volume in such tubing was reported to be 10480 m (in 1973), with tube sizes ranging from 130 to 350 mm i.d., in wall thicknesses from 24 to 60 mm, primarily in alloy KH40. The tubes were used mainly in ethylene, ammonia, hydrogen, and paper production, and are reported to give excellent service. Several variants of the production sequence have been used, giving tubes with varying section, elbows, oval sections, and also header tubes. The mechanical and service testing of these castings appear to have conformed to ASTM/ASME codes and thus it is well established that this version of ESC will provide a satisfactory product.

The second major category of ESC production is that of shafts, rolls, and gears. Workers in the USSR report[47] the manufacture of diesel crankshafts up to 160 t in weight by this technique. The 150 t crankshafts described in detail by Medovar et al.[45] in steel 20G (0.30C—0.33Si—0.68Mn—1.10Cr—0.56Ni—0.89Mo—0.37W—0.009P—0.005S) had highly uniform properties. The casting was tested in fatigue, as well as by conventional tension
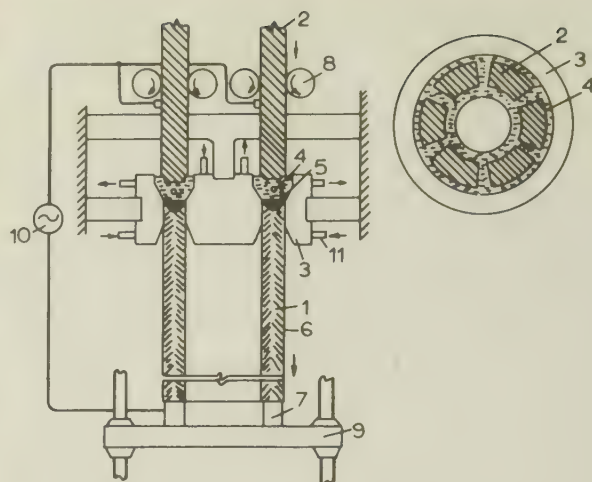
tests, with satisfactory results. These workers[45] claim that the cost of this manufacturing route is only 60% that of the conventional forging. There is, however, some ambiguity about the economic boundaries used to derive that figure and the 60% may exclude the very considerable cost of the ESC mould. The method is evidently used in the routine production of such shafts, and although no test experience is reported with the components outside the USSR, they are being offered for sale in the USA.

The production of gears using ESC is reported by Braun et al.[58] and by Paton et al.[50] The gear sizes apparently range from 5—10 kg to several tonnes, in material close to AISI 4340 in specification. There are no test results available on large gears, but the smaller ones show very significant improvements in wear life over conventional material. It is to be noted that the final gear shape, including relatively intricate profiles, has been cast by this method.

The manufacture of rolls is reported by Paton et al.[50,59] for use in the as-cast condition, in the hot rolling of steel. The rolls are described in weights up to 40 t, and are held to give satisfactory service. There are no published reports of similar work in Europe, Japan, or North America, but tests have been carried out on cold rolls of AISI 52—100 made by ESC and it has been shown that the material is satisfactory. Similar work has also been carried out on Sendzimir rolls with the same result.
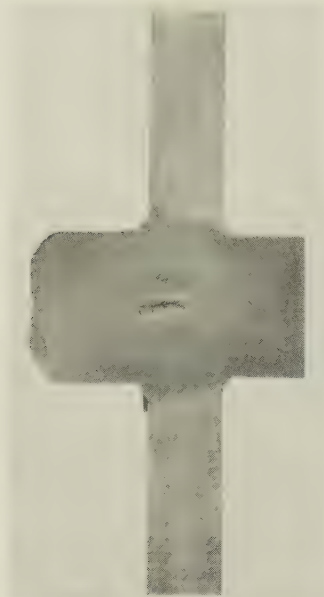
From the above discussion it is reasonably clear that, for many steels, the cast ESR quality is adequate to pass property qualifications normally applied to wrought steels. Furthermore, it is evident that the cast ESR quality is likely to be significantly better than a large fraction of commercial worked steels because of the intrinsically lower impurity content. The comparison frequently drawn in literature in the USSR is between cast-ESR and forged open-hearth steel, on which basis the conclusion is reached that cast-ESR steel is superior to forged steel. It is highly questionable, however, that cast-ESR steel is superior to all forged steel in all steel grades for all applications.

The enhancement of properties due to very low sulphur content is not unique to ESR steel. Work[65a] on several high-strength low-alloy (HSLA) steels (e.g. HY130, X80 pipeline steel) demonstrates that a substantial property increase is gained in these steels by the lowering of sulphur content, independent of the method used to achieve that composition. It is also very likely that the same argument may be applied to oxide inclusion content. None the less, ESR does offer a potential in property improvement over conventional castings by virtue of the reduction in segregation and also in the virtual absence of feeding defects. Its weakness lies in the lack of ductility in those steels whose fracture properties are a sensitive function of grain size. We may expect that the HSLA low-carbon steels will exhibit adequate strength levels in cast-ESR steel, but the present indications[64] are that this class of alloy does not possess adequate fracture toughness in cast-ESR steel. For the higher carbon levels of, say, SAE 4340 this drawback is not seen and the cast-ESR steel possesses very acceptable fracture properties. Also for the lower strength steels, which have considerable ductility (A517, A533, etc.) we should also expect to see adequate fracture properties.

Structural problems in cast-ESR steel

The above discussion relates entirely to the acceptability, or otherwise, of test samples of cast-ESR steels. The problem of acceptability in a cast-ESR component made from such steel is a more extensive question and requires further examination.
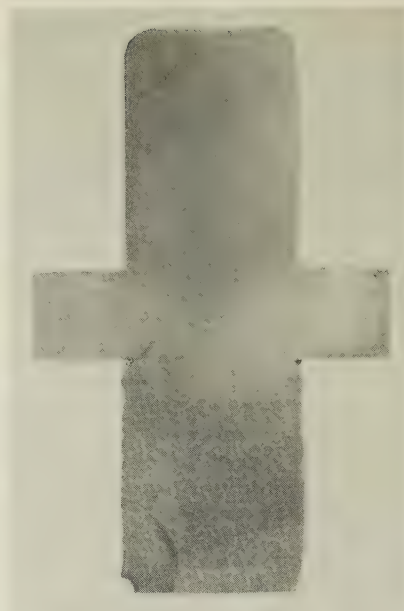
The component is formed inside a rigid mould and there is always a possibility that constraint will lead to solidification cracking, hot tears, or even cold cracking in certain steels. The formation of these defects is illustrated in Figs. 15 and 16 for a simple test shape: a solidification crack is shown in Fig. 17, identifiable in this case by the nearby presence of a 'bent' dendrite. If the mould contains abrupt re-entrant angles, hanger cracks may develop due to shrinkage stresses. Such cracks may also occur if the metal has been accidentally welded to the mould by momentary arcing through the slag skin. This defect is readily caused by undue misalignment of the feed

14   Fracture-toughness values for series of ESC SAE 4340 steel containing varying amounts of sulphur[64]

The rather specialized category of die blocks and tools has attracted considerable attention in ESC. Demidov *et al.*,[60] Petrman,[61] and Boiko *et al.*[62] all report very satisfactory results from die blocks made by ESC in alloys similar to H11 and H13, cast close to the finished shape. Hobbing cutters made from T1 and M2 are reported[61] to give excellent service life, cast by ESC to the semi-finished shape.

In high-strength materials, Flemings *et al.*[63] report data on SAE 4340, 300M, D6, 17—4PH, and a 250 ksi maraging steel. All of these steels show satisfactory strength levels, but in all cases the ductility of the cast material is slightly lower than that of the equivalent, heavily forged steel. This effect would presumably be reflected in somewhat reduced fracture properties for the cast steel as compared with forged steel.

The steel SAE 4340 is also examined by Mitchell and Aktar,[64] who report on the fracture behaviour of various ESR cast ingots containing different levels of sulphur. It is evident from this work that at least part of the enhanced mechanical properties found in ESR steels is due to extremely low sulphur levels. The fracture toughness of SAE 4340, as determined by Mitchell and Aktar, is shown in Fig. 14.

15   Centreline constraint cracking in ESC cast nozzle; A533B steel plate 2.5in thick[65a]

16   Corner cracking in similar structure to that of Fig. 15 (Ref. 65a)

electrode, or inadequate power control, or even inattention to the regularity of deoxidant feeding. Since the slags used for electroslag (ES) casting are intentionally of a composition which forms very thin solid skins (to allow accurate contour following), this particular defect can be difficult to avoid.

As in any other type of casting, the possible occurrence of the type of defect outlined above means that the ES casting must be subject to adequate quality-control procedures. In small sections (about ≤200 mm), such a requirement does not present a problem since conventional non-destructive testing performs adequately.[52] However, in heavier sections, the large columnar grain size in the centre of the casting introduces severe difficulties in ultrasonic testing and radiography becomes necessary. The significance of this situation is apparent when one considers the problem of qualifying an ES-cast component under the various mechanical codes (ASME, APS, etc.). Since the component is a casting, each of a series of similar components must pass all inspection procedures. Since, in heavy section, we are compelled to use high-resolution radiography, this procedure will be very costly. A similar series of forgings, on the other hand, may be qualified from one batch of steel and may also be tested by ultrasonic inspection. A further complication in code requirements arises in the case of ES castings which have been made by building up the component on a pre-existing structure, e.g. an entry nozzle built up on a pressure vessel. In this case, the resulting structure might be considered to be a weld, and hence subject to costly, periodic in-service inspections. Problems in code qualification and inspection have not been resolved with respect to ES-cast components and there re-

mains the distinct possibility that the added cost of such procedures may make the process non-competitive with forgings in many countries.

The ES-cast component may be made quite close to the finished size and shape. It is almost inevitable, however, that some finish machining will be necessary in most cases, if only to provide bolt holes, etc. in the structure. This provision could potentially cause difficulties with some high-strength materials since it would remove, or weaken, the fine-grained skin on the ES-cast surface. In the case of some brittle superalloys and high-speed steels, removal of this surface layer is known to make an ESR ingot much less forgeable. In the case of an ES casting, the removal of the fine-grained skin could possibly render the structure more susceptible to crack initiation. Some evidence of this exists, in that ES-cast steel which was mechanically acceptable on the basis of test coupons from a structure was found to be more susceptible to fatigue failure than forged material of the same composition. In this latter case, a cold-worked roll steel composition, the potentially attractive application of ES-cast steel must include consideration of the surface condition, as well as the bulk material properties.[65b]

ES casting equipment

The equipment used for shape casting by several workers[46-49,61,66,67a] is very closely similar to those employed in ESR ingot manufacture. The mould is formed from water-cooled copper sections designed in a manner which will permit their release from the ES-cast shape after melting. The more complex shapes, such as crankshafts, are made by successive operations in which a

17 Solidification crack in ESC material Cr—Mo—V steel ×5

otherwise the section profile will not be replicated by the ES casting. The level of control which this procedure requires can probably be automated with existing ESR technology, but in the present state of the art the feedback for the control appears to be manual. From the viewpoint of laboratory or development demonstrations of feasibility, this method is adequate, but it would cause substantial control problems as a production technique. As with the question of mould cost, discussed above, the development of routine operating controls for the process still awaits commercial demonstration.

It is clear that ES casting offers some interesting alternatives to conventional production routes. The ES-cast material is adequate in properties for many potentially useful products. While the method has been demonstrated in many applications, there remain important questions about its commercial viability in respect of mould design and process control.
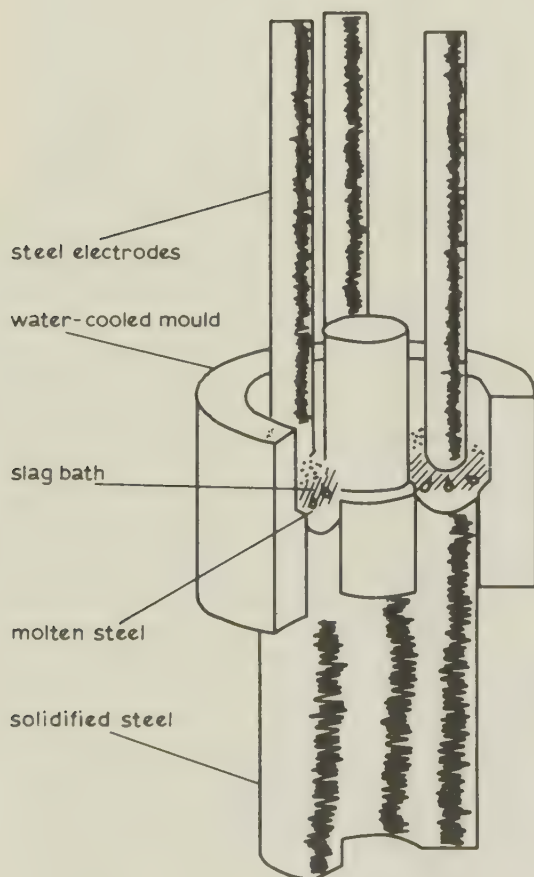
ESR HOLLOW INGOTS

Manufacture and properties

The manufacture of hollow, cylindrical ingots by ESR is now an established production route. Such ingots are manufactured on a routine basis in Japan, the USSR, Sweden, and the USA. The two earliest methods in production, developed by Ujiie *et al.*[51,57] and Paton *et al.*[68-70] are quite different in their product aim, although their design is similar. The method of Ujiie (Fig. 13) was commissioned initially with the manufacture of reformer tubes as the product aim. These tubes were intended to substitute for centrifugally cast tubes in the HK series of alloys, and to provide better mechanical properties through the absence of inner-region defects in the tube. Extensive mechanical-property tests have been carried out on this material, and a considerable quantity has been put into service with good results.[62] It appears that the development effort has been concentrated towards making long (~10 m) lengths of relatively light wall tubing (wall thicknesses in the range 10—100 mm) in relatively high-cost material. The method of Paton,[68] in contrast, has been directed towards the manufacture of short lengths of heavy-wall cylindrical ingot for subsequent mechanical-working purposes such as ring rolling, forging, or extrusion. The materials appear to be concentrated in low-alloy steels. For these reasons, although there are apparent similarities between the equipment used by Paton and Ujiie, the detailed designs are quite different.

previously cast component forms part of the mould and is welded into the new casting during the process. The principal disadvantages of this method are clear, namely, the mould cost and the necessary level of control on the melting operation.

The construction of large, water-cooled copper moulds is very costly and it is consequently necessary to amortize this cost against a large number of similar castings. This has evidently been done with success in the case of tube production,[46] but may prove a substantial difficulty in the case of the more specialized shapes such as large crankshafts. Some effort has been made to reduce the mould cost by using modular mould sections,[67b,67c] but these methods, apparently, have not been used in production. Other variations in mould design with the same objective[64] include water-cooled steel and also water-cooled aluminium moulds. The basic solution, however, remains as yet undefined and the function of mould cost in determining the ES casting method's commercial viability is not understood.

The aspect of casting control in the process is of considerable importance since most of the shapes proposed involve large changes in shape section during casting, or periods of welding into inserted pieces. When the section of the shape changes, the slag volume and heat flow also change. As a consequence, the melting rate must also change to the new rate required by the new section containing the process. Also, at points involving welding, the process heat flow must be increased to accommodate the increased heat leak from the system into the steel weldment. Both of these melt-rate and/or heat-input changes must be carried out in a small time period at the precise moment when the section change is taking place,

It is instructive to examine the different design choices in hollow-ingot production in the light of the routes chosen since the decisions made highlight the inherent problems in hollow-ingot manufacture. First, we must consider the production objective in respect of the hollow dimensions at the ingot stage. In the case of the Ujiie route, the product is to be used in the as-
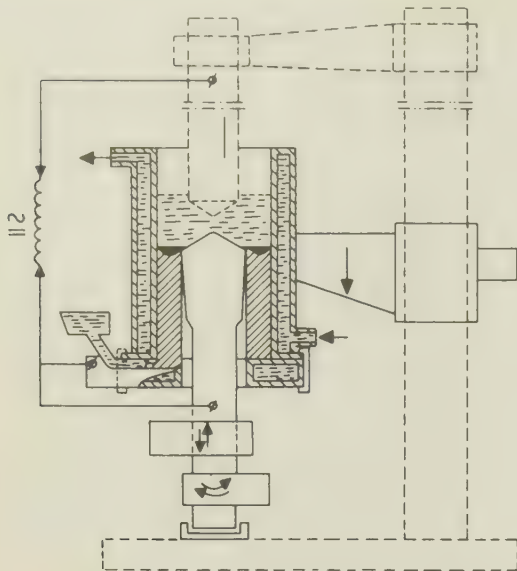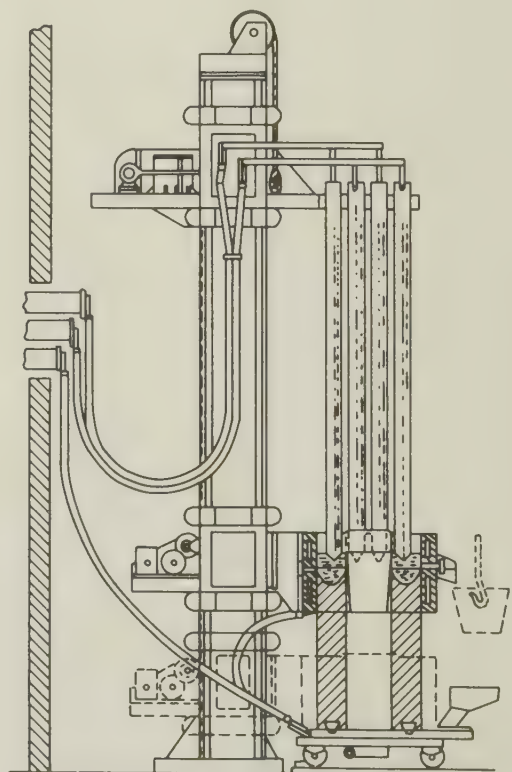
18   Mandrel-piercing method of hollow-ingot ESR (Ref. 73)

cast condition in a thin-wall configuration. For this reason, the ESR furnace must produce an ingot of light section and it follows that if reasonable geometrical clearances are observed in a conventional mould, there must be allowance for either continuous electrode feed (e.g. wire) or electrode changing. This problem may be alleviated slightly by the use of a tapered mould section, allowing larger electrodes to be used, but is evidently a substantial economic penalty in the method. The product, therefore, must be used in the as-cast condition to offset the additional process cost involved in electrode manufacture. Consequently, the design philosophy becomes clear: the production of a thin-wall hollow ESR ingot is viable only when the product is used in the cast condition.

The ESR furnace designed by Paton,[68] on the other hand, is clearly intended to make heavy-section hollows for mechanical working. Considerable effort has been devoted[70-72b] to reducing the electrode cost by arranging the mandrel in a 'piercing' mode (Fig. 18, Ref. 73), which is the route followed by US production facilities.[73] The installation reported by Akesson,[75] however, relies on a taper-section mould (Fig. 19) and a conventional through-mandrel together with several separated electrodes (Fig. 20). In this case, the ingot wall thicknesses are 120 mm (o.d. 340 mm) and 210 mm (o.d. 875 mm). The Cabot Corp. production facility[74] makes ingots of wall thickness 125 mm (750 mm o.d.) by the mandrel-piercing

steel electrodes

water-cooled mould

slag bath

molten steel

solidified steel

19   Schematic of SKF method of hollow-ingot manufacture

20   Schematic of hollow-ingot ESR furnace[76]

technique, in weights up to 15 t. In both the taper-section mould and mandrel-piercing techniques, the object is to reduce the electrode cost by permitting the use of heavier section electrodes than is possible in the Ujiie method. The cost component thus saved may then be set against the cost of mechanically working the ingot. Although a cost advantage is claimed[74] for this route as against the trepanning, or piercing of a solid ESR ingot, there appears to be some controversy over the magnitude of the advantage claimed. The contention originates in a combination of the equipment available to the processor (e.g. forging-press size) and also in the potential workability of the alloy. However, it is clear that the cost advantage of hollow-ingot manufacture for mechanical-working processes is sufficiently marginal to warrant close attention to the cost of electrodes as it relates to the furnace design.

The second point of technical concern in all hollow-ingot ESR furnaces relates to both of the design philosophies discussed above. It is the control of the position of the slag/metal interface with respect to horizontal position in the mould. In the case of both the taper-mould and the mandrel-piercing method, the local thermal regime changes very rapidly with vertical displacement around the equilibrium positions shown in Figs. 13 and 19. The results of such displacements are either a runout of slag and metal below the mould due to excessive heat input to the ingot, or a freezing of the ingot surface in the upper-mould section due to inadequate heat input. In either case, the operation must be terminated. At present, the position control in US furnaces is made by means of a radiation-density detector using a sealed γ-radiation source and a detector to identify when the slag/metal interface crosses the fixed radiation path.

A different approach has been taken by workers in the USSR, who determine the position of this interface by means of a heat-flux meter.[77–79] The meter is a calibrated thermal resistance inserted in the mould wall in such a manner that the point axial heat flux is registered as a signal from the meter's thermopile. The arrangement is illustrated in Fig. 21. Detection of the slag/metal interface is accomplished by the rapid change in heat flux into the mould in this region, as shown in Fig. 21. This heat-flux peak is also accompanied by a change in mould current, as shown in Fig. 22, but the current change is not sufficiently large to use as a detection point. The heat-flux peak value is a function of metal and slag composition, melting rate, electrode immersion, and power input. It is not possible, apparently, to use the absolute value of the peak for sensing purposes, but instead a series of sensors placed in a vertical direction may be used to detect the peak position. This position is then used as the furnace control point.[80]

Finally, since no successful hollow-ingot process appears to have been developed using a
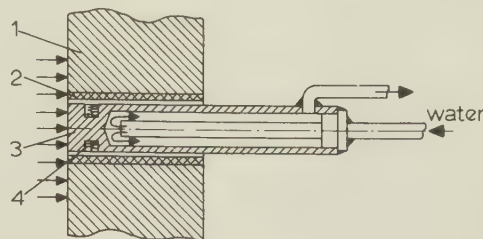

1 mould wall, 2 thermal insulation, 3 water-cooled copper probe, 4 thermopile

21 Heat-flux meter for mould-wall insertion[84]

stationary mandrel—stationary mould, all the processes involve movement between ingot and mould. For this reason, there is a situation in which the surface quality of the ingot is extremely sensitive to slag composition and slag temperature. Consequently, the process procedure must contain the appropriate allowance for these conditions.
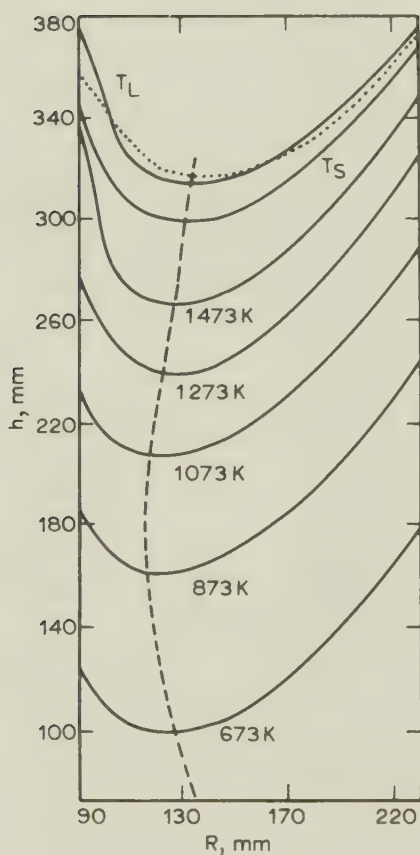
Melting rates, LST values, and heat flow

It is instructive to consider a particular case of melting rates in a hollow ingot in relation to some equivalent solid shape. In a thick-wall section, for example 500 mm o.d. × 250 mm i.d., the metal/slag interfacial area approaches that of the equivalent solid. For the example given, the metal/slag interfacial area is 75% that of a 500 mm dia. solid round section; the peripheral contact area between the high-temperature system and the mould is ×1.5 larger in the case of the hollow than in that of the solid. The combination of the above dimensional relations leads to a situation where a thick-wall hollow ingot has a significantly shorter centreline LST than the equivalent diameter solid, when both are melted at the same rate. This effect is given in Table 1, for the case of IN 718 alloy. The impact of the smaller LST values on steel properties is not known but, in principle, this effect
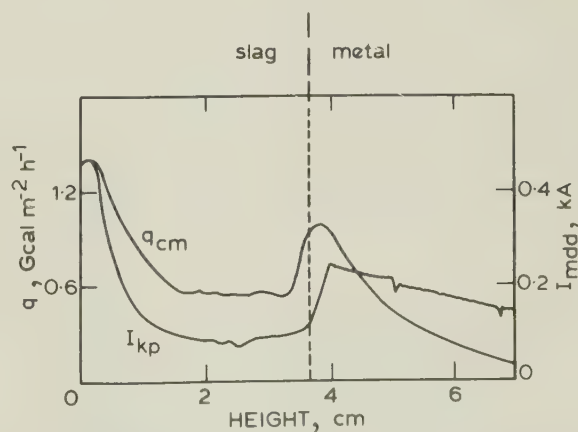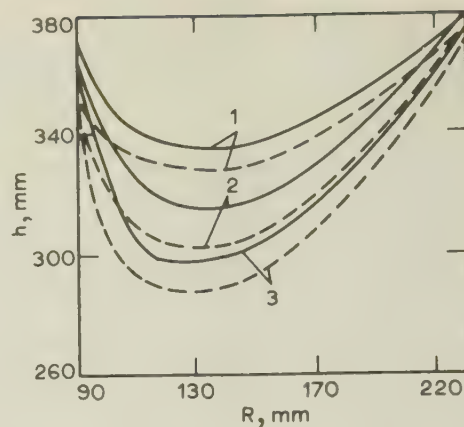

22 Mould heat flux and mould-wall current flow: 1 kcalm^{-2}h^{-1} = 1.17 Jm^{-2}s^{-1}; I_{kp} = process current, q_{cm} = interface heat flow

Table 1 Solidification conditions for alloy IN 718 in hollow and solid ingots

Ingot dimensions	Steady-state conditions		
	Pool depth, mm	Mushy zone width, mm	Local solid time, s
508 × 254 mm hollow 508 kgh⁻¹ Centreline	75	48	478
508 × 254 mm hollow 700 kgh⁻¹ Centreline	93	73	523
508 mm solid 508 kgh⁻¹ Centreline 127 mm from edge	345	155	1722 872

1 30 gs⁻¹ melt rate, 2 60 gs⁻¹ melt rate, 3 90 gs⁻¹ melt rate

24   Liquidus/solidus lines for hollow ESR ingot

should lead to enhanced ductility in the case of hollow ingots over the conventional equivalent solid.

Considerable attention has been paid by workers in the USSR to the problem of computing the thermal field in ESR hollow ingots. Paton *et al.*[81] have computed isotherms for the case of an ingot of SAE 52100 (440 mm o.d. × 180 mm i.d.: 220 kgh⁻¹) with good results when the actual liquidus line is compared to the calculated one (Fig. 23). They also examine the effect of melting rate (Fig. 24), showing that even at high rates (325 kgh⁻¹) the centreline LST is still at a very acceptable value, in this case about 800 s. Previous work[82] on SAE 52100 has established that adequate solidification structures can be obtained in SAE 52100 with LST values considerably in excess of this time.

23   Temperature field in hollow ESR ingot
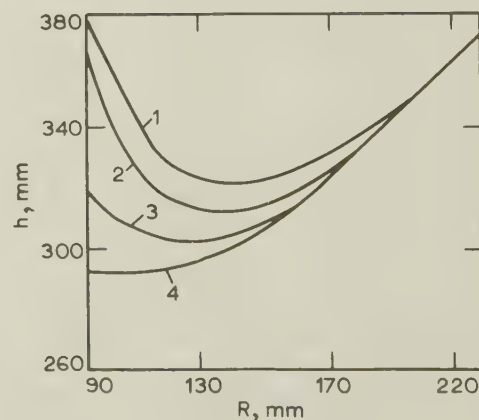
1 0 mm slag skin, 2 1.5 mm slag skin, 3 10 mm slag skin, 4 50 mm slag skin

25   Effect of slag-skin thickness at mandrel side on hollow ESR ingot liquidus line

It is clear from Fig. 24 that the heat flow in a hollow ingot is not symmetrical about the melting region's geometrical centre. The contraction of the ingot around the central cooling mandrel has a significant influence on heat transfer, as does the equivalent asymmetry of heat generation. The model of Paton *et al.*[81] allows for changes in the axial heat-transfer conditions (Fig. 25), but assumes that in all cases the slag temperature is constant. Nevertheless, the strong effect of radial asymmetry in heat transfer can be seen clearly. The extent to which this effect is reduced by increasing the ingot wall section has also been examined,[81] with the expected result that as the section increases, the asymmetry is reduced. A similar heat-transfer model of hollow-ingot ESR, developed by Ballantyne,[83] has been applied to hollow ingots of IN 718 with similarly successful results in predicting liquidus profiles and LST.

The industrial results obtained in hollow-ingot ESR have been summarized by Medovar,[84] who details remelting conditions for a number of alloys and configurations.

LIQUID-SLAG TECHNOLOGY

ESR practice originally developed using the technique of arc starting, followed by the addition of cold slag powder to convert the arc to electroslag heating. In a large ESR furnace this technique imposes two penalties: first, the process does not attain a high melt rate until all the slag is liquid; second, the ingot base may contain defects. With the development of experience in ESR, it has been possible to minimize these two problems, but the technique is none the less a continuing source of practical difficulty.

The alternative method is that of melting the slag in a separate furnace and then pouring it into the ESR crucible to initiate the process. Although this technique permits a rapid, high-power start under reproducible conditions it is far from simple in practice. The problems associated with the technique lie in the slag furnace design, the slag composition control, and the slag crucible materials.

Furnace structures

There are three principal configurations of slag-melting furnaces for use in conjunction with molten-slag starting of electroslag remelting equipment. The earliest, and still used at present on small to moderate sized furnaces, is a solid graphite crucible. This one-piece graphite crucible is obtained from a solid graphite cylindrical section with the centre bored out to accommodate the melting volume. With this technique, there are no joints or seams that may lead to possible molten-slag breakouts (Figs. 26a, 26b, and 27).

In some installations, namely moderate-sized furnaces, water-cooled carbon steel slag-melting

dimensions in mm
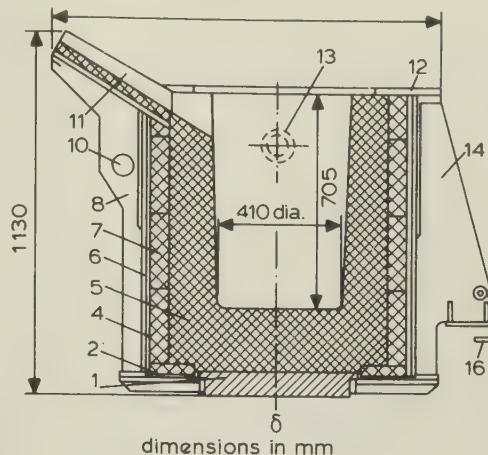
1 graphite contact pad, 2 steel shell, 4 refractory liner, 5 graphite crucible, 6 castable refractory, 7 refractory powder, 8 support 10 pivot, 11 runner, 12 lid, 13 pivot lift, 14 back rest, 16 hook

26a USSR slag-melting furnace Y—560

furnaces have been in routine operation for many years. While there are obvious potential hazards with the use of a water-cooled crucible, the production reality of this process must be recognized. In this case, the crucible wall is relatively thin-gauge carbon steel, approximately 6 mm thickness, and in contact with high-velocity cooling water. It is claimed that a thin slag skin is formed against the steel wall, and that heat losses are not substantially greater than that for massive carbon-lined crucibles.
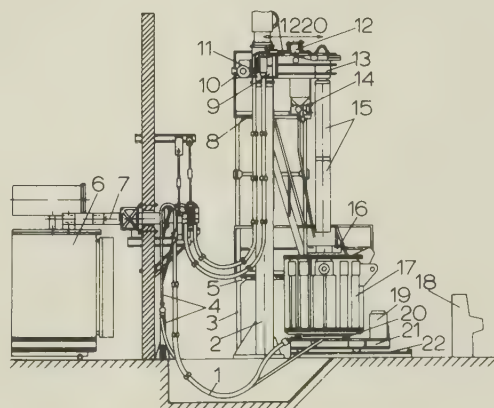
1 cables, 2 stand, 3 support structure, 4 water lines, 5 platform, 6 transformer, 7 bus bar, 8 roof, 9 drive support, 10 drive motor, 11 drive cable, 12 addition hopper, 13 electrode holder, 14 addition valve, 15 electrode, 16 roof, 17 crucible, 18 controls, 19 motor movement, 20 contact pad

26b USSR slag-melting furnace Y—360 M
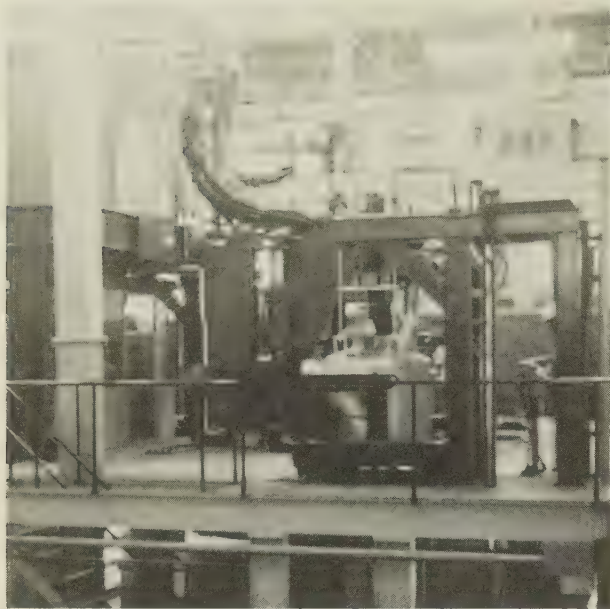
27   Consarc slag furnace: 300 kg capacity[106]

The larger sized slag-melting furnaces commonly utilize a carbon brick-lined crucible (Fig. 28). Conventional furnace refractory design criteria are used to develop the appropriate thicknesses of a variety of refractories, such that heat loss may be minimized and the thermal gradient requirements satisfied with a minimum refractories cost. Carbon brick-lined furnaces have been constructed with and without a backup carbon brick safety lining. Because of the high thermal conductivity of the carbon brick, any of the molten slag which may penetrate the joint in the brick would be exposed to temperatures high enough to ensure a high degree of fluidity and chemical activity of the slag. Therefore, in the absence of a

28   Consarc slag furnace shell, showing graphite lining

safety or backup carbon brick lining, a molten slag at this point would readily penetrate conventional furnace refractories, leading to a massive breakout. It is necessary if the use of carbon brick linings is to be successful that a high level of craftmanship be employed by the bricklayers to ensure a tight working lining which will not be subject to molten-slag penetration.

In almost all cases, it is necessary to have a roof for the slag-melting furnace which serves a dual function: to collect the fumes given off in the slag-melting process and to minimize radiant heat losses. Such furnace roofs, not in direct contact with the molten slag, are commonly made of high-alumina castable or plastic refractory materials.

Because of the relatively large mass of high-heat-capacity refractories in contact with the molten slag, electrical energy substantially in excess of that required for slag fusion is necessary to satisfy the heat absorption and losses to the furnace refractories. The amount of heat necessary to bring the furnace refractory system up to an equilibrium condition with operating slag-melting temperatures must be included in the design of the electrical system to provide the energy for melting of the flux raw materials.

Several types of electrical circuits are used in slag-melting furnaces. Many of the smaller furnaces employ a single-phase electrical system with one graphite electrode and the one-piece graphite crucible as the opposing current path. With larger flux volume associated with larger ESR furnaces, the tendency is to utilize a three-phase power system, similar to that of a small electric arc furnace. In this case, three graphite electrodes are connected to a three-phase power transformer. Improved operating efficiencies result from the use of a multiple-tap power transformer to provide appropriate range in operating voltages. Commonly used secondary voltages range from about 150 V max. to 30 V min. The actual voltage tap used on a particular furnace will depend upon the electrode spacing requirements as well as on the depth of immersion necessary for uniform energy release. Slag-melting furnaces are different from conventional arc furnaces in that the heat generation is by resistance heating which is determined by the $I^2 \times R$ components of the system. Because the electrodes are normally submerged at a significant distance in the molten flux, it is possible to use the three electrodes rigidly fixed to a common moving platform. It is not necessary to incorporate conventional three-phase independently current-balanced automatic-positioning equipment for each electrode. The use of multiple voltage taps in the power transformer enables the operator to obtain a sufficient degree of immersion of the electrodes to avoid a superheated surface condition, high electrode voltage, or excessive electrode current and very deep immersion resulting from too low a tap voltage.
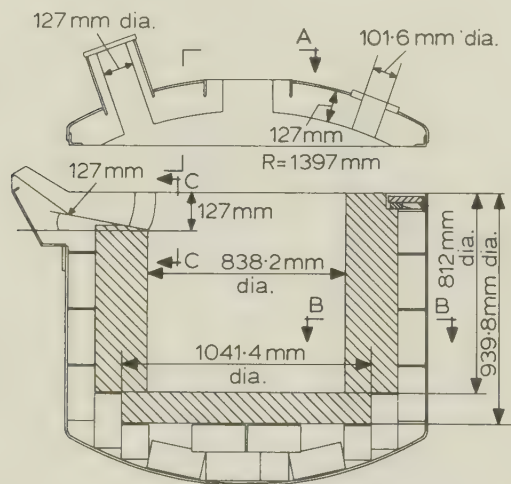
Slag melting

Typical fluxes made from the raw materials CaF_2, Al_2O_3, and CaO clearly do not 'melt' in the normal sense when heated. The process, as with most metallurgical fluxes, involves the melting of one component followed by a dissolution of the remaining composition. In the ESR compositions, the only component which melts at normal process temperatures is CaF_2 (m.p. 1423°C) and it is this compound which forms the first liquid phase on heating the slag composition from room temperature. It may be expected, therefore, that the liquid will form by dissolution of Al_2O_3 and CaO following a pattern of phase relationships defined by established phase diagrams.[85-91]

The rate of dissolution of Al_2O_3 and CaO will be controlled by temperature, but also by the stability of intermediate phases. For example, it has been shown that Al_2O_3 dissolves essentially by an acid—base reaction

$$Al_2O_3 + O^{2-} = 2AlO_2^-$$
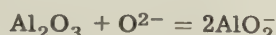
and hence is dissolved much faster by a flux containing CaO than by CaF_2 alone. In the latter solvent, the requisite O^{2-} ion concentration can form only by the volatilization of AlF_3. It is clear, therefore, that a slag with a large concentration of CaO will liquefy much faster than an acid system. This finding reflects into the apparent melting efficiency through the time of melting rather than through any influence of absolute thermal capacity. It follows that a composition in which the slag ingredients have been preformed by prior fusion or sintering will liquefy faster than one based on mixed raw materials. This aspect has been utilized in slag-forming materials based on sintered mixtures of CaF_2 and calcium aluminates.

The theoretical energy requirement to melt 1 t of 70 wt-%CaF_2 +30 wt-%Al_2O_3 and to raise the liquid to 1700°C is 602 kWh. This value is to be contrasted with the industrial value of about 1300 kWh[-1].

The problem of chemical vaporization from ESR slags has been studied by Schwerdtfeger and Klein,[92] who identify the vapour species as primarily fluorides. The CaF_2—oxide liquid produces volatile fluorides of Al and Si:

$$3CaF_2 + Al_2O_3 = 2AlF_3 + 3CaO$$

$$2CaF_2 + SiO_2 = SiF_4 + 2CaO$$
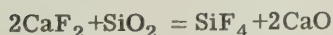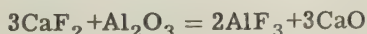
in addition to establishing a vapour pressure of CaF_2 itself. The systems appear to follow equilibrium thermodynamic routes in producing these vapours and consequently we may anticipate that any ESR furnace or slag-melting furnace will emit fume containing fine powder CaF_2, AlF_3, and gaseous SiF_4. On contacting a typical moist-air atmosphere these compounds hydrolyse, e.g.

$$SiF_4 + 2H_2O = 4HF + SiO_2$$
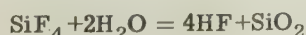
resulting in the need for careful fume collection and monitoring on the furnace.

The fume-collection system on an open-atmosphere furnace is normally an exhaust system discharging into a dry bag house. The nature and concentration of the fume from the industrial process has not been discussed in the literature.

Slag raw materials

The specification of the raw materials used in the makeup of the appropriate slag composition depends primarily upon the specifications of the metal products to be remelted through the slag system. Besides the chemistry of the metals to be melted, slag composition is also strongly influenced by the electrical characteristics of the slag desired, as well as the viscosity-related effects of the slag upon the surface quality in the resulting ingot. Additionally, the slag chemistry may be further modified to accommodate atmospheric conditions above the molten slag in the ESR furnace with respect to transfer of gases to the remelting electrode. Therefore, all these above-mentioned factors relate to the determination of the optimum slag composition, as well as the specification of the raw materials from which the slag is constituted.

The general observation may be made that the quality of the slag-making raw materials varies in direct proportion to the value of the remelted metal in the ESR system. That is, reactive alloys or very high-performance alloys may require and justifiably use previously melted and crushed slag-making materials. As the value of the remelted metal approaches lower limits, slag-making raw materials may approach the value of fluxes commonly employed in arc furnace steel-making. Additionally, the requirement for pre-fusion of the flux material may be governed by whether the molten-slag start or a 'dry'-slag start is used in the ESR process. The dry-starting operations generally require the use of prefused-flux raw material to avoid moisture-related problems in the resolidified metal.

The three principal ingredients (fluorspar CaF_2, alumina Al_2O_3, and lime CaO) may be purchased over a relatively wide range of specifications and prices depending upon the requirements of a given ESR furnace installation. Typical specification compositions are shown in Table 2. Because of the harmful influence of relatively small amounts of impurities in the principal slag-making materials, exacting specifications are normally required for each of these items. Special packaging techniques may also be required in the case of those materials subject to absorption of moisture from the atmosphere, for applications where hydrogen pick-up in the remelting metal systems represents a deleterious situation.

Whether the raw materials are purchased, prefused, premixed, or batch blended at the ESR furnace, these mixtures are then placed into the slag-melting furnace. In many cases, the flux-

Table 2 Typical analyses of ESR raw materials, wt-%

Acid-grade fluorspar	
CaF_2	97.4
$CaCO_3$	1.0
SiO_2	1.1
$BaSO_4$	0.15
Pb	0.15
Fe_2O_3	0.03
Total S	0.06
Lime	
CaO	95.7
MgO	0.9
SiO_2	1.5
S	0.025
Al_2O_3	0.075
Fe_2O_3	0.20
Loss on ignition	0.5
Alumina	
Al_2O_3	98.9
SiO_2	0.02
Fe_2O_3	0.03

melting furnace is not designed to accommodate the entire charge of unmelted raw materials so that, after an initial filling of the furnace, the remainder of the flux weight is added to the partially melted bath. As the slagmaking raw materials are not electrically conducting, special starting techniques are used to initiate a molten pool underneath the graphite electrodes. A variety of techniques may be employed, but commonly metal turnings (compatible with the metal system to be remelted) are spread to form a conduction path between the electrodes in a three-phase system. However, in the case of the single-phase electrode system, it is common practice for the single electrode to be placed against the bottom of the graphite crucible, followed by filling of the crucible with the initial charge of material to be melted. In this single-phase case, power is applied momentarily in an almost short-circuited condition with the electrode promptly raised sufficient to initiate an arc. Following a relatively short time interval of arc operation between the electrode and the crucible bottom, a molten pool is quickly formed to sustain the continued arcing condition until a sufficient molten-slag volume is generated to sustain resistance heating. In the three-phase electrode system, carbon or graphite chips may also be utilized either with the metal turnings or in lieu of these metal turnings to form an electrically conducting path. The initial slag melting

is greatly facilitated by the use of a high-voltage tap for arc initiation. Following the initial period of arcing, a molten pool readily forms within the electrode delta region. As this molten-slag pool becomes of sufficient volume, electrode voltage is reduced and resistance melting is continued. Following the melting of the initial charge of flux raw materials to the flux-melting furnace, after a sufficient amount of superheat is obtained, the additional flux raw materials may be added either continuously or batchwise to obtain the desired slag volume. Control of slag-melting temperatures are important to avoid excessive selective volatilization of slag constituents, which would lead to a change in the resulting slag composition.

For the condition of dry-starting operation, a slight change in start-up procedures is required. Normally, a bed of turnings of a metal compatible with the electrode to be remelted is positioned against the base plate and the electrode is lowered with pressure applied against this bed of metal turnings. The unmelted flux raw materials (which commonly may contain previously melted and crushed raw materials) are then poured into the surrounding annulus between the electrode and the mould walls. As the volume of the annulus between the electrode and the mould wall is much less than the volume of the flux required, it is necessary to continuously add additional flux to this annulus during flux-melting operations.

Flux melting begins with power applied across the short-circuit current path established by the metal turnings underneath the electrode. Sufficiently high power levels are required to obtain melting and/or subsequent arcing in this region between the electrode and the base plate. The heat energy liberated in this operating mode is then sufficient to cause melting of the flux raw materials adjacent to the steel turnings. Following the melting of a sufficient quantity of molten flux, the arcing phase is terminated and resistance-induced heating is continued for the melting of the remainder of the flux raw materials.

Control of flux chemistry often involves practices to minimize carbon pick-up associated with the electrode operation, as well as from the carbon or graphite crucible. While it is not possible to eliminate completely any carbon pick-up by the molten-flux melting operation, operating practices can influence very substantially the degree to which carbon is dissolved in the flux. In some cases[11] it is possible to reduce this carbon pick-up to lower levels by the addition of iron oxide to the molten flux within the ESR mould, before the start of remelting.

However, techniques related to the oxidation of carbon from the slag also lead to a condition that may require deoxidation of the slag before metal remelting. This is necessary to prevent loss of oxidizable elements such as aluminium, titanium, zirconium, niobium, etc. If alumina is an ingredient of the flux, it is common

practice to deoxidize the slag with an aluminium addition before melting-in a substantial proportion of electrodes. It is also possible to utilize other elements for the slag deoxidation to maintain compatibility with the electrode—metal system.

Carbon is soluble in ESR slags as the carbide ion, carbonate ion, and cyanide ion. All these forms have been shown to exist in CaF_2-based slags.[93-96] The ions form by reaction with the graphite crucible and the atmosphere, in the case of carbide and cyanide

$$3/2O^{2-}+3/2C+1/2N_2 = N^{3-}+3/2CO$$

$$O^{2-}+3C = C_2^{2-}+CO$$
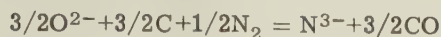
or from CO_3^{2-} in the initial material in the case of carbonate.

There have been no reports of nitrogen contents in ESR ingots which are clearly attributable to initial contents of CN^- in the liquid starting slag. On the other hand, carbon pick-up from the starting slag has been known as a problem for some time. It evidently arises primarily from C_2^{2-} ion, the formation of which is encouraged by high O^{2-} ion concentrations and by low effective pressures of CO gas. The reaction also favours the formation of C_2^{2-} as the temperature is increased. In order to minimize the introduction of C_2^{2-} into the liquid slag it is necessary, therefore, to minimize the time spent at high temperature, to minimize the O^{2-} content, and to maximize the ambient pressure of CO. All of these practices are used to facilitate the melting of low-carbon alloys with the liquid-slag starting method.

It is reported that the problem of carbon pick-up becomes significant for alloys containing less than 0.1 wt-%C. However, owing to the intrinsic difficulty of analysing C_2^{2-} in ESR slags, the slag carbon levels equivalent to this have not been defined reliably.

The problem of moisture in ESR slag mixtures has been the subject of much discussion at the practical level but unfortunately little definitive information is available in the literature. It appears that OH^- is extremely stable in fluoride-base solutions, leading to the situation that significant quantities of OH^- are retained in liquid slag after melting in graphite. The hydrogen content of this ion passes into the ingot base on contact with liquid metal:

$$2(OH^-) + Fe(l) = 2[H]_{Fe} + [O]_{Fe} + (O^{2-})$$

An increase in ingot hydrogen content is therefore observed in the foot of the ingot, decaying along an exponential curve as the melt progresses (Fig. 29).

Various methods have been tried to prevent this effect, but it appears that only three have any practical merit. These are: (a) to specify very dry raw materials (e.g. Table 3), or (b) to use a large proportion of recycled slag from previous ESR melts (this proportion is reportedly as high as 70% for large ESR installations[99]; or (c) to adjust the slag composition into a range where OH^- becomes less stable. Since its decomposition by
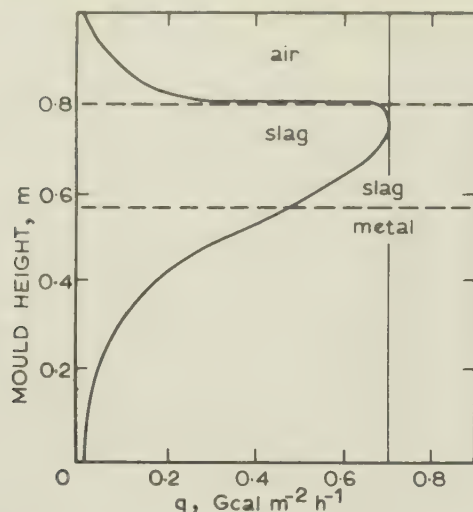
$$2(OH^-) \rightarrow H_2O(g) + (O^{2-})$$
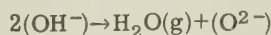
is obviously a function of slag basicity, we may assist its removal by making the slag less
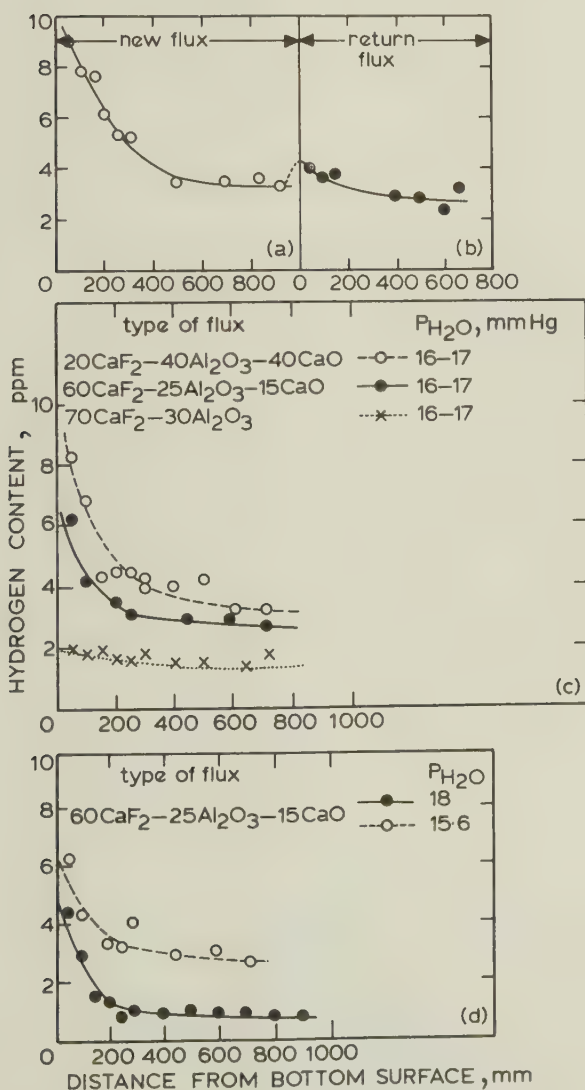
29 Hydrogen behaviour in ESR[97]

Table 3 Characteristics of sintered slags[98]

Pellet size	0.25 in dia.
Fusion range	~100K
Loss on ignition after 24 h exposure to air at 95% rel. humidity	0.3%
Composition range	±2% in each component

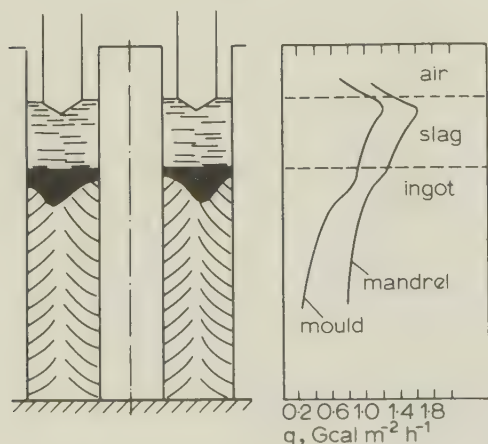30 Heat transfer at mould wall[106]: $1 \text{ kcalm}^{-2}\text{h}^{-1} = 1.17 \text{ Jm}^{-2}\text{s}^{-1}$

basic.[100,101] This requirement implies the development of a range of ESR fluxes which are essentially acidic and hence imposes further limitations on reactions such as desulphurization.

Normal slag-melting practice allows sufficient residence time at temperatures below the liquidus to allow any $Ca(OH)_2$ to decompose as a standard-state reaction, not permitting any solution in CaF_2. By this means a minimum residual OH^- content is obtained before any stabilization by slag solution may take place. The slag is then liquefied in the usual manner.

ESR MOULD DESIGN

Process heat fluxes

It is generally agreed[102-104] by various investigators on ESR that about 35—50% of the total power generated in an ESR slag passes directly to the mould in the slag region. Indirectly, over 80% of the total heat generated passes into the mould cooling circuit in a static-crucible process, a value which falls only to 70% in a moving-crucible—ingot configuration. For these reasons, the mould construction and the manner in which it is designed to extract this high heat flow are extremely important in the successful operation of the ESR process.

The distribution of heat flux into the mould is normally symmetrical in a radial or horizontal plane, but is far from uniform in an axial direction. Early workers in the VAR field[105] noted that this process produced a marked peak in crucible heat flux in the region immediately adjacent to the contact rim of the ingot against the crucible wall. A similar general pattern is observed[8] in ESR, although the peak is not as pronounced as in VAR. In the bifilar-electrode ESR configuration, the mould heat flux shows a steady decrease below an abrupt maximum reached at a position radially opposite the electrode-tip region (Figs. 30—32). This heat flux reflects the pattern of heat generation in the latter process geometry (Fig. 32). In contrast, it has been noted[103,108] that in a single-electrode system, there is a marked increase in heat flow into the mould in the region of the slag/metal interface. In both cases, however, the peak heat flux is about the same, giving a range of 20—40 $\text{calcm}^{-2}\text{s}^{-1}$ to be dissipated by the mould at the maximum value.

The above heat flux is conducted away from the process region through a series of thermal resistances, one of which is the mould wall. The detailed configuration of these resistances has been studied,[102,109] and the individual values of the resistances determined. The local heat-transfer regime is shown in Fig. 33, and the system may be divided into three sections, in respect of heat transferred into the mould. The upper region receives only radiation from the slag: the middle region receives heat by conduction through a slag skin in close contact with the mould: the lower region receives heat by radiation, conduction, and convection across an air gap of a thickness which depends on the ingot temperature. From the point

31 Heat transfer in hollow-ingot ESR furnace[107]: $1 \text{ kcalm}^{-2}\text{h}^{-1} = 1.17 \text{ Jm}^{-2}\text{s}^{-1}$
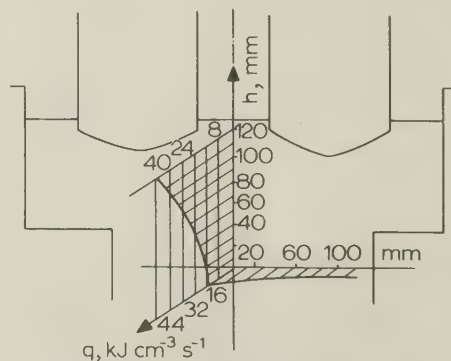
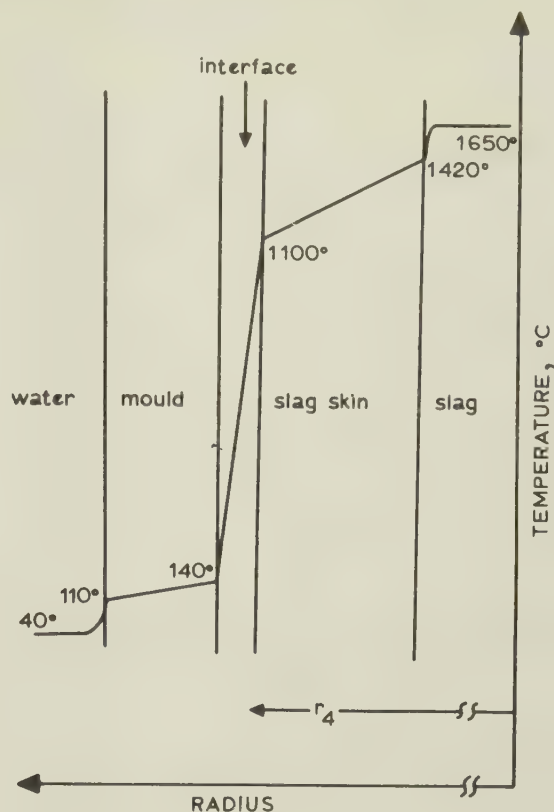32 Heat transfer in bifilar ESR furnace slag region[107]
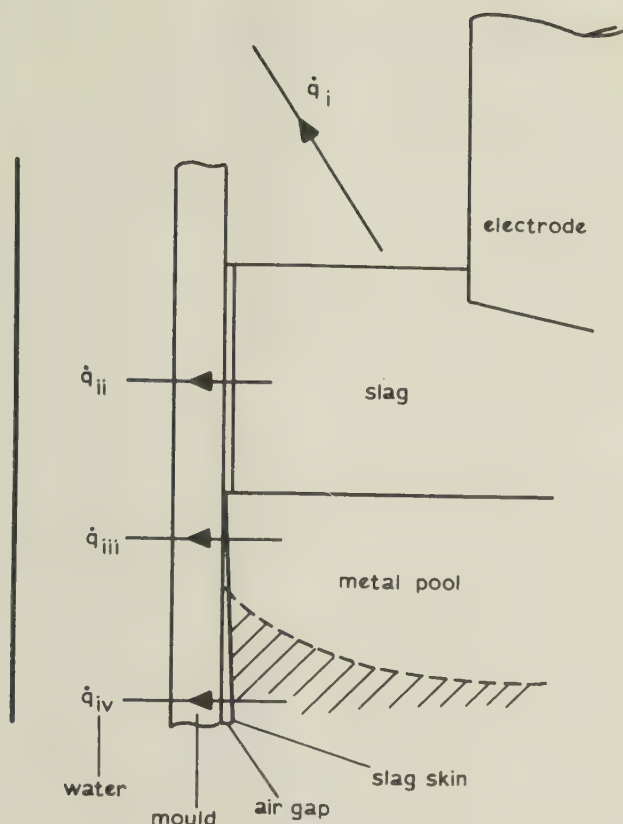
33 Scheme of heat flow in ESR furnace[102]: q_i = heat loss to atmosphere, q_{ii} = heat loss in slag region, q_{iii} = heat loss in 'good-contact region', q_{iv} = heat loss in 'air-gap region'

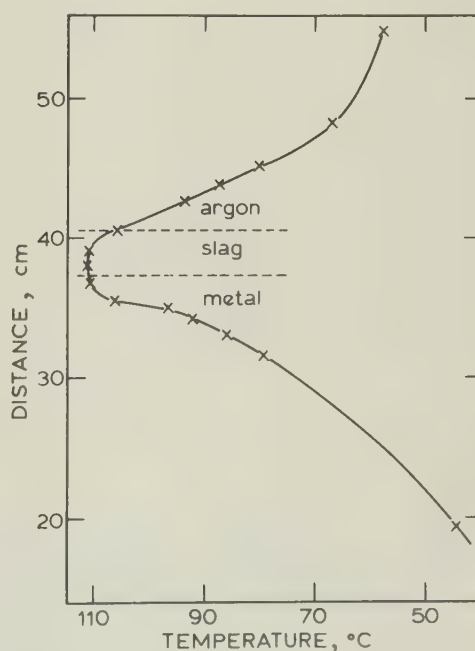34 Thermal gradients in q_{ii} region of Fig. 33, when q_{ii} = 20 cals^{-1}cm^{-2} (Ref. 102)

of view of mould design, the only important region is the middle section, since it is in this region that the highest heat fluxes develop. Using a heat-flux value of 20 calcm^{-2}s^{-1} and the heat-transfer coefficients developed by Mitchell and Joshi[102] a system of typical temperatures across the mould/slag or mould/metal interface may be developed as shown in Fig. 34. The only reported measurements of temperature in such a system were made[103] on the water/copper interface under similar heat-flow conditions, as shown in Fig. 35. It is seen from Fig. 35 that the mould/water interface is significantly above the boiling point of water, and the implications of this in mould design must therefore be considered.

Mould temperatures and heat extraction

It has been established by the preceding discussion that the major design requirements of an ESR mould are that it should be capable of removing up to 40 calcm^{-2}s^{-1} from a process region of up to 5 cm in depth and that it should be capable of removing up to 80% of the total process heat at any given time. The conventional mould design uses water-cooled copper and this combination under the above restrictions in heat flow will be considered first.

35 Heat flow in mould region as represented by temperature of mould/water interface, for conditions of Fig. 34 (Ref. 102): water flow-rate at mould surface is 0.5 ms^{-1}
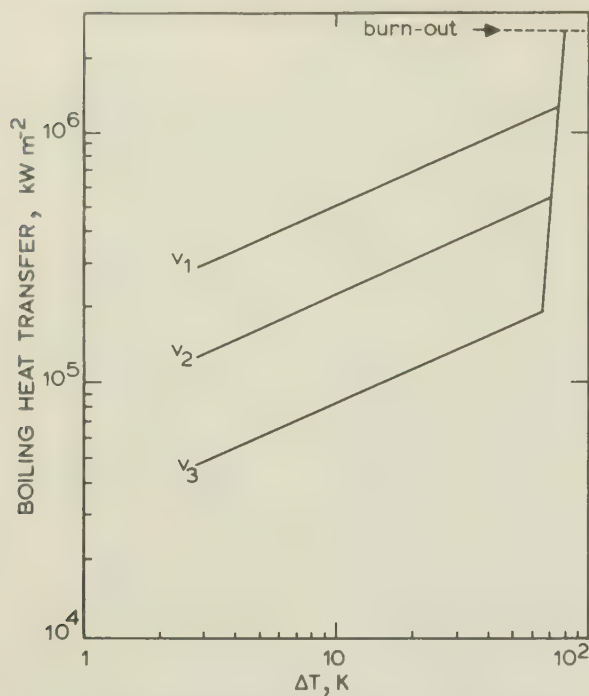
36 Boiling heat transfer data for subcooled
    forced convection (Ref. 110): $v_1 = 2.6$ ms^{-1},
    $v_2 = 1.3$ ms^{-1}, $v_3 = 0.3$ ms^{-1}, $\Delta T =$
 $T_{surface} - T_{bulk\ fluid}$

The transfer of heat from metal to water surfaces has been studied very extensively.[110-115] On combining this information with our present knowledge of mould heat fluxes and temperatures it is clear (Fig. 36) that the ESR mould/water interface is in a thermal regime where relatively small changes in heat flux, mould temperature, water temperature, water velocity, and mould-surface condition will all strongly influence the surface heat-transfer condition by changing the mode between boiling and non-boiling. The choice should therefore be made between either of two fundamentally different mould designs, namely, the boiling mould and the non-boiling mould. In the former, the heat flux is accommodated with a relatively high mould temperature and a low bulk-water velocity, making use of the very high nucleate boiling heat-transfer coefficient. In the latter, boiling is prevented by using a very high surface water velocity and hence the required heat flux is transferred at a lower mould temperature.

The early designs used by workers in the USSR[116] and the spray-cooled moulds used in some European ESR furnaces[117] are boiling moulds, intended to minimize water flow and hence simplify mould design. The mould designs using annular water jackets,[118,119] and those using channel cooling,[120,121] are intended largely to prevent boiling by providing a high surface-water velocity. In order to compare these two philosophies of design the implications of mould tem-

perature, which is the main variable between the two cases, must be considered.

The mechanical properties of most commercially available grades of high thermal conductivity copper follow the general curves shown[122] in Fig. 37. It will be noted that the alloys close to pure copper in composition have low creep strengths, becoming particularly weak as the temperature rises above 150°—200°C. It is advisable, therefore, to keep the copper mould wall at as low a temperature as possible, and certainly below 200°C, if it is to be subjected to a finite level of stress.

In the case of a boiling-water mould, the active region of the mould is kept at a superheat temperature above 100°C which depends on the bulk temperature of the cooling water (Fig. 36). Under normal conditions, the bulk-water temperature will be not greater than 25°C, leading to a maximum projected mould/water interface temperature of 120°C. Following the data of Fig. 34, such a regime would produce an inner-face temperature (on a 30 mm thick copper wall) of 240°C. Under these conditions, most of the mould wall is at an acceptably low temperature. It can be seen that such a mould-cooling system, therefore, is a viable method for ESR heat fluxes, provided that steady nucleate boiling can be maintained at all times. Examination of Fig. 36, however, shows that at the very low bulk-water velocities employed in boiling-water moulds, any momentary interruption in water supply to the active mould region will produce a rapid increase
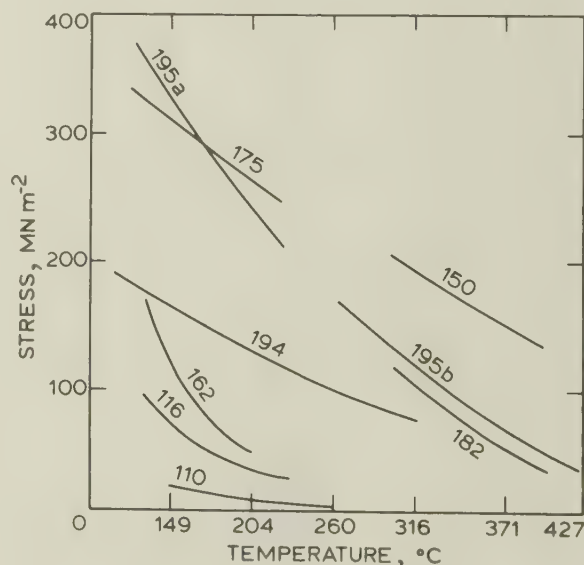
37 Creep strength of various copper alloys[122]:
    110 = annealed Cu, 116 = 0.05%Ag, 150 =
    0.15%Zr, 162 = 1.0%Cd, 175 = 2.5Co—0.6Be,
    182 = 0.9%Cr, 194 = 2.4Fe—0.13Zn—0.4P,
    195a = 1.5Fe—0.8Co—0.6Sn—0.1P, worked,
   195b = 195a annealed

to an unacceptably high mould temperature. Equivalently, any transient, unusually high heat fluxes will lead to film boiling and hence also to unacceptably high mould temperatures. We may conclude, then, that while the boiling-water mould appears to offer an adequate steady-state cooling system, it does not provide adequate protection against the transient adverse situations which frequently occur in ESR practice.

The non-boiling-water-cooled mould is intended to operate close to the initiation point for nucleate boiling on the mould/water interface. It may readily be seen from Fig. 36 that under the normal range of ESR heat flux such a condition demands surface-water velocities of at least 3 ms^{-1}. The design consequence of such a condition is that large volumes of cooling water are required. As an example, we may consider the case of a 500 mm dia. static ESR mould, with a mould wall thickness of 20 mm. An annular gap of 20 mm is required for adequate operating clearances (unless special ribbing, etc. is used), leading to a minimum acceptable water flowrate of 106 ls^{-1}. Increasing the annular gap to 50 mm raises this water requirement by almost three times. It can be seen that the condition of 3 ms^{-1} minimum velocity is therefore a very serious design restriction unless the system is to circulate completely unreasonable volumes of cooling water, or to use equally unreasonable circulating water pressures for narrow-gap cooling annuli.

The non-boiling system operates at lower mould temperatures than does the boiling system, but the absolute temperature difference is not great unless the impinging water flow is at a low bulk temperature. However, if the bulk temperature is at the assumed level of 25°C, the difference between the mould surface temperatures in the two systems is about 70K. In the example case above of a 30 mm mould wall carrying 30 calcm^{-2}s^{-1}, the mould inner-face temperature would hence be 170°C, the mould/water interface remaining at 50°C. Such a lowering of overall mould-wall temperature is quite significant in increasing the effective creep resistance of the mould.

In addition to the above advantage in overall mould temperature, the non-boiling system contains an important inherent ability to accommodate both transient high-heat flows and perturbations in the local condition of the mould/water interface. Significant transient heat-flux peaks can be dissipated by the system passing into nucleate boiling.

Few details are available on the extent to which ESR mould designs seek to take advantage of the mechanism available for increasing heat transfer under either of the above modes. For example, boiling may be influenced by the surface condition of the mould[112] so that a change from a mechanically roughened surface to a smooth-plated surface changes the temperature of onset of boiling by almost 10 K (Fig. 38). In a similar manner, the chemical composition of the water, with respect to gas content, has a great influence
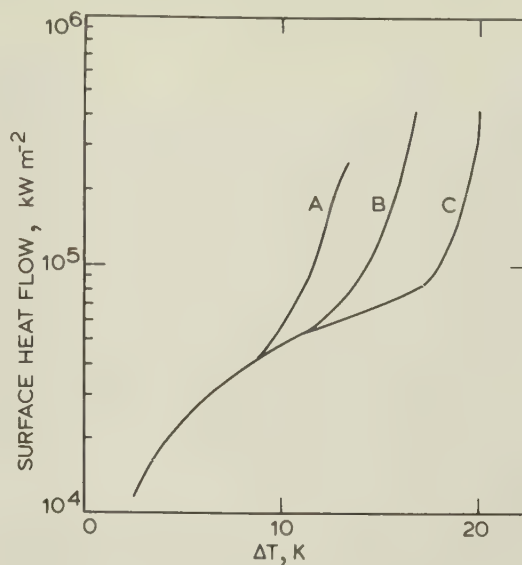

38 Surface heat flow for various heated surfaces cooled by water[112]: A as manufactured, B mechanically roughened, C chromium plated; $\Delta T = T_{\text{surface}} - T_{\text{bulk fluid}}$

on the temperature at which nucleate boiling commences. There is equally little information on the influence of chemical surface scale in retarding ESR heat transfer. Under the heat fluxes experienced in ESR, only a very thin layer of low-conductivity scale is required to raise the mould temperatures by a significant amount. As an example, we calculate that a 0.5 mm thickness of calcium carbonate scale would raise all mould temperatures by 100 K in the example case given above. Evidently, close attention should be given to the possibility of controlling the formation of such scales.

A great deal of work has been done in the USSR relating to the control of mould inner-face temperature through the means of cooling rate. Shevtsov *et al.* report[120] a method of calculating cooling rates in both annular and channel-cooled moulds, based on the effective heat-transfer contact area between the mould and cooling water.
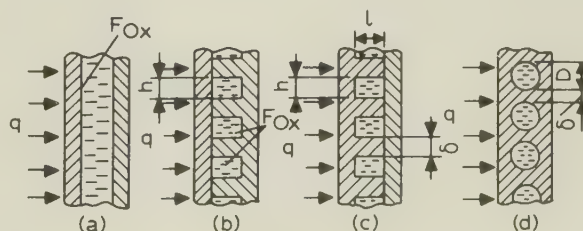
39 Various types of cooling channels used in ESR moulds[120]: F_{Ox} = water/process heat-transfer surface
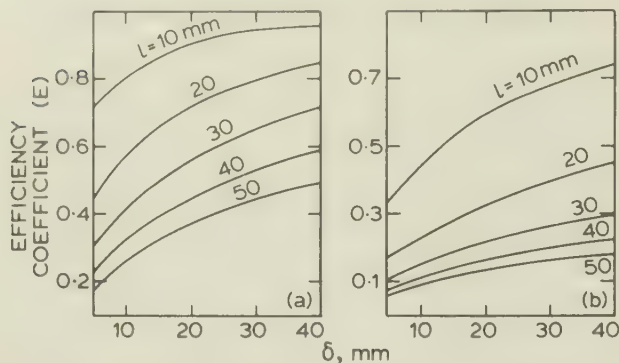
40   **Efficiency coefficient for fin dimensions (Fig. 39c) in *a* copper and *b* steel[120]**

Four cases are reported:

(i)   the water flows in an annular water jacket (Fig. 39a). In this case the effective heat-transfer area F_{eff} is the total mould/water interface area $F_{contact}$

$$F_{eff} = F_{contact} \quad \cdot \quad \cdot \quad \cdot \quad \cdot \quad \cdot \quad \cdot \quad (1)$$

(ii)   the water flows in channels made in the jacket wall (Fig. 39b)

$$F_{eff} = nSh \quad \cdot \quad \cdot \quad \cdot \quad \cdot \quad \cdot \quad \cdot \quad \cdot \quad (2)$$

where S and h are the length and width, respectively, of the cooling channels, n in number

(iii)   the water flows in channels made in the mould wall, and is confined on one side only by the annular jacket (Fig. 39c)

$$F_{eff} = nS(h + 2El) \quad \cdot \quad \cdot \quad \cdot \quad \cdot \quad \cdot \quad (3)$$
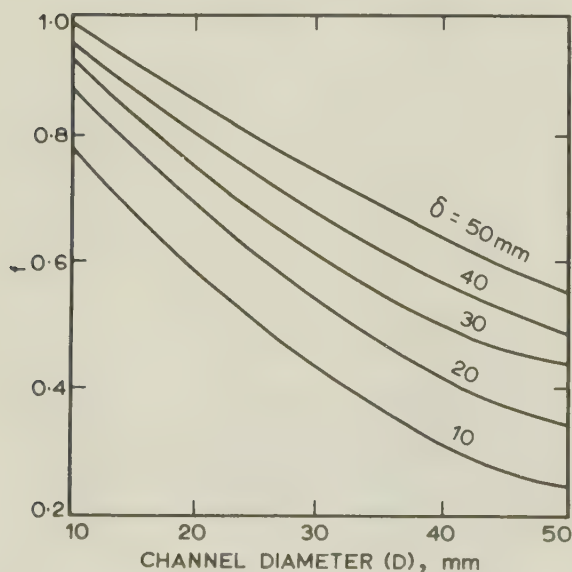
41   **Relationship between coefficient *f*, cooling channel diameter *D*, and separation δ (Fig. 39d) (Ref. 120)**

where l is the depth of the cooling 'fin' and E is an efficiency factor introduced to take account of the varying radial temperature of the fin during heat transfer. Values of E for copper and for steel are shown[120] in Fig. 40

(iv)   the water flows in vertical channels inside the mould (Fig. 39d)

$$F_{eff} = nD(1 + 2.14f)S$$

where f is an efficiency factor selected from Fig. 41 for a particular channel diameter D and n is the number of channels in the mould.

Using these values of F_{eff} together with the appropriate heat-flux values and a boiling or non-boiling heat-transfer coefficient for the metal/water interface and water velocity involved, the temperature distribution in the mould may thus be computed. This method has also been extended to shaped moulds and hollow-ingot moulds by Marinskii and Shevstov,[106] who have developed the concept of effective heat-transfer area for a number of shaped systems.

It is interesting to note that the thermal regime adopted in furnace designs in the USSR leads to mould-face temperatures which are relatively high. A typical regime is shown in Fig. 42, in which the face temperature is seen to rise to over 300°C.

**Practical aspects of cylindrical mould design**

What has become the classic mould design for VAR furnaces (a closed-end tube submerged in an annular cooling jacket) is not used in most ESR furnaces. On the one hand, moving-mould (or moving-ingot) furnaces obviously cannot use such a design and, on the other, assembly of static-crucible furnaces is much simplified by using an open-ended mould resting on a fixed, separate base-plate. Such mould designs have been discussed and illustrated in the literature.[118-120] The practical problems appear to arise from a common cause, namely, the severe thermal cycling of the copper
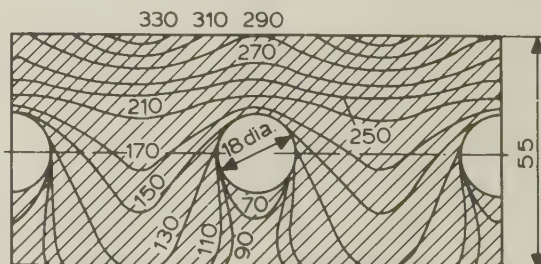
42   **Temperature distribution in typical channel-cooled ESR mould wall: $q_i = 20$ cal cm^{-2} s^{-1} (Ref. 121), dimensions in mm; temperatures in °C**

mould. The thermal cycle discussed above results in a substantial portion of the mould experiencing a temperature of at least 200°C on a cyclic basis. The resulting expansion results in the development of a stress field which may cause mould-wall failure by either creep deformation or fatigue. The former mechanism leads to a gradual distortion of the mould section which rapidly deteriorates as it is subsequently damaged by the withdrawal of mis-shaped ingots. The latter effect is more pronounced on moulds containing weldments, which are particularly prone to fatigue failure. For these reasons, mould design has been directed towards, first, minimizing the stress field and, secondly, using alloys and structures less prone to deformation and fatigue failure.

The conventional annular cooled static-mould crucible consists of a copper tube held in a stainless steel water jacket by seals and/or flanges at each end. It is removed from the ingot by simply raising it upwards while the ingot and mould are in a vertical position (Fig. 43). The copper tube may be an extruded or forged tube, an electroplated form, or a rolled plate with a one (or more) longitudinal seam weld. The effect of thermal distortion is usually minimized by maintaining the wall thickness at the thinnest permissible level (usually 20–30 mm), by using a high water velocity, and by using clean, recycled water. The reaction
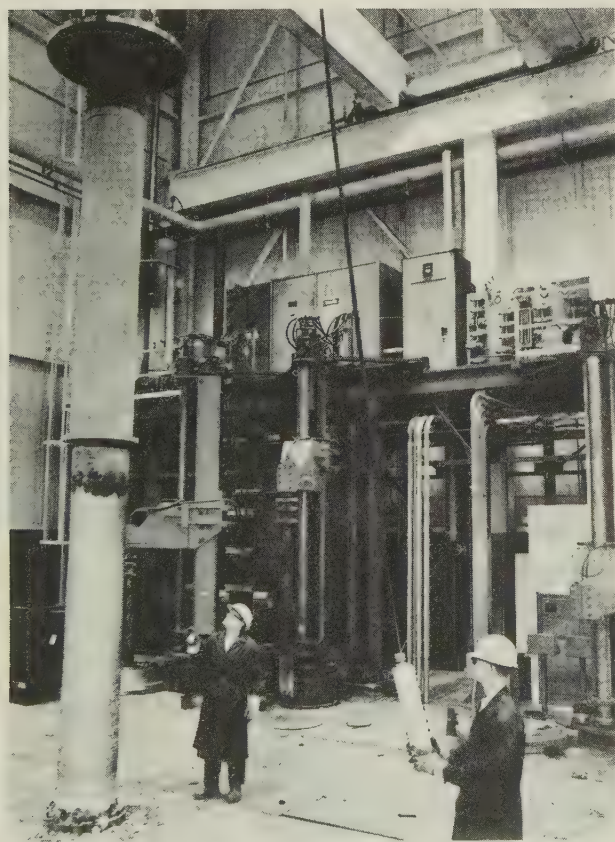
of the above copper fabrications to stress differs between the structures.[123] The single-piece tube normally deforms slowly in a symmetrical manner, leading to the 'coke-bottle' defect.[123] The electroformed plate is susceptible to exfoliation between the various plated layers. The welded structure is prone to non-symmetrical deformation or fatigue cracking in the weld region. It appears that, in practical terms, the small ESR moulds (200–500 mm dia.) may be made by any of the three methods, but that the large moulds must be weld fabricated. For this reason, mould designers generally have attempted to minimize the stress field, rather than accommodating stress, in using copper alloys which have improved creep strength, since most of such alloys cannot be welded to give high-strength welds by conventional welding methods. Reviews of the welding methods used[124–126] indicate that because of the high preheat required in welding, the mould becomes fully annealed and thus loses the valuable strength increment due to cold work. In this connection, it is worth noting that delay in removing the mould from a hot ingot after the cooling water has been disconnected can lead to thermal stress levels much higher than those normally experienced during melting. Indeed, much of the mould damage attributed to ESR arises in mould handling before and after melting rather than during the process itself.

The moving mould–ingot crucible design has closely followed the design trends evident in continuous-casting moulds. Most of such moulds are channel cooled with high-velocity water (2–6 ms^{-1}), following the layout shown in Fig. 39. It is evident from the literature[127–131] that the heat fluxes in continuous casting of steel are very similar to those in ESR and, hence, it is logical that the mould design should be a close parallel. Measurements of heat flux[132] show (Fig. 44) that the vertical profile reaches significantly higher peak values in continuous-casting moulds than in

43 Mould-stripping stage in 500 mm dia. ESR furnace
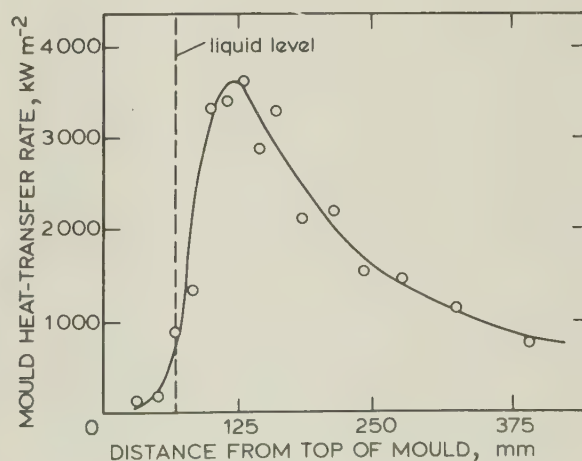
44 Continuous-casting mould heat-transfer rate for 1.5%C steel, 20 mms^{-1} (Ref. 132)
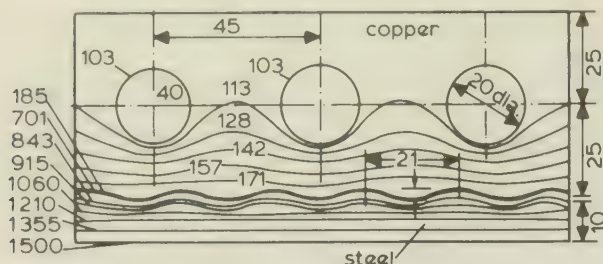
45 Thermal gradients developed in typical slab mould (channel cooled) for continuous casting of steel: dimensions in mm, temperatures in °C (Ref. 128)

ESR, but that the form of the profile is similar. In general, it appears that in ESR as in continuous casting, the moulds are designed with cooling channels of 15—25 mm dia. (Figs. 42, 45) and wall thicknesses of 50—70 mm, leading to hot-face temperatures of 200°—300°C. It is probable that, in both cases, some nucleate boiling takes place on the 'hot' side of the channel, but almost all the heat transfer is by forced convection. Both types of mould have been found to suffer from failures due to thermal distortion and cracking in the same manner as for static crucibles. However, detailed calculations of the stresses developed appear to have been carried out only in the case of continuous-casting moulds,[128] where it was suggested that less efficient cooling, leading to lower temperature gradients, might be effective in reducing mould damage.

An additional mechanism for mould wear appears in moving mould—ingot ESR systems which is not significant in static crucibles, namely, arc damage. A significant fraction of the process current in ESR is carried[103] by the mould wall, which encounters the high-temperature region through a series of point contacts. In the portion of the mould close to the slag/metal interface in a moving system, the mould wall is in good electrical contact with the ingot and no arcing normally takes place. At the slag/atmosphere interface, however, almost the full working potential exists across a thin layer of solidifying slag and the current is transmitted into the mould by a series of small, transient point arcs. Since (as described by Ballantyne and Mitchell[133]) it is important as a process control to maintain a constant vertical position of the slag/metal interface in the mould, the portion of mould surface subjected to such arcing remains the same for long periods of time. The resulting arc damage resembles spark erosion and has been described in detail by Medovar *et al.*[134] The mould is thus eroded around a narrow ring at the slag/atmosphere interface in a manner which is difficult to repair. There has been no published report of a design solution to this problem.

A number of reports[106,108,116,117,121] have described the use of shaped ESR moulds. In such a

system	dimension, mm	% of heat into mould
	350 dia.	59
	100 dia.	63
	25 x 1000	59
	500 x 1200	48
	120 x 1100	67
	400 / 400 dia.	46

46 Heat flow into mould in ESR shaped casting (Ref. 135)

mould configuration, the portion containing the electrode melting region normally has a larger diameter than that containing the ingot (Fig. 46). The basic reason for applying this concept to cylindrical ingots appears to be that the effective fill-ratio of electrode/mould diameter is much larger and, therefore, the problems of wall erosion do not take place.[121] The use of such moulds does, however, introduce a new and significant difficulty in that it is now necessary to maintain very close control over the slag/metal interface position in the mould.[135]

Practical aspects of slab-mould design and use

The conditions for the severity of the heat-flux gradients in slab-mould ESR operations are similar to those in the use of round moulds. However, the similarity stops at that point. Most notable is that in slab-mould design, there is a basic non-symmetrical heat flow in the horizontal plane.

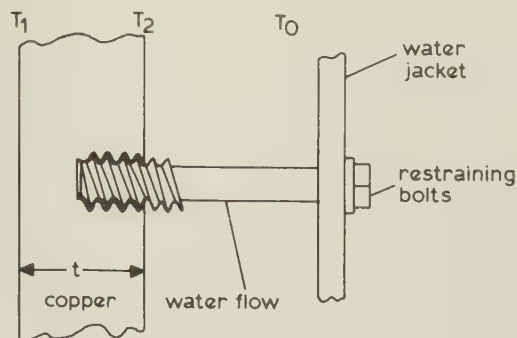47 Schematic of mould structure around restraining bolt

The design of slab moulds has generally evolved into two basic forms: a four-piece or 'book'-style mould, and a continuous copper liner formed and shaped with a welded joint. A major problem in the design of slab or rectangular-section ESR moulds is to maintain flat mould surfaces for a relatively long interval between maintenance repairs. The inherent thermal stresses tend to set up a variety of expansion and contraction stresses in the copper, tending to make the flat sides bow with respect to the vertical plane.

Early slab-mould designs of the book style had many problems with respect to the sealing between the copper and the water jacket. A variety of rubber and/or silicone rubber materials and retaining configurations were employed to provide adequate resistance to both the heat-related effects and also the stress and thermal distortion of the copper relative to the water jacket. As may be selfevident, it is imperative that there be no water leaks into the mould cavity during the electroslag process. While a relatively small water seepage may not present an explosion hazard, it may provide a source for considerable hydrogen pick-up in those materials sensitive to hydrogen.

Operating problems with the use of larger slab moulds appear to increase in direct proportion to the maximum horizontal dimension of the mould. The degree of this operating problem may be illustrated by recognizing that it is common to obtain more than 1000 heats on a cylindrical ESR mould, while the typical service life until repair for a slab mould is in the order of a few hundreds of heats. The resultant design considerations for a slab mould tend to make their price in the order of 50—200% greater than an equivalent cross-sectional area in a cylindrical mould.

One design consideration which may be apparent is that a cylindrical mould design is inherently a balanced system with respect to the hoop stress of either the mould wall or the water jacket as opposed to the hydraulic pressure exerted by the cooling water. In the case of the slab mould, all stresses resulting from the hydraulic forces of the cooling water must be completely contained and balanced between the two parallel faces of the copper liner and the cooling-water jacket. A substantial amount of internal fabrication and also complex methods for connecting the copper to the water jacket all tend to complicate the design of these moulds with resulting increased costs.

While some of the earlier (1969) 350×1000 mm section slab moulds may have operated under boiling-water cooling conditions, the tendency has been towards the use of non-boiling water systems as the mould dimensions have grown towards 750 × 2000 mm in 1975. It has become apparent that the increased creep resistance afforded by the lower average copper temperature produced by high-velocity cooling water has substantially improved the in-service performance of these moulds. Because of the relatively large water-channel areas for large slab moulds, rather large cooling-water pumping systems must be employed, leading to an additional power consumption.

A general discussion of the current status of ESR mould design is given by Zak.[136] His report highlights the large, slab-mould design for Lukens Steel (Coatesville, Pa) measuring 750×2000×2900 mm for 33 ton ingots. Several photographs of various large slab moulds are given, along with general descriptions of the principles of mould design and the problems of dimensional stability.

The economic analysis as given by Zak[136] indicates a justification of liner replacement for the 750×2000 mm size at 257 heats and the replacement of a 750×1500 mm size at 360 heats.

Some details[137] of the stresses, properties of copper alloys, and typical design considerations for slab moulds are developed below. The stress system in the mould material (usually copper) must be examined carefully in order to design properly adequate structural support and achieve mould longevity. Among the considerations are the water flowrate next to the copper and the overall hydraulic pressure of the system, as shown in Fig. 47.

The water flowrate and temperature near the cold face of the copper will greatly influence the stress in the copper by altering both T_2 and T_1. As the flowrate increases so that heat removal becomes primarily convective, the differential between T_1 and T_0 will become less, and hence the hot-face temperature will be reduced. This will reduce the bending stresses in the copper and thus
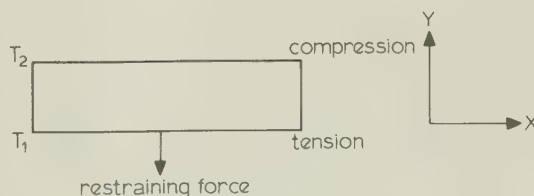
48 Bending stresses in heat mould section

reduce stresses in the restraining bolts. However, increased water velocities are normally accomplished by increasing the water pressure, and hence, the hydraulic forces of the water will add back a portion of the stresses removed because of lower copper temperatures.

It is generally believed that water flowrates of 2–3 ms^{-1} near the copper will minimize the T_1-T_0 temperature differential at normal ESR power levels. This assumes, of course, a clean copper surface. Oxidation films or particulate build-ups will drastically decrease the heat-removal rates and increase copper operating temperatures and stresses.

Bending stresses caused by the temperature differential through the copper wall thickness will also influence mould design. Figure 48 reflects the stress state of any flat portion of an ESR mould (square or slab cross-section) during the time period when the molten-slag zone is passing it. The X and Y directions are the width and thickness directions of the copper. The Z direction, or height, is the viewing direction.

The maximum stress, assuming the copper is restrained to remain flat, is[138]

$$\sigma_{max} = \frac{E\alpha(T_2-T_1)}{Z}$$

where

σ_{max} = the maximum ligament stress

E = modulus of elasticity

α = coefficient of linear expansion

T_2, T_1 = hot and cold face temperatures.

Typically, T_2-T_1 ranges between 50 and 100K/in of copper for the slags and power levels normally used for industrial ESR equipment. This corresponds to maximum stress levels of 45–90 MNm$^{-1/2}$ for 25 mm copper or 90–180 MNm$^{-1/2}$ for 50 mm copper.

Operating temperatures of the hot face of the copper depend greatly on water flowrates and oxidation films on the copper, but generally will range between 85° and 140°C for 25 mm copper

and 140° and 240°C for 50 mm copper for properly designed moulds and water flowrates.

An assessment of the data in Table 4 indicates that electrolytic tough-pitch copper is not suitable for creep resistance, even at 25 mm thickness. Silver-bearing copper is marginal at 25 mm thickness. At 50 mm copper thickness chrome-bearing copper is marginal and the magnesium—zirconium—chromium copper is preferred.

The mould is observed to undergo long-term shape changes owing to creep. This is because the hot face creeps in compression before the cold face yields in tension, and hence there is an overall tendency for a flat copper plate to shrink in the two large dimensions (particularly width) and grow in thickness. This has been found to occur on numerous occasions and is a major cause for mould repair.

The copper material chosen and the thickness chosen should reflect consideration for the potential for mechanical abuse and arc damage. Indeed these factors are probably overriding in some instances. Most mould builders and ESR manufacturers prefer to use heavy-walled copper (over 35 mm) despite the extra potential for mould distortion, discussed above, because of the extra safety factor and because of the ease of attaching restraining bolts by drilling and tapping.

Some large slab moulds used in furnaces constructed in the USSR are also of the book design, and are described by Medovar and Paton.[139,140] However, most smaller slab moulds used in furnaces in the USSR appear to use the channel design discussed above.

There has been relatively little growth of ESR furnaces employing a large slab-mould design. Table 5 indicates the location and approximate date of commissioning of the largest slab section for various countries.

In summary, the application of cylindrical ESR mould design to that of slab-mould design has not been at all straightforward. Instead, a considerable amount of new technology had to be developed and the resulting complications in design and practice have led to a substantially greater operating cost with respect to the slab-

Table 4 Creep resistance of various materials

Material	Test temperature °C	Stress level for 1% creep in 100 000 h, MNm$^{-1/2}$
Electrolytic tough-pitch copper	150	6.4
Silver-bearing copper	205	6.4
Chrome-bearing copper	300	8.2
Magnesium—zirconium—chromium copper	400	14.5

Table 5 Dates of commissioning of largest slab section in various countries

Company	Country	Mould dimensions, mm	Weight, t	Date
Nippon Steel Co.	Japan	510 × 2400	40	1974
		570 × 1900	29	
		300 × 1900	17	
		450 × 1200	5	1971
Lukens Steel Co.	USA	750 × 2000	33	1975
		750 × 1500	25	
Inco Huntington Alloys	USA	300 × 1300	10	1971
Rheinstahl	Germany	600 × 1000	6.2	1968
Boehler Bros.	Austria	260 × 1150	2.2	1962
Avesta	Sweden	400 × 1200	9.0	1970
Electrometal AS	Brazil	430 × 910	7.0	1973
British Steel Corporation	UK	305 × 1420		
		250 × 1100		
		203 × 1015		
		1000 × 3000		1977
Cyclops Specialty Steel Corp.	USA	300 × 1100	8.5	1975
Zaporoziyhe	USSR			
(Y—436M)		630 × 1430	18	1966
		630 × 1340		—1973
		630 × 1100		
(Y—436Y)		400 × 1200		
(Y—436C)		120 × 1530		
		120 × 1250		
		120 × 1000		

mould operation. Perhaps it is the cost associated with the purchase and operation of large slab moulds that serves to exert the greatest limitations on the expansion of ESR into substantially heavier ingot sections. An attempt to overcome some of these costs has resulted in additional interest in operating a short or 'collar'-mould design with a relative ingot—mould movement. Successful operations of this sort are routine in sizes up to 510×2400 mm. However, at this time it does not appear that there is any completely successful or universal solution to low-cost operation of large rectangular-section ESR slab-mould operations.

REFERENCES

1. H. Hinze *et al.*: 'Proc. 3rd int. symp. on ESR', Part 2, (eds. G. K. Bhat and A. Simkovitch), 159; 1971, Pittsburgh, Pa, Mellon Institute.
2. A. S. Ballantyne and A. Mitchell: *Ironmaking Steelmaking*, 1977, 4, 222—239.
3. A. S. Ballantyne and A. Mitchell: 'Proc. 5th int. conf. on ESR', Vol. 1, (eds. G. K. Bhat and A. Simkovitch), 345; 1974, Pittsburgh, Pa, Mellon Institute.
4. S. Kou, D. R. Poirier, and M. C. Flemings: *Metall. Trans.*, 1978, 9B, 711—719.
5. A. S. Ballantyne, R. J. Kennedy, and A. Mitchell: 'Proc. 5th int. vac. met. conf.', 181—185; 1976, Munich, Leybold-Hereaus.
6. W. Holzgruber: 'Proc. 5th int. conf. on ESR', Vol. 1, (eds. G. K. Bhat and A. Simkovitch); 1974, Pittsburgh, Pa, Mellon Institute.
7. F. S. Suarez, J. E. Roberts, and L. D. Schley: 'Proc. 5th int. conf. on ESR', Vol. 1, (eds. G. K. Bhat and A. Simkovitch); 1974, Pittsburgh, Pa, Mellon Institute.
8. P.-O. Mellberg: PhD thesis, Royal Technical University, Stockholm, 1974.
9. M. Flemings: 'Solidification processes'; 1974, New York, McGraw-Hill.
10. A. S. Ballantyne and A. Mitchell: 'Solidification and casting of metals', 363—370; 1979, London, The Metals Society.
11. A. S. Ballantyne *et al.*: 'Proc. 6th int. vac. met. conf.', American Vacuum Society, San Diego, 1979, in press.
12. P. Dewsnap and R. Schlatter: 'Proc. 6th int. vac. met. conf.', Vol. 1, 91; 1979, San Diego, American Vacuum Society.

13. A. Mitchell, J. Szekely, and J. F. Elliot. 'Electroslag refining', 3—15; 1973, London, The Iron and Steel Institute.

14. B. E. Paton *et al.*: *Special Electrometallurgy,* 1972, (1), 144.

15. A. S. Ballantyne and A. Mitchell: Proc. 7th Int. Forgemasters Conf., International Society of Forgemasters, Paris, 1975, Paper 29.

16. M. A. Maulvault and J. F. Elliot: *AIME Elec. Furn. Conf. Proc.,* 1970, **28**, 13—20.

17. B. E. Paton, B. I. Medovar, D. A. Kozlitin, Yu. G. Emel'Yanenko, Yu. A. Sterenbogen, and V. M. Baglai: 'Electroslag refining', 16—20; 1973, London, The Iron and Steel Institute.

18. A. Mitchell: Proc. World Electrotechnical Congress, Moscow, 1977, in press.

19. M. Wahlster: 'Proc. 5th int. symp. on ESR', Vol. 1, (eds. G. K. Bhat and A. Simkovitch); 1974, Pittsburgh, Pa, Mellon Institute.

20. M. Wahlster: 'Proc. 4th int. symp. on ESR', 337; 1973, Tokyo, Iron and Steel Institute of Japan.

21. I. Niimi: 'Proc. 4th int. symp. on ESR', 322; 1973, Tokyo, Iron and Steel Institute of Japan.

22. R. Schumann and C. Ellebrecht: 'Proc. 5th int. symp. on ESR', Vol. 1, (eds. G. K. Bhat and A. Simkovitch), 180; 1974, Pittsburgh, Pa, Mellon Institute.

23. J. H. Little, T. J. Queen, and I. M. Mackenzie: 'Electroslag refining', 43—53; 1973, London, The Iron and Steel Institute.

24. L. Stupak: 'Proc. 5th int. conf. on ESR', Vol. 1, (eds. G. K. Bhat and A. Simkovitch), 62; 1974, Pittsburgh, Pa, Mellon Institute.

25. 'Electroslag remelting and plasma arc remelting', NMAB Report 324, National Academy of Sciences, Washington 1976, 16—24.

26. P. Machner: *Berg. Hüttenmann. Monatsh.,* 1973, **118**, 365.

27. R. A. Swift and J. A. Gulya: *Weld. J.,* 1973, **52**, 537s.

28. T. Miyawaki: Proc. 7th Int. Forgemasters Conf., Paris, 1975, Paper 27.

29. H. Takada *et al.*: *Special Electrometallurgy,* 1970, 81.

30. V. J. Colangelo and K. E. Holmes: 'Proc. 4th int. symp. on ESR', 291; 1973, Tokyo, Iron and Steel Institute of Japan.

31. A. Kawaguchi: Proc. 7th Int. Forgemasters Conf., Paris, 1975, Paper 8.

32. R. J. Roberts: 'Proc. 2nd int. symp. on ESR'; 1969, Pittsburgh, Pa, Mellon Institute.

33. R. O. Jackson *et al.*: 'Proc. 4th int. vac. met. conf.', 63; 1972, New York, American Vacuum Society.

34. R. Wood and A. Mitchell: 'Electroslag processing for large forgings', EPRI Report, EP79—TPS77—721, Electric Power Research Institute, Palo Alto, Cal., 1978.

35. H. Jaeger *et al.*: 'Proc. 5th int. conf. on ESR', Vol. 1, (eds. G. K. Bhat and A. Simkovitch), 306; 1974, Pittsburgh, Pa, Mellon Institute.

36. R. Tricot: 'Production and applications of clean steels', 199—204; 1972, London, The Iron and Steel Institute.

37. T. C. Tygun-Belous: *Avtom. Svarka,* 1958, 36.

38. V. I. Yavoiskii *et al.*: *Stal',* 1962, 523.

39. L. A. Kamenskii *et al.*: *Sb. Trudov. Moskovskogo Vech. Met. Inst.,* 1971, **10**, 146.

40. A. B. Kinzel: US Patent 2 240 405, 1941.

41. E. Ploeckinger, G. Kuehnelt, P. Machner, H. Straube, and F. J. Weiss: *Iron Steelmaker,* 1976, **3**, (5), 26—31.

42. L. Cooper: 'Proc. 5th int. conf. on ESR', Vol. 1, (eds. G. K. Bhat and A. Simkovitch), 202; 1974, Pittsburgh, Pa, Mellon Institute.

43. B. E. Paton, B. I. Medovar, V. P. Andreev, G. A. Boiku, Yu. G. Emel'yanenko, V. G. Dykau, V. V. Kosyan, V. M. Baglai, Yu. V. Sobolev, and A. I. Shavrin: 'Electroslag refining', 105—112; 1973, London, The Iron and Steel Institute.

44. B. E. Paton, B. I. Medovar, and T. A. Boiko: 'Electroslag casting', 92; 1976, Kiev, Naukova Dumka.

45. B. I. Medovar, B. E. Paton, and G. A. Boiko: 'Electroslag casting', 46; 1976, Kiev, Naukova Dumka.

46. A. Ujiie, S. Sato, and J. Nagata: 'Electroslag refining', 113—125; 1973, London, The Iron and Steel Institute.

47. B. E. Paton *et al.*: 'Proc. 4th int. symp. on ESR', 209—218; 1973, Tokyo, Iron and Steel Institute of Japan.

48. B. E. Paton *et al.*: 'Proc. 5th int. conf. on ESR', Vol. 1, (eds. G. K. Bhat and A. Simkovitch), 239—251; 1974, Pittsburgh, Pa, Mellon Institute.

49. A. Ujiie: 'Proc. 5th int. conf. on ESR', Vol. 1, (eds. G. K. Bhat and A. Simkovitch), 251—272; 1974, Pittsburgh, Pa, Mellon Institute.

50. B. E. Paton *et al.*: *Special Electrometallurgy,* 1972, 169—174.

51. A. Ujiie *et al.*: US Patents nos. 3 683 997; 3 835 914; 3 921 699; 3 834 443; 3 835 916.

52. B. I. Medovar *et al.*: US Patents nos. 3 896 878; 3 878 882; 3 892 271; 3 894 574.

53. D. M. Longbottom: US Patent no. 3 902 543.

54. A. Schneidholfer: US Patent no. 3 804 148.

55. E. F. Dubrovskaya *et al.*: *Vestn. Mashinostr.,* 1975, **IV**, 62—64.

56. V. I. Rabinovitch *et al.*: *Special Electrometallurgy,* 1972, 231—237.

57. A. Ujiie *et al.*: 'Proc. 4th int. symp. on ESR'. 168—182; 1973, Tokyo, Iron and Steel Institute of Japan.

58. M. P. Braun, E. I. Mirouskii, and L. V. Chekotilo: 'Electroslag casting', 44—45; 1976, Kiev, Naukova Dumka.

59. B. E. Paton *et al.*: *Fonderie,* 1974, **29**, no. 340, 435—442.

60. L. D. Demidov, O. S. Yakushev, and V. F. Fomingykh.: 'Issled protsessov obrabotki metall davleniem', Vol. III, 173—178; 1969, Moscow, State Publishing House.

61. I. Petrman: 'Proc. 3rd int. symp. on ESR', Part 1, (eds. G. K. Bhat and A. Simkovich), 108—124; 1971, Pittsburgh, Pa, Mellon Institute.

62. G. A. Boiko *et al.*: *Rafiniruyushchie Pere-plavy*, 1974, (1), 138—142.

63. M. C. Flemings *et al.*: 'Electroslag remelting and plasma arc melting', 122; 1976, Washington DC, National Academy of Sciences.

64. A. Mitchell and A. Aktar: ASME Symp. on Materials, Nov. 1977, 1—21.

65a. A. Mitchell: Unpublished work.

65b. T. Bagshaw, P. Letcher, and R. Crofts: 'Electroslag refining', 126; 1973, London, The Iron and Steel Institute.

66. G. Bernard, M. Grumbach, and F. Moliexe: *Met. Technol.*, 1975, **2**, 512—521.

67a. G. Hoyle: 'Electroslag refining', 136—144; 1973, London, The Iron and Steel Institute.

67b. A. Schneidhofer: US Patent no. 3 804 148, 1974.

67c. D. M. Longbottom: US Patent no. 3 904 543, 1975.

68. B. E. Paton: *Problems of Special Electro-metallurgy*, 1970, 61.

69. B. E. Paton: *Special Electrometallurgy*, 1972, (1), 174.

70. B. E. Paton *et al.*: US Patents nos. 3 807 487, 1974; 3 721 286, 1973; 3 687 188, 1972; 3 768 541, 1973; 3 863 699, 1975.

71. J. P. Shtanko *et al.*: US Patent No. 3 944 714, 1976.

72a. B. I. Medovar *et al.*: US Patents nos. 3 848 657, 1974; 3 610 320, 1971.

72b. O. Kleinhagauer and W. Holzgruber: US Patent no. 3 610 319.

73. J. Klein: US Patent no. 3 721 286, 1973.

74. J. Klein *et al.*: 'Proc. 5th int. vac. met. conf.', 167—173; 1976, Munich, Leybold-Hereaus.

75. J. Akesson: *Iron Steel Int.*, 25 Feb. 1977, 74—83.

76. US Patent no. 3 944 714, 1976.

77. B. I. Medovar *et al.*: *Special Electrometal-lurgy*, 1975, (1), 9.

78. B. I. Medovar *et al.*: *ibid.*, 1975, (2), 26.

79. O. A. Terashenko *et al.*: *ibid.*, 1975, (5), 10.

80. B. E. Paton *et al.*: *ibid.*, 1975, (5), 36.

81. B. E. Paton *et al.*: *Rafiniruyushchiye Pere-plavy*, 1975, (2), 42—48.

82. A. S. Ballantyne and A. Mitchell: *ibid.*, 1979, (9), in press.

83. A. S. Ballantyne: PhD thesis, University of British Columbia, 1977.

84. B. I. Medovar: 'Electroslag remelting', 275—295; 1976, Kiev, Naukova Dumka.

85. R. H. Nafziger: *J. High. Temp. Sci.*, 1973, 5, 414.

86. G. I. Zmoidin *et al.*: *Izv. Akad. Nauk SSSR Met.*, 1976, (5), 71.

87. G. I. Zmoidin *et al.*: *ibid.*, 1974, (10), 1846.

88. G. I. Zmoidin *et al.*: *ibid.*, 1977, (3), 552.

89. G. I. Zmoidin *et al.*: *ibid.*, 1969, (6), 9.

90. G. I. Zmoidin *et al.*: *ibid.*, 1971, (6), 46.

91. A. K. Chatterjee and G. I. Zmoidin: *ibid.*, 1972, (8), 886.

92. K. Schwerdtfeger and K. Klein: 'Proc. 4th int. symp. ESR', 81—90; 1973, Tokyo, Iron and Steel Institute of Japan.

93. N. F. Yakovlev *et al.*: *Izv. Akad. Nauk SSSR Met.*, 1977, (2), 83.

94. K. Schwerdtfeger and H. G. Schubert: *Metall. Trans.*, 1977, **8B**, 535.

95. K. Schwerdtfeger and H. G. Schubert: *Arch. Eisenhüttenwes.*, 1974, **45**, 437.

96. A. Mitchell: *Trans. AIME*, 1968, **242**, 2507.

97. A. Masui, T. Sasajima, and M. Yamamura: 'Proc. 1st symp. on ESR', Vol. 1, 11—12; 1974, Tokyo, Special Melting Group, Iron and Steel Institute of Japan.

98. W. W. Scott: US Patent no. 3 857 702, 1974.

99. M. Nishiwaki *et al.*: 'Proc. 5th int. vac. met. conf.', 197—201; 1976, Munich, Leybold-Hereaus.

100. M. Allibert, J. F. Wadier, and A. Mitchell: *Ironmaking Steelmaking*, 1978, **5**, 211—216.

101. V. Ya. Saenko *et al.*: *Special Electrometal-lurgy*, 1976, (5), 27-30.

102. A. Mitchell and S. Joshi: *Metall. Trans.*, 1971, **2**, 449—455.

103. A. Mitchell and S. Joshi: *ibid.*, 1973, **4**, 631—642.

104. B. I. Medovar *et al.*: *Special Electrometal-lurgy*, 1975, (1), 9—13.

105. P. G. Clites and R. A. Beall: 'Heat balance in VAR', US Bureau of Mines Report of Investigation no. 7035, 1967.

106. G. S. Marinskii and V. L. Shevtsov: *Special Electrometallurgy*, 1975, (1), 19—20.

107. B. E. Paton *et al.*: 'Proc. 5th int. symp. on ESR', Vol. 1, (eds. G. K. Bhat and A. Simko-vitch), 411—424; 1974, Pittsburgh, Pa, Mellon Institute.

108. O. A. Terashenko *et al.*: *Special Electrometal-lurgy*, 1976, (5), 10—13.

109. B. E. Paton *et al.*: *Rafiniruyuschiye Pere-plavy*', 1975, (2), 34—41.

110. F. Kreith: 'Principles of heat transfer'; 1969, Scranton, Pa, Int. Textbook Co.

111. K. Engelberg-Forster and R. Grief: *J. Heat Transfer (Trans. ASME, C)*, 1959, **81**, 43—53.

112. I. S. Hall and P. Hatton: *Proc. Inst. Mech. Eng.*, 1965, **180**, (3c), 160—179.

113. C. Corty and A. S. Foust: *Chem. Eng. Proc. Symp. Ser. 17*, 1955, **51**, 1—28.

114. W. M. Rohsenow: *Trans. ASME*, 1952, **74**, 969—976.

115. W. H. McAdams *et al.*: *Ind. Eng. Chem.*, 1949, **41**, 1945—1953.

116. B. I. Medovar *et al.*: 'Electroslag remelting', 200; 1963, Moscow, State Scientific and Technical Publishing House of Literature on Ferrous and Non-Ferrous Metallurgy.

117. W. E. Duckworth and G. Hoyle: 'Electroslag refining', 83—87; 1969, London, Chapman and Hall.

118. J. Luchok and R. Roberts: 'Proc. 4th int. vac. met. conf.', 149—158; 1973, Tokyo, Iron and Steel Institute of Japan.

119. R. S. Cremisio and E. D. Zak: 'Proc. 4th int. vac. met. conf.', 137—149; 1973, Tokyo, Iron and Steel Institute of Japan.

120. V. L. Shevtsov *et al.*: *Rafiniruyuschiye Pereplavy*, 1972, (1), 40—45.

121. B. I. Medovar: 'Electroslag processes',
      90—109; 1976, Kiev, Naukova Dumka.
122. J. J. Cronin: *Met. Eng. Q.*, Aug. 1976, 1—9.
123. R. J. Holmes: 'Trans. vac. met. conf.',
      551—567; 1968, New York, American Vacuum
      Society.
124. Ya. L. Klyachkin: 'Svarka tsvetnykh metallov
      i ikh splavov', 284—325; Moscow Academy of
      Sciences.
125. V. Ledvinka *et al.*: *Hutnik (Prague)*, 1966, **16**,
      (6), 275—276.
126. I. M. Schetky and B. B. Moreton: *Metallurgie*,
      1975, **15**, (3), 118—124.
127. A. D. Akimenko *et al.*: *Izv. VUZ Chernaya
      Metall.*, 1961, (10), 29—36.
128. A. I. Chizhikov *et al.*: *Stal' in English*, 1968,
      11, 921—924.
129. A. D. Akimenko and A. A. Skvortsov: *Izv. VUZ
      Chernaya Metall.*, 1958, (12), 45—50.
130. T. Miyake *et al.*: *Tetsu-to-Hagané (J. Iron
      Steel Inst. Jpn)*, 1974, **60**, S101—102.
131. A. Yoshihara *et al.*: *ibid.*, 1975, **61**, S59.

132. S. N. Singh and K. E. Blazek: NOH—BOSC
      Meeting, 28 March 1976, AIME.
133. A. S. Ballantyne and A. Mitchell: 'Proc. 5th
      int. symp. on ESR', Vol. 1, (eds. G. K. Bhat
      and A. Simkovitch), 115—130; 1974, Pittsburgh,
      Pa, Mellon Institute.
134. B. I. Medovar *et al.*: *Rafiniruyuschiye Pere-
      plavy*, 1974, (1), 35—40.
135. B. E. Paton *et al.*: *Special Electrometallurgy*,
      1975, (1), 5—8.
136. E. Zak: 'Proc. 4th int. conf. on ESR', 139;
      1973, Tokyo, Iron and Steel Institute of Japan.
137. W. W. Scott: Lukens Steel Co., personal
      communication.
138. J. Timoshenko: 'Strength of materials', 3;
      1976, New York, Robert E. Krieger.
139. B. I. Medovar: 'Electroslag processes', 96, 97;
      1976, Kiev, Naukova Dumka.
140. B. E. Paton and B. I. Medovar: 'Problems of
      electroslag technology', 168—174, 234—250;
      1978, Kiev, Naukova Dumka.

George Sachs Prize 1979

The Deutsche Gesellschaft für Metallkunde
presented the George Sachs Prize for 1979
to Dr W. J. Huppmann for his achievements
in powder metallurgy research. The review
article 'Powder forging', which appeared in
International Metals Reviews (1978, **23**, 209—
239, by W. J. Huppmann and M. Hirschvogel),
together with a paper on liquid-phase
sintering, is termed an outstanding contri-
bution to powder metallurgy in the text of
the prize certificate.

Dr Huppmann, who carried out the work
at the Max-Planck-Institute for Metals
Research in Stuttgart, is now Director for
Research and Development at Sintermetall-
werk Krebsoge, a leading powder metallurgy
firm in Germany. Dr Huppmann is a member
of the Powder Metallurgy Committee of The
Metals Society.

INTERNATIONAL METALS REVIEWS
COMMITTEES IN UK AND USA

MULTICOMPONENT ALLOY CONSTITUTION BIBLIOGRAPHY 1955–1973

by A. Prince

A knowledge of phase equilibria is basic to all interested in materials whether they be metallurgists, materials scientists, ceramicists, geologists, chemists, physicists, or engineers. The relation between the constitution, the microstructure as affected by the constitution, and the material properties as reflected by the microstructure, is of paramount importance to the understanding of materials, to the development of new materials, and to the improvement of existing materials.

The literature on alloy constitution is a rich one. To tap these riches requires that the literature be known and readily available. The purpose of this compilation is to provide a bibliography of references to published work on the constitution of multicomponent systems as a sequel to the references published in Monograph No. 2 of The Institute of Metals, London ('The constitutional diagrams of alloys: a bibliography', J. L. Haughton and A. Prince, 1956, pp. 230–324). The current compilation contains references to work published from January 1955 to December 1973. For the year 1955 only references additional to those included in The Institute of Metals Monograph have been incorporated.

The current compilation contains over 18000 references. References have been given for alloy systems, systems containing metalloids, sulphide systems, and oxide systems where equilibrium with a metal is dealt with. In general, references to equilibria between oxides have not been included. References to crystal structure determinations have been included in addition to publications on phase equilibria. The inorganic synthesis of ternary compounds has been included as have references to work on property–composition relations that provide constitutional data. The growing interest in the calculation of phase equilibria has been recognized by the inclusion of such work.

xxxviii+1100 pp (code 195) ISBN 0 904357 19 8   229×153 mm

Price: UK £30·00 (Members Metals Society £24·00) post free; Overseas $90.00 (Members $72.00) post free

Send orders with correct remittance and quoting ordering code no. to:

Sales Department, The Metals Society, 1 Carlton House Terrace, London SW1Y 5DB